Radiative Processes in Active Galactic Nuclei

Thesis by

Paolo Severo Coppi

In Partial Fulfillment of the Requirements
for the Degree of
Doctor of Philosophy

California Institute of Technology
Pasadena, California

1991

(Submitted October 23, 1990)

Acknowledgements

After enduring five years of scientific hard labor, one would have thought that this section of the thesis was the easiest to write. Wrong. As I think back on my experience at Caltech, there are many faces that come to mind of people who either were instrumental in furthering my scientific development or simply made existence here bearable, enriching, and, yes, even enjoyable at times. So many, unfortunately, that I don't know what to do. The list below is but a small sampling of them. To those who have been omitted, my apologies. You have not been forgotten.

The first to whom I owe a debt of gratitude are my parents, Bruno and Maria Coppi. To them this thesis is dedicated. Without their unflagging support and encouragement, I never would have even made it to Caltech.

Next are the faculty members of the Theoretical Astrophysics group, Peter Goldreich, Sterl Phinney, and Kip Thorne. Through their seminars and willingness to talk and share ideas, they provided an incredible environment in which to learn. I would especially like to thank Sterl Phinney for his role as *ersatz* advisor when my true advisor, Roger, was busy or away (much of the time). Whenever I found myself particularly befuddled, it was always reassuring to know I could walk into his office and have the veil of ignorance lifted. Peter Goldreich also deserves mention for his concern in the welfare of graduate students and willingness to dispense general advice. At the very least, his constant goading on of the graduate students and postdocs to exercise has prevented me from becoming a complete physical wreck. (In this regard, my father and I would like to thank him for a memorable hike.)

An essential part of the learning environment was also provided by the postdocs in our group. These include: Omer Blaes, Robert Emmering, Chuck Evans, Piero Madau, Norm Murray, Pierre-Yves Longaretti, Bharat Ratra, Isaac Shlosman, Chris Thomson, Jens Villumsen, Tim de Zeeuw, and Andrzej Zdziarski. I would like to thank them for being friends as well as unwitting teachers and receptacles for a barrage of silly graduate student questions. The last of these, Andrzej Zdziarski, deserves special mention for introducing me to the subject of pair plasmas. Either directly or indirectly, he is responsible for much of what is in this thesis. I am grateful to have been given the opportunity to collaborate with him in the years since he left here.

Although the work I did with him is not represented in this thesis, I would also like to thank Charlie Kennel, a visiting professor, for showing me how to attack a problem patiently and systematically.

The practical aspects of life in the group and as a graduate student were dealt with by the secretaries Pat Lyon and Donna Driscoll. Without them I never would have remembered to register, pick up my paychecks, and, probably, tie my shoes. Thank you.

Instrumental in preserving my sanity here were the friends with whom I engaged in often frivolous, non-scientific activity. These include the Braun/M.J. House gang of Mark Looper, Dan Ashlock, Phil Haubert, and Cole Miller (who put up with me as an officemate and valiantly tried to instruct me in the ways of basketball). Also instrumental in my survival was the "astronomy" cohort. This has included at various times: John "the Greek" Apostolakis, Johners "D.A." Conway, Helen Johnston, my erstwhile room/officemate Chris Kochanek (who for three years fought to keep me from malnutrition), the cynical Steve Myers, Julie Moses, the saucy French Canadian Alain Picard, the ever cool Rich Rand, the fierce Scotsman Ian "Neill" Reid, Chris Tinney, and Chris Wilson. I thank them for many memorable outings, softball games, and soccer matches. Equally important, but not included in either of these groups are fellow graduate students Stuart Anderson, Olivier Espinosa, Irwin Horowitz, Miloje Makivic, Alice Quillen, Steinn Sigurdsson, Sandip Trivedi, and Lin Yan.

Last, but definitely not least, I would like to thank my advisor Roger Blandford. Without him, none of what follows would have been possible. I would particularly like to thank him for the vast patience shown in dealing with one of his more trying students, a student who kept strange hours, never finished a thing on time (least of all this thesis), and had much to learn about the ways of doing scientific research. The accumulated wisdom he has tried to pass on to me in many hours of talking will not be forgotten. Roger's virtues as an advisor have been abundantly listed in the theses of his past students. I will not attempt to repeat the exercise here as I would surely do a worse job of it. The only thing I might add is that I too was extremely impressed with him, not just as a scientist, but as a person. Every young person has his role models; Roger is one of mine. It is my sincerest hope to one day repay the investment he made in me, hopefully with a little interest.

Abstract

A study of processes relevant to the electron-positron pair plasmas thought to exist in Active Galactic Nuclei is undertaken. The processes considered include: Compton scattering, pair annihilation, two photon pair production, synchrotron emission, e-e bremsstrahlung, and Coulomb scattering. Approximations used in the past to treat these processes in the context of a kinetic code are examined, and improvements are presented. A two-moment scattering formalism is presented to allow for important energy dispersion effects in scattering. This improved treatment of microphysical processes is implemented in a time-dependent, kinetic code incorporating Klein-Nishina effects on both the pair and photon distributions, relativistic thermal Comptonization, and synchrotron reabsorption.

The effects of pair plasma reprocessing on the emergent radiation spectrum are examined. Time-varying and stationary spectra are computed. Good qualitative agreement with previous calculations is found, except when the differences are attributable to the improved treatment of the microphysics. These differences can be substantial, particularly in the "photon-starved" regime where the effects of Coulomb scattering by suprathermal pairs off thermal pairs significantly modify the spectra. The spectral response of the pair plasma to variations in the particle injection is found to depend sensitively on the plasma parameters. A transitional spectrum may look very different from the spectra of either the stationary initial or final states. The highest energies (gamma-rays) are found to respond most rapidly to changes and should vary more than the X-rays. Pair plasmas can produce soft X-ray excesses. This happens under conditions independently favored by current pair plasma-Compton reflection models of the hard X-ray spectrum.

Table of Contents

Chapter 1

INTRODUCTION

1. The AGN Phenomenon

The discovery almost 30 years ago (Schmidt 1963) that powerful radio sources, identified at optical wavelengths with bright blue "quasi-stellar objects," were at cosmological distances marked the beginning of one of the more intriguing puzzles in astrophysics. From the first, it was clear that these objects ("quasars") represented a very unusual class. Their optical spectra looked nothing like that of any known stars. Superposed on an underlying power-law continuum were unusually prominent, broad emission lines. The widths of these lines indicated the presence of matter moving at velocities $\sim 10,000$ km/s (velocities typical of supernova ejecta), an indication that these objects were the site of violent activity. More importantly, their large redshifts, when interpreted as distance indicators, gave them enormous luminosities $\gtrsim 10^{44}$ ergs s^{-1}, making them the most powerful objects known in the universe.

Further study of the radio survey used to discover the quasars (the Cambridge 3C survey) revealed many of the remaining objects to be bright elliptical galaxies that showed intense emission from an unresolved source in their nuclear regions. Like the optical emission from quasars, this emission appeared distinctly non-stellar and, in fact, shared many of the same spectral characteristics (e.g., prominent, broad emission lines). Noting these similarities, the hypothesis was put forth that quasars were extreme examples of a more common phenomenon of nuclear activity in galaxies – more common because it was already known at the time that other galaxies showed evidence of similar phenomena. In the case of Seyfert I galaxies, for example, it was known that the nuclear luminosity could exceed that from the rest of the galaxy. We now know that "Active Galactic Nuclei" or AGN (unresolved sources with *non-stellar* spectra found at the centers of galaxies) are in fact relatively common. (Note the emphasis on non-stellar. We draw a distinction here between AGN and the so-called "starburst galaxies" which also show luminous nuclei but whose emission is attributed to stellar processes.) Even our own galaxy shows evidence of containing an unresolved, non-stellar source, albeit one that emits at a much lower luminosity.

The fact that Active Galactic Nuclei (AGN) occur in many different types of galaxies (containing different distributions of gas and stars) was and continues to be a source of confusion. Each newly discovered object was found to be slightly different from the previous ones seen (e.g., in the relative prominence of certain spectral lines). In time-honored astronomical tradition, a rather confusing taxonomy of subclasses within subclasses of classes (e.g., Seyfert 1,2, and 1.2's) quickly ensued. (For a discussion of this taxonomy, see Weedman 1986.) In some cases, the confusion was understandable: Seyfert 2 galaxies, for example, were thought not to exhibit the broad emission lines of Seyfert 1 galaxies. However, recent observations in polarized optical light (Antonucci & Miller 1985, Miller & Goodrich 1990) showed that Seyfert 2s do indeed emit the same broad emission lines as Seyfert 1s. This was explained by postulating the existence of an obscuring dust torus which blocked direct viewing of an otherwise Seyfert 1 nucleus, allowing it to be seen only in light scattered (and consequently polarized) off matter with an unblocked line of sight to the nuclear region. As more wavelengths were made accessible and observations improved, the consensus grew that all AGN phenomena, not just Seyfert 1 and 2 galaxies, are different manifestations of a common mechanism. The quest for the "Grand Unification" of AGN observations and a determination of the truly essential parameters that differentiate objects is one that still continues today, however. (See Lawrence 1987 for a review.)

While observers continue to catalogue the diversity of these objects, the theorist has his own difficult challenge to face. The picture of an AGN that has gradually emerged from the haze is by no means easy to explain. Unlike a star which emits most of its luminosity within two octaves of frequency, an AGN emits roughly equal amounts of power over nine decades of frequency, from meter wavelengths to at least 100 MeV gamma-ray energies. (To first order, the emission spectrum of an AGN is a power law with flux per unit frequency $\propto \nu^{-1}$. See Fig. 1 for an example.) Moreover, the size scales from which this emission comes range over about 10 decades: to explain the megaparsec (10^{24} cm)-sized giant double radio lobes, one must follow them down to their ultimate energy source in the inner nuclear region, which from measurements of rapid X-ray variability and light-crossing time arguments, can be $\lesssim 10^{14}$ cm in size (e.g., Tennant *et al.* 1981). Understanding an AGN thus requires understanding physical processes over an unprecedented set of size and energy scales.

The physics of the inner emitting region is particularly problematic if one reflects on the large amount of power it emits and its small size. At optical wavelengths, a region roughly 10^{-5} the radius of a galaxy can outshine the rest of the galaxy. At X-ray energies, the problem is even worse. The processes responsible must therefore be remarkably efficient in their conversion of rest mass to radiant energy, probably more efficient than any nuclear or atomic process. Lynden-Bell (1969) and others have argued that this leaves gravitational release of energy, probably via a black hole, as the most plausible mechanism. (Because of dynamical instabilities, it is argued that any alternative to a black hole such as compact cluster of relativistic stars will inevitably end up as a black hole, e.g., Begelman & Rees 1978.) This is the main consideration leading to the elaboration of the "standard" (at least today) black hole model of AGN.

In this model, gas and matter spiral in from the surrounding galaxy to "feed" a massive black hole sitting at the center. The gravitational binding energy released in this process is converted into an intense radiation field which escapes from the nuclear region. However, probably only a relatively small fraction of this initial radiation escapes unscathed through the surrounding matter. The remainder is reprocessed and reappears at different energies, much the way an energetic cosmic ray hitting a particle detector is transformed into a shower of low energy pairs and photons. Nevertheless, the black hole is believed to be the "central engine" which powers AGN over the many wavelengths and length scales in which they are seen.

Differences between the classes of AGN may then be explained as differences in the central engine, differences in the reprocessing, or differences in the angle from which the system is viewed. For example, the masses of the central black holes would be expected to vary due to differences in their formation or subsequent histories (e.g., how much matter they had a chance to swallow). Differences in mass (i.e., the depth of the gravitational potential) would translate into differences in maximum luminosity. Observed luminosity differences between classes might then be attributable to characteristic black holes masses associated with those classes. Alternatively, some of the distinctions between AGN might be attributable simply to variations in the mass accretion rate. A black hole which has swept in all of the immediately surrounding gas, for example, will not form a luminous accretion disk. (Many galaxies could thus be dormant AGN, merely waiting for a cataclysmic event like a tidal interaction with another galaxy to trigger them into activity again.) An example of a possible difference in the reprocessing might be the presence or absence of a molecular dust torus that completely blocks the outgoing radiation in certain directions and causes it to be re-emitted only at much lower infrared energies (e.g., perhaps as in the IRAS ultra-luminous infrared galaxies). Finally, if the particles in the radio jets move relativistically, one would expect strong orientation effects due to relativistic beaming of the radiation in the jet direction.

Corroborative evidence for the presence of a black hole (and this standard picture) is provided by the stellar velocity dispersion which appears to increase rapidly towards the center of some galaxies (as the black hole mass presumably dominates the potential, see Dressler 1989, Kormendy 1988, Tonry 1987). Dynamical estimates of the central (black hole) mass derived from this velocity dispersion cover the same range as the Eddington luminosity estimates discussed below. Additional evidence is the observation of radio jet axis orientations which appear to have been constant for periods of at least $\gtrsim 10^6$ years (e.g., see Bridle & Perley 1984). A rapidly spinning black hole would behave as a gyroscope, maintaining its orientation (and presumably that of the jet). We stress, though, that while the black hole picture is compelling, it is currently still a matter of conjecture and not proven fact.

If one accepts the black hole hypothesis, a lower bound may be placed on the mass of the central black hole by assuming that it cannot radiate at significantly more than its Eddington luminosity (the luminosity at which radiation pressure on an electron balances the gravitational force a proton feels from the black hole). This may be expressed (e.g., Rees 1984) as

$$L_E = \frac{4\pi G M m_p c}{\sigma_T} \approx 1.3 \times 10^{46} M_8 \mathrm{ergs/sec} \tag{1.1}$$

where M_8 is mass measured in units of 10^8 solar masses. Typical masses obtained by inserting the observed luminosities are in the range $10^6 - 10^9$ solar masses.

Associated with the black hole is also the size scale of its event horizon,

$$r_{hole} = \frac{GM}{c^2} \qquad (1.2).$$

Nothing inside this radius can communicate with the outside world. One therefore expects a characteristic minimum timescale for variability given by the light-crossing time

$$r_{hole}/c \sim 500 M_8 \mathrm{sec}. \qquad (1.3)$$

As noted above, rapid X-ray variability on these timescales has indeed been observed.

One other important element of the standard picture must be mentioned. This arises from the consideration that matter falling into the hole must first find a way to lose its angular momentum. This is thought to occur in an accretion disk which will extend down to a few r_{hole}. The exact form of this accretion disk is a subject of much debate (see Begelman 1985 for a review of thick vs. thin disks, stability issues and the like). As a key ingredient in the physics (an understanding of the effective viscosity in the disk, the α parameter) is still missing, this debate may continue for some time. A non-controversial aspect of accretion disk models, however, is that the disk is an important source of energy release (the in gravitational binding energy of infalling particles is released as radiation). See Frank, King, & Raine (1985) for a discussion of how this occurs. Generally, the rate of release of gravitational energy increases with decreasing distance from the center. Consequently the emission peak from a particular disk radius also increases, going (in typical models) from optical frequencies at the outer edge to soft X-ray ($\lesssim$ 0.1 keV) energies at the inner edge. (A general prediction of this, that variability decreases with increasing frequency, appears to be satisfied.) Unfortunately, as knowledge of the disk structure is crucial in determining the integrated disk spectrum, the topic of disk emission is equally controversial. Other effects such as the presence of a hot corona (much like that of the Sun) over the disk's surface and general relativistic redshifting of photons from the inner edge may play important roles in determining the overall spectrum. These problems aside, disk emission is generally considered the most likely source for the so-called "blue bump" spectral feature (an optical-UV excess over the overall power law continuum, see Fig. 1) and perhaps the reprocessed infrared emission seen in many objects.

In the context of the pair plasma models discussed below, the accretion disk is also the source of the seed photons that are Compton upscattered to much higher X- and gamma-ray energies by energetic (non-thermal) electrons and positrons. In addition, the disk may intercept and reprocess a significant fraction of the luminosity emerging from the pair plasma (significantly modifying the final spectrum seen by an observer). Finally, the accretion disk may be directly responsible for energizing the pair plasma. The material in the disk is likely to be shocked and significant particle acceleration could occur across these shocks. The disk may also be threaded by a magnetic field that, by processes perhaps analogous to those seen in the solar corona (e.g., magnetic reconnection), could also give rise to strong particle acceleration.

A magnetic field in the disk may also be responsible for channeling some of the gravitational energy released directly into particle kinetic energy (e.g., Blandford & Payne 1982), leading to the creation of the powerful radio jets seen to emerge from many AGN. These jets are among the most dramatic (and maybe puzzling) manifestations of AGN activity. Although many ideas have been proposed to account for them (e.g., see Begelman, Blandford, & Rees 1984), it is not yet clear how these jets originate (magnetic fields in disks may not be responsible) and how they remain collimated over the long distances they are seen to span. The most intriguing observations of jet phenomena are perhaps those obtained by radio VLBI (Very Long Baseline Interferometry) techniques which can resolve features in AGN down to the scale of parsecs. The core-jet structures often revealed (thought to be associated with the jets seen on larger scales) show evidence of "superluminal expansion" as well as of extremely high brightness temperatures, $\gtrsim 10^{12}K$ in a few cases. (Superluminal expansion is the apparent increase in separation of two source features at a rate greater than that of the speed of light. The brightness temperature at a frequency is $\propto$ observed flux/(angular source size)^2 and is an indication of the photon occupation number at that frequency.) Conventional wisdom has it that these are the consequences of non-thermal emission processes and relativistic fluid velocities in the jet. (See Zensus & Pearson 1987 for discussions of this as well as of the observations.)

2. Radiative Processes in AGN

The best way to test the black hole-accretion disk hypothesis is to analyze the radiation emitted by AGN. This requires an understanding of the mechanisms behind the emission. Helping to further this understanding is the primary goal of this thesis. I consider here the primarily high energy processes associated with the electron-positron pair plasma thought to surround the central engine of an AGN. These processes might be termed exotic in that they are not usually encountered under laboratory conditions. In an astrophysical context, however, the conditions under which they are important are not all that unusual. For example, pair plasmas are probably also found in pulsar magnetospheres (e.g., Arons 1981), gamma-ray bursters (e.g., Liang & Petrosian 1986), and the early universe (e.g., Weinberg 1972). The results and techniques presented here may thus prove relevant in the study of other (non-AGN) environments.

The application of the theory of elementary radiative processes to an environment as complex as that of an AGN is difficult. This may be surprising to some as the underlying microphysical processes (e.g., Compton scattering) are completely understood and their cross-sections appear in any good quantum electrodynamics book. However, an understanding of how two particles interact does not necessarily imply knowledge of how an ensemble of such particles behaves. (Despite having had Newton's laws for over three centuries, we still do not understand galactic structure very well.) In the case of AGN, difficulties arise because of the non-linearity of the relevant kinetic equations, and because of complications introduced by spatial transport. The latter problem is probably the more important and troublesome. The central engine of AGN with all its violent outbursts and shocks probably running across it is not well-approximated by a spherical volume filled with isotropically moving electrons of uniform density. This ultimately requires keeping track of the full seven-dimensional particle phase space (momentum, space, time). Even with today's supercomputers, the full problem is not tractable and severe approximations must be made.

The existence of electron-positron pair plasmas in AGN is a hypothesis, like that of the existence of the central black hole in an AGN. No unambiguous signs, such as an emission line at .511 MeV (the electron rest mass) have yet been detected in AGN. (The one possible exception is our Galactic center where such a line has been seen, although here the identification is questionable.) Nevertheless, the theoretical reasons for the existence of pair plasmas are fairly compelling.

As first noted by Jelley (1966) and Herterich (1974), the large X-ray luminosities of AGN and the small size of the region from which they are inferred (by variability measurements) to come, imply large number densities of energetic photons – so large that any gamma-ray trying to escape the region would have a high probability of annihilating with one of them to create an electron-positron pair. Specifically (see Guilbert, Fabian & Rees 1983, Done & Fabian 1989 for a more detailed exposition of this argument), one may define a dimensionless "compactness parameter"

$$l \sim \frac{L}{R} \frac{\sigma_T}{m_e c^3}$$

where L is the observed X-ray ($h\nu \lesssim m_e c^2$) luminosity, and R is the characteristic source size, $\sim c\Delta t$ where Δt is the minimum variability timescale. This is essentially an estimate of the optical depth to photon-photon pair production for a gamma-ray of energy $\sim m_e c^2$. Inserting the observed values of L and Δt, one obtains values greater than unity for many sources, i.e., the X-ray emitting regions are optically thick to photo-production of pairs. Consequently, if the source produced any gamma-rays, it would quickly acquire an electron-positron pair plasma. Theoretical prejudices about energy generation mechanisms and the fact that significant gamma-rays luminosities have been observed in a few AGN lead one to guess that a sufficient number of pairs would be created to make this plasma optically thick to Thomson scattering.

In this case, reprocessing by the pair plasma would be significant, i.e., the "output" spectrum that eventually escaped through the electron-positron plasma would look very different from the original incident spectrum. In particular, energetic pairs could upscatter the soft (e.g., IR, UV) end of the spectrum to X- and gamma-ray energies, while cooler pairs would downscatter gamma-rays and their annihilation would add an emission feature at $h\nu \sim m_e c^2$. In addition, the plasma would alter the perceived time variability of the source (increasing the minimum observed variability timescale at keV energies, for example). For a review of the physical processes that might be important in the context of a pair plasma and their possible effects, see Svensson (1986).

Early attempts at describing pair plasmas (e.g., Bisnovatyi-Kogan, Zel'dovich & Sunyaev 1971) made the simplifying assumption that the pairs were in thermal equilibrium, i.e., that their distribution functions could be characterized by a (relativistic) Maxwellian of fixed temperature and density. Unfortunately, there are two problems with this. First, the processes of Compton scattering, pair production, and pair annihilation change the number and energy of the thermal pairs. Hence, the pair distribution must be determined self-consistently at the same time as the radiation field. Second, there is good reason to be believe a pair plasma is not in thermal equilibrium. Thermalization timescales for mildly relativistic pairs are typically longer than the Compton cooling time and other relevant timescales in the problem. Hence, the pair distribution is likely to have a significant non-thermal tail.

To solve the pair plasma problem, one therefore needs a method for evolving arbitrary photon and pair distribution functions. Two approaches have been employed thus far. The first is a Monte Carlo approach where individual particles are followed as they undergo interactions inside the source. The main advantage of such a scheme is that it is usually easy to model the radiative transfer well. However, such a scheme typically suffers from relatively poor photon statistics at high frequencies (even when variance-reducing techniques like photon splitting are used) and does not lend itself to time-dependent calculations. For examples of the Monte Carlo calculations performed to date, see Stern (1985), Novikov & Stern (1986), and Stern (1988).

The second approach involves solving the relevant kinetic equations. Following the time evolution of the system in such an approach is straightforward and photon statistics are not an issue. However, these methods have their own problems. First, the resulting integro-differential equations can be quite cumbersome and "stiff" (i.e., there may be widely varying timescales in the problem). Second, only simple prescriptions for radiative transfer (such as an escape probability formalism) can be implemented easily on present-day computers (primarily because of memory limitations). In practice, these kinetic treatments must throw out all angular and spatial information and assume the source region to be homogeneous and isotropic. One then solves for the particle distributions at one point in space and hopes that they will resemble those in a realistic source. For examples of kinetic equation treatments see Fabian *et al.* (1986), Ghisellini (1987a, 1987b), Lightman & Zdziarski (1987), Svensson (1987), and Done & Fabian (1989).

The work presented here is an extension of this research and makes use of the kinetic equation approach (together with the same assumptions of a homogeneous and isotropic source region). It was intended as a general study of pair plasmas, motivated by, but not strictly tied to, the problem of AGN. A primary goal was to remove as many approximations as possible from past work to see what results were artifacts of the approximations and which were true physical effects. These approximations are discussed and improvements to them are presented in Chapter 2. In Chapter 3, this improved treatment of the microphysical processes is implemented in a kinetic code. The conclusion from this exercise is that results presented in earlier work generally appear to be qualitatively correct, but can easily be in error by factors of two.

An exception to this conclusion is the "photon-starved" regime where the Compton cooling times are long because of a deficit of soft photons in the source. In this case, usually negligible processes such as Coulomb scattering between pairs and bremsstrahlung emission can be important. This regime is the focus of Chapter 4. As expected, the spectra produced including these effects are found to differ significantly from those presented in previous work. An additional motivation of this work was to see if these spectra resemble those of "hard" sources such as gamma-ray bursters and some AGN (e.g., 3C273) which show X-ray spectral indices $\alpha_x < 0.5$ (where the flux per unit frequency, F_ν, goes as $\nu^{-\alpha_x}$). Non-thermal pair plasmas of the type considered here cannot produce spectral indices < 0.5 unless an X-ray photon experiences multiple Compton upscatterings before escaping, i.e., only in the photon-starved regime. The answer is a qualified yes, although observations are not yet good enough to make definitive statements.

A second goal of the study conducted here was to elaborate on the effects a pair plasma has on the variability of a source. This is described in Chapter 3. The general conclusion is that a pair plasma can have a significant effect, especially when its Thomson optical depth exceeds unity. To first order, a pair plasma acts much like a capacitor, storing up particles and energy, and smearing out the response of the system to changes in injection. (If a Thomson thick plasma inhabits a source, estimates of the source size from variability measurements are thus *overestimates*.) The response function to changes in energy injection rates, however, depend strongly on energy. Two frequencies, depending on the details of the source changes and the times they are looked at, can show either correlated or anti-correlated behavior. Spectral variability data such as the relative intensity of two frequencies is therefore *not* useful in constraining or ruling out the existence of a pair plasma. Much more detailed (i.e., broad band) spectral information is required. In addition, it is pointed out that spectra in transition between two source states (e.g., high and low) may look nothing like the spectrum at either of those two states. One should take this into account before drawing too many conclusions from a single spectrum (snapshot) of a source. A final observation of this chapter is that the gamma-rays generally respond more rapidly to changes in particle injection and are relatively immune to the time-smearing effects of a pair plasma. The gamma-ray emission of AGN should therefore exhibit more rapid variability than the X-ray emission. This may have consequences for planned gamma-ray telescopes (e.g., GRO) that have week-long source integration times. If this variability is not seen at some point, current pair plasma explanations for the high energy continuum of AGN will be in serious trouble.

A third goal of the work presented was to see if current (very simplified) pair plasma models can reproduce real spectra. In the calculations of Chapter 3, synchrotron radiation is included to see whether observed AGN infrared spectra can be produced by the same non-thermal pair plasma inferred to be responsible for the X-rays. The answer is again a qualified yes. Spectra with approximately the right slopes can be constructed, but infrared variability similar to that of X-rays is predicted (and has not been seen). In addition, it appears very difficult (but not impossible) to create synchrotron self-absorbed slopes with a spectral index harder than (less than) -2.5 needed to explain the far-infrared end of the spectrum. Moreover, any inhomogeneities in the magnetic field (which are not considered here) would tend to reduce this slope significantly. This appears difficult to reconcile with indications of recent observations that the spectral index in the far-infrared may in fact be as large as -3.0 (Chini *et al.* 1990).

A striking observational fact is the clustering of the 2-10 keV X-ray spectral indices of Seyfert 1 galaxies about the value $\alpha_x = 0.7$ (e.g., Turner & Pounds 1989). The explanation of this fact is one of the major puzzles facing pair plasma research today. Originally it was hoped that feedback mechanisms in the pair plasma might create an island of stability in the input parameter space such that a spectral index ~ 0.7 would be produced over a large range of source compactness. (While the X-ray spectral indices of Seyfert 1s may be similar, their luminosities and inferred X-ray compactness parameters can easily vary by more than a factor two.) However, the results of current studies, including this one, have been disappointing in this regard. The only preferred spectral index appears to be $\alpha_x \sim 1$ for source compactnesses much greater than unity when the pair plasma becomes "saturated" (Svensson 1987), and, in general, predicted values of α_x range through the interval $[0.5, 1]$ with no particular preference for $\alpha_x \sim 0.7$. This appears to indicate that an essential ingredient is still missing in our current understanding of the mechanism of X-ray production in Seyfert 1s. Either some other part of the central engine affects the X-ray spectrum, or there is an additional (unknown) physical mechanism which always selects out the right combination of input parameters for the pair plasma.

Indications of a possible answer to this problem have come in the last year or so with the discovery of variable K_α iron lines (at $6-7$ keV) in the X-ray spectra of some AGN. In one case, (NGC 6814, Kunieda *et al.* 1990) the line appeared to respond to changes in the continuum with a lag time less than ~ 5

minutes. Two important inferences follow from these observations (if correct): (i) there is cold matter (X-ray absorbing matter) very near to the X-ray emitting region (presumably the pair plasma), (ii) this cold matter probably is intercepting a significant amount of the outgoing X-ray flux. A hard incident radiation spectrum, like that from a pair plasma, is primarily absorbed and re-emited at much lower energies when it encounters such a lump of cold ($T \lesssim 10^6$ K) matter. A fraction ($\sim 10\%$), however, is "Compton reflected" (see White, Lightman, & Zdziarski 1988), ending up at X-ray energies typically in the range $5 - 60$ keV. This "reflected" component, when added to the original pair plasma radiation, appears to be exactly what is needed to bring a 2-10 keV spectral index ~ 1 (the pair saturated, "stable" value) up to $\sim .7$. A discussion of this mechanism may be found in Zdziarski *et al.* (1990) and Chapter 5. Only time and further observations will tell whether or not it is a sensible picture.

The final chapter, Chapter 5, addresses another region of the AGN spectrum, the soft X-rays ($\sim 0.1 - 1$ keV in energy), where an excess of emission over the extrapolated 2-10 keV power law has been seen. It is noted there that pair plasmas, for a certain region of parameter space, can produce steep power law emission on top of an underlying X-ray power law, i.e., a soft X-ray photon excess. This is due to Comptonization by cool, thermalized pairs of the soft (UV) "blue bump" photons. Examples of possible time variability are shown, and it is seen that pair plasmas can produce behavior consistent with the observations. The parameter space over which visible soft excesses are produced encompasses that in which the Compton reflection models discussed above are claimed to work best. Thus, a prediction of pair plasma-reflection models is that soft X-ray excesses should be relatively common in AGN.

References

Antonucci, R.R.J. & Miller, J.S., 1985. *Astrophys. J.,* **297**, 621.

Arons, J., 1981. *Astrophys. J.,* **248**, 1099.

Begelman, M.C., 1985. In: *Astrophysics of Active Galaxies and Quasi-Stellar Objects*, p. 416, ed Miller, J.S., University Science Books, Mill Valley.

Begelman, M.C. & Rees, M.J., 1978. *Mon. Not. R. astr. Soc.,* **188**, 847.

Begelman, M.C., Blandford, R.D., & Rees, M.J., 1984. *Rev. Mod. Phys.,* **56**, 255.

Bisnovatyi-Kogan, G.S., Zel'dovich, Ya B. & Sunyaev, R.A., 1971. *Sov. Astr.,* **15**, 17.

Blandford, R.D. & Payne, D.G., 1982. *Mon. Not. R. astr. Soc.,* **199**, 883.

Bridle, A.H. & Perley, R.A., 1984. *Ann. Rev. Astr. Astrophys.,* **22**, 319.

Chini, R., Kreysa, E. & Biermann, P.L, 1990. *Astr. Astrophys.*, submitted.

Done, C. & Fabian, A.C., 1989. *Mon. Not. R. astr. Soc.,* **240**, 81.

Dressler, A., 1989. In: *Active Galactic Nuclei*, p. 217, eds Osterbrock, D.E. & Miller, J.S., Kluwer, Dordrecht.

Fabian, A.C., Blandford, R.D., Guilbert, P.W., Phinney, E.S., Cuellar, L., 1986. *Mon. Not. R. astr. Soc.,* **221**, 931.

Frank, J., King, A.R., & Raine, D.J., 1985. *Accretion Power in Astrophysics*, Cambridge University Press, Cambridge.

Ghisellini, G., 1987a. *Mon. Not. R. astr. Soc.,* **224**, 1.

Ghisellini, G., 1987b. Ph.D. Dissertation Thesis, ISSA, Trieste.

Guilbert, P.W., Fabian, A.C., & Rees, M.J., 1983. *Mon. Not. R. astr. Soc.,* **205**, 593.

Herterich, K., 1974. *Nature,* **250**, 311.

Jelley, J.V., 1966. *Nature,* **211**, 472.

Kormendy, J., 1988. *Astrophys. J.,* **325**, 128.

Kunieda, H., Turner, T. J., Awaki, H., Koyama, K., Mushotzky, R. F., & Tsusaka, Y., 1990. *Nature,* **345**, 786.

Lawrence, A., 1987. *Pub. Astr. Soc. Pac.*, **99**, 309.

Liang, E.P.T. & Petrosian, V., 1986. *Am. Inst. Phys. Conf. Proc.*,**141**, 321.

Lightman, A.P. & Zdziarski, A.A., 1987. *Astrophys. J.,* **319**, 643.

Lynden-Bell, D., 1969. *Nature,* **223**, 690.

Miller, J.S. & Goodrich, R.W., 1990. preprint.

Novikov, I.D. & Stern, B.E, 1986. In: *Structure and Evolution of Active Galactic Nuclei*, p. 149, eds Giuricin, G. *et al.* , Reidel, Dordrecht, Holland.

Rees, M.J., 1984. *Ann. Rev. Astr. Astrophys.,* **22**, 471.

Schmidt, M., 1963. *Nature,* **197**, 1040.

Stern, B.E., 1985. *Sov. Astr.,* **29**, 306.

Stern, B.E., 1988, NORDITA - 88/51 A, Denmark, preprint.

Svensson, R., 1986. In: *Radiation Hydrodynamics in Stars and Compact Objects, IAU Coll. No. 89*, p. 325, eds Mihalas, D. & Winkler, K.-H. A., Springer-Verlag, Berlin.

Svensson, R., 1987. *Mon. Not. R. astr. Soc.,* **227**, 403.

Tennant, A.F., Mushotsky, R.F., Boldt, E.A., & Swank, J.H., 1981. *Astrophys. J.,* **251**, 15.

Tonry, J.L., 1987. *Astrophys. J.,* **322**, 622.

Turner, T.J. & Pounds, K.A., 1989. *Mon. Not. R. astr. Soc.,* **240**, 833.

Weedman, D.W., 1986. *Quasar Astronomy*, Cambridge University Press, Cambridge.

Weinberg, S., 1972. *Gravitation and Cosmology: Principles and Applications of the General Theory of Relativity*, John Wiley & Sons, New York.

White, T.R., Lightman, A.P., & Zdziarski, A.A., 1988. *Astrophys. J.,* **331**, 939.

Zdziarski, A. A., Ghisellini, G., George, I. M., Svensson, R., Fabian, A. C., & Done, C., 1990. Astrophys. J. (Letters), in press.

Zensus, J.A. & Pearson, T.J., 1987. *Superluminal Radio Sources*, Cambridge University Press, Cambridge.

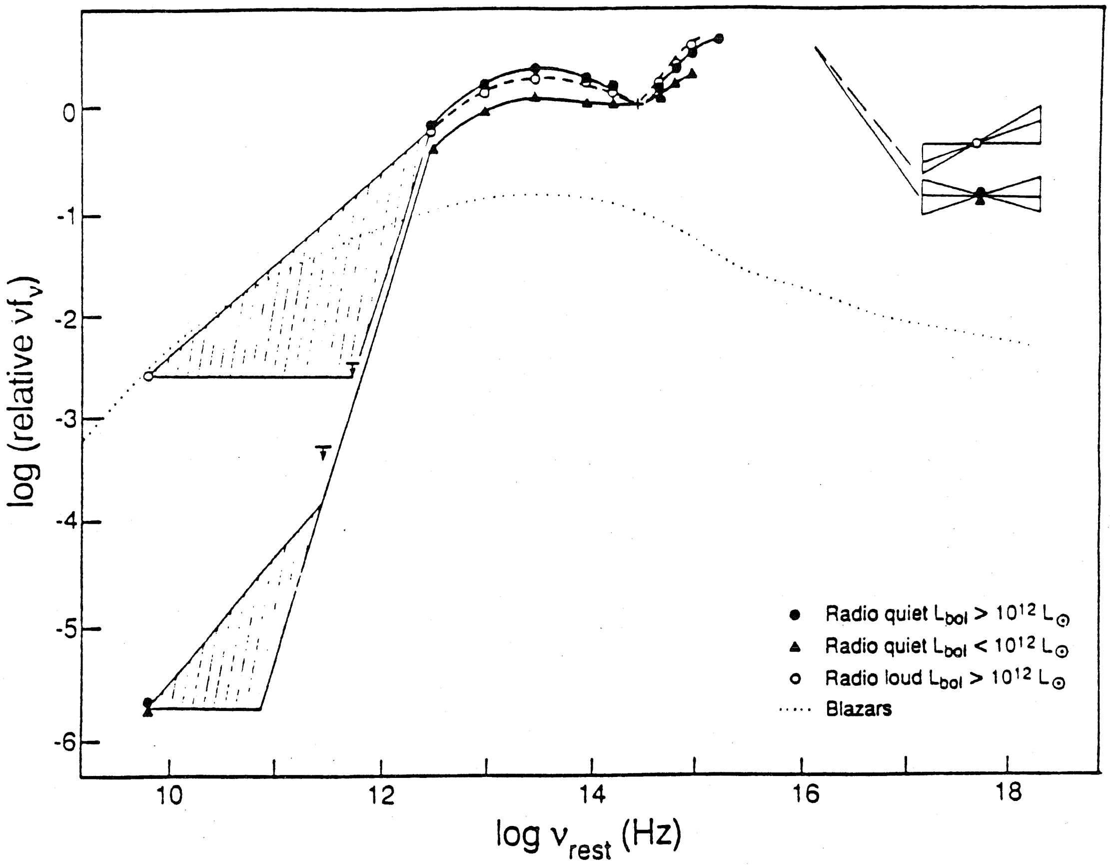

Figure 1. A composite AGN spectrum, taken from Sanders *et al.* , Ap. J., 347, 29 (1990). The spectrum was obtained by averaging spectra of the radio loud and radio quiet quasars in the PG (Palomar-Green) survey. Note the "blue bump" at $\nu \sim 10^{15}$ Hz thought to originate from the accretion disk of the central black hole. The spectrum of an object that emitted constant power per decade would appear as a horizontal line on this diagram. Though not shown on the diagram, the spectra of AGN can extend to frequencies $\gtrsim 10^{20}$ Hz (MeV energies).

Chapter 2

REACTION RATES AND ENERGY DISTRIBUTIONS FOR ELEMENTARY PROCESSES IN RELATIVISTIC PAIR PLASMAS

in collaboration with

Roger D. Blandford,
California Institute of Technology

Originally appeared in *Mon. Not. R. astr. Soc.* (1990) **245**, 453-469.

Abstract

Reaction rates are given for two body processes in an isotropic pair plasma. The rates are accurate over mildly relativistic energies and are given as functions of the incident particle energies rather than integrated over a thermal distribution. The processes considered are as follows: Compton scattering, pair annihilation, two photon pair production, Coulomb scattering, and e-e bremsstrahlung. For the first three processes, the mean energy of the final states together with the dispersion in energy about their mean energies are computed. Approximate expressions are presented where these have proven useful. The results have been tabulated for use in kinetic equation studies of pair plasmas.

1. Introduction

The discovery of rapidly variable X-ray and γ-ray emission from active galactic nuclei (AGN), γ-ray bursters, and the Galactic center has prompted investigation of "electron-positron pair plasmas." [For a general discussion of AGN and pair plasmas, see Svensson 1986, Zdziarski & Lightman 1987; for γ-ray bursters see Lamb 1988, Zdziarski 1987; for the Galactic center see Ramaty & Lingenfelter 1987.] Most of the initial attention focused on pair plasmas characterized by a single temperature. (See, for example, Bisnovatyi-Kogan *et al.* 1971, Takahara 1980, Zdziarski 1985, Guilbert & Stepney 1985 and references contained therein.) Unfortunately such plasmas do not easily reproduce observed AGN spectral features and are unlikely to be produced because of the relatively long thermalization timescales expected (e.g., Kusunose 1987, Stepney 1983).

More recent theoretical studies of pair plasmas therefore attempt to solve self-consistently for the particle distributions. Two methods have been followed: solving the kinetic equations for the electron and photon distribution functions (e.g., Guilbert 1981, Fabian *et al.* 1986, Ghisellini 1987a, Svensson 1987, Lightman & Zdziarski 1987), and direct Monte Carlo simulations (e.g., Novikov & Stern 1986, Stern 1985). Both approaches are useful, the former when the computation must encompass a large range of energies or time-dependence is relevant, the latter when complex radiative transfer considerations are needed. The kinetic equation approaches employed to date, however, have been hampered by the use of oversimple approximations for interaction rates and scattered/emitted particle distributions. It is our purpose here to improve on some of these approximations.

In this paper, we re-examine the kinetic approach and set up a systematic framework for dealing with the "primary" pair processes of Compton scattering, pair annihilation, and two photon pair production. For these processes, we give both exact expressions and useful approximations for interaction rates, mean scattered energies, and dispersions about these mean energies as functions of the incident particle energies. The incident particle distributions are assumed isotropic and unpolarized. From these quantities we then construct an approximation for the energy distribution of the outgoing particles. The resulting formalism is designed to improve the computation of pair and high energy photon yields. Also discussed are the processes of Coulomb scattering and e-e bremsstrahlung under approximations useful for kinetic calculations. The rate equations developed here are used in a time-dependent pair plasma code, Coppi (1990).

2. Compton Scattering

2.1. *Kinematics*

Compton scattering is most conveniently parametrized using two electron (or positron) rest frame quantities: the scattering angle θ between the ingoing and outgoing photon momenta, and the azimuthal angle ϕ. Assume now that the incoming electron and photon have (lab frame) energies γ $(= (1-\beta)^{-1/2})m_e c^2$ and $\omega' m_e c^2$ respectively, and let the outgoing (scattered) photon have energy $\omega m_e c^2$. Using standard kinematic relations (e.g., Rybicki & Lightman 1979), we obtain

$$\omega = \frac{\gamma[\gamma(1-\beta\mu) + \gamma\beta\cos\theta(\mu-\beta) + \beta\sin\theta(1-\mu^2)^{1/2}\cos\phi]\omega'}{1+\gamma(1-\beta\mu)(1-\cos\theta)\omega'} \tag{2.1}$$

where μ is cosine of the (lab frame) angle between the incoming electron and photon momentum vectors. The relevant scattering cross-section is given by the polarization-averaged Klein-Nishina cross-section, σ_{KN} (e.g., Berestetski *et al.* (BLP) 1982, p.356). Ignoring induced scattering effects and assuming homogeneous, isotropic distributions, the photon occupation number $n(\omega)$ will then evolve according to

$$dn(\omega)/dt = -n(\omega)\int d\gamma N(\gamma)R(\omega,\gamma) + \int\int d\omega' d\gamma P(\omega;\omega',\gamma)R(\omega',\gamma)n(\omega')N(\gamma). \tag{2.2}$$

Here $n(\omega)$ is the number of photons per unit volume with energies between ω and $\omega + d\omega$, $N(\gamma)$ is the analogous electron energy distribution, $R(\omega,\gamma)$ is the scattering rate between photons of energy ω and electrons of energy γ, and $P(\omega;\omega',\gamma)$ is the probability that the outgoing photon has energy ω given that the incoming photon and electron had energies ω' and γ respectively. ($P(\omega;\omega',\gamma)$ is normalized so that $\int d\omega P(\omega;\omega',\gamma) = 1$.)

2.2. *Scattering Rate*

The angle-averaged scattering rate is given by

$$\begin{aligned} R(\omega,\gamma) &= c\int_{-1}^{+1}\frac{d\mu}{2}(1-\beta\mu)\sigma_{KN}(\beta,\omega,\mu) \\ &= \frac{3c\sigma_T}{32\gamma^2\beta\omega^2}\int_{2\gamma(1-\beta)\omega}^{2\gamma(1+\beta)\omega} dx[(1-\frac{4}{x}-\frac{8}{x^2})\ln(1+x)+\frac{1}{2}+\frac{8}{x}-\frac{1}{2(1+x)^2}] \end{aligned} \tag{2.3}$$

where $x = 2\gamma(1-\beta\mu)\omega$. The integration over the variable x may be done analytically (e.g., Aharonian & Atoyan 1981a, Protheroe 1986), but the resulting expression which contains a dilogarithm is not very useful. $R(\omega,\gamma)$ is easily evaluated numerically.

Standard asymptotic forms for the rate R are:

(i) $\beta \ll 1$ and $\omega \ll 1$ (non-relativistic case),

$$R(\omega,\gamma) \approx c\sigma_T(1-2\gamma\omega) \tag{2.4}$$

(ii) $\omega \ll 1/(2\gamma(1+\beta))$ (i.e., $x \ll 1$),

$$R(\omega,\beta) \approx c\sigma_T[1-\frac{2\gamma\omega}{3}(3+\beta^2)];$$

(iii) $\omega \gg 1/4\gamma$ and $\gamma \gg 1$ (extreme relativistic case),

$$R(\omega,\gamma) \approx \frac{3c\sigma_T}{8\gamma\omega}\ln(4\gamma\omega). \tag{2.5}$$

In the "mildly relativistic" scattering regime (e.g., $2 \lesssim \gamma \lesssim 30$, $0.01 \lesssim \omega \lesssim 30$) a useful interpolation for R is given by

$$R(\omega,\gamma) \approx R(\omega\gamma) = \frac{3c\sigma_T}{8\gamma\omega}[(1-\frac{2}{\gamma\omega}-\frac{2}{(\gamma\omega)^2})\ln(1+2\gamma\omega)+\frac{1}{2}+\frac{4}{\gamma\omega}-\frac{1}{2(1+2\gamma\omega)^2}]. \tag{2.6}$$

This expression is good to within 10% for all energies and becomes exact in the limits $\beta \to 0$ and $\gamma\omega \to \infty$. A graph comparing the approximate to the exact values for $\gamma = 20$ is given in Fig. 1. Note that in (2.6), there is only one independent variable, $(\gamma\omega)$. The step function (Klein-Nishina "cutoff") approximation $R = \sigma_T c H(1-\gamma\omega)$ (e.g., Fabian *et al.* 1986) does not work well in this scattering regime.

2.3. Scattered Photon Distribution

The scattered photon energy distribution $P(\omega;\omega',\gamma)$ was derived by Jones (1968). (Unfortunately, the formulas given there appear to contain several misprints — see the appendix.) The most common approximation to $P(\omega;\omega',\gamma)$ is the "delta-function approximation" $P(\omega;\omega',\gamma) \approx \delta(\omega - \langle\omega\rangle)$ with $\langle\omega\rangle$, the mean scattered photon energy, approximated by $\frac{4}{3}\gamma^2\omega'$. To avoid negative scattered electron energies and further simplify the equations, a cutoff approximation to the rate is also used, i.e., $R(\omega,\gamma) \approx \sigma_T c H(1 - \frac{3}{4}\omega\gamma)$. The inadequacy of this combination of approximations is shown in Fig. 2.

Use of the correct scattering rate and $\langle\omega\rangle$ significantly improves accuracy (e.g., Fig. 2), but reveals another limitation of delta-function approximations. The neglect of "dispersion" in scattered photon energies about $\langle\omega\rangle$ often results in equilibrium spectra which are too soft at the high energy end (e.g., Fig. 2

again). This has serious consequences in calculations with significant two photon pair production (e.g., Fabian *et al.* 1986 and Lightman & Zdziarski 1987) as it leads to corresponding errors in the distribution of created pairs and propagates the errors in the high energy photon distribution to lower energies. Errors of order unity at intermediate photon energies ($10^{-3} \lesssim \omega \lesssim 1$) can also be expected in this case.

To date, most attempts to include some form of dispersion have relied on a double expansion in ω'/γ and γ^2 (e.g., Jones 1968, Blumenthal & Gould 1970, Aharonian *et al.* 1981a, 1985, and Zdziarski 1988). Unfortunately, the expansion fails when the scattered energy ω is not much greater than the incident energy ω' and gives quite misleading results when downscattering is important (e.g., Fig. 2). This approximation is also computationally intensive and not well-suited for calculations where many iterations are required.

We have experimented with several schemes to allow for dispersion in the scattered photon distribution and found the best approximation to be

$$P'(\omega,\omega',\gamma) = \frac{1}{2D(\omega',\gamma)} H[D(\omega',\gamma) - |(\omega - \langle\omega\rangle)|] \tag{2.7}$$

where $H(x)$ is the Heaviside function, $D(\omega',\gamma) = \min[(\sqrt{3\langle(\Delta\omega)^2\rangle}), (\langle\omega\rangle - \omega_{min}), (\omega_{max} - \langle\omega\rangle)]$, and $\langle(\Delta\omega)^2\rangle$ is the mean square dispersion about the mean scattered energy. Here ω_{min} and ω_{max} are either the minimum and maximum photon energies handled by the numerical code under consideration, or 0 and ∞ in the general case. This procedure always gives the correct value for $\langle\omega\rangle$ and a good approximation for $\langle\omega^2\rangle$, the second moment of the scattered photon distribution.

The most serious limitations of this scheme arise from the "top hat" shape assumed for $P'(\omega;\omega',\gamma)$. The real scattered distribution is often peaked and may be quite asymmetric. The electron and photon distributions typically considered in AGN models (extended power laws) appear broad enough to smooth away most of the effects of this discrepancy. However, as seen in Fig. 2, there may be a residual deficit of high energy photons.

Based on several comparisons with results obtained using the exact probability distribution, errors up to $\sim 25\%$ in the photon distribution are found for values of $\omega \lesssim 0.1\omega_{max}$ when pair production is not important. (ω_{max} is the maximum photon energy for the problem under consideration. When $\omega > \omega_{max}$, problems due to the inadequate dispersion discussed above set in, and the errors can be significantly larger.) For models with significant pair production, the maximum deviation seen was of the order of 40% percent, with the typical error, however, still $\lesssim 25\%$ (for $\omega \lesssim 0.1\omega_{max}$). Including dispersion even in this simplified manner produces significant gains in accuracy over a delta-function approximation, especially at the highest energies. The resulting scheme is quite fast and vectorizable.

In closing, we note that the approach described may be easily extended to thermal Comptonization problems (where the inclusion of dispersion is essential – omitting it leads to incorrect spectral indices and artificial features in the stationary spectra). For temperatures $\tau = kT_e/m_ec^2 \lesssim 0.1$, using the top hat approximation with $\langle\omega\rangle$ and $\langle\omega^2\rangle$ averaged over a Maxwellian electron energy distribution gives answers accurate to $\sim 25\%$, except at the highest energies where the spectrum again rolls off prematurely. For $\tau \gtrsim 0.1$, the fractional change in photon energy per scattering becomes large and this method fails. (A series of bumps appears in the expected power law spectrum, corresponding to the distinct steps in the upscattering of a soft photon.) A better scattering kernel which remedies both this and the premature roll-off problem may be constructed by doing a Laguerre integration over top hat distributions, i.e., by using

$$K(\omega,\omega',\tau)=n_T(\sum_{i=1}^{N}c_iP'(\omega,\omega',\gamma_i)R(\omega',\gamma_i))/\sum_{i=1}^{N}c_i \tag{2.8}$$

where $c_i=w_i\gamma_i(\gamma_i^2-1)^{1/2}$, $\gamma_i=x_i\tau+1$, and x_i and w_i are the zeros and weight factors for the N^{th} Laguerre polynomial (see Abramowitz & Stegun 1965, p. 923). Here n_T is the total number of thermal electrons, and $K(\omega,\omega',\tau)$ is the scattering rate of photons with energy ω' into energy ω by those electrons. For $N=6$, reasonable agreement ($\lesssim 30\%$) with Monte Carlo calculations is obtained for temperatures up to $\tau\sim 10$. This kernel proved convenient in our numerical applications as it used the same tables we had computed to deal with non-thermal Comptonization. With regards to alternative kernels, we remark that a Gaussian kernel (with $\sigma=\langle(\Delta\omega)^2\rangle^{1/2}$, e.g., as used in Kusunose & Takahara 1985) works better than the simple top hat approach at low temperatures (it does not roll off quite as prematurely) but fails in a similar manner for $\tau\gtrsim 0.1$.

2.4. Mean Scattered Photon Energy, $\langle\omega\rangle$

To derive the required quantity $\langle\omega\rangle$, it is much easier to work with the angular probability distribution $P_{\mu,\alpha}(\mu,\alpha;\omega',\gamma)$ where $\alpha=cos(\theta)$ than with $P(\omega;\omega',\gamma)$. $\langle\omega\rangle$ is then given by:

$$\langle\omega\rangle(\omega',\gamma)=\int_{-1}^{+1}\frac{d\mu}{2}\int_{-1}^{+1}d\alpha\overline{\omega}(\alpha,\mu)P_{\mu,\alpha}(\mu,\alpha;\omega',\gamma) \tag{2.9}$$

where

$$\overline{\omega} = \gamma\omega'[\gamma(1-\beta\mu) + \gamma\beta\alpha(\mu-\beta)](\frac{x'}{x}),$$

and

$$P_{\mu,\alpha}(\mu,\alpha;\omega',\gamma) = c(1-\beta\mu)\frac{d\sigma(\mu,\alpha,\omega',\gamma)}{d\alpha}/R(\omega',\gamma) \tag{2.10}$$

with

$$\frac{d\sigma(\mu,\alpha,\omega',\gamma)}{d\alpha} = \frac{3}{8}\sigma_T(\frac{x'}{x})^2(\frac{x}{x'} + \frac{x'}{x} - 1 + \alpha^2). \tag{2.11}$$

$x = \gamma\omega'(1-\beta\mu)$ and $x' = x/(1+(1-\alpha)x)$ are respectively the incident and scattered photon energies as viewed in the electron rest frame.

In evaluating this expression, it proves most convenient to perform the first integral analytically and the second numerically. (The second integration may be done analytically, however — see the expression for $\langle d\gamma/dt\rangle$ in Jones 1965.) Making the variable change (suggested to us by P. Madau) $\alpha \rightarrow x'$, the integrand becomes an easily integrated polynomial in x'. The end result is

$$\begin{aligned}\langle\omega\rangle(\mu,\omega',\gamma) = \frac{3\sigma_T cx}{8\gamma\omega R(\omega',\gamma)}\Big\{&\frac{2}{(1+2x)}[a + \gamma(x-2) \\ &\qquad - (2\gamma+a)/x - a(6x^{-2}+3x^{-3})] \\ &+ \frac{\ln(1+2x)}{x^2}[\gamma - a + 3a(x^{-1}+x^{-2})] \\ &+ \frac{1}{2x}(1 - \frac{1}{(1+2x)^2})[a(3x^{-2}+x^{-3}) + (a+\gamma)x^{-1} + 2\gamma] \\ &+ \frac{1}{3}(1 - \frac{1}{(1+2x)^3})[\gamma + a(x^{-1}+x^{-2})] - 2ax^{-3}\Big\}\end{aligned} \tag{2.12}$$

where $a = \gamma^2\beta\omega'(\mu-\beta)$. The desired $\langle\omega\rangle$ is then $\int_{-1}^{+1}\frac{d\mu}{2}\langle\omega\rangle(\mu,\omega',\gamma)$. (For scattering off a thermal pair distribution, Barbosa 1982 has derived a somewhat complicated series expansion for $\langle\omega\rangle$ and $\langle\omega^2\rangle$.)

Some useful limiting forms for $\langle\omega\rangle$ are:

$$\langle\omega\rangle \approx (1 + 4/3\beta^2 - \omega')\omega', \quad \beta, \omega' \ll 1, \tag{2.13}$$

and

$$\langle\omega\rangle \approx \frac{4}{3}\gamma^2\omega', \quad 1 \ll \gamma \ll \omega'^{-1}. \tag{2.14}$$

Note the conditions for the validity of this last asymptotic form. In particular, when there are significant numbers of scatterings with $\omega'\gamma \sim 1$ (e.g., Fig. 2), it may be a very bad approximation to use for $\langle\omega\rangle$.

These limits unfortunately do not suggest any approximations valid over a sufficiently wide range of γ and ω'. Also, because $\langle\omega\rangle$ is a function of two variables, other standard approximation techniques (e.g., fitting with a polynomial) do not appear very useful in providing an analytic approximation both simple and accurate enough for use in a calculation. A good, relatively fast numerical approximation may always be constructed through the use of an interpolation table. A table of 20×20 entries covering the range $1 < \gamma < 10^2$, $10^{-2} < \omega' < 10^2$ gives values accurate to $\sim 5\%$.

2.5. Dispersion about $\langle\omega\rangle$

Following the previous section, we write

$$\langle\omega^2\rangle(\omega', \gamma) = \int_{-1}^{+1} \frac{d\mu}{2} \int_{-1}^{+1} d\alpha \overline{\omega}^2 P_{\mu,\alpha}(\mu, \alpha; \omega', \gamma) \tag{2.15}$$

where

$$\overline{\omega}^2 = \frac{\gamma^2\omega'^2[(\gamma(1-\beta\mu) + \gamma\beta\alpha(\mu-\beta))^2 + \frac{1}{2}\beta^2(1-\alpha^2)(1-\mu^2)]}{[1+\gamma(1-\beta\mu)(1-\alpha)\omega']^2}. \tag{2.16}$$

The dispersion is then given by $\langle(\Delta\omega)^2\rangle = \langle\omega^2\rangle - \langle\omega\rangle^2$. Note that, as above, the integral over α may be done analytically. The result is too cumbersome to include here, however. $\langle\omega^2\rangle$ has been evaluated numerically and tabulated. We have found only two useful limiting forms. These are:

$$\langle\omega^2\rangle \approx \frac{14}{5}\gamma^4\omega'^2(1-\frac{176}{35}\gamma\omega'), \qquad 1 \ll \gamma \ll \omega'^{-1} \tag{2.17}$$

and

$$\begin{aligned} R(\omega',\gamma)\langle\omega^2\rangle \approx & \frac{1}{64\beta\gamma^2\omega'^2}\times \\ & [(6\gamma\omega'(1+\beta)(2\gamma^2+1)+6\gamma^2+3)\ln(2\gamma\omega'(1+\beta)+1) \\ & -(6\gamma\omega'(1-\beta)(2\gamma^2+1)+6\gamma^2+3)\ln(2\gamma\omega'(1-\beta)+1)] \\ & +\frac{9}{32}(1-\beta^2)^2\gamma^3\omega' - \frac{58\gamma^2+1}{64\gamma\omega'} + \frac{7}{32}[2\gamma^2(1-\beta^2)+1], \\ & \omega'\gamma \gg 1. \end{aligned} \tag{2.18}$$

Using (2.5) for $R(\omega',\gamma)$, one obtains an approximation for $\langle\omega^2\rangle$ good to within 10% by $\gamma\omega' \sim 40$.

3. Pair Annihilation

3.1. Cross-Section

As in past work (e.g., Aharonian *et al.* 1981b, 1983b, Ramaty & Mészáros 1981, and Svensson 1982), we assume that the incident electron and positron distributions are isotropic and unpolarized. The invariant differential cross-section (e.g., BLP § 88.15) may be integrated to give the total cross-section as a function of the center-of-mass speed β' of the incident particles:

$$\sigma(\beta') = \frac{1}{2}\int d\sigma = \frac{3\sigma_T(1-\beta'^2)}{32\beta'}\Big[\frac{3-\beta'^4}{\beta'}\ln(\frac{1+\beta'}{1-\beta'}) - 2(2-\beta'^2)\Big]. \tag{3.1}$$

Note that to avoid double counting in the derivation of the *total* cross-section, the cross-section obtained by integrating $d\sigma$ must be divided by two since the two photons produced are *identical* particles.

3.2. Pair Annihilation Rate

The pair annihilation rate is

$$R(\gamma_-,\gamma_+) = c\int_{-1}^{+1}\frac{d\mu}{2}f_{kin}(\beta_-,\beta_+,\mu)\sigma(\beta_-,\beta_+,\mu) \tag{3.2}$$

where

$$f_{kin}(\beta_-,\beta_+,\mu) = \sqrt{\beta_-^2+\beta_+^2-\beta_-^2\beta_+^2(1-\mu^2)-2\beta_-\beta_+\mu}, \tag{3.3}$$

and $\sigma(\beta_-,\beta_+,\mu)$ is the total cross-section (3.1) with

$$\beta'^2 = \frac{(\gamma_+\gamma_-(1-\mu\beta_+\beta_-)-1)}{(\gamma_+\gamma_-(1-\mu\beta_+\beta_-)+1)}.$$

The integral can be performed analytically, e.g., eq. 18, Svensson (1982).

Useful asymptotic forms for $R(\gamma_-,\gamma_+)$ are:

(i) $\beta_-,\beta_+ \ll 1$ (non-relativistic regime),

$$R(\gamma_-,\gamma_+) \to \frac{3}{8} c\sigma_T; \tag{3.4}$$

(ii) β_- or $\beta_+ \ll 1$ (useful for energetic pairs impinging on a non-relativistic pair population),

$$R(\gamma_-,\gamma_+) \to R(\beta) = c\beta\sigma(\beta'); \tag{3.5}$$

where β represents the non-vanishing β_- or β_+, $\sigma(\beta')$ is defined above,

and β' reduces to $(\gamma - 1/\gamma + 1)^{1/2}$ with $\gamma = (1-\beta^2)^{-1/2}$.

(iii) $\gamma_-\gamma_+ \gg 1$ (relativistic regime),

$$R(\gamma_-,\gamma_+) \to R(\gamma_-\gamma_+) = \frac{3}{8} c\sigma_T \ln(\gamma_-\gamma_+)/\gamma_-\gamma_+. \tag{3.6}$$

One should note that for case (iii), R converges slowly to the limit given. The difference between the two only decreases from 10% to 4% as $\gamma_-\gamma_+$ increases from 10 to 10^8.

A simple approximation to the exact $R(\gamma_-,\gamma_+)$ may be found by interpolating between the limiting cases (i) and (iii). The expression we have found to work best is:

$$R(\gamma_-,\gamma_+) \approx R(x) = \frac{3\sigma_T c}{8x}[\frac{1}{\sqrt{x}} + \ln(x)],\ \ x = \gamma_-\gamma_+. \tag{3.7}$$

This expression is accurate to within 14% for all γ_-,γ_+. A graph showing the exact and approximate pair annihilation rate for $\gamma_- = 5$ is shown in Fig. 3.

3.3. *Average Photon Energy, $\langle\omega\rangle$, and Dispersion about $\langle\omega\rangle$*

Energy conservation and the fact that the created photons are identical particles implies

$$\langle\omega\rangle = \frac{\gamma_- + \gamma_+}{2}. \tag{3.8}$$

Following the example of Compton scattering,

$$\langle\omega^2\rangle = \frac{c}{2R(\gamma_-,\gamma_+)}\int_{-1}^{+1}\frac{d\mu}{2}f_{kin}(\mu)\int_{-1}^{+1}d\alpha[\frac{d\sigma(\alpha,\mu)}{d\alpha}][\bar{\omega}^2(\alpha,\mu)] \tag{3.9}$$

where α is the cosine of the center-of-mass scattering angle, and:

$$\frac{d\sigma}{d\alpha} = \frac{3\sigma_T}{16\beta'\gamma'^2}\Big[\frac{1+\beta'^2(2-\alpha^2)}{(1-\beta'^2\alpha^2)} - \frac{2\beta'^4(1-\alpha^2)^2}{(1-\beta'^2\alpha^2)^2}\Big], \tag{3.10}$$

$$\bar{\omega}^2(\alpha,\mu) = \frac{\gamma'^2}{(1-\beta_{CM}{}^2)}[1+2\alpha\beta_{CM}\cos\xi' + \beta_{CM}{}^2[\frac{1-\alpha^2}{2} + \frac{1}{2}\cos^2\xi'(3\alpha^2-1)]], \tag{3.11}$$

$$\beta_{CM} = \frac{(\gamma_-^2\beta_-^2 + \gamma_+^2\beta_+^2 + 2\gamma_+\gamma_-\beta_+\beta_-\mu)^{1/2}}{\gamma_+ + \gamma_-}, \tag{3.12}$$

$$\cos\xi' = \beta_{CM}^{-1}\beta'^{-1}(\frac{\gamma_+ - \gamma_-}{\gamma_+ + \gamma_-}), \tag{3.13}$$

and $\gamma' = (1-\beta'^2)^{-1/2}$. There do not appear to be any useful analytic approximations for $\langle\omega^2\rangle$. ($\langle\omega^2\rangle$ was calculated numerically and tabulated.)

3.4. *Comparison with Exact Results*

To demonstrate the accuracy of the prescription just presented, we calculate (numerically) the photon distribution produced by power law "non-thermal" pairs annihilating on cold pairs. This corresponds to the "cosmic ray" case discussed in Aharonian *et al.* (1983b) and Svensson (1982) for which a relatively simple analytic expression for the annihilation spectrum exists (e.g., Svensson

1982, eq. 41). This is also the typical situation encountered in codes of the type described in paper II (Coppi 1990), where cooling (approximately power law) non-thermal pairs annihilate primarily with cool ($kT \lesssim 0.01 m_e c^2$) thermal pairs. As can be seen in Fig. 4, for example, the approximation is adequate, with an error of less than than 10% over the range $0.8 < \omega < 35$, the range in which most of the annihilation photons lie. Note, though, that this approximation tends to overestimate the production rate of low energy photons. In applications of the type discussed in paper II, however, these photons may usually be ignored as the photon distribution at such energies is dominated by photons from other sources.

4. Photon-Photon Pair Production

4.1. Cross-Section

As in previous work (e.g., Gould & Schréder 1967, Aharonian *et al.* 1983a, 1985, and Zdziarski 1988), we assume that the distribution of incident photons is unpolarized and isotropic. Photon-photon pair production is the inverse process to pair annihilation. The cross-section is therefore identical to equation 3.1 except for a different phase space factor and a factor of 2 due to the fact the electrons and positrons produced are no longer identical particles, that is (e.g., BLP § 89):

$$d\sigma_{\gamma\gamma\rightarrow ee} = \beta'^2 d\sigma_{ee\rightarrow\gamma\gamma}; \quad \sigma_{\gamma\gamma\rightarrow ee} = \underline{2}\beta'^2 \sigma_{ee\rightarrow\gamma\gamma}. \tag{4.1}$$

The total cross as a function of β', the center-of-mass speed of the electron and positron, is thus

$$\sigma(\beta') = \int d\sigma = \frac{3\sigma_T(1-\beta'^2)}{16}\left[(3-\beta'^4)\ln\left(\frac{1+\beta'}{1-\beta'}\right) - 2\beta'(2-\beta'^2)\right]. \tag{4.2}$$

4.2. Pair Production (Photon Annihilation) Rate

The desired rate of conversion of photons into electron-positron pairs by photon-photon pair production is given by

$$R(\omega_1,\omega_2) = c\int_{-1}^{\mu_{max}} \frac{d\mu}{2}(1-\mu)\sigma(\omega_1,\omega_2;\mu) \tag{4.3}$$

where $\sigma(\omega_1,\omega_2;\mu)$ is the total cross-section (4.2) with $\beta' = (1-2/\omega_1\omega_2(1-\mu))^{1/2}$. The upper limit of integration $\mu_{max} = \max(-1, 1-2/\omega_1\omega_2)$ is determined by the requirement that β' remain real. Note that $R(\omega_1,\omega_2)$ is really a function of one variable, $x = (\omega_1 \omega_2)$. A graph of this function is shown in Fig. 5 (see also Gould & Schréder 1967).

Two useful asymptotic limits for $R(\omega_1, \omega_2) = R(x)$ are as follows:

(i) $x \to 1$ (threshold),

$$R \to \frac{1}{2} c\sigma_T (x-1)^{3/2}, \tag{4.4}$$

(ii) $x \gg 1$ (ultra-relativistic limit),

$$R \to \frac{3}{4} c\sigma_T \ln(x)/x. \tag{4.5}$$

As in the case of pair annihilation, R approaches the ultra-relativistic limit slowly.

A fairly good approximation may again be constructed by interpolating between the limiting cases, e.g.,

$$R(x) \approx c\sigma_T \frac{(x-1)^{3/2}}{x^{5/2}} (\frac{1}{2} x^{-1/2} + \frac{3}{4} \ln x) H(x-1), \tag{4.6}$$

which has a maximum error of 12%. Aharonian *et al.* (1983a) have derived a more complex alternative expression (eq. 6 of their paper) with the same limiting behavior, but accurate to better than 5% at all energies. A simpler alternative to either, very accurate near the peak of $R(x)$ (at $x_{peak} \approx 3.7$), is given by

$$R(x) \approx 0.652\, c\sigma_T \frac{(x^2-1)}{x^3} \ln(x) H(x-1) \qquad (4.7).$$

Over the range $1.3 < x < 10^4$ (which usually dominates in calculations), this expression is accurate to better than 7% (see Fig. 5).

4.3. *Average Pair Energy,* $\langle\gamma\rangle$*, and Dispersion about* $\langle\gamma\rangle$

From energy conservation and symmetry considerations,

$$\langle\gamma\rangle = \frac{\omega_1 + \omega_2}{2}, \tag{4.8}$$

while $\langle\gamma^2\rangle$ is given by

$$\langle\gamma^2\rangle = \frac{c}{R(\omega_1, \omega_2)} \int_{-1}^{+1} \frac{d\mu}{2}(1-\mu) \int_{-1}^{+1} d\alpha[\frac{d\sigma(\alpha,\mu)}{d\alpha}][\overline{\gamma}^2(\alpha,\mu)] \tag{4.9}$$

where α is the cosine of the center-of-mass angle, and:

$$\frac{d\sigma}{d\alpha} = \frac{3\sigma_T(\omega'^2-1)^{1/2}}{16\omega'^3}\left[\frac{\omega'^2 + (\omega'^2-1)(2-\alpha^2)}{\omega'^2-(\omega'^2-1)\alpha^2} - \frac{2(\omega'^2-1)^2(1-\alpha^2)^2}{(\omega'^2-(\omega'^2-1)\alpha^2)^2}\right] \tag{4.10}$$

$$\overline{\gamma}^2(\alpha,\mu) = \frac{\omega'^2}{(1-\beta_{CM}^2)}[1+2\alpha\beta'\beta_{CM}\cos\xi' + \beta_{CM}{}^2\beta'^2[\frac{1-\alpha^2}{2}+\frac{1}{2}\cos^2\xi'(3\alpha^2-1)]], \tag{4.11}$$

$$\beta_{CM} = \frac{(\omega_1^2+\omega_2^2+2\omega_1\omega_2\mu)^{1/2}}{\omega_1+\omega_2}, \tag{4.12}$$

$$\cos\xi' = (\omega_1-\omega_2)(\omega_1^2+\omega_2^2+2\omega_1\omega_2\mu)^{-1/2}, \tag{4.13}$$

and $\omega' = \gamma' = (1-\beta'^2)^{-1/2}$. The dispersion was evaluated numerically.

4.4. *Photon Absorption Probability*

We comment briefly on an approximation that has been used to estimate the value of $d\tau_{\gamma\gamma}/ds(\omega)$, the absorption probability per unit path length of a photon due to pair production. In calculations of the type carried out in Svensson (1987) and Lightman & Zdziarski (1987), the process of pair production is often quite significant in determining the overall shape of the equilibrium particle distributions. Accurately estimating the pair injection spectrum produced by an annihilating photon spectrum is thus important and requires a correspondingly accurate estimate of the absorption probability. (The absorption probability $d\tau/ds(\omega)$ is closely related to the pair production rate $R(x)$, and for a general photon distribution $n(\omega)$, is given by $\frac{1}{c}\int_0^\infty dx R(x\omega)n(x)$.)

Svensson (1987, Appendix B.2) has shown that for a photon power law extending from $\omega = 0$ to $\omega = \infty$, $d\tau_{\gamma\gamma}/ds$ is given by the formula

$$d\tau_{\gamma\gamma}/ds(\omega) = \eta(\alpha)\sigma_T \frac{n(\frac{1}{\omega})}{\omega}. \tag{4.14}$$

(Here α is the index of the power law, and η runs between 0.24 for $\alpha = 0.5$ and 0.12 for $\alpha = 1.0$.) A simple approximation can thus be constructed by taking this result and fixing the value of η at some intermediate value (usually 0.2). (One might arrive at the same estimate for $d\tau/ds$ by noting that $R(\omega_1, \omega_2)$ has a maximum value $\approx 0.2\sigma_T c$ for $\omega_2 \sim 1/\omega_1$. Hence,

$$d\tau/ds(\omega_1) \sim 0.2\sigma_T n(\frac{1}{\omega_1})(\frac{1}{\omega_1}) \tag{4.15}$$

where the range of energies over which the integrand is taken to be "large" is $\sim 1/\omega_1$.) However, as seen in Fig. 6, this approximation can lead to serious errors of order a factor 2 or more when applied to a realistic photon distribution.

4.5. Accuracy of Present Approximation

To check the validity of the dispersion prescription presented, we have compared the distribution of produced pairs calculated with our method against that calculated using the exact distribution (see Appendix A.2). A sample calculation is shown in Fig. 7. The results agree to better than 15% at all energies, with the largest errors at the minimum and maximum pair energies. The good agreement reflects the fact that the exact distribution is always symmetric about $\langle\gamma\rangle$ and has a shape often resembling the "top hat" shape assumed for the approximation.

Also shown in Fig. 7 are calculations based on the approximate distribution presented in eq. 11 of Aharonian *et al.* (1985) and the delta-function approximation (where all pairs are produced at the average energy $\langle\gamma\rangle$). The Aharonian approximation is similar to the one made in Jones (1968) for Compton scattering and is valid in the regime $\omega_1 \gg \max(\omega_2, 1)$ (where ω_1 is the larger of the incoming photon energies). Use of the approximation works extremely well at high energies but leads to errors of order unity at energies $\gamma \sim 1$. (There most of the pairs come from the annihilation of photons with $\omega_1 \sim \omega_2 \sim 1$). As expected, use of the delta-function approximation also leads to errors of order unity, particularly at the highest and lowest pair energies. These disagreements can impact significantly the equilibrium pair distribution (and hence the equilibrium photon distribution) calculated by a code such as that of Lightman & Zdziarski (1987).

5. Coulomb Scattering

Coulomb scattering usually represents only a minor contribution to the overall energy balance, although substantial changes in the equilibrium pair and photon distributions can ensue if it is neglected. For most applications, the effects of Coulomb scattering may be treated as an energy exchange term between non-thermal and thermal pairs in the pair kinetic equations. (For a full Fokker-Planck treatment, see Dermer & Liang 1989). For the non-thermal pairs, this term takes the form

$$\dot{\gamma} = c \int_1^{\infty} d\gamma_1 P(\gamma_1) \int_{-1}^{+1} \frac{d\mu}{2} f_{kin}(\gamma, \gamma_1, \mu) \langle \sigma \Delta\gamma \rangle_\alpha (\gamma, \gamma_1, \mu) \tag{5.1}$$

(see Stepney 1983, Baring 1987a,b, Haug 1988). Here, $\dot{\gamma}$ is the rate of change of energy for an electron or positron of initial energy γ scattering off an isotropic thermal distribution of electron or positrons described by

$$P(\gamma_1) d\gamma_1 = N_T \frac{\gamma_1^2 \beta_1 \exp(-\gamma_1/\tau)}{\tau K_2(1/\tau)} d\gamma_1 \tag{5.2}$$

where $\tau = k_B T / m_e c^2$, $K_2(x)$ is a modified Bessel function, and N_T is the total number of thermal electrons or positrons. $f_{kin}(\gamma, \gamma_1, \mu)$ is the kinetic factor of eq. 3.3, and

$$\langle \sigma \Delta\gamma \rangle_\alpha (\gamma, \gamma_1, \mu) = \int_{\alpha_{min}}^{\alpha_{max}} d\alpha [\frac{d\sigma(\alpha, \gamma, \gamma_1, \mu)}{d\alpha}][\Delta\gamma(\alpha, \gamma, \gamma_1)] \tag{5.3}$$

where α is the cosine of the center-of-mass scattering angle. For electron-positron or electron-electron Coulomb scattering, $\Delta\gamma(\alpha, \gamma, \gamma_1) = \frac{1}{2}(\gamma_1 - \gamma)(1 - \alpha)$, and $d\sigma/d\alpha$ is the differential cross-section for: (i) "Babha scattering" (e.g., BLP 81.20) in the case of an electron scattering off a positron, or (ii) "Möller scattering" (e.g., BLP 81.10) in the case of an electron (positron) scattering off another electron (positron). The usual Coulomb divergence of (5.3) is eliminated by ignoring scatterings smaller than some angle θ_{min}, i.e., setting $\alpha_{max} = \cos(\theta_{min})$ where $\ln(1/\theta_{min}) \approx \ln\Lambda$, the Coulomb logarithm. For Babha scattering, $\alpha_{min} = -1$, while for Möller scattering (to avoid double counting), $\alpha_{min} = 0$.

When $\ln\Lambda \gtrsim 10$, ($\ln\Lambda$ is typically ~ 25 under conditions in AGN), $\langle\sigma\Delta\gamma\rangle_\alpha$ is well-approximated by

$$\langle\sigma\Delta\gamma\rangle_\alpha = \frac{3\sigma_T(\gamma_1-\gamma)}{64\epsilon^2}\times$$
$$[(4\ln\Lambda + 4\ln 2)(\frac{\epsilon^2+p^2}{p^2})^2 - 2(\frac{8\epsilon^4-1}{p^2\epsilon^2}) + \frac{12\epsilon^4+1}{\epsilon^4} - \frac{8p^2}{3}\frac{(\epsilon^2+p^2)}{\epsilon^4} + \frac{2p^4}{\epsilon^4}] \tag{5.4}$$

in the case of Babha scattering, and

$$\langle\sigma\Delta\gamma\rangle_\alpha = \frac{3\sigma_T(\gamma_1-\gamma)}{32\epsilon^2}[(\frac{\epsilon^2+p^2}{p^2})^2(2\ln\Lambda + 1 - \ln 2) + 1/2 + 4\ln 2] \tag{5.5}$$

for Möller scattering. $\epsilon = (\frac{1}{2}[1+\gamma\gamma_1(1-\beta\beta_1\mu)])^{1/2}$ is the center-of-mass energy of one of the incoming particles, and $p = \sqrt{\epsilon^2-1}$. The remaining integrals are best evaluated numerically (although one more integration may be performed analytically by means of the variable substitution discussed in Haug (1988), eq. 14-15). For $\tau \ll 1$, the integration over γ_1 may be done quickly by a Laguerre integration method. For $\tau \gtrsim 1$, however, care must be taken because of the large negative exponents that can arise if terms are not combined in the right order (e.g., as in eq. 15 of Haug 1988).

In the limit of relativistic pairs scattering off a cool thermal pair distribution ($\tau \ll 1$, $\gamma \gg 1$), it follows from (5.4,5) that $\dot\gamma \approx -\frac{3}{2}\sigma_T c N_T \ln\Lambda$, or $1/\tau_{ee} = -\dot\gamma/\gamma \approx 4\pi c r_0^2 N_T \gamma^{-1}\ln\Lambda$, the result of Gould (1975). As noted there, the relevant value of Λ to be used is $\approx \gamma^{1/2} m_e c^2/\hbar\omega_p$, where $\omega_p = (4\pi N_T e^2/m_e)^{1/2}$

is the plasma frequency. In calculations where τ is typically $\lesssim 0.1$ (e.g., Fabian *et al.* 1986), this approximation is adequate for energies $\gamma \gtrsim 10$. A better approximation may be constructed by interpolating between various limits given in Dermer (1985), Frankel *et al.* (1979), and Haug (1988):

$$\dot{\gamma} \approx -\frac{3\sigma_T c N_T \epsilon (x - x_0) x^{1/2}}{2p(x^{3/2}+1)} \left(\frac{1}{1/(1+\tau)+2\tau}\right) A(\epsilon) \tag{5.6}$$

where

$$A = 1/2 - \ln(\sqrt{2}\theta_{min}) + \left(\frac{\epsilon-1}{2\epsilon}\right)^2 (2\ln 2 + 1/4), \quad \theta_{min} = \frac{\hbar\omega_p(\epsilon_s^2 + p_s^2)}{m_e c^2 \epsilon_s p_s^2}, \tag{5.7}$$

$\epsilon_s = ((\epsilon+1)/2)^{1/2}$, $p_s = ((\epsilon-1)/2)^{1/2}$, $x = (\epsilon-1)/\tau$, $x_0 = 1 + \tau/(1+\tau)$, $p = (\epsilon^2-1)^{1/2}$, and ϵ is the energy of the *non*-thermal electron. This expression is good to within 10% for $x \gtrsim 6x_0$, and to within $\sim 25\%$ at $x \sim 2x_0$. The largest errors occur in the neighborhood of $x = x_0$ since the fit near $\dot{\gamma} = 0$ is not very accurate.

6. e-e Bremsstrahlung

Electron-electron (positron) bremsstrahlung is usually of minor importance in determining the photon and electron distribution functions. As a first step towards gauging what effects it may have, we consider two contributions: (i) radiation from a thermal electron-positron plasma and (ii) emission by a non-thermal electron (positron) plasma interacting with a cold background electron-positron plasma. Contribution (i) has been dealt with extensively in the literature and good fits to cooling rates and emmission spectra are available (see Dermer 1984, 1986; Haug 1975a,b, 1985a,b, 1987; Stepney & Guilbert 1983). To estimate contribution (ii), we have taken the cross-sections given in Haug (1975a, 1985a) (cf.

also Alexanian 1968, Bayer *et al.* 1968) and numerically computed the cooling rates for an electron (positron) of energy γ as well as the corresponding emission spectra. Numerical tables (and the subroutines for generating them) are available. Note that the total radiated luminosity from non-thermal pairs (contribution ii) can be comparable to or exceed that from the thermal pairs alone (contribution i).

7. Discussion

It has been realized over the past ten years that electron-positron pair plasmas are probably present in a variety of astronomical sources, and that they can be observed, both directly with γ-ray telescopes and indirectly through their influence on lower energy photons. Modelling of pair plasmas has been hindered by the complexity and strong energy-dependence of the cross sections. A variety of approximations has been devised to deal with this, many of which have proven inadequate. In this paper, we have collected and developed a set of rate coefficients to deal with relevant elementary processes in the context of a kinetic approach to the problem (cf. Paper II). Kinetic approaches are most useful for dealing with environments where there are large ranges of photon frequency present and consequently, large ratios of soft photon to γ-ray densities. Their most serious deficiency is that radiative transfer can be easily handled in only the most primitive manner (but see Kusunose 1987).

The two most serious shortcomings of our work are the immediate assumption that the radiation and the pairs are isotropically distributed and the neglect of polarisation effects. A small, tangled magnetic field will guarantee electron isotropy which will vindicate our assumption for electron-electron and electron-photon processes. However, under the conditions of small optical depth we encounter, pair production and photon-escape are not necessarily well simulated. Additional complications arise in expanding or highly magnetized sources where additional preferred directions are introduced into the problem. If the plasma contains a significant magnetic field, then Faraday rotation can depolarise the radiation between scatterings at low frequencies (Blandford & Rees 1978). However, this will not occur at X- and γ-ray energies and as the expected optical depths are small, large degrees of polarisation might be measurable. This deserves further study.

Acknowledgments

The authors are indebted to A. Fabian, G. Ghisellini, S. Phinney, R. Svensson and especially A. Zdziarski and P. Madau for extensive discussions of pair plasmas. The reader should be indebted to the referee for insisting upon a major shortening of the manuscript. Support under NSF grant AST 86-15325 and NASA grant NAGW1301 is gratefully acknowledged.

Appendix

A.1 Exact Energy Distribution of Compton Scattered Photons

Equation 20 of Jones (1968) appears incorrect and should read

$$\frac{d^4N}{dt\,d\alpha\,dz'\,d\eta} = \frac{c r_0^2 \alpha}{2\gamma^4 \alpha_1^2 (\beta^2 + \epsilon^2 + 2\beta\epsilon z')^{1/2}} \Big[\frac{1 + y_0^2 + 2y_0\delta\eta + \delta^2\eta^2}{(a + b\eta)} + \frac{(\alpha/\gamma)^2 (1 - y_0 - \delta\eta)^2}{(1 - \beta z')(a + b\eta)^2} \Big] \frac{1}{(1 - \eta^2)^{1/2}(1 - \beta z')} \tag{A.1.1}$$

The subsequent equations (21,24-27) also appear incorrect. Integrating the corrected version of eq. 20 over η, one obtains (changing notation slightly)

$$\begin{aligned} \frac{dP}{dz}(\omega;\omega',\gamma) = & \frac{3\sigma_T c\omega}{16\gamma^4 \omega'^2 R(\omega',\gamma)(\beta^2 + \epsilon^2 + 2\beta\epsilon z)^{1/2}(1 - \beta z)} \\ & \times \Big[2y_0 k - ak^2 + (a^2 - b^2)^{-1/2}[(1 + y_0^2) - 2ay_0 k + a^2k^2] \\ & + \frac{1}{k^2(1 - \beta z)}[k^2 + k^2(a^2 - b^2)^{-1/2}\frac{a(2b - a)}{(a - b)} \\ & + (a^2 - b^2)^{-3/2}[a(1 - y_0)^2 + 2kb^2(1 - y_0) - ba^2k^2]]\Big] \end{aligned} \tag{A.1.2}$$

where $\epsilon = \omega'/\gamma$, $k = \gamma/\omega$, $a = 1 - \beta z - (1 - y_0)/k$, $b = \delta/k$, and

$$y_0 = \frac{(\epsilon + \beta z)(\rho + \epsilon\rho - 1 + \beta z)}{\rho(\beta^2 + \epsilon^2 + 2\beta\epsilon z)}, \tag{A.1.3}$$

$$\delta = \frac{\beta(1 - z^2)^{1/2}[\rho^2\beta^2 + 2\rho\epsilon(1 - \rho)(1 - \beta z) - (\rho - 1 + \beta z)^2]^{1/2}}{\rho(\beta^2 + \epsilon^2 + 2\beta\epsilon z)}, \tag{A.1.4}$$

with $\rho = \omega/\omega'$. Somewhat time-consuming integrals needed to evaluate this are as follows:

$$\int_{-1}^{1} d\eta \frac{\eta^2}{(a + b\eta)(1 - \eta^2)^{1/2}} = \pi\Big[\frac{a^2}{b^2(a^2 - b^2)^{1/2}} - \frac{a}{b^2}\Big], \tag{A.1.5}$$

and

$$\int_{-1}^{1} d\eta \frac{\eta^2}{(a+b\eta)^2(1-\eta^2)^{1/2}} = \pi\left[\frac{1}{b^2} + \frac{a}{b^2}\frac{(2b-a)}{(a-b)(a^2-b^2)^{1/2}} - \frac{a^2}{b(a^2-b^2)^{3/2}}\right]. \tag{A.1.6}$$

The required energy distribution of Compton scattered photons is then given by $P(\omega;\omega',\gamma) = \int_{z_-}^{z_+} dz\frac{dP}{dz}$ where

$$z_- = \max[-1, \beta^{-1}[1-\rho(d+(d^2-1/\gamma^2)^{1/2})]], \tag{A.1.7}$$

and

$$z_+ = \min[+1, \beta^{-1}[1-\rho(d-(d^2-1/\gamma^2)^{1/2})]], \tag{A.1.8}$$

and $d = 1+\epsilon-\epsilon\rho$. The minimum and maximum values of the scattered energy ω may be determined by using Fig. 3 of Jones (1968) and following the accompanying discussion. Although the integral over z may be performed analytically, the resulting expression is even more complicated and for some parameter regimes, difficult to evaluate numerically (see again Jones 1968). $\frac{dP}{dz}$, on the other hand, is relatively well-behaved and easily integrated numerically.

A.2 Exact Pair Energy Distribution for Photon-Photon Pair Production

Aharonian *et al.* (1983a) contains a derivation for the energy distribution $P(\gamma_\pm;\omega_1,\omega_2)$ of pairs produced in the annihilation of two photons with energy ω_1 and ω_2. Unfortunately the expressions given there appear to contain misprints. Also, we do not find the logarithmic divergence in the pair energy spectrum claimed for the case $\gamma_\pm=\omega_1=\omega_2$. An alternate expression may be derived by following the analysis of Svensson (1982) and making the minor modifications required for the case of photon-photon pair production. The result is

$$P(\gamma_\pm;\omega_1,\omega_2)=\frac{c}{\gamma_{cm}\beta_{cm}\gamma_c\beta_c R(\omega_1,\omega_2)}\times \int_{-1}^{+1}\frac{d\mu}{2}(1-\mu)\int_0^{2\pi}d\phi H(\gamma_{cm}^2-1)H(1-|z|)\frac{d\sigma}{d\Omega_{cm}}(\mu,\phi), \tag{A.2.1}$$

where $\gamma_{cm}^2=\frac{1}{2}\omega_1\omega_2(1-\mu)$, $\beta_{cm}=(\gamma_{cm}^2-1)^{1/2}/\gamma_{cm}$, $\gamma_c=(\omega_1+\omega_2)/2\gamma_{cm}$, $\beta_c=(\gamma_c^2-1)^{1/2}/\gamma_c$, $z=(\gamma_\pm-\gamma_{cm}\gamma_c)/\gamma_{cm}\gamma_c\beta_c\beta_{cm}$, and

$$\frac{d\sigma}{d\Omega_{cm}}(\mu,\phi)=\frac{3\sigma_T\beta_{cm}}{32\pi\gamma_{cm}^2}\Big\{-1+\frac{1}{2}(3-\beta_{cm}^4)\Big[\frac{1}{1-\beta_{cm}x}+\frac{1}{1+\beta_{cm}x}\Big] -\frac{1}{2\gamma_{cm}^4}\Big[\frac{1}{(1-\beta_{cm}x)^2}+\frac{1}{(1+\beta_{cm}x)^2}\Big]\Big\} \tag{A.2.2}$$

with $x=yz+(1-y^2)^{1/2}(1-z^2)^{1/2}\cos\phi$, and $y=(\omega_1-\omega_2)/\beta_c(\omega_1+\omega_2)$. $R(\omega_1,\omega_2)$ is the pair production rate (eq. 4.3), and $H(x)$ is the Heaviside function.

This expression is easily evaluated numerically. We have verified (numerically) that it gives the correct first and second moments of the pair distribution (eq. 4.8, 4.9) and is properly normalized to unity ($\int P(\gamma_\pm;\omega_1,\omega_2)d\gamma_\pm=1$). We also obtain excellent agreement with the Aharonian *et al.* (1985) approximation in the region where the approximation is expected to work. The minimum and maximum possible pair energies for a given ω_1, ω_2 agree with the limits given in Aharonian *et al.* (1983) (see their equation 22 and accompanying discussion).

References

Abramowitz, M. & Stegun, I.A., 1965. *Handbook of Mathematical Functions,* Dover, New York.

Aharonian, F.A. & Atoyan, A.M., 1981a. *Astrophys. Space Sci.,* **79**, 321.

Aharonian, F.A. & Atoyan, A.M., 1981b. *Phys. Lett.,* **99b**, 301.

Aharonian, F. A., Atoyan, A.M., & Nagapetyan, A.M., 1983a. *Astrophys.,* **19**, 323.

Aharonian, F.A., Kirillov-Ugryumov & Kotov, Yu. D., 1983b. *Astrophys.,* **19**, 139.

Aharonian, F.A., Kirillov-Ugryumov, V.G. & Vardanian, V.V., 1985. *Astrophys. Space Sci.,* **115**, 201.

Alexanian, M., 1968. *Phys. Rev.,* **165**, 253.

Barbosa, D.P., 1982. *Astrophys. J.,* **254**, 301.

Baring, M., 1987a. *Mon. Not. R. astr. Soc.,* **228**, 681.

Baring, M., 1987b. *Mon. Not. R. astr. Soc.,* **228**, 695.

Bayer, V.N., Fadin, V.S. & Khoze, V.A., 1968. *Sov. Phys.,* **26**, 1238.

Berestetski, V.B., Lifshitz, E.M. & Pitaevski, L.P., 1982. *Quantum Electrodynamics, Landau and Lifshitz Course of Theoretical Physics, Vol 4*, 2nd edn, Pergamon Press, Oxford. (BLP)

Bisnovatyi-Kogan, G.S., Zeldovich, Ya B. & Sunyaev, R.A., 1971. *Sov. Astr.,* **15**, 17.

Blandford, R.D., & Rees, M.J., 1978. In: *Pittsburgh Conference on BL Lac Objects*, p. 328, ed Wolfe, A.M., University of Pittsburgh, Dept. of Physics and Astronomy, Pittsburgh.

Blumenthal, G.R. & Gould, R.J, 1970. *Rev. Mod. Phys.,* **42**, 237.

Coppi, P.S., 1990. Caltech Theoretical Astrophysics Preprint GRP-209, submitted to *Mon. Not. R. astr. Soc.*

Dermer, C.D., 1984. *Astrophys. J.,* **280**, 328.

Dermer, C.D., 1985. *Astrophys. J.,* **295**, 28.

Dermer, C.D., 1986. *Astrophys. J.,* **307**, 47.

Dermer, C.D. & Liang, E.P., 1989. *Astrophys. J.,* **339**, 512.

Fabian, A.C., Blandford, R.D., Guilbert, P.W., Phinney, E.S., & Cuellar, L., 1986. *Mon. Not. R. astr. Soc.,* **221**, 931.

Frankel, N.E., Hines, K.C., Dewar, R.L., 1979. *Phys. Rev. A,* **20**, 2120.

Ghisellini, G., 1987a. *Mon. Not. R. astr. Soc.,* **224**, 1.

Ghisellini, G., 1987b. Ph.D. Dissertation Thesis, ISSA, Trieste.

Gould, R.J. & Schréder, G.P., 1967. *Phys. Rev.,* **155**, 1404.

Gould, R.J., 1975. *Astrophys. J.,* **196**, 689.

Guilbert, P.W., 1981. *Mon. Not. R. astr. Soc.,* **197**, 451.

Guilbert, P.W. & Stepney, S., 1985. *Mon. Not. R. astr. Soc.,* **212**, 523.

Haug, E., 1975a. *Naturforsch,* **30a**, 1099.

Haug, E., 1975b. *Naturforsch,* **30a**, 1546.

Haug, E., 1985a. *Phys. Rev. D,* **31**, 2120.

Haug, E., 1985b. *Astr. Astrophys.,* **148**, 386.

Haug, E., 1987. *Astr. Astrophys.,* **178**, 292.

Haug, E., 1988. *Astr. Astrophys.,* **191**, 181.

Jones, F.C, 1965. *Phys. Rev.,* **137**, 1306.

Jones, F.C, 1968. *Phys. Rev.,* **167**, 1159.

Kusunose, M. & Takahara, F., 1985. *Prog. Theor. Phys,* **73**, 41.

Kusunose, M., 1987. *Astrophys. J.,* **321**, 186.

Lamb, D.Q., 1988. *Am. Inst. Phys. Conf. Proc.*, **170**, 265.

Lightman, A.P. & Zdziarski, A.A., 1987. *Astrophys. J.,* **319**, 643.

Novikov, I.D. & Stern, B.E, 1986. In: *Structure and Evolution of Active Galactic Nuclei*, p. 149, eds Giuricin, G. *et al.* , Reidel, Dordrecht, Holland.

Protheroe, R.J., 1986. *Mon. Not. R. astr. Soc.,* **221**, 769.

Ramaty, R. & Mézsáros, P., 1981. *Astrophys. J.,* **250**, 384.

Ramaty, R. & Lingenfelter, R.E., 1987. *Am. Inst. Phys. Conf. Proc.,* **155**, 51.

Rybicki, G. & Lightman, A.P., 1979. *Radiative Processes in Astrophysics*, John Wiley & Sons, New York.

Stepney, S., 1983. *Mon. Not. R. astr. Soc.,* **202**, 467.

Stepney, S. & Guilbert, P.W., 1983. *Mon. Not. R. astr. Soc.,* **204**, 1269.

Stern, B.E., 1985. *Sov. Astr.,* **29**, 306.

Svensson, R., 1982. *Astrophys. J.,* **258**, 321.

Svensson, R., 1986. In: *Radiation Hydrodynamics in Stars and Compact Objects, IAU Coll. No. 89*, p. 325, eds Mihalas, D. & Winkler, K.-H. A., Springer-Verlag, Berlin.

Svensson, R., 1987. *Mon. Not. R. astr. Soc.,* **227**, 403.

Takahara, F., 1980. *Prog. Theor. Phys,* **63**, 1551.

Zdziarksi, A.A., 1985. *Astrophys. J.,* **289**, 514.

Zdziarski, A.A., 1987. In: *Proceedings of the 13th Texas Symposium on Relativistic Astrophysics*, p. 553, ed Ulmer, M., World Scientific Press, Singapore.

Zdziarski, A.A. & Lightman, A.P., 1987. In: *Proceedings of Workshop on Variability in Galactic and Extragalactic X-ray Sources*, p. 121, ed Treves, A., Associazione per l'Avanzamento dell'Astronomia, Milan.

Zdziarski, A.A, 1988. *Astrophys. J.,* **335**, 786.

Figure Captions

Figure 1. The Compton scattering rate $R(\omega,\gamma)$ vs. the approximation given in eq. 2.6. The electron energy has been fixed at $\gamma = 20$. Note that $R(\omega,\gamma)$ begins to deviate significantly from $\sigma_T c$ well before $\omega\gamma = 1$.

Figure 2. Comparison of the results of using various approximations to the distribution of Compton scattered photons $P(\omega;\omega',\gamma)$. The electron distribution used was generated by running a "photon-starved" model ($l_s/l_e = 0.03$) with steep ($\Gamma = 2.4$,$\gamma_{max} = 10^3$) power-law pair injection. (See for example Lightman and Zdziarski 1987; the model corresponds roughly to their model "h." l_s/l_e is the ratio of the injected soft photon luminosity to the injected pair luminosity, and the pair injection rate goes as $\gamma^{-\Gamma}$ up to a maximum injection energy γ_{max}.) For the calculation shown, the electron distribution was held fixed and the photon distribution that would be in kinetic equilibrium with it was then determined by adding up several "orders" of Compton scattering (e.g., see Ghisellini 1987b). Note that in this calculation, electrons with low γ are very important and that many (~ 10) orders of scattering contribute. The $P(\omega) \propto \delta(\omega - 4/3\gamma^2\omega_0)$ scattering approximation employs a Klein-Nishina cutoff for the scattering rate and is the same as used in Lightman & Zdziarski (1987) and (modulo a factor of 4/3) Fabian *et al.* (1986). The "corrected" ($P(\omega) \propto \delta(\omega - \langle\omega\rangle)$) delta-function approximation is the same except that the correct scattering rate and average scattered energy $\langle\omega\rangle$ are used. The "Jones" approximation uses the approximate scattered distribution derived in Jones (1968) and employed, for example, in Zdziarski (1988). The "two moment" approximation is the one presented in this paper, and the "exact" scattered distribution was computed using eq. A.1.2.

For $\omega < 100$, the maximum error of the "corrected" delta-function approximation is $\approx +50\%$, while the two moment approximation has a maximum error of $\approx +25\%$. The Jones approximation has a maximum deviation of $\approx 50\%$ at $\omega \sim 1$. Note the premature roll-off of both the corrected delta-function and two moment approximations at the high energy end of the photon spectrum.

Figure 3. The exact annihilation rate $R(\gamma_-, \gamma_+)$ vs. the approximation given in eq. 3.7. The electron energy has been fixed at $\gamma_- = 5$. The maximum deviation between the two rates is less than 14%.

Figure 4. The annihilation spectrum (in arbitrary units) produced by power law pairs ($N(\gamma) \propto \gamma^{-2}$, $1.1 < \gamma < 10^3$) annihilating on cold ($\beta = 0$) pairs. The exact spectrum was calculated using eq. 41 of Svensson (1982) while the approximate spectrum was calculated using the two moment approximation presented here. For $0.8 \lesssim \omega \lesssim 35$, the maximum deviation between the two is less than 10%, and less than 30% for $0.75 \lesssim \omega \lesssim 500$.

Figure 5. The pair production rate $R(\omega_1\omega_2)$ vs. the approximation given in eq. 4.7. Over the range $1.3 \lesssim \omega_1\omega_2 \lesssim 10^4$, the maximum deviation between the two is less than 7%.

Figure 6. The "optical depth" to photon-photon pair production (see sec. 4.4) calculated for a photon distribution corresponding roughly to that of model "P" in Lightman & Zdziarski (1987). The approximation $\tau_{\gamma\gamma}(\omega) \propto 0.2n(1/\omega)/\omega$ is the one employed in Svensson (1987) and Lightman & Zdziarski (1987). The other curves were calculated by integrating the photon distribution over the exact pair production rate $R(\omega_1\omega_2)$ and the approximation given in eq. 4.7. Using eq. 4.7 gives an answer accurate to better than 2% over the frequency range shown.

Figure 7. The pair "spectrum" (in arbitrary units) produced by the annihilation of photons in the same distribution as considered for Fig. 6. The "AKV" approximation uses the approximate distribution presented in Aharonian *et al.* (1985). Note that this approximation is not very good for $\gamma \sim 1$. The "delta-function" approximation curve is calculated using the exact pair production rate but assuming that the created pairs all have energy $\langle\gamma\rangle = (\omega_1 + \omega_2)/2$. The "two moment" approximation is the one presented in sec. 4 of the text, and the "exact" distribution of pairs was computed using eq. A.2.1. The "two moment" and "exact" results agree to within 15%.

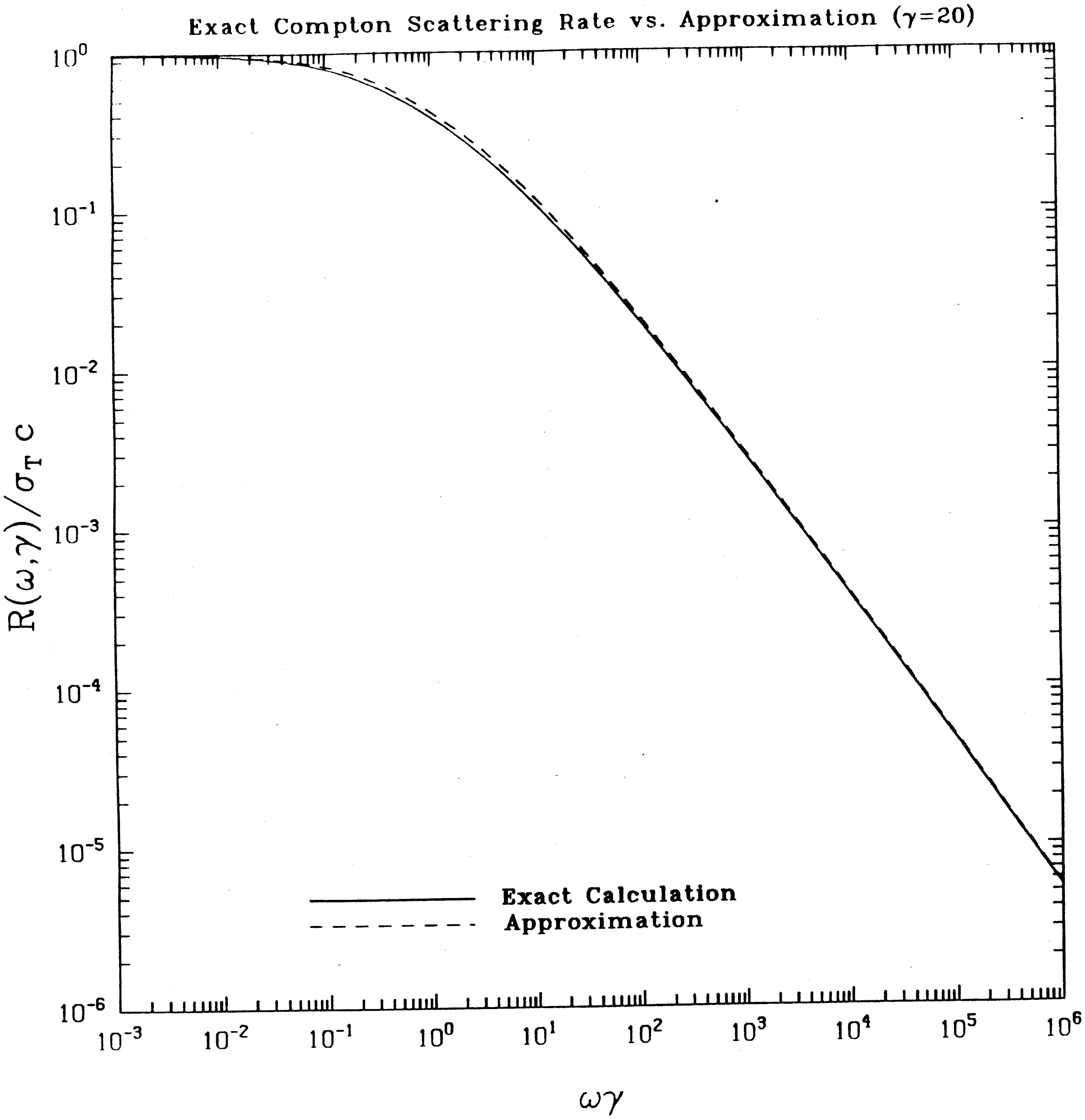
Exact Compton Scattering Rate vs. Approximation (γ=20)
10^{0}
10^{-1}
10^{-2}
10^{-3}
10^{-4}
10^{-5}
10^{-6}
$R(\omega,\gamma)/\sigma_T c$
10^{-3}
10^{-2}
10^{-1}
10^{0}
10^{1}
10^{2}
10^{3}
10^{4}
10^{5}
10^{6}
$\omega\gamma$
Exact Calculation
Approximation

Figure 1

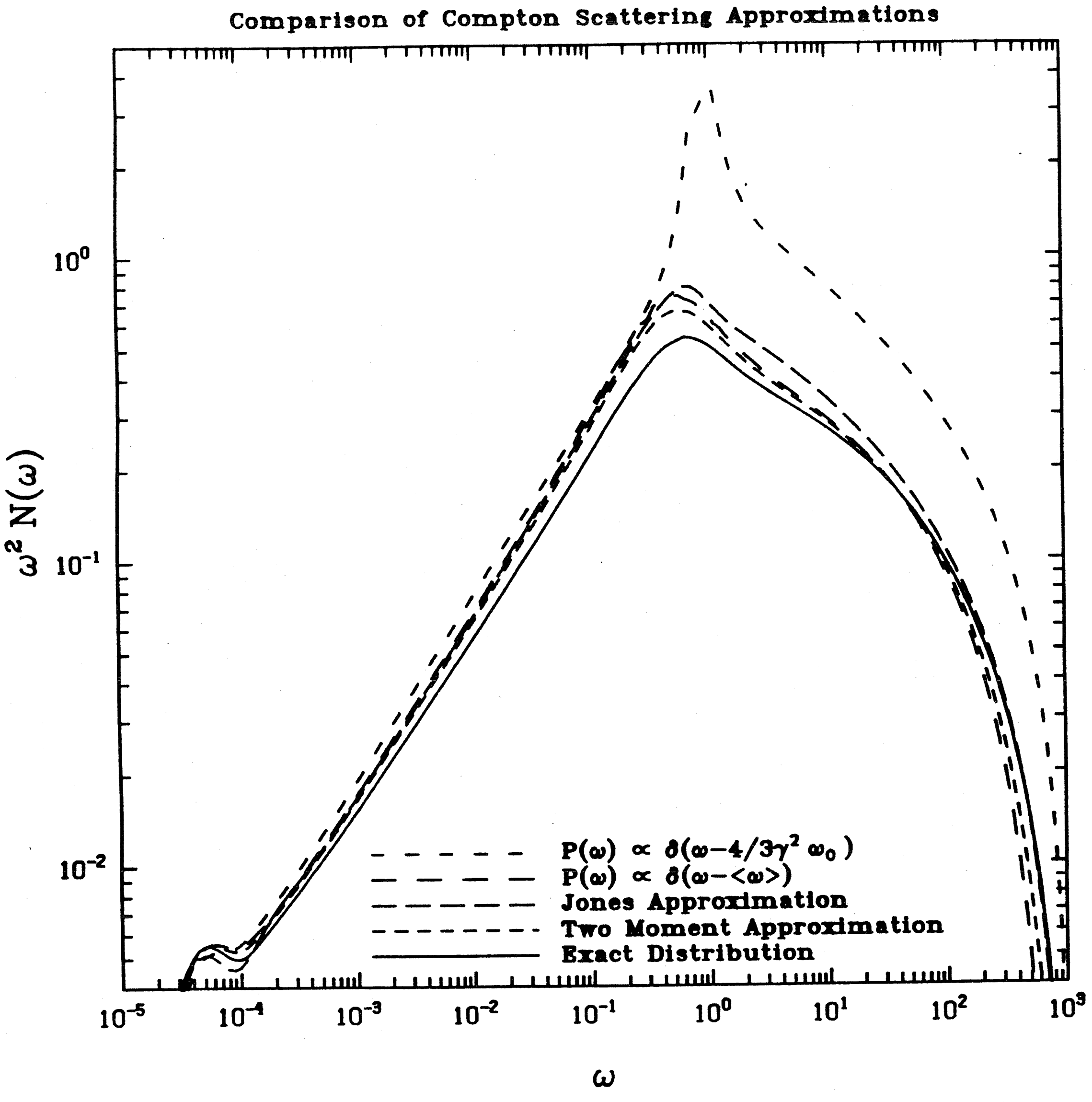
Comparison of Compton Scattering Approximations
$\omega^2 N(\omega)$
10^0
10^{-1}
10^{-2}
10^{-5}
10^{-4}
10^{-3}
10^{-2}
10^{-1}
10^0
10^1
10^2
10^3
ω
$P(\omega) \propto \delta(\omega-4/3\gamma^2\omega_0)$
$P(\omega) \propto \delta(\omega-\langle\omega\rangle)$
Jones Approximation
Two Moment Approximation
Exact Distribution

Figure 2

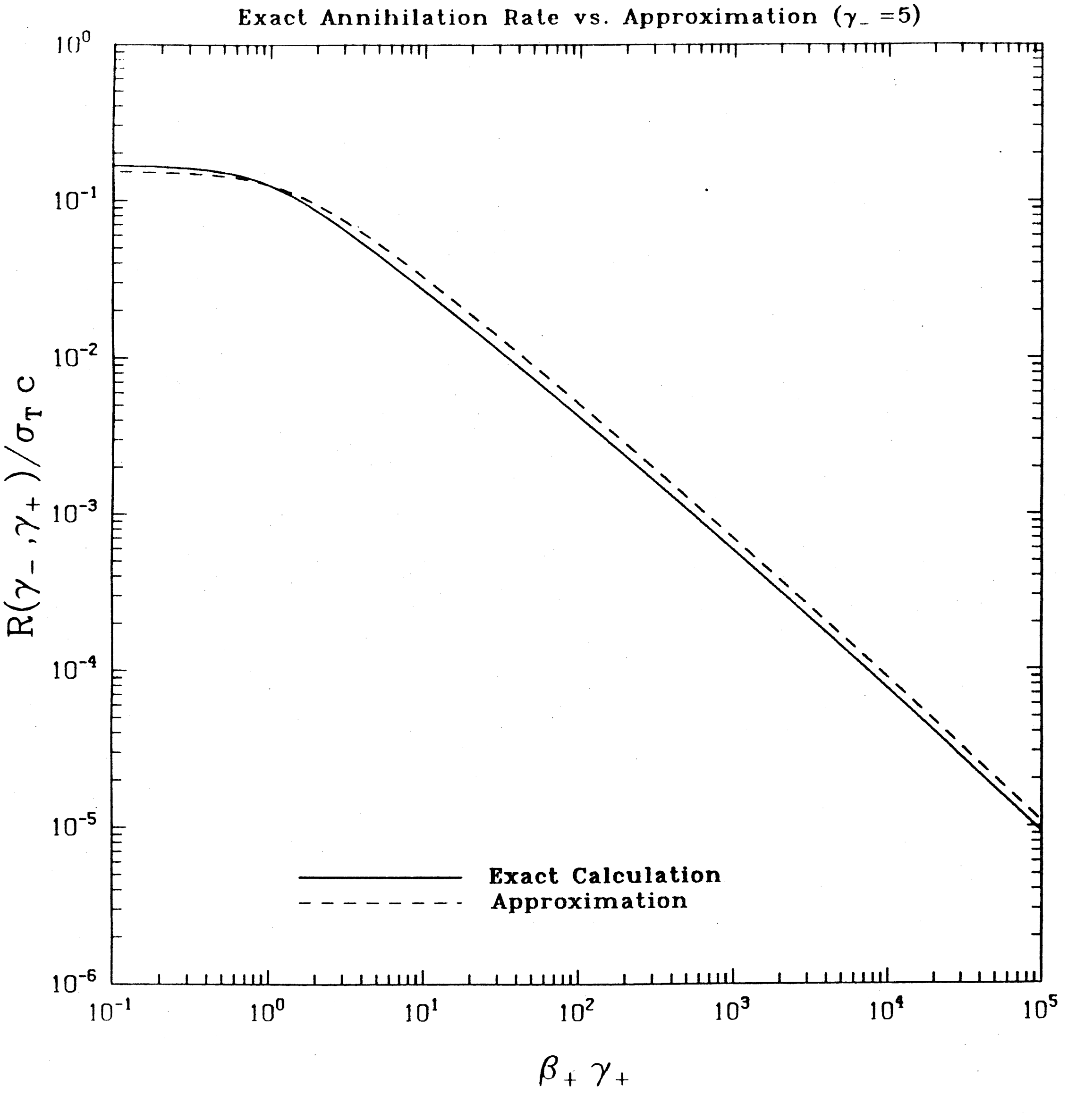
Exact Annihilation Rate vs. Approximation (γ_- =5)
$R(\gamma_-,\gamma_+)/\sigma_T c$
10^0
10^{-1}
10^{-2}
10^{-3}
10^{-4}
10^{-5}
10^{-6}
10^{-1}
10^0
10^1
10^2
10^3
10^4
10^5
$\beta_+ \gamma_+$
Exact Calculation
Approximation

Figure 3

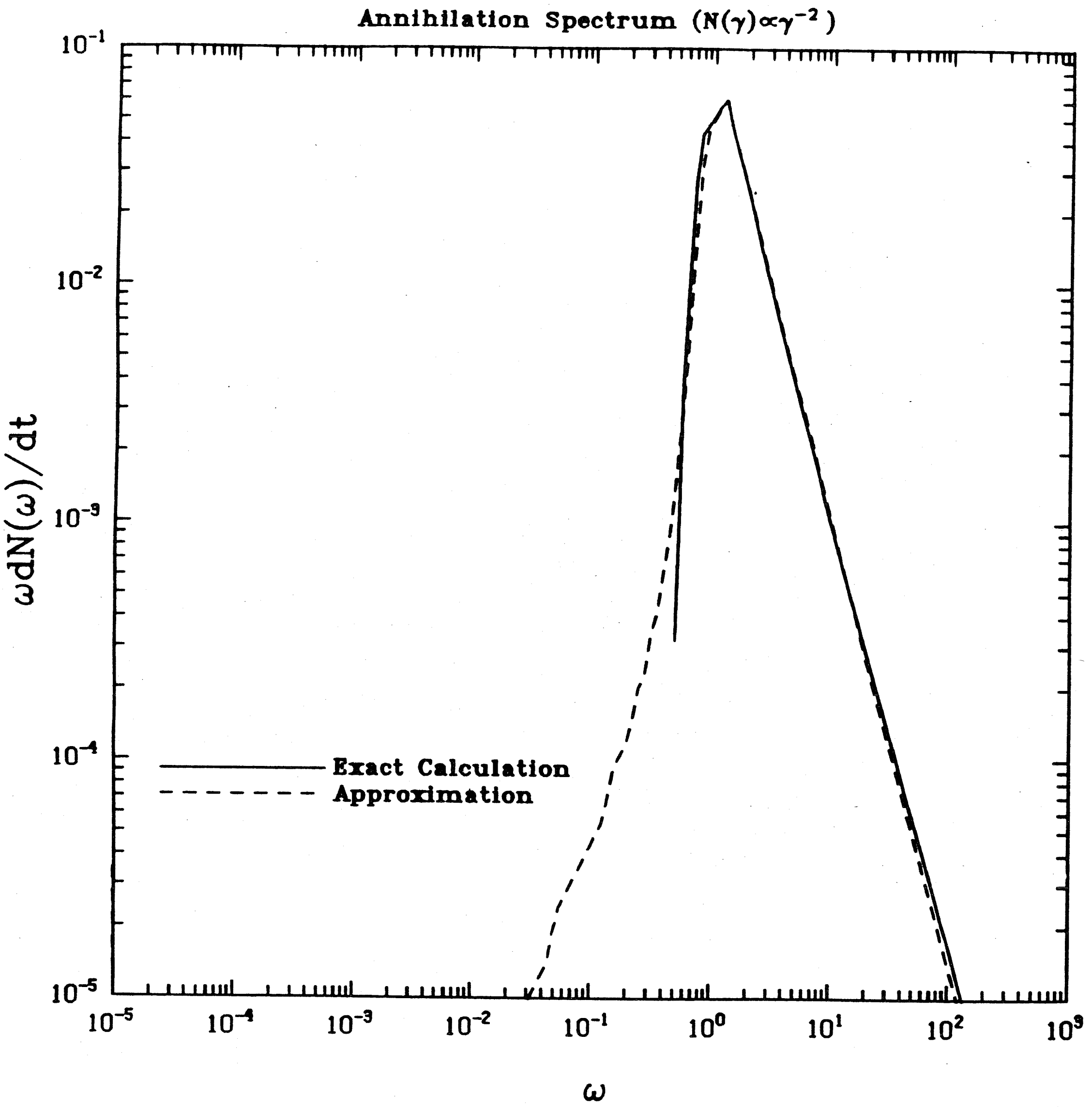
Annihilation Spectrum ($N(\gamma)\propto\gamma^{-2}$)
$\omega dN(\omega)/dt$
10^{-1}
10^{-2}
10^{-3}
10^{-4}
10^{-5}
Exact Calculation
Approximation
10^{-5}
10^{-4}
10^{-3}
10^{-2}
10^{-1}
10^{0}
10^{1}
10^{2}
10^{3}
ω

Figure 4

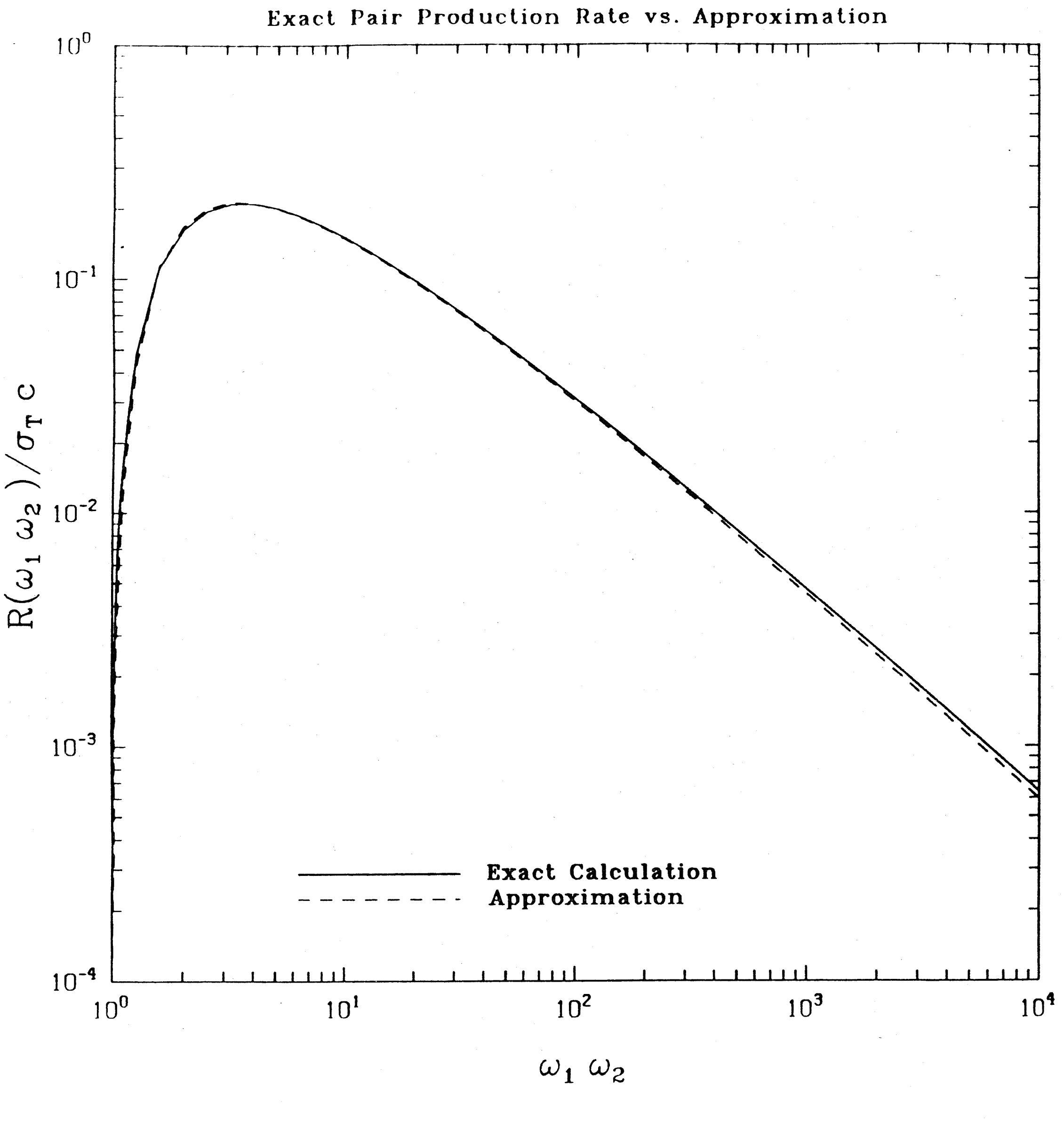
Exact Pair Production Rate vs. Approximation
10^0
10^{-1}
10^{-2}
10^{-3}
10^{-4}
$R(\omega_1\ \omega_2)/\sigma_T\ c$
10^0
10^1
10^2
10^3
10^4
$\omega_1\ \omega_2$
Exact Calculation
Approximation

Figure 5

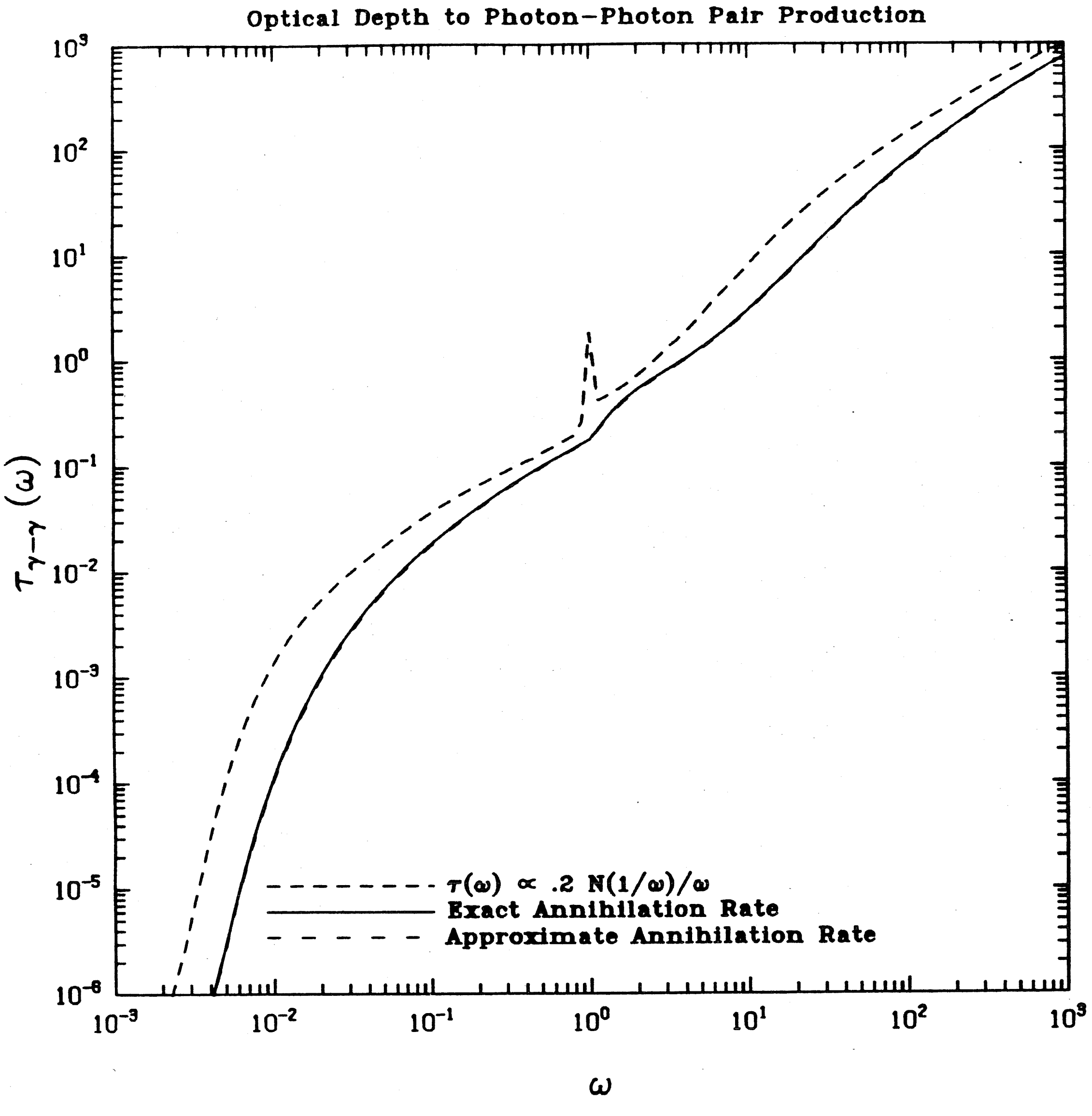
Optical Depth to Photon–Photon Pair Production
$\tau_{\gamma-\gamma}(\omega)$
10^3
10^2
10^1
10^0
10^{-1}
10^{-2}
10^{-3}
10^{-4}
10^{-5}
10^{-6}
$\tau(\omega) \propto .2\ N(1/\omega)/\omega$
Exact Annihilation Rate
Approximate Annihilation Rate
10^{-3}
10^{-2}
10^{-1}
10^0
10^1
10^2
10^3
ω

Figure 6

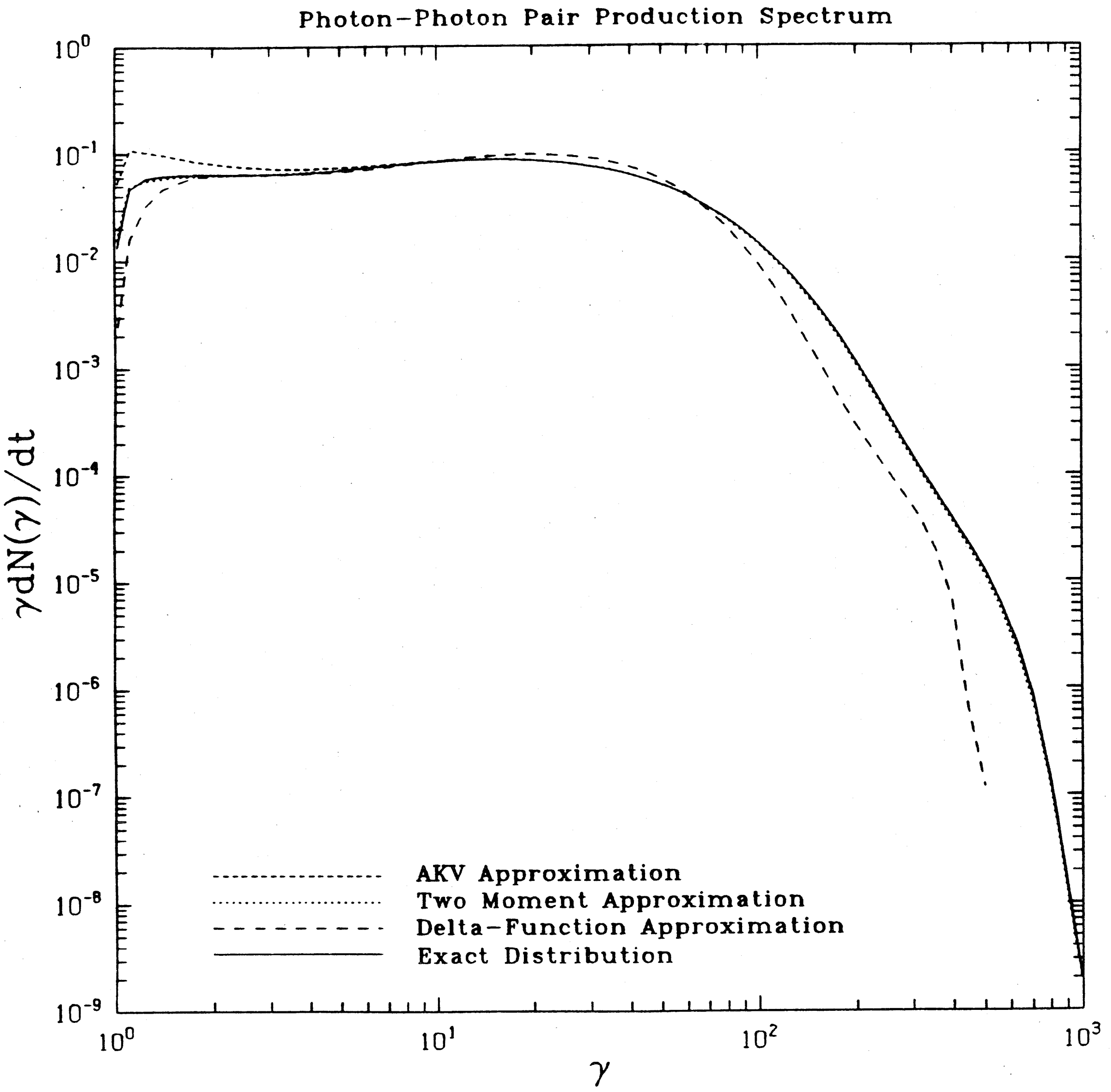
Photon–Photon Pair Production Spectrum
$\gamma dN(\gamma)/dt$
10^0
10^{-1}
10^{-2}
10^{-3}
10^{-4}
10^{-5}
10^{-6}
10^{-7}
10^{-8}
10^{-9}
10^0
10^1
10^2
10^3
γ
AKV Approximation
Two Moment Approximation
Delta–Function Approximation
Exact Distribution

Figure 7

Chapter 3

TIME-DEPENDENT MODELS OF MAGNETIZED PAIR PLASMAS

Submitted to *Mon. Not. R. astr. Soc.*

Abstract

A numerical code has been developed to study the time evolution of electron-positron plasmas. The code solves in a self-consistent manner kinetic equations describing the effects of: Compton scattering, two photon pair production, pair annihilation, cooling of pairs via Coulomb scattering, e-e bremsstrahlung, and synchrotron radiation. The kinetic equations are derived under the approximation of homogeneous and isotropic particle distributions following the discussion in Coppi & Blandford (1990). Both stationary (equilibrium) and time-varying output radiation spectra have been computed. Good qualitative agreement with previous calculations is found, except where the differences are attributable to the improved treatment of the microphysics. These differences can be substantial. In magnetized plasmas, the self-absorption turnover frequency is found to vary weakly with the model input parameters. In particular, for mono-energetic injection at energy γ_{inj}, the turnover frequency ν_t is $\sim 3 \times 10^{13} U_{10^4}^{1/3} \gamma_{inj}^{-1/3}$ Hz, where U is the smaller of either the magnetic or photon energy density (measured in units of 10^4 ergs/cm^3). This may be relevant to the spectra of radio-quiet AGN. Also, the spectral index of the inverse Compton scattered radiation can differ significantly from the associated synchrotron radiation spectral index. (In fact, the equilibrium photon and pair distributions are often not well-described by power laws.) Varying the energy and particle inputs to the pair plasma gives rise to many different types of spectral variability. The response of the plasma depends sensitively on both the current state of the plasma and the details of the changes in particle injection. Using time variability as a diagnostic (e.g., to determine the relevance of the models considered here) may thus prove difficult. A possible signature, however, is the response to a significant decrease in the injection of energetic pairs. If the initial Thomson optical depth is order unity or

more, the photon spectrum decays from the high energy end downwards (lower frequencies lag higher frequencies). The decay of the continuum usually uncovers a prominent, long-lived annihilation feature.

1. Introduction

As noted by Jelley (1966) and Herterich (1974), significant electron-positron pair production is likely to occur in a compact energetic source such as the central engine of an AGN. The resulting "pair plasma" can radically alter the emergent spectrum of radiation that must pass through it. Energetic pairs in the plasma can Compton upscatter an initially soft (e.g., IR, UV) spectrum to X- and gamma-ray energies, while cool pairs can add an annihilation feature at ~ 0.5 MeV (e.g., as seen in the Galactic center). The plasma may also effectively reprocess gamma-rays into X-rays (see Svensson 1987), disguising the true nature of the source. Finally, the plasma, with its characteristic (non-zero) response times, will play a large role in determining the observed source variability.

Early attempts to describe pair plasmas (e.g., Bisnovatyi-Kogan, Zel'dovich & Sunyaev 1971) made the simplifying assumption that the pairs were in thermal equilibrium, i.e., that their distribution functions could be characterized by a (relativistic) Maxwellian of fixed temperature. The first detailed investigations concentrated on understanding the effects of pair-photon Compton scattering. These culminated in the work by Sunyaev & Titarchuk (1980) who studied "Comptonisation" in plasmas with low pair temperatures and large Thomson optical depths using the Kompaneets (1957) equation. Their results were verified in Monte Carlo simulations (e.g., Lorentz 1981, Górecki & Wilczewski 1984) and extended to mildly relativistic pair temperatures by Zdziarski (1985).

A more complete description of a pair plasma and photon-pair interactions, however, must also treat the processes of pair production and annihilation. Moreover, since Compton scattering and these two processes alter the number and energy of the pairs in the thermal distribution, one cannot realistically assume a fixed pair distribution. Much work has thus been devoted to self-consistently determining the combined effects of these processes in a thermal plasma. The most advanced treatments to date are probably those of Guilbert & Stepney (1985) and Kusunose (1987) which are based on a time-dependent, kinetic equation code and attempt to explicitly solve the radiative transfer equations. (For previous treatments, see Lightman & Band 1981, Araki & Lightman 1983, Svensson 1982 for analytical approaches to the problem, and Guilbert 1981,1983, Zdziarski 1984,1985 for the numerical approaches.)

Unfortunately there is good reason to believe that the pairs in a pair plasma are *not* in thermal equilibrium. Assuming, for example, that pair annihilation balances pair production in a thermal pair plasma leads to a maximum source luminosity which appears to be exceeded in observed AGN (e.g., Araki & Lightman 1983). More importantly, thermalisation times for mildly relativistic pairs are likely to be quite long compared with other timescales in the problem, see Stepney (1983). The pair distribution is thus likely to have a significant non-thermal tail. This tail is often approximated by a power law. However, one can show that a power law does not even satisfy the stationary plasma kinetic equations which include only Compton scattering, pair annihilation, and pair production. Significant deviations from power law behavior can be expected, especially if additional processes such as synchrotron self-absorption are included. To solve the pair plasma problem satisfactorily, one therefore needs a method for handling *arbitrary* photon and pair distribution functions. In addition, since pair plasmas are likely to live in variable sources, whatever method is employed should be able to trace the evolution of the particle distributions in time.

Two approaches have been employed thus far. The first, using the technique described in Pozdnyakov *et al.* (1977), is a Monte Carlo approach where individual particles are followed as they undergo interactions inside the source. The main advantage of such a scheme is that it is usually easy to model the radiative transfer well. However, such a scheme typically suffers from relatively poor photon statistics at high frequencies (even when variance-reducing techniques like photon splitting are used) and does not lend itself to time-dependent calculations. For examples of the Monte Carlo calculations performed to date, see Stern (1985), Novikov & Stern (1986), and Stern (1988). The second approach involves solving the relevant kinetic equations. Following the time evolution of the system in such an approach is straightforward and photon statistics are not an issue. The major problems facing this method are: (i) the resulting integro-differential equations can be quite cumbersome as well as "stiff"(i.e., there are widely differing timescales in the problem), (ii) only simple prescriptions for radiative transfer (such as an escape probability formalism) can be implemented easily on present-day computers. For examples of kinetic equation treatments see Fabian *et al.* (1986) (henceforth referred to as FBGPC), Ghisellini (1987a, 1987b), Lightman & Zdziarski (1987) (henceforth referred to as LZ), and Svensson (1987).

In this paper, we have chosen to follow the kinetic equation approach. The code employed for the work presented here is most similar to that of FBGPC. Like them, we "discretise" the kinetic equations, placing particles in bins of definite energy. We also make similar assumptions about the isotropy and spatial uniformity of the pair and photon distributions. Our particular code, however, is distinguished from previous codes in that we have significantly improved the treatment of microphysical processes (see Paper I – Coppi & Blandford 1990) and added the effects of synchrotron radiation, electron thermalisation (Coulomb cooling), and e-e bremsstrahlung.

After discussing in section 2 the physical details of the model considered along with some numerical "details" of the code, we proceed in section 3 to consider the case of a stationary pair plasma with no magnetic field, comparing our results with those obtained in previous work. In section 4, we consider the effects of adding a magnetic field. Finally, in section 5 we consider the time behavior of the system.

2. Model Description

2.1. Microphysics, Physical Assumptions and Definitions

In the present version of the code, we consider the standard "pair" processes of Compton scattering ($\gamma e \rightarrow \gamma e$), pair annihilation ($e^+e^- \rightarrow \gamma\gamma$), and pair production ($\gamma\gamma \rightarrow e^+e^-$). To these we add the processes of e-e bremsstrahlung ($ee \rightarrow ee\gamma$), Coulomb "cooling" ($ee \rightarrow ee$), and synchrotron radiation ($eB \rightarrow eB\gamma$). (See Svensson 1986 for a general discussion of which processes are relevant.) All these processes are described by kinetic equations derived under the assumption of *homogenous* and *isotropic* particle distributions, as well as of tangled, relatively weak magnetic fields. We present here a discussion of only those terms not already discussed in paper I. In what follows, we refer only to the *pair* distribution $N(\gamma)$ since we we assume (as do LZ and FBGPC) that the electron and positron distributions are identical, i.e., $N_{e^-}(\gamma) = N_{e^+}(\gamma)$. Also, all energies will be measured in units of $m_e c^2$. $N(\gamma)$ is thus the number density of pairs with energy $\gamma m_e c^2$, and $n(x)$ will be the number density of photons with energy $x m_e c^2$.

Our treatment of synchrotron radiation tries to avoid some of problems inherent in past treatments, e.g., Ghisellini (1987a). For the synchrotron emissivity, we have taken the relativistic limit averaged over an isotropic pitch angle distribution, i.e.,

$$p_\nu(\nu, \gamma) = \frac{\sqrt{3}e^3 B}{m_e c^2}\left(\frac{\nu}{\nu_c}\right)\int_0^\pi \frac{d\alpha}{2}\sin\alpha \int_{\nu/\nu_c \sin\alpha}^{\infty} dx K_{5/3}(x), \tag{2.1}$$

where $\nu_c = \frac{3}{4\pi}\gamma^2(eB/m_e c)$. (See Crusius & Schlickeiser 1986 for a more detailed discussion.) This is a good approximation down to energies $\gamma \sim 3$ and avoids the problems associated with delta-function approximations (e.g., premature cutoffs in the spectra, artificial "spikey" spectral features – see the discussion in paper I on Compton scattering). Because a simple cutoff approximation to the synchrotron cooling rate misses many important effects (see Ghisellini 1987b), we have used the Fokker-Planck formalism of McCray (1969). Note that this treatment of synchrotron radiation is essentially the same as employed in de Kool *et al.* (1989) and Ghisellini *et al.* (1988). Our code, however, makes no assumptions about the size of the radiation field energy density (i.e., the importance of Compton scattering) as the Compton and synchrotron terms appear on the same footing in the pair kinetic equations. Note also that Ghisellini *et al.* (1988) have included non-relativistic corrections to their equations which for certain parameter regimes can affect the very low energy ($\gamma \lesssim 2$) pair distribution. (The McCray 1969 equations are strictly valid only in the limit $\gamma \gg 1$.) These corrections, however, do not appear to affect significantly the photon spectra presented here.

In modeling particle escape, we follow LZ and FBGPC. Pairs are assumed to be trapped (e.g., by a weak magnetic field), and there is no pair escape term in our kinetic equations. Photon escape is modeled using a simple escape probability, i.e., by a term in the photon kinetic equations of the form:

$$\dot{n}_{esc}(x) = -\frac{c}{R} n(x)[1 + \tau_{KN} f(x)]^{-1} \tag{2.2}$$

where

$$f(x) = \begin{cases} 1 & \text{for } x \leq 0.1; \\ (1-x)/0.9 & \text{for } 0.1 < x < 1; \\ 0 & \text{for } x \geq 1. \end{cases} \tag{2.3}$$

and

$$\tau_{KN}(\theta, x) = 2R\langle\sigma_{KN}\beta\rangle_T(\theta, x)N_T \tag{2.4}$$

as in LZ, eq. 21a. Here N_T is the number density of cool, thermal pairs, $\langle \sigma_{KN} \beta \rangle_T$ represents an average over the thermal particle distribution, σ_{KN} is the Klein-Nishina cross-section, and R is the source radius. The function $f(x)$ compensates for the fact that as the photon energy x increases, forward scatterings predominate, reducing the photon escape time. Under this approximation, photons with energy $x > 1$ are assumed to free stream out of the source with a characteristic escape time given by R/c, the light-crossing time. This approximation appears to reproduce reasonably well the results of Monte Carlo calculations which deal with the radiative transfer problem correctly (Zdziarski, private comm).

To deal with particle injection/acceleration, we adopt the simplified description of LZ and FBGPC, i.e., we assume particles are injected uniformly into the interaction region from some *external* source(s). Under this assumption, particle injection can be described by two functions, $S(x,t)$ and $Q(\gamma,t)$, which do not depend on the pair and photon distributions present in the interaction region. (Feedback mechanisms such as "pair loading," see Done & Fabian 1989, will thus not be considered here.) $S(x,t)$ is the rate of injection (per unit volume) of photons of energy x at time t, and $Q(\gamma,t)$ is the analogous injection rate of *pairs* at energy γ and time t. We will consider here functions of the form $S(x,t) = S(x)f_s(t)$ and $Q(\gamma,t) = Q(\gamma)f_q(t)$. Motivated by the desire to model pair plasmas which might be found in AGN, we take the photon injection function $S(x)$ to be a black body with temperature $\theta_{rad} = kT_{rad}/m_e c^2 \sim 10^{-5}$, the sort of spectrum that might be radiated by a black hole accretion disk. The pair injection function $Q(\gamma)$ is taken to be either mono-energetic at some injection energy $\gamma_{inj} \sim 10^{3-4}$ (i.e., $Q(\gamma) \propto \delta(\gamma - \gamma_{inj})$), or a power law of index Γ (i.e., $Q(\gamma) \propto \gamma^{-\Gamma}$) extending from some γ_{min} to $\gamma_{max} \sim 10^{3-4}$ as might be produced in shock particle acceleration. The time behavior of the injection functions considered here will be mostly discontinuous, i.e., changes in particle injection are impulsive — the case studied by FBGPC.

Having specified the form of the injection functions, their normalizations remain to be specified. As discussed in FBGPC, this is most conveniently done by specifying the dimensionless "compactness parameters" (luminosities) l_s and l_e where:

$$l_s = \frac{L_s \sigma_T}{R m_e c^3} = \frac{4\pi R^2 \sigma_T}{3c} \int x S(x) dx, \tag{2.5}$$

and

$$l_e = \frac{L_e \sigma_T}{R m_e c^3} = \frac{8\pi R^2 \sigma_T}{3c} \int \gamma Q(\gamma) d\gamma \tag{2.6}$$

Here R is the characteristic size of the interaction region (thought to be $\sim 10^{14} - 10^{15}$ cm. in AGN), $L_s = \frac{4\pi}{3} R^3 m_e c^2 \int_0^\infty x S(x) dx$ is the injected (soft) photon luminosity, and $L_e = \frac{8\pi}{3} R^3 m_e c^2 \int_1^\infty \gamma Q(\gamma) d\gamma$ is the total injected pair luminosity. Note that these definitions do not match exactly the ones given in either FBGPC or LZ. Like LZ (and unlike FBGPC), we take the interaction region to be spherical with radius R. Hence the overall factors of $\frac{4\pi}{3}$ in the definitions. Unlike LZ, however, we inject *pairs*, not just electrons. An extra factor of two is thus required in our definition of L_e, and the factor of $(\gamma - 1)$ in the LZ definition (eq. 2a) must be replaced by γ since the rest mass of the injected pairs can be effectively transferred to the radiation field via pair annihilation.

A convenient way of normalizing output spectra is similarly given by using the escaping luminosity compactness parameter, $l(x) = \frac{4\pi}{3c} R^2 \sigma_T x \dot{n}_{esc}(x)$. When the computed models reach an equilibrium (stationary) state, the total injected energy flux must equal the total escaping energy flux. We thus have $l_{tot} = \int_{x_{min}}^{x_{max}} l(x) dx = l_e + l_s$. The quantity $x l(x)$ plotted in the figures is a dimensionless escaping luminosity per logarithmic energy interval directly proportional to the more usual $\nu F(\nu)$, the flux per logarithmic frequency interval. For use in the discussion which follows, we also define the diagnostic quantities:

(i) $\tau_T = 2N_T\sigma_T R$, the optical depth to Thompson scattering, where N_T is the number of thermal electron/positrons and R is the source radius;

(ii) $\tau_C = 2R\sigma_T \int_1^{\gamma_{max}} N(\gamma)d\gamma$, an analogous optical depth for Compton scattering off non-thermal pairs;

(iii) $\theta = kT_{pairs}/m_e c^2$, the equilibrium temperature of the thermal pair distribution;

(iv) $\tau_{\gamma\gamma}(x) = \frac{R}{c}\int_{1/x}^{x_{max}} n(x_1)R_{pp}(x,x_1)dx$, the "optical depth" to photon-photon pair production, where $R_{pp}(x,x_1)$ is the pair production rate for photons of energy x annihilating with photons of energy x_1.

2.2. *Numerical Approach*

The kinetic equations are solved using a simple first order difference scheme. We have found this adequate except when dealing with synchrotron reabsorption and the evolution of the pair distribution. For this we have used a second order monotonicity scheme with upwind differencing (see Norman & Winkler 1986). The particle distributions are discretised, with a resolution of 20 bins/decade of energy. The photon bins span 12 decades of energy, from $x_{min} = 10^{-9}$ to $x_{max} = 10^3$, while the pair bins span 3 decades of energy, from $\gamma_{min} = 1$ to $\gamma_{max} = 10^3$. The first pair bin contains the thermal pairs with a variable temperature θ. The number (N_T) and total energy (E_T) of the pairs in this thermal bin are explicitly followed, with the temperature being derived from these quantities. Since processes other than Compton scattering can exchange energy with thermal pairs, this temperature need not be the "Compton" temperature (e.g., as assumed in LZ) at which Compton heating balances Compton cooling. A useful approximation for θ in terms of $u = E_T/N_T$ is

$$\theta = \frac{4}{45}[\frac{15u-27}{8} + (\frac{(15u-27)^2}{64} - \frac{45}{2}(1-u))^{1/2}]. \tag{2.7}$$

The approximation becomes exact in the limits $u \to 1, \infty$ and is accurate to 5%.

To allow easy vectorization and obtain reasonable execution times, we have pre-computed and stored in tables as many quantities as possible. Memory constraints required the use of approximate final particle energy distributions for the processes of pair production and annihilation. These "two moment" approximations have been discussed extensively in paper I. For less complicated runs (e.g., those shown in Fig. 1), the exact scattered particle distribution for the process of non-thermal Compton scattering has been used. Unless explicity stated, though, it should be assumed that a two moment approximation for Compton scattering was also used.

The "stiffness" problem referred to in the introduction occurs mainly in the evolution of the pair distribution. (High energy pairs typically cool on times much shorter than any other timescale in the problem.) The stiffness is handled by making the "stationary" approximation used in FBGPC and LZ, i.e., assuming that

$$N(\gamma) = -\frac{\int_\gamma^{\gamma_{max}}[Q(\gamma') + P(\gamma')]d\gamma']}{\dot{\gamma}(\gamma)},$$

where $Q(\gamma)$ is the rate of injection of pairs of energy γ by the external source, $P(\gamma)$ is the rate at which pairs of energy γ are created via pair production, and $\dot{\gamma}$ is the cooling rate for pairs at energy γ due to Compton scattering, Coulomb cooling, and synchrotron radiation. Note that for this approximation to be valid at energy γ, not only must the cooling time $\gamma/\dot{\gamma}$ be significantly shorter than any other timescale (e.g., the timescale for the photon distribution to change), but the evolution of the pair distribution at that energy must be well-described by the equation $\frac{dN}{dt}(\gamma) = -\frac{d}{d\gamma}[\dot{\gamma}N(\gamma)] + P(\gamma) + Q(\gamma)$. This will *not* be the case for energies γ where synchrotron self-absorption effects are non-negligible, or where $\Delta\gamma/\gamma$, the fractional change in energy after one Compton scattering, is not much less than unity (e.g., when most scatterings are in the Klein-Nishina regime). As pointed out in Blumenthal (1971) and Zdziarski (1988), errors of order unity can be incurred if the stationary approximation is used in such cases. Our code contains explicit checks for these conditions and switches the approximation off when its use becomes inappropriate.

If one is not interested in the time evolution of the system, one can avoid the stiffness altogether by solving directly for the stationary particle distributions. For use in problems not involving synchrotron self-absorption, we have modified one version of our code to converge on the stationary solution iteratively. The method is similar to that described in LZ and uses the fact that the stationary equation for a bin N_i has the general form

$$0 = -f(N_i) + g(N_i, N_{i\neq j}) + h(N_{i\neq j}) + Q(i)$$

where f,g, h are (usually algebraic) functions describing respectively: the rate at which particles are scattered/annihilated out of bin i, the rate at which particles in bin i are scattered back into bin i, and the rate at which particles in other bins are scattered in bin i. $Q(i)$ represents the rate at which particles are created/injected into bin i. Taking the bins $i \neq j$ $(N_{i\neq j})$ to be fixed, one can then solve for N_i. Inserting the newly found bin values back into the kinetic equations and solving again, one obtains a mapping $N_i^k \rightarrow N_i^{k+1}$ which when repeated converges to the stationary value of N_i. For example, when only Compton scattering is being considered, this is equivalent to adding up the "orders" of Compton scattering. The method appears quite stable provided the various bin values are solved for in the right order. Our code first does one iteration on the photon bins assuming the pair distribution is fixed. The code then iterates repeatedly on the pair bins until the pair distribution is in equilibrium with the photon distribution. The entire process is repeated until the fractional change $(|N_i^{k+1} - N_i^k|/N_i^k)$ in all photon bins is less than some specified amount. We note that for synchrotron self-absorption, the functions f, g, and h contain derivatives of the pair distribution. This leads to numerical instabilities in our simple implementation of the method described.

3. Unmagnetized Equilibrium Plasmas

There have been extensive discussions of equilibrium (stationary) pair plasmas with no magnetic fields in past work (e.g., LZ, FBGPC, Svensson 1986,1987, Ghisellini 1987a, 1987b). To ascertain the impact of the "improved" microphysics employed here, we have repeated these calculations over a wide range of compactness parameters, $.01 \lesssim l_e, l_s \lesssim 1000$. The results obtained are qualitatively similar and do not alter the most important conclusions of previous work. (Hence we will not repeat those discussions here.) The quantitative differences, however, are not so negligible (e.g., see Fig. 1) and are ascribable to the differences in the microphysics which we now discuss.

3.1. Compton Scattering by Thermal Pairs

As discussed in paper I, the inclusion of dispersion in the scattered photon distribution is necessary to generate modestly accurate spectra. The scheme employed here has been checked against published Monte Carlo simulations (e.g., Górecki & Wilczewski 1984) for $\theta = kT_{pair}/m_e c^2$ up to ~ 10 and agrees reasonably well. The errors are dominated by the uncertainties in the radiative transfer. The LZ escape probability employed here attempts to mock up a spherical source with soft photon injection that varies radially as $\sin(kr)/kr$ (see eq. 8 of Sunyaev & Titarchuk 1980). In practice, however, the approximation does not quite succeed and the results obtained generally fall somewhere between those for a sphere with central injection and those for a sphere with uniform injection. When the diffusion approximation holds ($\tau_T \gg 1, \theta \ll 1$) and the exact escape probability is known (e.g., Sunyaev & Titarchuk 1980), the results agree to better is underestimated (see discussion in paper I). Our results appear consistent with an alternative diffusive scheme employed by LZ.

3.2. Compton Scattering by Non-Thermal Pairs

The present code also improves upon its predecessors in its treatment of non-thermal Comptonization. The effects of the various approximations employed in past work (e.g., not using the Klein-Nishina cross-section, and ignoring "dispersion") have been discussed in paper I. These effects are most noticeable in "photon starved" ($l_s \ll l_e$) models where a photon is likely to undergo multiple scatterings off non-thermal pairs. We note that the approximations made can significantly affect *both* the photon and pair distributions. In particular, the use of the cooling approximation ($N(\gamma) = (\int Q(\gamma)d\gamma)/\dot{\gamma}$) in the photon starved regime can give poor results (discrepancies of order unity).

3.3. Pair Annihilation

In models without direct pair escape, pair annihilation is the process which allows the pair distribution to reach equilibrium, converting pairs into photons which may then escape the source. An accurate treatment of pair annihilation is therefore crucial to determining the equilibrium pair distribution and thus the final output photon spectrum. While dealing adequately with the annihilation of thermal pairs, previous treatments (e.g., LZ, FBGPC) have ignored the possibility of non-thermal pairs annihilating with themselves or with the thermal distribution. When Compton cooling is fast (e.g., large l_s), the injected pairs are brought into the thermal distribution in a time much shorter than the timescale to annihilate ($\sim R/c\tau_T$) and *non*-thermal pair annihilation is indeed unimportant. However, in a photon starved model (small l_s), the Compton cooling times at low γ can be quite long, causing pairs to "pile up" there. Including non-thermal pair annihilation in this case can alter the equilibrium photon spectrum significantly. A crude parameter for gauging the importance of non-thermal pair annihilation is given by the value of τ_T/l_s. (When $\tau_T/l_s \ll 1$, non-thermal pair annihilation is usually ignorable.)

Figure 2 shows an example of what happens when τ_T/l_s is not small. When non-thermal pair annihilation is turned off, the result is a visibly different output spectrum. The entire spectrum, not just the region around the annihilation line, is affected. To gauge the importance of non-thermal annihilation, note that in the case without Coulomb cooling, well over half the total annihilation luminosity comes from non-thermal pairs annihilating with either thermal pairs or other non-thermal pairs. Neglecting non-thermal pair annihilation can therefore be a dangerous assumption. Note, however, that the importance of non-thermal annihilation can be considerably lessened by the presence of a significant Coulomb cooling rate (see below). One should also remember that the usual estimate for τ_T obtained by balancing the total pair injection rate against the thermal pair annihilation rate breaks down when non-thermal annihilation is important. Significant numbers of cooling pairs may annihilate before joining the thermal distribution. Mention should also be made of the treatment of the "annihilation line" at $x \sim 1$. As in Fig. 2, it may be quite broad and also asymmetric (if the contribution from non-thermal pairs is important). Approximating it by a delta-function (e.g., FBGPC, LZ) is often not justified. (In our code we generate the thermal annihilation spectrum using the approximation of Svensson 1983 which appears to be quite good.)

3.4. *Pair Production*

As is evident from the series of models shown in Fig. 1, some of the most visible disagreement with previous results (in particular those of LZ) arise when the process of pair production becomes significant. As explained in paper I, the approximation used in Svensson (1987) and LZ can overestimate $\tau_{\gamma\gamma}$ by up to factors of order two. Also, the fact that it includes no dispersion may lead to significant errors in the shape of $P(\gamma)$, the energy distribution of "created" pairs. These two effects can lead to a serious underestimate of the γ-ray spectrum and a distortion of the X-ray spectrum (since the distribution of the non-thermal pairs which upscatter soft photons depends on $P(\gamma)$). Note, however, that when the plasma is pair dominated ($\tau_{\gamma\gamma} \gg 1$ for $x \gtrsim 1$, $P(\gamma) \gg Q(\gamma)$), the pair distribution and the photon distribution for $x < 1$ become relatively insensitive to even large discrepancies in $\tau_{\gamma\gamma}$. (To first order, the equilibrium high energy photon distribution simply readjusts itself to keep everything else the same.) Hence the surprisingly good – typically much better than a factor two – agreement with the results of LZ in quantities such as τ_T and the pair yield (e.g., Table I).

3.5. *Coulomb Cooling*

In the present version of the code, we make use of the treatment of Coulomb scattering presented in paper I, i.e., we simplify matters somewhat by considering only Coulomb collisions between non-thermal and thermal pairs (a well-justified approximation as long as $\int_1^\gamma d\gamma' N(\gamma') \ll N_T$ for $\gamma \lesssim 10$ – *usually* the case in models considered here) and treating the effects of these collisions as a cooling term, $\dot{\gamma}_{coul}[\gamma]$, for the non-thermal pairs and a heating term, $-\int d\gamma \dot{\gamma}_{coul} N(\gamma)$, for the thermal pairs. The process of thermalization is mocked up by transferring cooled pairs and their remaining energy to the thermal bin once they reach an energy $\gamma \lesssim 1+8\theta$. (The results prove insensitive to the exact details of how this is done.) The condition that this Coulomb "cooling" be negligible then translates into the requirement that $\dot{\gamma}_{coul}[\gamma] \ll \dot{\gamma}_{other}[\gamma]$ for all γ, where by "other" we mean cooling by other process such as Compton scattering or synchrotron radiation. For the purpose of making estimates, we may take $\dot{\gamma}_{coul}[\gamma] \approx \frac{3c}{2R} \ln \Lambda\tau$ and $\dot{\gamma}_{other} = \dot{\gamma}_{comp} \sim \frac{c}{\pi R}\gamma^2 l_s$. Coulomb cooling should therefore not be neglected for $\gamma \lesssim \gamma_c = (\frac{3\pi}{2} \ln \Lambda \frac{\tau}{l_s})^{1/2}$. ($\ln \Lambda$ is the usual Coulomb logarithm, typically $\sim 15-25$ for the models considered here.)

As an example of where Coulomb cooling has non-negligible effects, consider the model of Fig. 2 (for which the test described above gives a $\gamma_c \approx 50$). Turning on Coulomb cooling has two main consequences. First, Coulomb cooling allows injected pairs to transfer a non-negligible fraction of their injected energy directly to the thermal pairs (instead of losing all of it via Compton scattering to the radiation field). This tends to raise the equilibrium temperature of the thermal pair distribution (increasing it a factor 5 in the case of Fig. 2.) Coulomb cooling also prevents the accumulation of pairs near $\gamma = 1$ that would otherwise occur when $\dot{\gamma}_{comp}$ becomes small, sweeping the pairs into the thermal distribution (see Fig. 2b). As a side effect, this additional cooling, just like a large Compton cooling rate, prevents a significant amount of annihilation by cooling pairs while they are in their non-thermal state. To summarize, then, even though Coulomb scattering conserves total pair number and energy, the pair distributions calculated with and without Coulomb cooling can be quite different in the region near $\gamma = 1$. As seen in Fig. 2a, this difference is also reflected in the equilibrium photon distributions, especially in the region $x \sim 1$. Coulomb cooling should not be ignored in models with $l_e/l_s \gg 1, l_s \lesssim 1$.

3.6. Bremsstrahlung

Our code is also capable of (crudely) dealing w/e-e bremsstrahlung, another process not considered in previous treatments which could have a significant impact. (See paper I for a description of the method employed.) In models of the type considered here, bremsstrahlung serves two functions: (i) as an additional source of photons, (ii) as another pair cooling mechanism. Unlike Coulomb scattering, however, e-e bremsstrahlung really is a "higher order" process and for most choices of parameters may indeed be ignored. This is true of the models presented in the figures. It is *not* true, however, for extremely photon starved ($l_s \ll 1$) models where the thermal pairs may reach a relativistic temperature $\theta \sim 1$. This case will be examined in more detail elsewhere (see Zdziarski, Coppi, & Lamb 1990). We note that the contribution to the overall bremsstrahlung spectrum from non-thermal pairs can be quite significant. Like the contribution of non-thermal pairs to the annihilation spectrum, it should not be ignored.

4. Stationary Models with Magnetic Fields

We now consider the effects of adding a magnetic field to our model of a pair plasma. As discussed in section 2, our treatment of synchrotron radiation makes the assumptions of isotropic pitch angle and radiated photon distributions. This requires that the magnetic fields under consideration be relatively weak and tangled. In view of this, we shall restrict our attention here to field strengths $B_0 \lesssim 1000G$, values thought to be typical of what is found in AGN central engines. For such relatively low field strengths, synchrotron radiation represents another source of soft (IR→UV) photons which can replace or augment the external soft photon source. Thus, since the cooling rate for energetic ($\gamma \gg 1$) pairs Compton scattering off a soft photon field has (to first order) the same energy dependence as the cooling rate due to synchrotron emission, the spectra produced in such models will not differ grossly from those seen in "unmagnetized" models. (This is in contrast to some of the cases examined by Ghisellini 1987a, 1987b where the maximum synchrotron photon energy $x_{s,max}$ may exceed unity, and synchrotron radiation provides a source of hard photons which may pair produce immediately, without intermediate upscatterings.)

It is easiest to begin by examining models with only pair injection and no external photon source (i.e., models with $l_s = 0$) as such models contain most of the new physics and are easier to analyze. Note that in such models, the equilibrium radiation field is completely determined by the pair injection function $Q(\gamma)$, the source region radius R, and the magnetic field strength B_0. (Because of the inclusion of synchrotron self-absorption, R does *not* scale out of the problem as it does in "unmagnetised" models.) To help understand the spectra characteristic of such models, we consider two limiting cases: (i) the "synchrotron-dominated" regime where the Compton upscattering of photons can be treated as a perturbation; and (ii) the "Compton-dominated" regime where synchrotron effects may instead be treated as a perturbation. These two regimes may be distinguished through the use of the dimensionless energy "densities" $\hat{U}_B = \frac{R\sigma_T}{m_e c^2} U_B$ and $\hat{U}_{rad} = \frac{R\sigma_T}{m_e c^2} U_{rad}$. Here $U_B = \frac{B_0^2}{8\pi}$ is the magnetic energy density, and $U_{rad} = m_e c^2 \int x n(x) dx$ is the radiation energy density. Expressed in terms of these quantities, the cooling rate for pairs at energies high enough that synchrotron self-absorbtion may be neglected is given by

$$\dot{\gamma} \approx \frac{4c}{3R} \gamma^2 \hat{U}_B (1 + \hat{U}_{rad}/\hat{U}_B). \tag{4.1}$$

Thus, for $\hat{U}_{rad}/\hat{U}_B \gg 1$, Compton scattering dominates the pair cooling, while for $\hat{U}_{rad}/\hat{U}_B$ synchrotron emission dominates. Noting that at kinetic equilibrium energy conservation demands $\hat{U}_{rad}$ be $\sim l_e$, we thus see that "Compton-dominated" models correspond to models with input parameters such that $l_e/\hat{U}_B \gg 1$, while "synchrotron-dominated" models correspond to models with $l_e/\hat{U}_B \ll 1$. Examples of the spectra produced in these limiting cases (as well as for some intermediate values of $l_e/\hat{U}_B$) can be seen in Fig. 3-7.

4.1. *"Compton-dominated" Models*

For models with $l_e \gg \hat{U}_B$, Compton cooling in fact dominates synchrotron cooling (and heating via reabsorption) for all pair energies γ. Thus, the shape of the equilibrium pair distribution is quite similar to that seen in the unmagnetized models of the previous section (where the pair distribution is well-described by a power law at most energies). One would therefore expect to see an upscattered photon distribution that also resembles those obtained in the unmagnetized case. In fact, for $x \gtrsim x_{s,max}$ ($x_{s,max} \sim \gamma_{max}^2 B/B_c, B_c = 4.4 \times 10^{13} G$) the output spectrum is very close to that produced in an unmagnetized model with the same l_e and $l_s = l_{synch}$, e.g., see Fig. 3. Here l_{synch} is a synchrotron "compactness parameter" analogous to l_s, i.e., $l_{synch} = \frac{4\pi}{3} \int dx x \dot{n}_{synch}(x)$, where $\dot{n}_{synch}(x)$ is the rate of synchrotron emission per unit volume of photons of energy x. A crude estimate shows that (to within factors of order unity) l_{synch} is $\sim \hat{U}_B$. Compton-dominated models thus correspond to unmagnetized models with $l_s \ll l_e$, and once l_{synch} has been determined accurately, the analysis used to understand the unmagnetized case carries through essentially unchanged to the Compton-dominated case. Note an important characteristic of such ($l_s \ll l_e$, $\hat{U}_B \ll l_e$) models, namely the flat X-ray spectrum ($\alpha_x \lesssim .5$ with flux $F_\nu^x \propto \nu^{-\alpha_x}$) composed of several "orders" of Compton scattering. (For a discussion of such spectra, see the case where $\tau_C \sim 1$ in LZ and Ghisellini 1987b.) This is contrary to what one might expect from the analysis of Bonometto & Rees (1971) which would predict a spectral index ~ 1 (e.g., as in the pair dominated cases in Fig. 1). Unfortunately, since several orders of Compton scattering contribute to the photon spectrum, Klein-Nishina corrections cannot be neglected and the analysis of such models is somewhat complicated. (Hence, constructing a simple *and* accurate estimate for l_{synch} is difficult.)

The differences between Compton-dominated and unmagnetized spectra reflect the different origins of the soft photons in the models (non-thermal vs. assumed thermal). As the synchrotron spectrum radiated by power law electrons does not much resemble a Planck distribution, the agreement between the models is not very good for energies $x < x_{s,max}$. In particular, the photon distribution due to synchrotron radiation is typically much broader than the corresponding blackbody distribution, a fact which is also reflected in the upscattered photon distributions. (In general, when dealing with synchrotron emission, the finite width of the emitted photon distribution can never be neglected.) Note also that the synchrotron portion of a spectrum in the Compton-dominated case does not look much like the "conventional" spectrum obtained from radiating power-law electrons. The effects of thermal upscattering and multiple (non-thermal) Compton scattering (important in the $l_s, l_{synch} \ll l_e$ regimes) can significantly modify the part of the spectrum due to optically thin synchrotron emission, i.e., the result will *not* be a simple power law of index $(p-1)/2$ where p is the power law index of the pairs. Also, while the strongly self-absorbed part of the spectrum is well-described by the usual power law of index 2.5, there is typically no sharp self-absorption "break" (turnover) marking the changeover from optically thin to optically thick synchrotron emission. (It is smeared away.)

4.2. "Synchrotron-dominated" Models

In contrast to the Compton-dominated case, a synchrotron-dominated model cannot be conveniently related to an unmagnetized model with similar equilibrium pair and photon distributions. The reasons for this can be found by examining the (now non-negligible) effects of synchrotron emission/reabsorption on the equilibrium pair distribution. The most important of these is the "suppression" of the non-thermal pair distribution. At energies high enough that self-absorption effects can be neglected, the addition of a large synchrotron cooling rate to the usual Compton cooling rate means that $N(\gamma)$ at such energies is always smaller in the synchrotron-dominated model than in a pure Compton (unmagnetized) model with $l_s = l_{synch}$ and the same l_e. This suppression has several consequences. With fewer non-thermal pairs to upscatter soft photons, the high energy (X- and γ-ray) end of the photon distribution is correspondingly suppressed. (Note for example Fig. 4,5 where more and more of the emitted power is shifted to the synchrotron emission peak as $\hat{U}_B/l_e$ increases.) With fewer high energy photons present, pair production is also suppressed, and the pair yields obtained in synchrotron-dominated models can be much lower than would be expected from the corresponding pure Compton models. Synchrotron-dominated models therefore tend to have low values of τ_T and weak, if not invisible, annihilation lines. The suppression of the non-thermal pair distribution also means that typical values of τ_C (the optical depth to non-thermal Compton scattering) are much less than unity and secondary Compton scattering is consequently unimportant. Thus, unlike the Compton-dominated case, the part of the soft photon distribution due to optically thin synchrotron emission *is* well-described by the conventional power law of index $(p-1)/2$. (For these models, $p \sim \Gamma/2$ where the pair injection function $Q(\gamma) \propto \gamma^{-\Gamma}$.) To first order, the upscattered photon distribution is also described by a power law of the same index. Note, however, that the non-negligible width of the soft (synchrotron) photon distribution often causes the upscattered photon distribution to deviate from the predicted power law well before the maximum upscattered frequency ($\sim 4/3\gamma_{max}^2 x_{s,max}$) is reached.

At the low energy end of the pair distribution, synchrotron self-absorption effects become important and the deviations from what might be expected in the pure Compton case are even more marked. As noted by Rees (1967a) and McCray (1969), a power law distribution is in general not a stable equilibrium solution when the process of synchrotron radiation dominates the evolution of the pair distribution. In particular, there will be some energy γ_t for which heating from the reabsorption of photons becomes important, and for $\gamma \ll \gamma_t$, this heating will actually dominate (slightly) over the cooling (e.g., see de Kool *et al.* 1989). The energy γ_t is of order $(3x_t/4x_0)^{1/2}$ where $x_0 = B/B_c$, $x_t = h\nu_t/m_ec^2$, and ν_t is the frequency where self-absorption becomes important – see below. This causes the formation of a Maxwellian-like distribution (e.g., see Fig. 5b) at energies lower than $\gamma \sim \gamma_t$ and is referred to as the "synchrotron boiler" effect in Ghisellini *et al.* (1988).

As can be seen in Fig. 5b, however, Compton cooling off the synchrotron photons suppresses this tendency of low energy pairs to form a Maxwellian. As U_{rad}/U_B increases, the peak of the Maxwellian-like shape gets pushed to lower and lower energies. In Fig. 5b, not much of a Maxwellian remains by $l_e = 10$. Consequently, we would argue that the synchrotron boiler is not a widely applicable method for creating thermal distributions with $\theta \gtrsim 1$. Rather, it will only be of interest in the limited parameter space $l_e \lesssim 1$. Note also in Fig. 5b that Coulomb cooling tends to destroy the Maxwellian shape, primarily at the low energy end. One might not expect this since τ_T in these models is quite small, and the corresponding Coulomb cooling rates are also small. However, as noted above, for $\gamma \ll \gamma_t$, heating from reabsorption almost exactly cancels the cooling from emission. A small additional cooling rate (Compton or Coulomb) can therefore have a very important effect. As a final observation, note the "disjointed" power law shape taken on by the pair distribution as U_{rad} increases. This appears to be in accord with the predictions of de Kool *et al.* (1989).

The possibly large deviation from power law behavior at energies $\gamma < \gamma_t$ is also reflected in the photon distribution. An "excess" of pairs at these energies should produce a corresponding excess of (upscattered) photons at energies $x_{s,max} \lesssim x \lesssim 4/3\gamma_t^2 x_{s,max}$. This can be clearly seen in Fig. 5a. A non-power law pair distribution at energies $\gamma < \gamma_t$ (i.e., for which self-absorption is important) will also give a strongly self-absorbed part of the photon spectrum that has a spectral index different from the usual value of 2.5 obtained with a power law pair distribution. In fact, as $\hat{U}_B$ beomes much greater than l_e and the pair distribution becomes more and more a Maxwellian, the spectral index (for frequencies $v \ll v_t$) approaches a limiting value of 2.0 ($F_v \propto v^2$), the value for a strongly self-absorbed photon distribution in equilibrium with a thermal pair distribution. The spectral index thus varies continuously with $\hat{U}_B/l_e$, going from 2.5 ($\hat{U}_B \ll l_e$) to 2.0 ($\hat{U}_B \gg l_e$). The detailed dependence on $\hat{U}_B/l_e$ appears to be quite complicated, and we have not found an easy way of extricating the effects of Compton scattering from those of synchrotron emission/absorption. We remind the reader that discontinuites in the pair distribution (e.g., as seen in Fig. 5b) may give rise to spectral indices (over a limited range of energies) that *exceed* 2.5. See de Kool & Begelman (1989) for some detailed examples of this.

In contrast to Compton-dominated models, synchrotron-dominated models tend to show a fairly sharp break in their spectra at v_t, the frequency at which $R\alpha_\nu \sim 1$ and the synchrotron absorption of photons becomes important. (α_ν is the synchrotron absorption coefficient.) One can often make a simple estimate for this "turnover" frequency, ν_t. In the simplest case of mono-energetic pair injection, taking $N(\gamma \geq \gamma_t) \approx -\int Q(\gamma)d\gamma/\dot{\gamma}$ (with $\dot{\gamma}$ as given in eq. 4.1) and using the approximation for the absorption coefficient discussed in McCray (1969), we have:

$$v_t \approx 3.2 \times 10^{13}(\frac{\hat{U}_B\hat{U}_{rad}}{\hat{U}_B + \hat{U}_{rad}})^{1/3}\gamma_{inj}^{-1/3}R_{14}^{-1/3}Hz, \tag{4.2}$$

where again $\hat{U}_{rad} \approx \frac{3}{4\pi}l_e$. This estimate should be valid even in the transition regime $l_e \sim \hat{U}_B$ and appears to work reasonably well as can be seen by examining the spectra shown in Fig. 1 and 2. Note the form this expression takes when $\hat{U}_{rad}/\hat{U}_B$ is very small and U_{rad} and U_B are used instead of $\hat{U}_{rad}$ and $\hat{U}_B$):

$$\nu_t \sim 3 \times 10^{13} U_{rad}^{1/3} \gamma_{inj}^{-1/3}, \tag{4.3}$$

where U_{rad} is measured in units of 10^4ergs/cm^3. The magnetic field and radius of the source drop out completely. (An interesting result if U_{rad} scales as M, the mass of the central black hole.) The important observation to draw from these expressions (and the models shown) is that the turnover frequency is relatively insensitive to the input model parameters. Thus, if the models discussed prove relevant to real AGN, one might expect to find a turnover always in the neighborhood of $\sim 10^{13} Hz$.

4.3. Models with External Soft Photon Injection

Nothing very remarkable happens when an external photon source is added (e.g., as in Fig. 7,9a,10a). Although the detailed variation of equilibrium spectra with the injection parameter l_s is hard to estimate analytically, the limiting case of $l_s \gg \hat{U}_B$ is clear. In this limit, l_s is also $\gg l_{synch}$ and pairs cool primarily by Compton scattering off the soft externally-injected photons rather than by synchrotron emission or Compton scattering off synchrotron photons. The equilibrium pair distribution is thus independent of U_B and for $x > x_s$, one obtains spectra identical to those obtained with an unmagnetized model with the same l_e and l_s. The synchrotron part of the spectrum ($x < x_s$) may then be treated as a perturbation, determined by considering the spectrum radiated by a fixed pair distribution. As above, note that although they originate from the same pair distributions, the X-ray and optically thin synchrotron portions of the spectrum are not identical in shape. In particular, the spectral indices may be rather different.

One particular model with differing indices that may be of interest is obtained by taking $l_s \sim \hat{U}_B, B_0 \lesssim 1000$G and injecting pairs in a steep power law of index $\Gamma \sim 2.4$. As noted in Zdziarski (1986), the resulting spectrum (e.g., Fig 7) often resembles the canonical (radio quiet) AGN spectrum with $\alpha_{IR} \sim 1.1$, $\alpha_x \sim 0.7$, and a sharp break/turnover at $\sim 10^{13}$ Hz. (Here α_{IR} and α_x are the near infrared and X-ray spectral indices.) The "blue bump" is provided by externally injected photons (e.g., from an accretion disk corona), and the infrared is synchrotron emission from pairs. Note one "feature" of this model: varying the minimum injection energy γ_{min} causes the infrared spectral index to vary (and can make it less than unity) without perturbing the X-ray portion of the spectrum very much. (See for example Fig. 7 and the values of α_x in Table II.) One could thus have a "universal" power law injection index, ~ 2.4, for the pairs and explain observed variations in α_{IR}/α_x as variations in γ_{min}. Such models also need not predict a strong correlation between α_x and α_{IR}. The non-thermal (synchrotron) hypothesis for the origin of the infrared continuum should therefore not be dismissed out of hand.

Unfortunately, the sort of model just discussed may have several difficulties matching observations. These mainly reflect the fact that the infrared and X-ray photons originate from the same pairs (source region). Based on limited experimentation, it may not be possible to obtain the correct ratios of the luminosities in the IR, UV, and X-ray (2-10 kev) bands and still have reasonable valus of α_{IR} and α_x. More importantly, one would expect variations in pair injection to show up both in the infrared and the X-rays, i.e., infrared and X-ray time variability should be about the same. This is typically not observed (but see the next section).

5. Time-Variation

In this section, we investigate the time-response of the model pair plasma system to impulsive (step-function) changes in the particle injection rates – such as might occur in a bursting compact source. Such variations reveal most of the dynamical effects at work in a pair plasma and are the easiest to understand. (This is also the case examined in FBGPC.) We will not perform any specific spectral analyses as in Done & Fabian (1989) since the detailed answers are likely to be quite sensitive to the model assumptions.

5.1. *Relaxation Timescales*

We begin by examining the various relaxation timescales for the particle distributions in our model. The more complex, "collective" time behavior seen in the following section may be understood as the interplay of these timescales.

Consider first the non-thermal pair distribution. When pair injection is changed, the relevant timescale for the pair distribution (at energy γ) to respond is the cooling time, $t_{cool} = -\gamma/\dot{\gamma}$. Typically, this cooling time is much shorter than any other timescale in the problem, and as a rule of thumb, the non-thermal pair distribution "equilibrates" much faster than the photon distribution. (Hence the validity of the stationary approximation discussed in §2.2.) Exceptions to this rule may occur, however, in "photon-starved" models with $l_s \ll l_e$ (Compton cooling is slow at low γ) or synchrotron-dominated models at energies where the emitted synchrotron radiation is strongly self-absorbed. When only photon injection is changed, variations in the pair distribution will be slower and occur on the timescales for the cooling and pair production rates (i.e., the soft photon distribution) to change. Note one semantic point. After the initial rapid response to a change in pair injection, the non-thermal pair distribution is essentially "locked" onto the more slowly varying photon distribution. Thus the timescale for the non-thermal pair distribution to approach its *final*, stationary value is really the longer photon-response timescale.

The thermal pair distribution and the corresponding annihilation line (whose luminosity is $\propto \tau_T^2$) generally vary much more slowly than the non-thermal distribution and can often be the most sluggish components of the pair plasma. Consider first the response to an increase in particle injection. Exactly how long the thermal distribution takes to build up depends on the total pair injection rate (external injection + pair production). When the stationary value of τ_T predicted from the new injection parameters is less than unity (e.g., for $l_e, l_s \lesssim 10$), the total pair injection rate is small. The number of thermal pairs along with the annihilation line intensity can thus take *many* light-crossing times, $t_{cross} = R/c$, to build up to their stationary value. When, on the other hand, the production rate of pairs is large and the predicted value of τ_T exceeds unity, the number of thermal pairs can build up quite fast, on a time $\sim t_{cross}$. In either case, note that there will always be a *lag* with respect to the rest of the photon spectrum (in particular the gamma-rays) as the photon distribution must first build up before pair production can increase significantly.

Consider now the response (relaxation) time when particle injection is reduced. If only (soft) photon injection is reduced, nothing significant happens until the soft photon distribution has had time to decrease, i.e., only after a time $\sim t_{esc}$ (computed using the initial value of τ_T) has passed. The thermal pairs will then approach equilibrium on the same timescale as for the soft photon distribution (t_{esc} computed using the final value of τ_T.) If pair injection is reduced, however, the response can be much more dramatic. Typically, the number of high energy photons drops rapidly (see below), causing a corresponding decrease in the total pair production rate. With the number of incoming (cooled) pairs signficantly reduced, the thermal pair distribution is then free to annihilate away on the timescale $t_{ann} \sim 1/\tau_T$ (the time required for half the pairs to annihilate). An initial $\tau_T \gg 1$ can therefore disappear in a time $\lesssim R/c$. Note, though, that once τ_T drops below unity, t_{ann} increases and the annihilation line becomes a persistent feature, still visible, in the case where particle injection is completely turned off, long after all other photons have escaped the source. (This behavior is to be contrasted with that in models with pair escape. There the annihilation line and thermal pairs will be gone in a few characteristic pair escape times.)

The relaxation times of the photon distribution remain to be discussed. In the simplest case where the old and new injection parameters are such that τ_T is always less than unity, the photon distribution behaves in a uniform manner, building up or decaying at all energies on a timescale $\sim t_{cross}$ (the escape time for photons in this case). Whenever τ_T starts out or becomes greater than unity, however, one must make a distinction between high ($x \gtrsim 1$) and low ($x \lesssim 1$) energy photons. Low energy photons are "trapped" in the source by the thermal pairs and respond on the longer timescale $t_{esc} \sim (1 + \tau_t/3)t_{cross}$ (the characteristic soft photon escape time). Note that the value of τ_T may change significantly during the evolution of the soft photon distribution. The soft photon distribution relaxes to its new stationary value after a few t_{esc}, computed using the *final* value of τ_T (see FBGPC).

Because of Klein-Nishina effects, high energy photons are not trapped significantly by thermal pairs and in principle should always respond on the timescale t_{cross}. High energy photons, however, do feel the effects of downscattering by the thermal pairs (which effectively acts as an absorption term) as well as of annihilation off soft photons (a true absorption) and a varying injection (upscattering) rate due to changes in the non-thermal pair and soft photon distributions. This has two consequences. When soft photon injection is varied or pair injection is increased, the high energy photon distribution, like the non-thermal pair distribution, becomes (after some initial transient behavior) "locked" onto the soft photon distribution and follows its evolution. The "relevant" relaxation timescale is then the soft photon timescale t_{esc}. When pair injection is significantly decreased, however, the high energy end of the non-thermal pair distribution drops rapidly in response as does the corresponding upscattering rate of high energy photons. The high energy photon distribution can then decay away on the (often) much shorter timescale $t_{hi} \sim t_{cross}/[1+\tau_{KN}(x)+\tau_{\gamma\gamma}(x)]$. Note that $t_{hi}(x)$ in general decreases with increasing photon energy x. Consequently, higher energies tend to *lead* lower energies in responding to a decrease in pair injection.

The preceeding discussion has ignored the fact that in a "real" source, changes in particle injection cannot take place simultaneously across the source, but will be spread out over a time $\gtrsim t_{cross}$ (e.g., imagine a shock wave propagating across the source that accelerates pairs behind it). The evolution of features on times $< t_{cross}$ seen in some of the output spectra discussed below is therefore artificial and reflects the crude radiative transfer employed here and in past treatments. For example, although *locally* τ_T (and the annihilation line luminosity) may drop significantly in a time much less than t_{cross}, this cannot happen *globally* in a time less than t_{cross}. Effects such as the sudden release of trapped photons (see FBGPC and below) which depends critically on the Thomson opacity disappearing in less than t_{cross} may then be much less dramatic (or not seen at all) and may vary with the particular source geometry (i.e., the details of radiative transfer). The observed time behavior of a source will be given by the local (since every region of the source is taken to be identical) responses of the model system considered here, convolved with a light- crossing time R/c. (The use of a photon escape probability with minimum escape time t_{cross} does do this to some extent.) Strictly speaking, then, the results of the present code are valid only when injection changes are slow enough (i.e., take place over times $\gg t_{cross}$) that the system has time to keep itself "homogenized." Regardless of the exact details, however, it is clear that the presence of a pair plasma can greatly alter the observed time variability of a source, especially when the value of τ_T exceeds unity. A pair plasma acts like a capacitor, storing up particles and energy, and smearing out the response of the system to changes in injection.

5.2. *Sample Results*

We now turn to some specific examples. Consider first the "easiest" case to understand (Fig. 8a), one where the value of τ_T is always much less than unity. Following the arguments above, t_{esc} will always be $\sim t_{cross}$ and the photon distribution, except the annihilation line, should relax to its equilibrium value on a timescale t_{cross}. The (normalized) escaping luminosity in the various wavebands shown should then go as $l(t) \approx 1 - e^{-t}$ for $0 < t < 12$ (injection on) and as

$l(t) \approx e^{-(t-12)}$ for $12 < t < \infty$ (injection turned off). The exception is the annihilation line intensity, which because the total pair creation/injection rate is relatively small and $\tau_T < 1$, should take many t_{cross} to build up and decay away. Comparing with Fig. 8a, this does not appear a bad first approximation. (Indeed it works very well for the UV luminosity since the only processes significantly affecting the soft photon distribution are photon escape and external photon injection.) However, the escaping γ-ray luminosity always leads the UV luminosity slightly, while the X-ray luminosity significantly lags the UV luminosity. The annihilation line intensity also continues to increase even after all particle injection is turned off. The explanation for this behavior is more subtle than one might have at first guessed.

Consider, for example, the fast rise of the $\gamma-$ray luminosity relative to the UV luminosity. Since the 2-10 MeV gamma-rays tracked in Fig. 8a are primarily upscattered soft photons, the "injection" rate of $\gamma-$rays goes approximately as the number of soft photons times the number of high energy pairs. Assume now that the pair distribution is fixed. The injection of $\gamma-$rays then will not turn on until the soft photon number has had time to build up, i.e., one might expect the rise in the $\gamma-$rays to *lag* slightly the rise in soft (UV) photons. The pair distribution is definitely not fixed in time, however. At early times ($\lesssim t_{cross}$) when when U_{rad} is still small, the cooling times are long and the high energy pair distribution is significantly enhanced over its stationary value. In the example shown, this larger number of higher pairs more than compensates for the initially small number of soft photons available to upscattered. In fact, the γ-ray luminosity actually overshoots its equilibrium value (very) slightly. (The decrease in the number of high energy pairs with increasing U_{rad} eventually wins out over the partially compensating increase in soft photon number.)

Given that the X-rays are also primarily upscattered soft photons, one might expect them to show the same behvior. However, the pairs responsible for upscattering soft (UV) photons to X-ray (2-10 keV) energies are ~ 30 times lower in energy than those responsible for the $\gamma-$rays. Their cooling times are signficantly longer ($\dot{\gamma} \propto \gamma^2$), and at early times when U_{rad} is small, they can be a non-negligible fraction of the photon response timescale $\sim t_{esc}$. Consequently, the "turn on" of the X-rays is delayed by about $.2 - .3t_{cross}$ until sufficient numbers of injected pairs have cooled down to build up the pair distribution at $\gamma \sim 10$. Also, although the maximum value of τ_T is $\ll 1$, the effects of pair production on this medium energy ($\gamma \sim 10 - 30$) range of the pair distribution cannot be neglected. The additional source of pairs represented by pair production leads to an enhancement by a factor ~ 3 in the number of these pairs and the upscattering rate of photons to X-ray energies. Pair production does not turn on fully, however, until the γ and hard X-ray distributions have had time to build up, i.e., only after a few t_{esc}. (This is reflected in the annihilation line intensity, a useful indicator of how the total pair production rate is behaving.) This then is the main cause of the observed X-ray to UV "lag" when injection is turned on.

The fact that pair production dominates external injection at pair energies responsible for the upscattered X-rays also explains the X-ray to UV lag when all particle injection is cut. Significant pair production ceases only when most gamma-rays have escaped the source region. For this model where $\tau_T \ll 1$ and $\tau_{\gamma\gamma} < 1$ for $x \lesssim 300$, this happens on a timescale $\sim t_{cross}$. (Note though, that, the effects of pair production on the γ-rays are not completely negligible and cause the $\gamma-$ray luminosity to decrease slightly faster than the UV luminosity.) Thus, the pair distribution at these energies is maintained by pair production for a few t_{cross}. This and the fact that soft photon number decays on a timescale also $\sim t_{cross}$ mean that the injection (upscattering) of X-rays does not stop completely until after a few t_{cross}. Hence the "slow" decay of the X-ray luminosity. A significant pair production rate after all particle injection is stopped also explains the behavior of the annihilation line. Only when the total pair production rate drops below the annihilation rate ($\propto \tau_T^2$) does its intensity begin to decrease. Note, then, that even in a model which is neither pair saturated nor Thomson thick, the process of pair production can have a non-negligible effect on the time evolution.

Turn now to the case (Fig. 8b) where the injection parameters are boosted to values which do put the pair plasma in a pair saturated and Thomson thick ($\tau_T \approx 12$) regime. In contrast to the previous case, the "transient" time behavior here is quite dramatic. One noticeable feature is the burst of gamma-ray luminosity that occurs just after injection is increased. For $\sim t_{cross}$, until increasing downscattering by thermal pairs and annihilation off lower energy photons (pair production) can catch up, the spectrum looks much harder than one might predict from the stationary states before and after the increase in injection. The rapid increase in the number of gamma-rays causes a corresponding jump in the total pair production rate. Note how rapidly (compared to Fig. 8a) the annihilation line builds up. Also note that the X-ray luminosity actually *leads* the UV luminosity in building up. Here there is no significant wait for pair production to turn on and all pair cooling times are $\ll t_{cross}$ (hence no wait for injected pairs to cool and build up the pair distribution in response to the increase in injection).

The burst in pair production and rapid rise in τ_T have another interesting consequence. For about $0.5R/c$ after injection is increased, the escaping X-ray and UV luminosity remain approximately constant. This is an example of the sudden "trapping/release" effect (anti-correlation of X-ray luminosity with changes in injection) discussed in FBGPC that occurs whenever τ_T can be made to change on a timescale faster than the photon response timescale $\sim t_{esc}$. Another example is the outburst of X-ray and UV luminosity that occurs when particle injection is cut. Because of the large value of $\tau_{\gamma\gamma}$ at most gamma-ray energies, the gamma-ray distribution quickly collapses, causing significant pair production to stop in $\ll t_{cross}$. The value of τ_T then drops to unity on the annihilation timescale $t_{ann} \sim 1/\tau_T$ (also $\ll t_{cross}$), allowing the previously trapped UV/X-ray photons to stream out of the source. (The escaping X-ray luminosity is not enhanced by quite the same factor as the UV luminosity due to downscattering by the relatively cold thermal pairs.) Note that in contrast to what appears to be implied in FBGPC, however, there is nothing special about the X-rays. Lower photon energies (e.g., UV) will show the same (temporary) "anti-correlation" with changes in injection. Also, this anti-correlation of escaping X-ray (UV) luminosity is not a universal behavior of pair plasmas. Rather extreme changes in injection, from or to states with high l_e and l_s, are required to obtain it. For mono-energetic pair injection at $\gamma_{inj} \sim 10^3$ and l_e, l_s always $\lesssim 300$, no such effects are seen in the models considered here. (LZ and Svensson 1987 suggest that typical AGN compactness parameters are in the range $1-30$.) Moreover, in a real source, the value of τ_T cannot be made to rapidly build up or drop throughout the source in less than a crossing time (see above). This gives the photon distribution time to respond to the changes in the escape rate and any trapping/release effects may be significantly reduced.

The last example we consider is the response of an "AGN-like" model of §4.3 to changes in the pair injection rate (see Fig. 9,10). Here the boost in pair injection at t=11 takes the pair plasma to a state where pair production is relatively important (more so than in the first case examined). However, because the maximum value of $\tau_T \approx 0.8 < 1$, one expects behavior on timescales similar to those in the first case, where the annihilation line builds up and decays slowly (over several t_{cross}) and the normalized escaping luminosities in other bands goes roughly as: $l(t) = 1 - (1 - 1/f)e^{-(t-t_0)}$ for injection boosted by a factor f at $t = t_0$, and $l(t) = 1/f - (1/f - 1)e^{-(t-t_0)}$ for injection reduced by a factor f at $t = t_0$. (The factor f is of course energy dependent.) It is interesting to note that an appreciable magnetic field such as in the Fig. 9 model does not cause major qualitative changes in the time behavior (except of course at the strongly self-absorbed frequencies). Besides adding a soft photon source, the main effect of synchrotron radiation in these models is simply to shorten further the pair cooling times. As above, however, it will still prove instructive to examine the deviations from the "predicted" $l(t)$ behavior evident in Fig. 9b.

Consider first the escaping X-ray luminosity. For much the same reasons as discussed above for Fig. 8a, the X-ray luminosity always lags behind $l(t)$. When injection is increased, the injection rate of X-rays again does not build up to its full value until after a $\sim t_{cross}$. This is the time required for the gamma-ray distribution to build up (and the pair production rate to increase – note the behavior of the annihilation line) as well as for the (IR-optical) synchrotron photon distribution to build up. The importance of pair production and the presence of synchrotron photons (which are upscattered to X-ray energies) may be gauged by noting that the X-ray luminosity increases by a factor ≈ 16 instead of the factor 10 one might have first guessed. Similarly, when injection is reduced, the injection rate of X-rays does not drop off significantly until after a time $\sim t_{cross}$ has passed (and the X-ray injection rate falls). However, because $\tau_{\gamma\gamma} \sim 1$, the gamma-rays (and pair production) cut off faster and the effect is not as pronounced as in Fig. 8a. An additional, though minor, factor contributing to deviations from $l(t)$ behavior is the non-negligible Thomson optical depth at $t \gtrsim 14R/c$, which traps the X-rays slightly, increasing the soft photon escape time to $\approx 1.2t_{cross}$.

Because it is mostly optically thin synchrotron emission from relatively high energy ($\gamma \gtrsim 50$) pairs (for which "injection" of pairs by pair production is not important), the IR luminosity behaves quite differently. Since the injection rate of IR photons goes crudely as l_e/U_{rad}, i.e., as the number of high energy pairs, the IR injection rate initially jumps by a factor 10 when l_e is increased but then quickly drops as U_{rad} builds up in response (on a time $\sim t_{cross}$). The IR luminosity thus appears to shoot up rapidly at first and then abruptly level off (as U_{rad} reaches a stationary value). Also, because of the dropping injection rate (the final rate is only a factor 6, not 10, higher), the IR luminosity finds itself close to its stationary value much sooner than the luminosity at other frequencies (see Fig. 9b). At later times ($t \gtrsim 14R/c$), the luminosity at IR and lower energies drops slightly because of "trapping" by thermal pairs, even though $\tau_T < 1$. (If $\dot{\tau}_T > \frac{c}{R} t_{esc}(x)[\dot{n}(x)/n(x)]$, the escaping luminosity will decrease, even if $\dot{n}(x) > 0$. By the time thermal pairs start building up, $\dot{n}(x \leq IR)$ is small, especially at the strongly self-absorbed frequencies.) The $\approx 20\%$ increase in t_{esc} due to $\tau_T \approx .8$ causes a corresponding 20% drop in the *escaping* IR and far-IR luminosity. When pair injection is reduced at $t = 22R/c$, the IR response is much more straightforward. The high energy pair distribution (the IR injection rate) quickly drops to its new stationary value and the time-response is well-described by $l(t)$.

For $l_e = 30$, the optical emission is also dominated by synchrotron radiation. The optical luminosity should thus respond in much the same manner as the IR luminosity. The differences seen in Fig. 9b can be accounted for by noting two facts. First, at $t = 11R/c$, the injection rate of optical luminosity from the external source is significantly larger than from optical synchrotron emission. Hence, the optical luminosity does not vary as much as the IR luminosity in response to the changes in pair injection (a factor 4 vs. a factor 6). Second, the presence of significant numbers of lower energy (IR) photons which can be Compton upscattered to optical energies partially compensates for the decrease in synchrotron luminosity that accompanies the increase in U_{rad}. This causes the optical luminosity to level off later than the IR luminosity and prevents the analog of the IR "overshoot" (at $t \gtrsim 14R/c$). Also, when pair injection is reduced, the upscattering of IR photons does not stop right away and this causes the optical luminosity to lag $l(t)$ slightly (though not as much as the X-ray luminosity).

In contrast, the escaping gamma-ray luminosity does not deviate much from an $l(t)$ curve with $f = 10$, at least when injection is increased. In this case, the decrease in number of high energy pairs (roughly $\propto 1/U_{rad}$) is (more) than compensated by the increase in the number of the soft photons ($\propto U_{rad}$) that can be upscattered. The good agreement with $l(t)$ is actually somewhat fortuitous. The "overcompensation" is just balanced by an increased photon-photon annihilation rate. This need not always occur, e.g., as in Fig. 8b where the increased photon-photon annihilation rate more than wins out. When pair injection is decreased, the effects of the non-negligible photon-photon annihilation ($\tau_{\gamma\gamma} \sim 1$)

cause the gamma-ray luminosity to drop off on the timescale $t_{hi} < t_{cross}$. The accompanying rapid drop in the total pair production rate prevents the overshoot in annihilation line intensity seen in Fig. 8a.

It is worth remarking on one characteristic of models where the IR is predominantly synchrotron radiation, namely that the IR emission always shows less variability than the X-ray emission. In Fig. 9+10, for example, the IR luminosity varies by only a factor 6 in response to a factor 10 change in pair injection while the X-ray luminosity varies by a factor 16. The reasons for this behavior (see above) may be crudely summarized as follows: when pair injection is changed by some factor N, the change in number of high energy non-thermal pairs and the synchrotron (IR) luminosity goes roughly as N, while the change in number of IR photons upscattered to X-ray energies goes as N^2. The fact that pair production can increase the number of pairs responsible for upscattering photons to X-ray energies while it does not appreciably change the number of pairs emitting at IR energies only makes the difference in IR vs. X-ray variability larger. Also, since the strongly synchrotron self-absorbed (far IR) tail is relatively insensitive to changes in input parameters, it will tend to show even less variability (e.g., see Fig. 9, 10).

As a practical consequence of this, non-thermal models of IR and X-ray emission from the same source region (e.g., as for AGN) are not necessarily doomed if the X-rays show variability that exceeds some threshold factor (say 2) and the IR does not. To illustrate this, we have carried out one simulation along the lines of Done & Fabian (1989). The run was started from an equilibrium model of the type shown in Fig. 9, 10, but with $l_e = 20$ and $l_s = 6$. (B_0 is again 300G.) The pair injection (l_e) was then varied up and down by a factor two following the prescription of Done & Fabian (1989). The emergent X-ray and IR luminosities, normalized by their $l_e = 20$ equilibrium values, are then plotted against l_e in Fig. 11. As expected, the IR varies significantly less in amplitude than the X-rays. Also as predicted from above, the IR tends to lead the X-rays in responding to the changes in l_e. Note, though, that neither the IR or X-ray luminosity track l_e very faithfully. The large excursions in X-ray flux seen in Done & Fabian (1989) are not seen here because the model parameters are not such that the model can hop back and forth between pair dominated and non-pair dominated states.

For completeness, we have also included a figure (Fig. 10c) showing the luminosity response when pair injection is ramped down over $4t_{cross}$ instead of being abruptly cut. (This presumably avoids the problems with radiative transfer/light-crossing time effects mentioned above.) As one might expect, the time behavior is qualitatively quite similar to that of Fig. 10b. Note that the gamma-rays, because they respond on the shorter timescale $t_{hi} < t_{cross}$, follow the pair injection most closely. Also, since the gamma-rays and the pair production rate take longer fall off, the X-rays lag the other frequencies even more and the annihilation line continues to build even after injection is reduced.

5.3. General Remarks

The examples presented are only an illustrative subset of the wide variety of responses possible for a pair plasma. Because of this variety, predicting the response requires a detailed knowledge of the initial state of the plasma and the changes in injection. Alternatively, determining whether an observed variation is consistent with a pair plasma or inverting the variation to constrain the changes injection requires (at the least) detailed knowledge of the photon distribution throughout the time on which the variation occurred. Observationally, this translates into having simultaneous multi-band observations over extended periods of time. If one has only a few snapshots of the plasma or continuous time information in only one or two bands, one can run into trouble (i.e., there will not be enough information to pose a well-constrained problem).

Consider again, for example, the problem of determining whether IR and X-ray emission are due to pairs in the same source region. One might look for correlations in IR and X-ray luminosity. However, depending on when one observes the model in Fig. 9+10, for example, one can see a positive correlation ($11R/c \gtrsim t \gtrsim 12R/c$), almost no correlation ($12R/c \gtrsim t \gtrsim 14R/c$), or a negative correlation ($t \gtrsim 14R/c$). Also if l_e is held constant and l_s is increased (a case not shown), the IR luminosity actually drops (since U_{rad} is increased) while the X-ray luminosity increases or stays about the same. Thus, unless one has additional information, e.g., that the UV luminosity (l_s) did not vary appreciably, it is not all clear what to expect. Similarly, if one were looking at an outburst resembling that of Fig. 8b and noticed the outburst only $\sim 2t_{cross}$ after it really began, one should not be dismayed to find that the gamma-rays show no variability while the X-rays are constantly increasing in intensity. This does not imply that the X-rays and the gamma-rays come from causally distinct regions.

One should also be careful about drawing too many conclusions from hardness ratios (e.g., L_γ/L_x) or spectral indices. For known changes in particle injection, definite predictions can be made about how their *stationary* values should change. Increasing the input luminosity keeping l_e/l_s constant, for example, generally results in more secondary pair production and gives softer (lower L_γ/L_x) spectra.

Increasing l_e/l_s, on the other hand, increases the number of non-thermal pairs and tends to give harder spectra. Thus, if one does not know how the injection changed, knowing L_γ/L_x before and after does not necessarily provide any useful constraint. Making use of the time-varying hardness ratios is also somewhat tricky. Hardness ratios do *not* always interpolate monotonically between the initial and final stationary values. (See Fig. 8b where the spectrum is initially very hard and Fig. 10b where the spectrum becomes and remains softer than final and initial states for $\sim 7t_{cross}$.) Also, to the extent $l(t)$ describes the evolution of the frequencies being looked at (usually the case for X-ray and lower energies, $\tau_T \lesssim 1$), quantities like hardness ratios and spectral indices will not vary significantly from their initial values until $\exp^{-(t-t_0)} \sim 1/(f-1)$. If the reduction in injection,f, is large, the shape of the spectrum may then look unchanged for several (many) t_{cross}, with all the spectral changes occurring in the last few t_{cross}. In short, then, a non-stationary spectrum may look nothing like the state it finally asymptotes to. The observation of a very steep (soft) spectrum, for example, does not automatically imply a steep pair injection function $Q(\gamma)$ if the source luminosity turns out to be varying appreciably. One should be careful not to misinterpret a time-varying spectrum as if it were a stationary one.

Yet another way of extracting information from time variability is to cross-correlate in time the measured intensity at two different frequencies. In a non-relativistic thermal pair plasma of fixed temperature and density where photons are injected at low energies, photons must "walk" their way up to higher (X-ray) energies via multiple Compton scatterings. Reaching a higher energy on average takes more scatterings and more time. One can thus make a definite prediction: whenever the source luminosity increases, higher frequencies should always lag lower frequencies. However, if one allows the temperature and optical depth to vary self-consistently and admits the possibility of a non-thermal tail, the situation is no longer so clear. In the first case (fixed temperature, density) it is relatively straightforward to write down a Green's function for the evolution in time (which may then be Fourier transformed, etc.). In the second case, however, the "transfer function" itself varies with time in a non-trivial manner. Again, then, unless one knows exactly what parameter regime is being observed, "lead/lag" information may not be very useful. Just looking at Fig. 8-10, it is possible to come up with examples where one frequency can either lead or lag another depending on the initial state of the plasma.

A relatively unexplored area that might prove useful to look at is the time variability of the hard ($\geq 511 KeV$) gamma-rays (preferably alongside simultaneous measurements at some lower energy). Because it has the shortest response timescale and (at least in the models considered here) is due to a portion of the pair distribution not directly affected by pair production, the gamma-ray end of the spectrum is probably the best indicator of changes in the "first order" pair injection spectrum $Q(\gamma)$. (Knowing the gamma-ray spectrum when the source is stationary is even more useful as it seriously constrains the possibilities for $Q(\gamma)$ – e.g., see LZ.) If the gamma-ray spectrum shows marked steepening or softening on a timescale $\sim t_{cross}$, one can be fairly sure a change in pair injection is involved — an important piece of information. (A change in soft photon injection typically results in a much more sluggish response, especially if $\tau_T > 1$. See §5.1.) The gamma-ray response to a decrease in pair injection also has the signature that higher energies drop off faster, i.e., higher frequencies lead lower frequencies. (Exactly how much they lead is of course a measure of $\tau_{\gamma\gamma}(x)$.) This behavior is hard to mimic by changes in soft photon injection. Observation of gamma-rays during a sizeable drop in pair injection can also lead to a rather unambiguous indication of pairs in a source. In the models considered, a relatively long-lived annihilation feature almost always emerges from the decaying continuum (e.g., Fig. 10a). Needless to say, finding no significant variability on timescales shorter than (or at least as short as) the shortest observed X-ray timescales would place current models in severe difficulty.

Unfortunately, the details of the time behaviors discussed here (e.g., the IR overshoot in Fig. 10b, the release of trapped X-rays in Fig. 8b) often depend sensitively on the relative values of the various relaxation timescales. Different microphysics (i.e., approximations) or assumptions about the geometry of the system can lead to different values for these timescales, and consequently, quite different behavior. This should not be forgotten when interpreting the results of numerical calculations. Although it does not contradict the qualitative results presented in FBGPC, for example, the code discussed here does not reproduce well the detailed time behavior presented in their figures (even accounting for differences in the definitions of l_e, l_s, etc.). This is not surprising considering the different treatments of the microphysics, e.g., the use of different escape probabilities. Similarly, the results presented here are based on a radiative transfer scheme which does not allow for variations in geometry, anisotropies in particle distributions, or spatial inhomogeneities. They should not be considered "definitive."

6. Discussion and Conclusion

Past studies of pair plasmas have suffered from two potentially serious shortcomings: i) unsophisticated treatments of the radiative transfer, and ii) overly simple approximations of the basic microphysical processes. We have concentrated on the second of these problems, trying to separate the real physical effects from the artifacts of approximations. The code described here can correctly handle Klein-Nishina scatterings where the photon and electron energies are of the same order. It can also solve self-consistently for the pair and photon distributions over a large range of values of U_{rad}/U_B.

Two general conclusions follow from the work presented here. First, approximations used in earlier work are reliable only in restricted parameter regimes. The Compton scattering approximation of LZ, for example, works well only when a few orders of Compton scattering are important and $\theta_{rad}\gamma_{max} < 1$. Errors of order unity occur when this is not the case. Some of the approximations for handling pair production have analogous limitations. Contrary to earlier assumptions, Coulomb scattering can indeed be important for non-thermal pairs. In the synchroton-dominated case even a small Coulomb cooling rate will modify significantly the low energy pair distribution. Moreover, interesting parameter regimes (e.g., $l_s \ll l_e$) exist where the Coulomb energy exchange times are similar to the other cooling timescales. The thermal component of pair distribution can then be quite hot ($kT/m_ec^2 \sim 1$) since not all the energy of the injected pairs is lost to the radiation field. In general, achieving more than order of magnitude accuracy appears to require a careful numerical treatment. Analytic approximations, though convenient, have limited validity and accuracy.

The second conclusion is that pair plasma models can reproduce a wide variety of spectral shapes and variability (see the figures in this paper). When the calculation is done self-consistently and details such as the presence of cool pairs are taken into account, the deviations from canonical spectral shapes (e.g., Bonometto & Rees 1971, Rees 1967b) can be quite significant. This should not be forgotten when comparing observations to theory. Power law pair injection with index Γ, for example, does not automatically imply a synchrotron or X-ray power law index of $\Gamma/2$. The portions of the spectrum due to optically thin synchrotron emission and Compton upscattering of soft photons (e.g., the IR and X-rays) can have different spectral indices and still arise from the same pair distribution, and a portion of the spectrum which is strongly synchrotron self-absorbed need not have a spectral index of 2.5. In considering variability, it is also worth remembering that a pair plasma acts essentially as a low pass filter, damping out rapid variations. A source size derived from variability measurements may well be an overestimate. More importantly, because the plasma's response function is energy dependent, luminosities measured at different frequencies can vary in rather different manners (and still originate from the source). Finally, a plasma in a non-stationary state can have an emergent radiation spectrum which looks different from that of any stationary state and apparently violates constraints derived from stationary models. In sum, it appears that models based on pair plasmas are sufficiently versatile to accomodate existing observations of the continua of AGN. Until the arrival of detailed (and simultaneous) multi-band observations, it is difficult to see how such models can be convincingly confirmed or ruled out.

Acknowledgments

Special thanks are due to Roger Blandford for supplying encouragement and guidance whenever they were needed, and to Andrzej Zdziarski for answering the questions of a novice and allowing the use of his code. The author would also like to thank M. de Kool, G. Ghisellini, P. Madau, E. S. Phinney, and R. Svensson for many enlightening discussions on the subject of pair plasmas. Support under NSF grant AST 86-15325 and NASA grant NAGW-1301 is gratefully acknowledged.

References

Araki, S. & Lightman, A.P., 1983. *Astrophys. J.,* **269**, 49.

Bisnovatyi-Kogan, G.S., Zel'dovich, Ya B. & Sunyaev, R.A., 1971. *Sov. Astr.,* **15**, 17.

Blumenthal, G.R., 1971. *Phys. Rev. D,* **3**, 2308.

Bonometto, S. & Rees, M.J., 1971. *Mon. Not. R. astr. Soc.,* **152**, 21.

Coppi, P.S. & Blandford, R.D., 1990. *Mon. Not. R. astr. Soc.,* **245**, 453.

Crusius, A. & Schlickeiser, R., 1986. *Astr. Astrophys.,* **164**, L16.

de Kool, M., Begelman, M.C., & Sikora, M., 1989. *Astrophys. J.,* **337**, 66.

de Kool, M. & Begelman, M. C., 1989, J.I.L.A., University of Colorado at Boulder, preprint.

Done, C. & Fabian, A. C., 1989. *Mon. Not. R. astr. Soc.,* **240**, 81.

Fabian, A.C., Blandford, R.D., Guilbert, P.W., Phinney, E.S., Cuellar, L., 1986. *Mon. Not. R. astr. Soc.,* **221**, 931.

Ghisellini, G., 1987a. *Mon. Not. R. astr. Soc.,* **224**, 1.

Ghisellini, G.,1987b. Ph.D. Dissertation Thesis, ISSA, Trieste.

Ghisellini, G., Guilbert, P.W., Svensson, R., 1988. *Astrophys. J.,* **334**, L5.

Górecki, A. & Wilczewski, W., 1984. *Acta Astronomica,* **34**, 141.

Guilbert, P.W., 1981. *Mon. Not. R. astr. Soc.,* **197**, 451.

Guilbert, P.W., 1983. *Mon. Not. R. astr. Soc.,* **218**, 171.

Guilbert, P.W. & Stepney, S., 1985. *Mon. Not. R. astr. Soc.,* **212**, 523.

Herterich, K., 1974. *Nature,* **250**, 311.

Jelley, J.V., 1966. *Nature,* **211**, 472.

Kompaneets, A.S., 1957. *Sov. Phys.,* **4**, 730.

Kusunose, M., 1987. *Astrophys. J.,* **321**, 186.

Lightman, A.P. & Band, D.L., 1981. *Astrophys. J.,* **251**, 713.

Lightman, A.P. & Zdziarski, A.A., 1987. *Astrophys. J.,* **319**, 643.

Lorentz, M. L., 1981, Max-Planck-Institut für Physik und Astrophysik, MPI-PAE/Extraterr. 171, preprint.

McCray, R., 1969. *Astrophys. J.,* **156**, 329.

Norman, M.L. & Winkler, K.-H. A., 1986. In: *Astrophysical Radiation Hydrodynamics*, p. 187, eds Winkler, K.-H. A. & Norman, M.L., Reidel, Boston.

Novikov, I.D. & Stern, B.E., 1986. In: *Structure and Evolution of Active Galactic Nuclei*, p. 149, eds Giuricin, G. *et al.* , Reidel, Dordrecht, Holland.

Pozdnyakov, L.A., Sobol', I.M., & Sunyaev, R.A., 1977. *Sov. Astr.,* **21**, 708.

Rees, M.J., 1967a. *Mon. Not. R. astr. Soc.,* **136**, 279.

Rees, M.J., 1967b. *Mon. Not. R. astr. Soc.,* **137**, 429.

Stepney, S., 1983. *Mon. Not. R. astr. Soc.,* **202**, 467.

Stern, B.E., 1985. *Sov. Astr.,* **29**, 306.

Stern, B.E., 1988, NORDITA - 88/51 A, Denmark, preprint.

Sunyaev, R.A. & Titarchuk, L.G., 1980. *Astr. Astrophys.,* **86**, 121.

Svensson, R., 1982. *Astrophys. J.,* **258**, 335.

Svensson, R., 1983. *Astrophys. J.,* **270**, 300.

Svensson, R., 1986. In: *Radiation Hydrodynamics in Stars and Compact Objects, IAU Coll. No. 89*, p. 325, eds Mihalas, D. & Winkler, K.-H. A., Springer-Verlag, Berlin.

Svensson, R., 1987. *Mon. Not. R. astr. Soc.,* **227**, 403.

Zdziarski, A.A., 1984. *Astrophys. J.,* **283**, 842.

Zdziarski, A.A., 1985. *Astrophys. J.,* **289**, 514.

Zdziarski, A.A., 1986. *Astrophys. J.,* **305**, 45.

Zdziarski, A.A., 1988. *Astrophys. J.,* **335**, 786.

Zdziarski, A.A., Coppi, P.S., & Lamb, D.Q., 1990. *Astrophys. J.,* **357**, 149.

Figure Captions

Figure 1. Comparison of results with those of the Lightman & Zdziarski (1987) code.

Figure 2. Effects of including Coulomb cooling and non-thermal pair annihilation in a photon-starved ($l_s \ll l_e$) model. The pair distribution shown in Fig. 2b is the sum of the thermal and non-thermal components.

Figure 3. A "Compton-Dominated" ($l_e \gg U_b$) model and its corresponding unmagnetized model. Note the similarity of the two spectra.

Figure 4. SSC (synchrotron self-Compton) spectra - constant pair injection luminosity, varying magnetic energy density. Pairs were injected mono-energetically at $\gamma_{inj} = 10^3$.

Figure 5. SSC spectra (Fig. 5a) - constant magnetic energy density, varying pair injection luminosity. Pairs were injected mono-energetically at $\gamma_{inj} = 10^3$. Fig. 5b shows the corresponding pair distributions. Note the effects of Coulomb cooling on the low energy pair distribution.

Figure 6. SSC spectra showing the results of varying the power law injection index Γ ($Q(\Gamma) \propto \gamma^{-\Gamma}$).

Figure 7. Model with both external photon injection and a magnetic field. Note the variation of the near IR (infrared) slope with decreasing minimum pair injection energy γ_{min}.

Figure 8. Luminosity response of unmagnetized models to impulsive changes in pair injection. Fig. 8a. shows a case where the injection parameters are such

that $\tau_T \lesssim 1$ at all times. Fig. 8b shows the opposite case where the increase in particle injection causes τ_T to significantly exceed unity. The various frequency bands referred to in this and the following figures are defined as follows: (IR): $90,000\AA$ - $30,000\AA$; (Opt): $9,000\AA$ - $3,000\AA$; (UV): $900\AA$ - $300\AA$; (X-Ray): 2 keV - 10 keV; (Gamma-Ray): 2 MeV - 10 MeV; and (Annihilation Line): the total annihilation luminosity, $l_{tot}^{ann} = \frac{4\pi}{3} R\sigma_T \int \dot{n}_{ann}(x)dx$, including the contribution from non-thermal pairs.

Figure 9. Spectral (Fig. 9a) and luminosity (Fig. 9b) response of a magnetized model of the type in Fig. 7 to an impulsive increase in injection. Pair injection is power law with index $\Gamma = 2.4$, extending from $\gamma_{min} = 100$ to $\gamma_{max} = 10^3$.

Figure 10. Spectral (Fig. 10a) and luminosity (Fig. 10b) response of a magnetized model of the type in Fig. 7 to an impulsive decrease in injection. Pair injection is power law with index $\Gamma = 2.4$, extending from $\gamma_{min} = 100$ to $\gamma_{max} = 10^3$. Fig. 10c shows the response when pair injection is decreased gradually over 4 light crossing times.

Figure 11. Luminosity response of the IR and X-ray bands to random variations of up to a factor 2 in the pair injection rate l_e about a median value of 20 (see text). The solid curve is the time-varying value of l_e. The dashed curve is the X-ray luminosity, and the dotted curve is the IR luminosity. As in Fig. 9-10, the pair injection is power law with index $\Gamma = 2.4$, extending from $\gamma_{min} = 100$ to $\gamma_{max} = 10^3$. The magnetic field has strength $B_0 = 300G$. The source region had radius $R = 10^{14}$ cm, and external photon injection was a blackbody at $x_s = 3 \times 10^{-5}$ with constant luminosity $l_s = 4$.

TABLE 1

Comparison with Models of Lightman & Zdziarski (1987)

$(l_e/l_s = 1/2.5)$

l_e	PY	τ_T	x^*	τ_C	θ	α_{2-10}
1	1.7×10^{-3}	.047	1000.	1.1×10^{-3}	7.9×10^{-3}	.637
L&Z:	2.0×10^{-3}	.062	1000.	1.0×10^{-3}	1.0×10^{-2}	.655
10	.023	.502	63.2	7.0×10^{-3}	5.7×10^{-3}	.863
L&Z:	.025	.574	38.9	6.9×10^{-3}	6.0×10^{-3}	1.03
100	.087	3.34	4.5	1.1×10^{-2}	2.2×10^{-3}	.979
L&Z:	.099	3.55	3.7	1.1×10^{-2}	2.5×10^{-3}	1.14
1000	.12	12.4	1.4	6.2×10^{-3}	6.2×10^{-4}	1.42
L&Z:	.14	13.4	.87	5.1×10^{-3}	5.3×10^{-4}	1.61

All models were computed assuming monoenergetic pair injection at $\gamma_{inj} = 10^3$ and blackbody soft photon injection at $\theta_{rad} = 1.07 \times 10^{-5}$. The exact energy distribution of Compton scattered photons was used in our calculations.

Key to symbols:

PY is the "pair yield" $= \int d\gamma P(\gamma) / \int \gamma Q(\gamma) d\gamma$ (eg. see LZ). $P(\gamma)$ is the creation rate of pairs of energy γ by two-photon pair production; $Q(\gamma)$ is the external pair injection rate.

x^* is the photon energy x where $\tau_{\gamma\gamma}(x) = 1$.

α_{2-10} is the best-fit spectral index ($F_\nu \propto v^{-\alpha}$) to the 2-10 keV x-ray band.

l_e, τ_T, τ_c, and θ are as defined in the text (see §2.1).

Table 2.

Selected Results for Models in Fig. 2-10

		PY	l_x/l_e	τ_T	x^*	τ_C	θ	α_{2-10}
Fig. 2:	All Processes	3.54×10^{-3}	7.70×10^{-3}	.638	795	6.40×10^{-3}	3.06×10^{-1}	.726
	No Coulomb	1.16×10^{-2}	7.19×10^{-2}	.194	1000	4.17×10^{-1}	4.92×10^{-2}	.681
	No Coulomb, NT Ann.	2.23×10^{-3}	8.59×10^{-2}	.554	1000	5.49×10^{-1}	4.11×10^{-2}	.668
Fig. 3:	$l_s = 0$	1.14×10^{-1}	1.44×10^{-1}	3.82	2.82	1.84×10^{-2}	2.22×10^{-2}	.721
	$l_s = 3.5$	1.38×10^{-1}	1.58×10^{-1}	4.21	2.82	2.19×10^{-2}	2.39×10^{-2}	.661
Fig. 4:	$B_0 = 1000\text{G}$	3.83×10^{-3}	2.42×10^{-2}	.152	200	2.32×10^{-3}	2.14×10^{-2}	.749
	$B_0 = 300\text{G}$	1.54×10^{-3}	5.86×10^{-2}	.393	44.7	2.94×10^{-2}	2.69×10^{-3}	.609
	$B_0 = 100\text{G}$	2.10×10^{-2}	8.24×10^{-2}	.462	28.2	4.64×10^{-2}	3.73×10^{-2}	.578
Fig. 5:	$l_+ = 0.1$	1.87×10^{-8}	1.48×10^{-3}	.000134	1000	3.42×10^{-4}	3.12×10^{-2}	1.62
	$l_+ = 1$	1.33×10^{-5}	5.96×10^{-3}	.00410	1000	1.18×10^{-3}	4.78×10^{-2}	1.08
	$l_+ = 10$	3.83×10^{-3}	2.42×10^{-2}	.152	200	2.32×10^{-3}	2.14×10^{-2}	.749
Fig. 6:	mono	3.85×10^{-4}	3.39×10^{-2}	.00300	1000	3.71×10^{-3}	1.05×10^{-2}	.666
	$\Gamma = 1.7$	1.69×10^{-4}	8.32×10^{-2}	2.08	1000	5.64×10^{-3}	1.45×10^{-1}	.976
	$\Gamma = 2.4$	1.65×10^{-3}	9.26×10^{-2}	.493	1000	8.69×10^{-3}	1.97×10^{-1}	.948
Fig. 7:	$\gamma_{min} = 100$	1.64×10^{-2}	1.15×10^{-1}	.842	14.1	4.88×10^{-3}	1.52×10^{-2}	.839
	$\gamma_{min} = 10$	1.20×10^{-2}	1.64×10^{-1}	1.34	11.2	1.30×10^{-2}	2.46×10^{-2}	.843
	$\gamma_{min} = 2$	9.06×10^{-3}	1.56×10^{-1}	2.44	11.2	1.78×10^{-2}	2.47×10^{-2}	.909
Fig. 8:	$t = 12R/c$	9.90×10^{-3}	3.65×10^{-2}	.123	317	3.89×10^{-3}	7.58×10^{-3}	.866
Fig. 9:	$t = 0R/c$	8.70×10^{-2}	1.82×10^{-1}	3.34	4.47	1.15×10^{-2}	2.16×10^{-3}	.979
	$t = 12R/c$	1.25×10^{-1}	1.66×10^{-1}	12.7	1.41	6.77×10^{-3}	6.15×10^{-4}	1.47
Fig. 10:	$t = 11R/c$	1.08×10^{-3}	7.20×10^{-2}	.0420	1000	4.12×10^{-3}	3.40×10^{-3}	.799
	$t = 22R/c$	1.48×10^{-2}	1.21×10^{-1}	.777	14.1	2.10×10^{-2}	9.82×10^{-3}	.909

External blackbody soft photon injection is at $\theta_{rad} = 1.07 \times 10^{-5}$. The maximum pair injection energy γ_{max} is 10^3 for all models. The two-moment ("top hat") approximation to the energy distribution of Compton scattered photons was used in these computations. $l_x/l_+ = L_x/L_+$ is the ratio of the escaping 2-10 kev x-ray luminosity to the pair injection luminosity. The remaining column headings are as defined in Table 1.

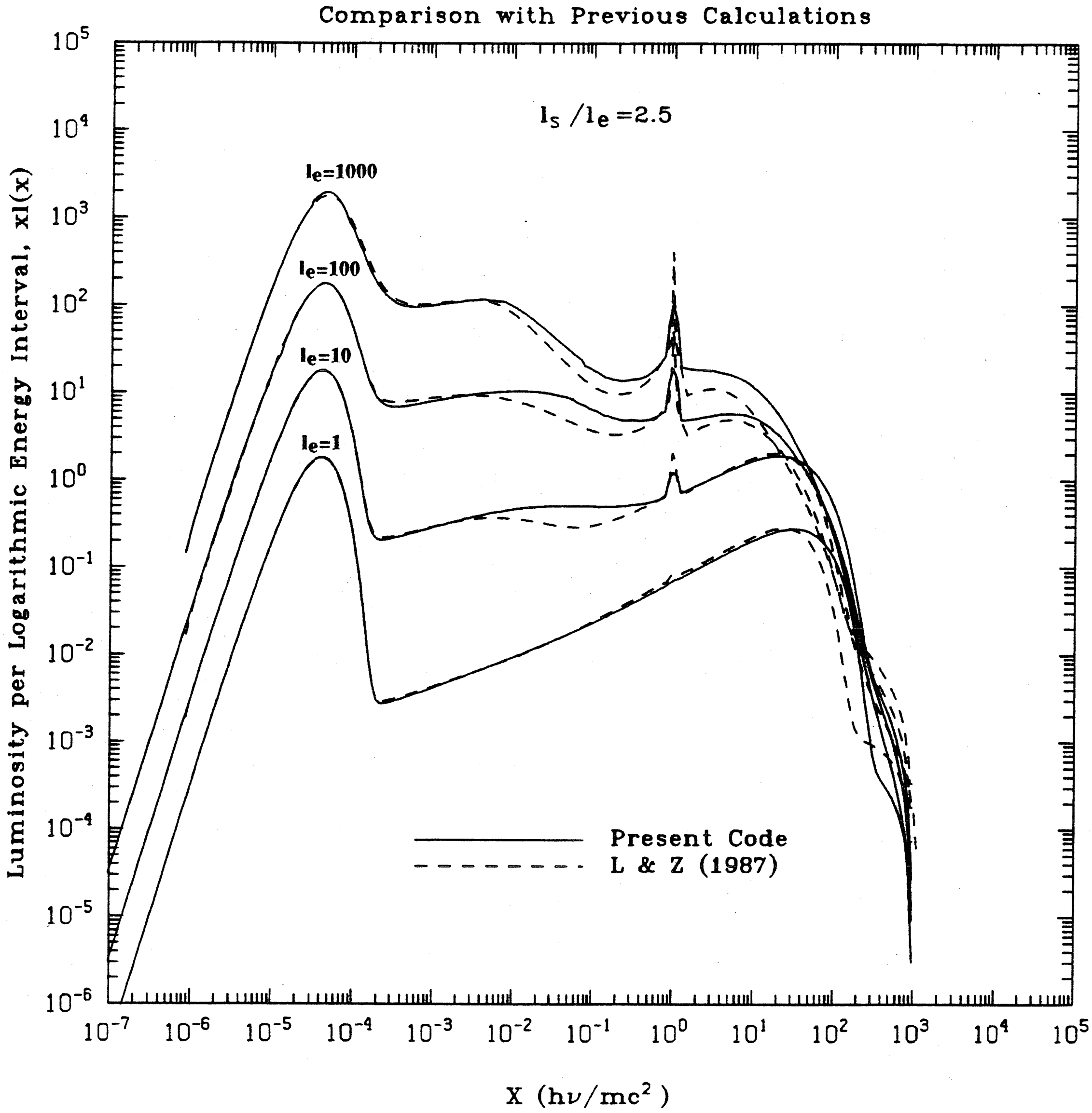
Comparison with Previous Calculations
$l_S / l_e = 2.5$
l_e=1000
l_e=100
l_e=10
l_e=1
Present Code
L & Z (1987)
Luminosity per Logarithmic Energy Interval, xl(x)
10^5
10^4
10^3
10^2
10^1
10^0
10^{-1}
10^{-2}
10^{-3}
10^{-4}
10^{-5}
10^{-6}
10^{-7}
10^{-6}
10^{-5}
10^{-4}
10^{-3}
10^{-2}
10^{-1}
10^0
10^1
10^2
10^3
10^4
10^5
X ($h\nu/mc^2$)

Figure 1

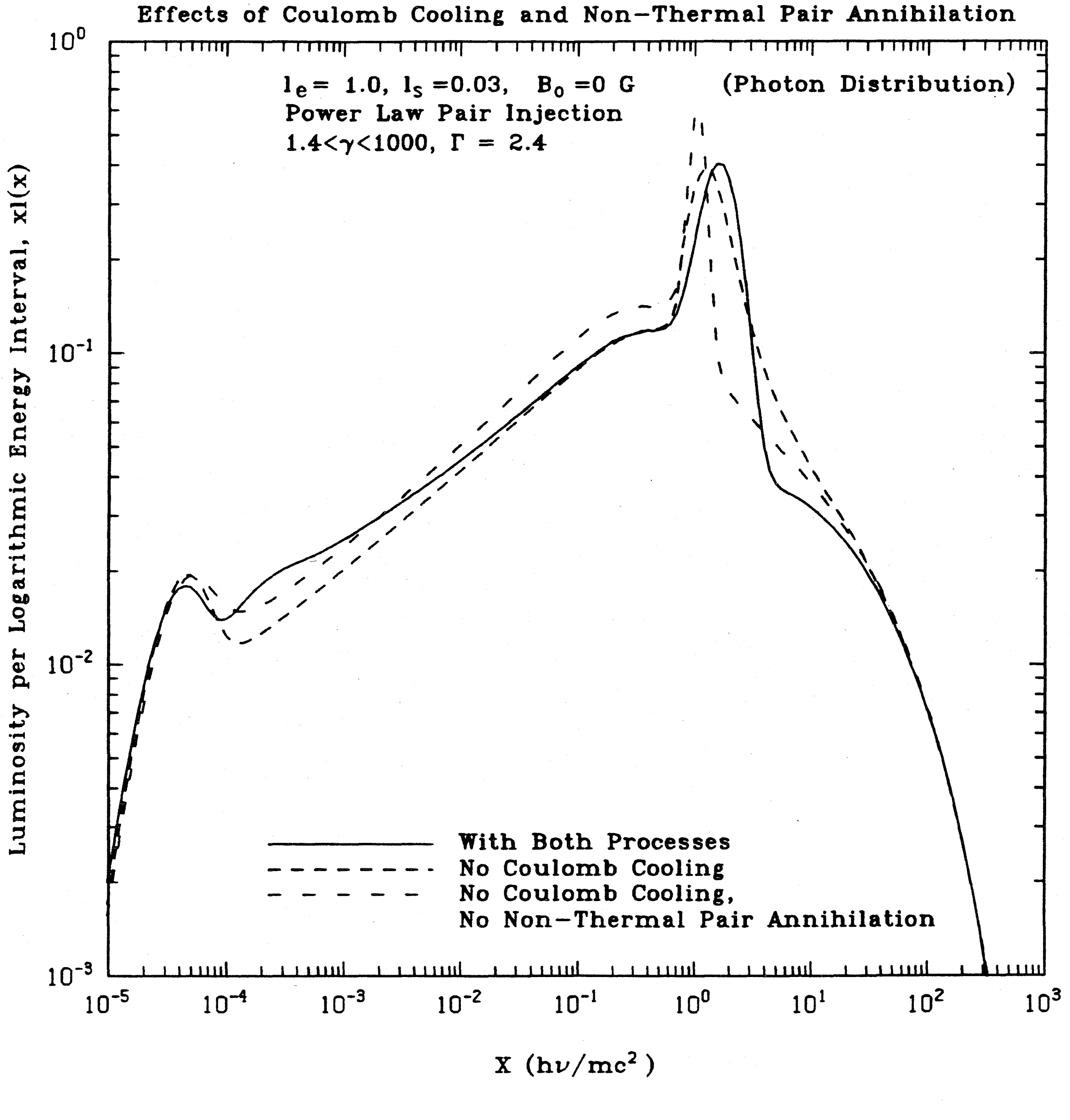
Effects of Coulomb Cooling and Non−Thermal Pair Annihilation
l_e = 1.0, l_s =0.03, B_0 =0 G
(Photon Distribution)
Power Law Pair Injection
1.4<γ<1000, Γ = 2.4
Luminosity per Logarithmic Energy Interval, xl(x)
10^0
10^{-1}
10^{-2}
10^{-3}
10^{-5}
10^{-4}
10^{-3}
10^{-2}
10^{-1}
10^0
10^1
10^2
10^3
With Both Processes
No Coulomb Cooling
No Coulomb Cooling,
No Non−Thermal Pair Annihilation
X (hν/mc²)

Figure 2a

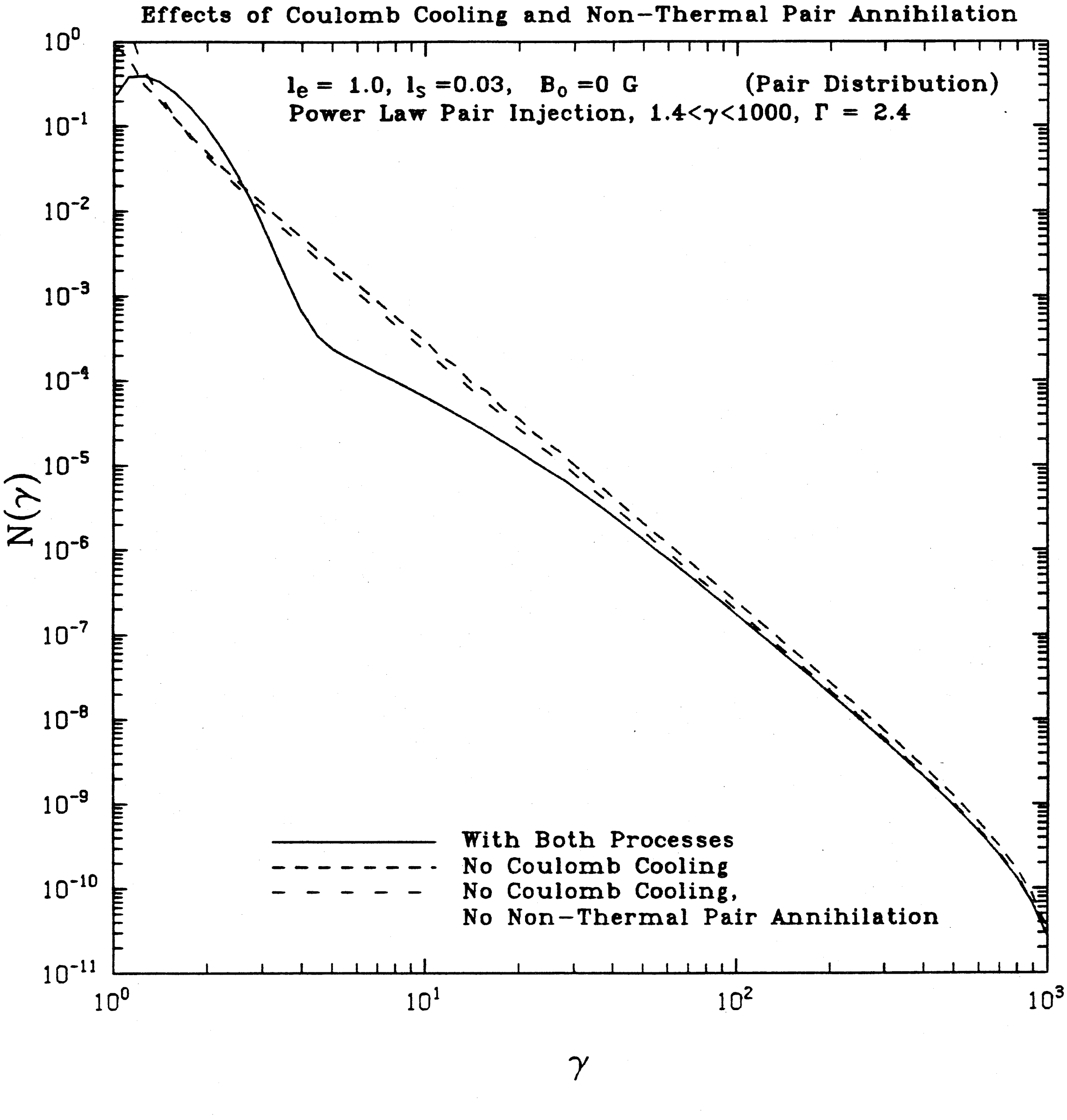
Effects of Coulomb Cooling and Non-Thermal Pair Annihilation
l_e = 1.0, l_s =0.03, B_0 =0 G (Pair Distribution)
Power Law Pair Injection, 1.4<γ<1000, Γ = 2.4
With Both Processes
No Coulomb Cooling
No Coulomb Cooling,
No Non-Thermal Pair Annihilation
N(γ)
γ
10^0
10^{-1}
10^{-2}
10^{-3}
10^{-4}
10^{-5}
10^{-6}
10^{-7}
10^{-8}
10^{-9}
10^{-10}
10^{-11}
10^0
10^1
10^2
10^3

Figure 2b

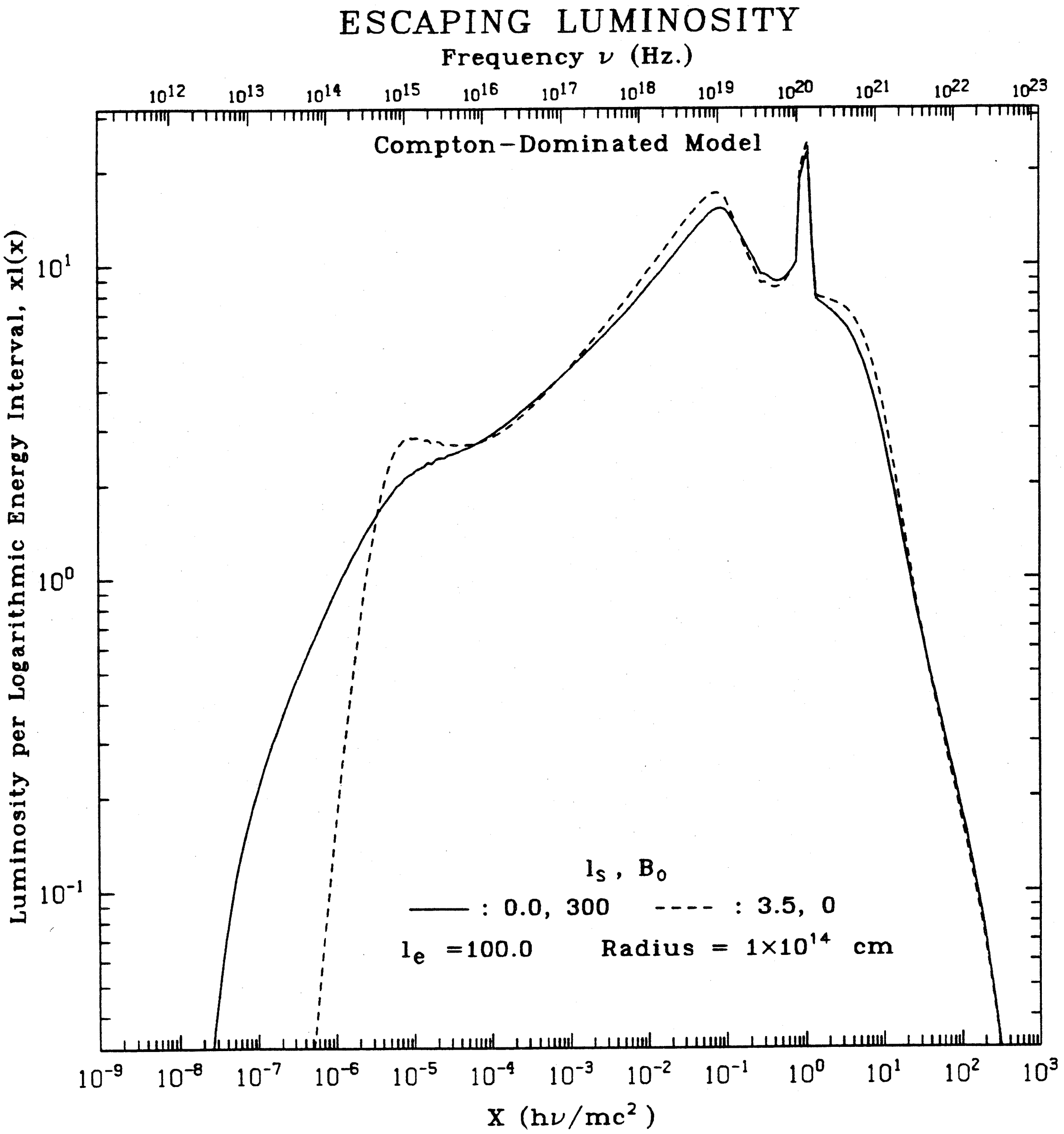
ESCAPING LUMINOSITY
Frequency ν (Hz.)
10^{12}
10^{13}
10^{14}
10^{15}
10^{16}
10^{17}
10^{18}
10^{19}
10^{20}
10^{21}
10^{22}
10^{23}
Compton-Dominated Model
Luminosity per Logarithmic Energy Interval, xl(x)
10^{1}
10^{0}
10^{-1}
l_s , B_0
: 0.0, 300
: 3.5, 0
l_e =100.0
Radius = 1×10^{14} cm
10^{-9}
10^{-8}
10^{-7}
10^{-6}
10^{-5}
10^{-4}
10^{-3}
10^{-2}
10^{-1}
10^{0}
10^{1}
10^{2}
10^{3}
X ($h\nu/mc^2$)

Figure 3

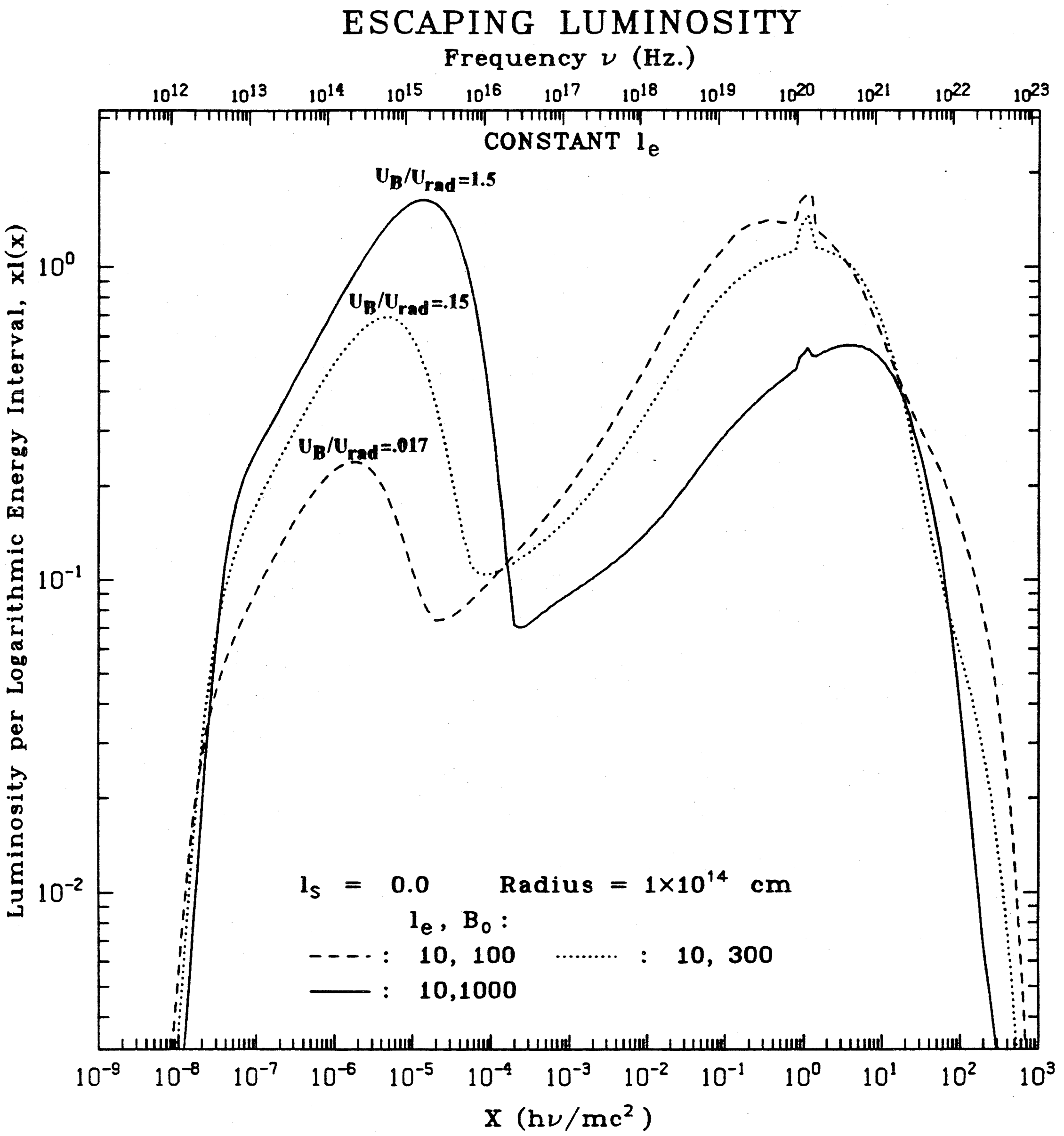
ESCAPING LUMINOSITY
Frequency ν (Hz.)
10^12 10^13 10^14 10^15 10^16 10^17 10^18 10^19 10^20 10^21 10^22 10^23
CONSTANT l_e
U_B/U_rad=1.5
U_B/U_rad=.15
U_B/U_rad=.017
Luminosity per Logarithmic Energy Interval, xl(x)
10^0
10^-1
10^-2
l_s = 0.0 Radius = 1×10^14 cm
l_e, B_0 :
- - - - : 10, 100
·········· : 10, 300
—— : 10,1000
10^-9 10^-8 10^-7 10^-6 10^-5 10^-4 10^-3 10^-2 10^-1 10^0 10^1 10^2 10^3
X (hν/mc^2)

Figure 4

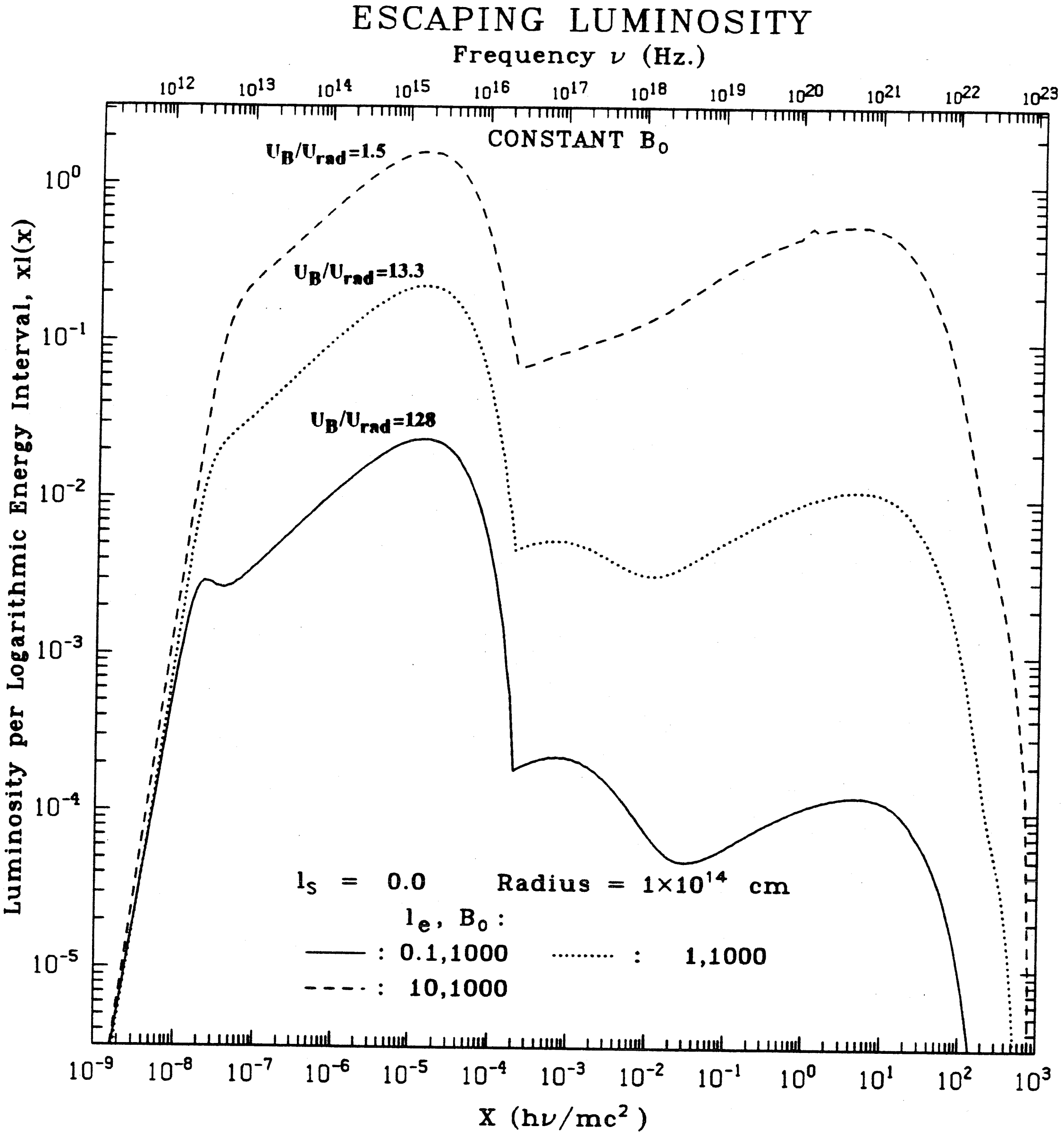
ESCAPING LUMINOSITY
Frequency ν (Hz.)
10^12
10^13
10^14
10^15
10^16
10^17
10^18
10^19
10^20
10^21
10^22
10^23
CONSTANT B_0
U_B/U_rad=1.5
U_B/U_rad=13.3
U_B/U_rad=128
Luminosity per Logarithmic Energy Interval, xl(x)
10^0
10^-1
10^-2
10^-3
10^-4
10^-5
l_s = 0.0 Radius = 1×10^14 cm
l_e, B_0 :
: 0.1,1000
: 1,1000
: 10,1000
10^-9
10^-8
10^-7
10^-6
10^-5
10^-4
10^-3
10^-2
10^-1
10^0
10^1
10^2
10^3
X (hν/mc²)

Figure 5a

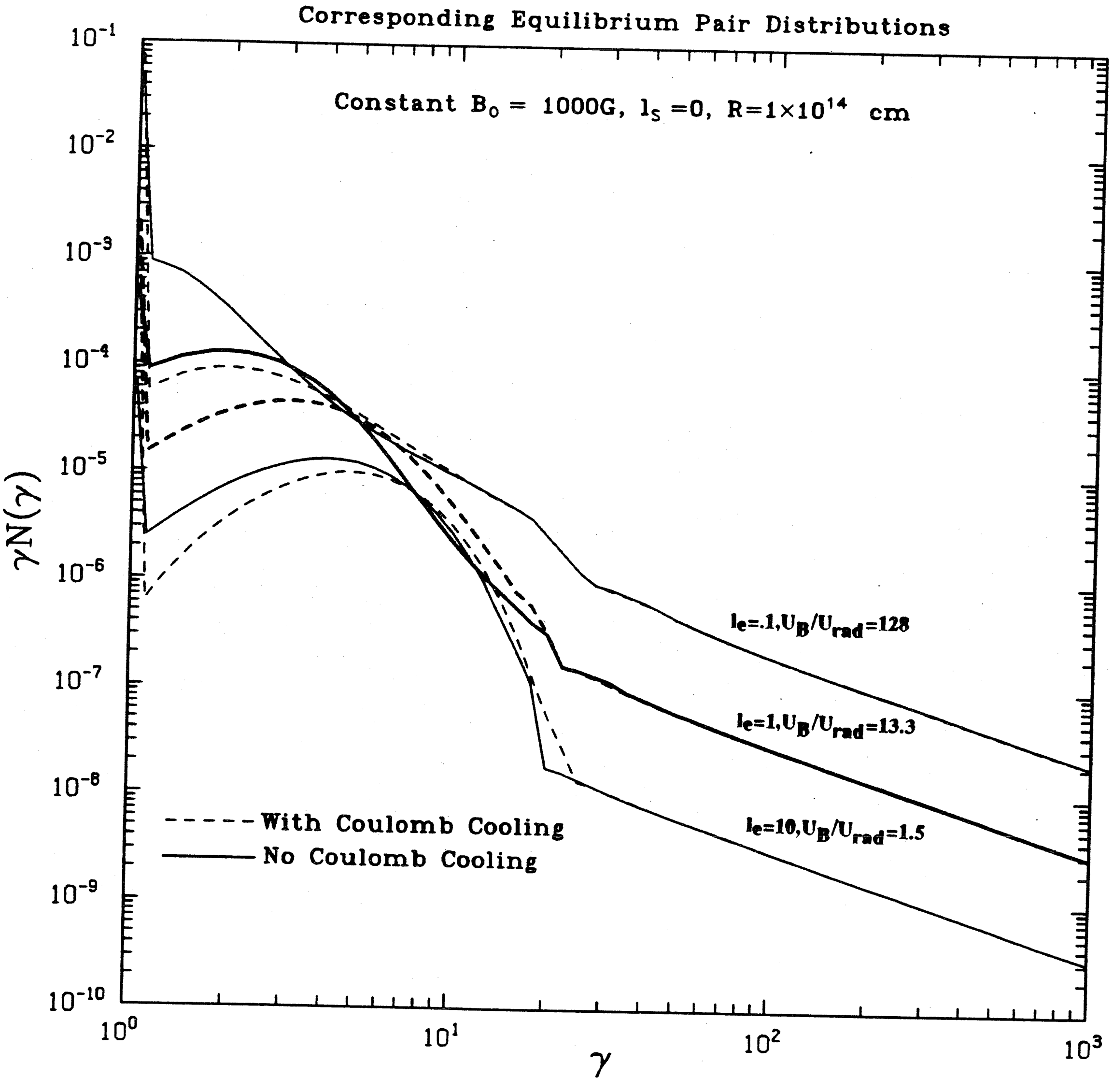
Corresponding Equilibrium Pair Distributions
Constant B_0 = 1000G, l_s =0, R=1×10^{14} cm
$\gamma N(\gamma)$
10^{-1}
10^{-2}
10^{-3}
10^{-4}
10^{-5}
10^{-6}
10^{-7}
10^{-8}
10^{-9}
10^{-10}
10^0
10^1
10^2
10^3
γ
l_e=.1,U_B/U_{rad}=128
l_e=1,U_B/U_{rad}=13.3
l_e=10,U_B/U_{rad}=1.5
With Coulomb Cooling
No Coulomb Cooling

Figure 5b

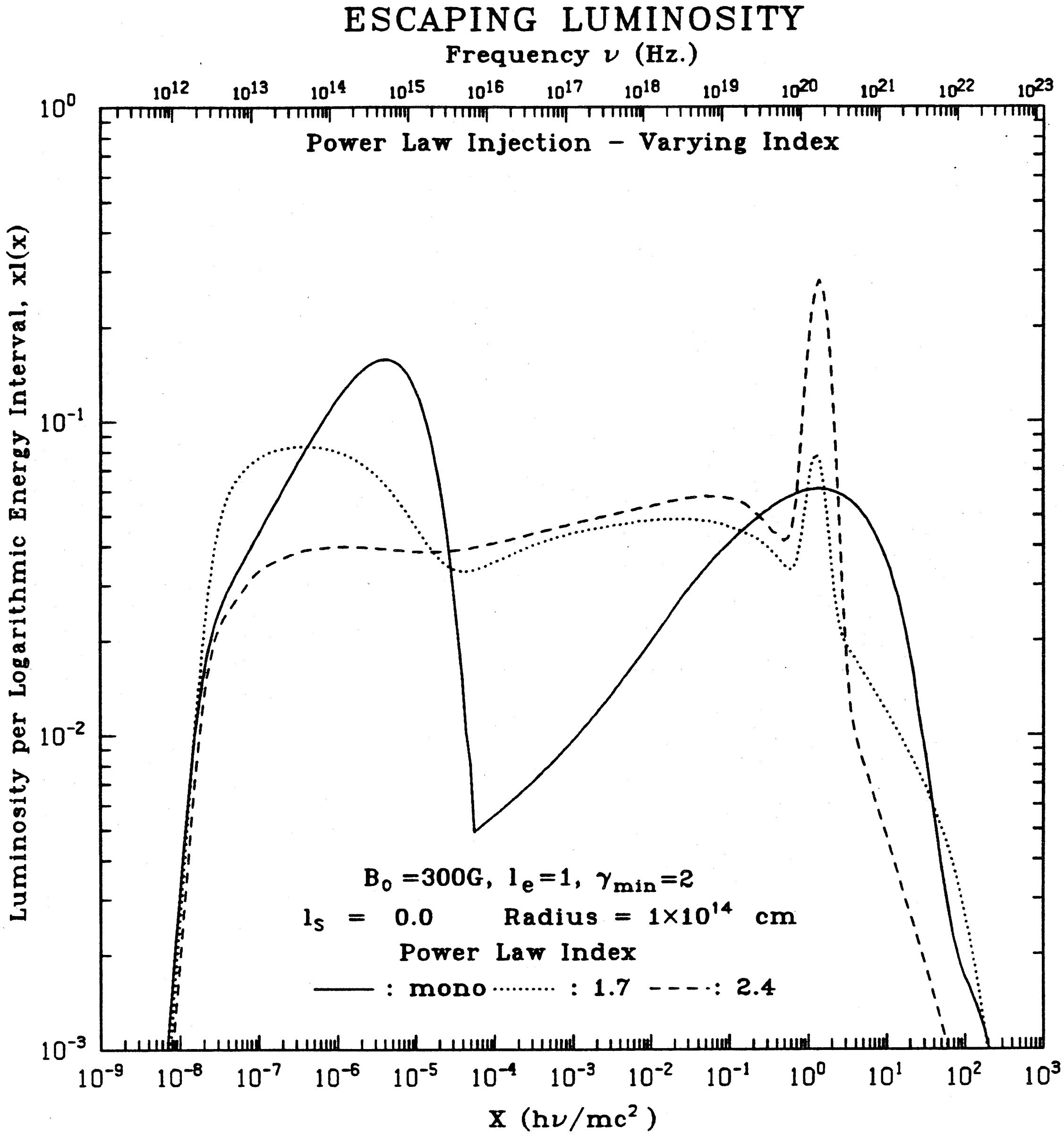
ESCAPING LUMINOSITY
Frequency ν (Hz.)
10^12
10^13
10^14
10^15
10^16
10^17
10^18
10^19
10^20
10^21
10^22
10^23
Power Law Injection - Varying Index
Luminosity per Logarithmic Energy Interval, xl(x)
10^0
10^-1
10^-2
10^-3
B_0 =300G, l_e=1, γ_min=2
l_s = 0.0 Radius = 1×10^14 cm
Power Law Index
: mono
: 1.7
: 2.4
10^-9
10^-8
10^-7
10^-6
10^-5
10^-4
10^-3
10^-2
10^-1
10^0
10^1
10^2
10^3
X (hν/mc²)

Figure 6

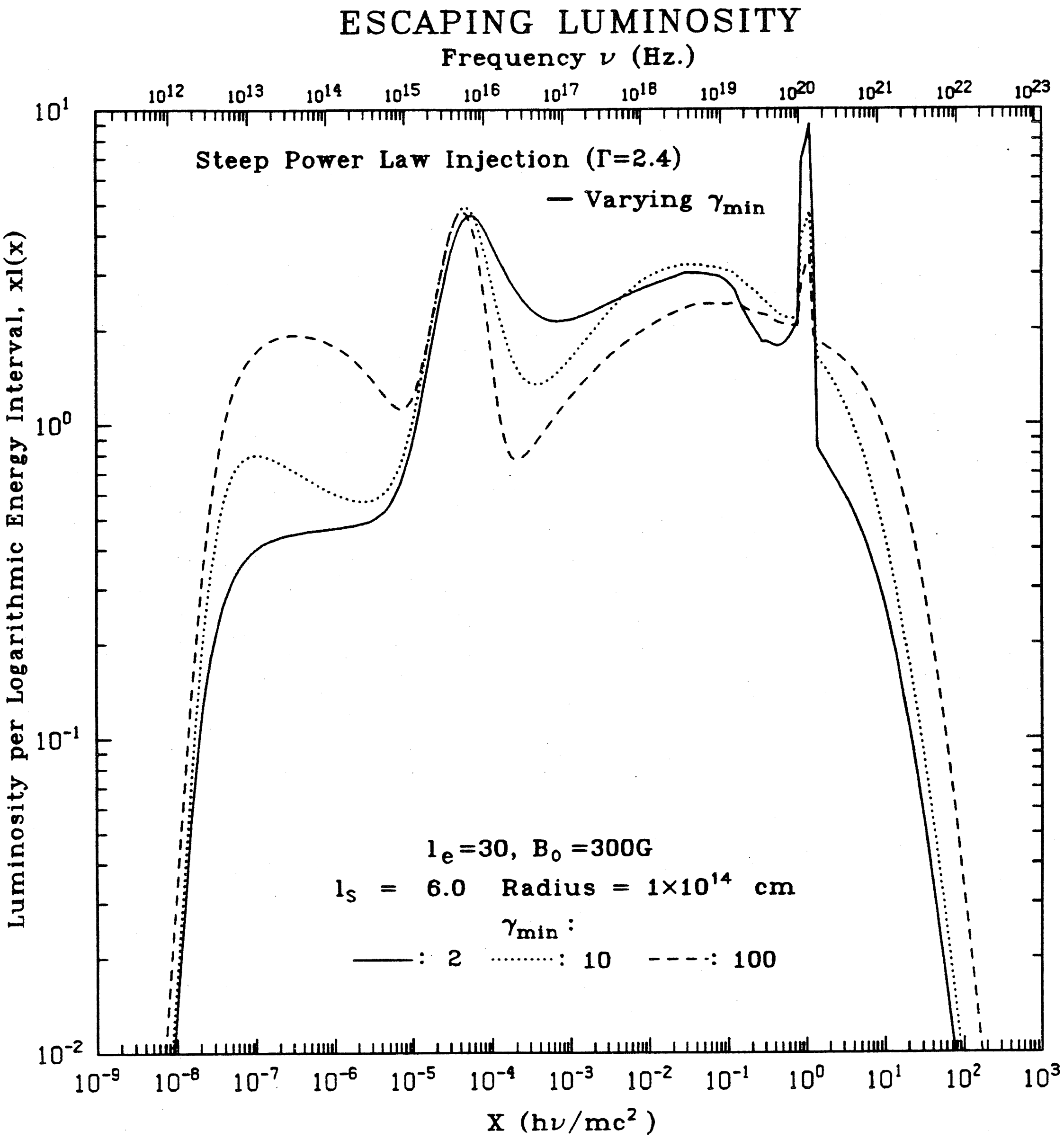
ESCAPING LUMINOSITY
Frequency ν (Hz.)
10^12
10^13
10^14
10^15
10^16
10^17
10^18
10^19
10^20
10^21
10^22
10^23
10^1
10^0
10^-1
10^-2
Luminosity per Logarithmic Energy Interval, xl(x)
Steep Power Law Injection (Γ=2.4)
— Varying γmin
le=30, B0 =300G
ls = 6.0 Radius = 1×10^14 cm
γmin :
——: 2 ········: 10 - - - -: 100
10^-9
10^-8
10^-7
10^-6
10^-5
10^-4
10^-3
10^-2
10^-1
10^0
10^1
10^2
10^3
X (hν/mc²)

Figure 7

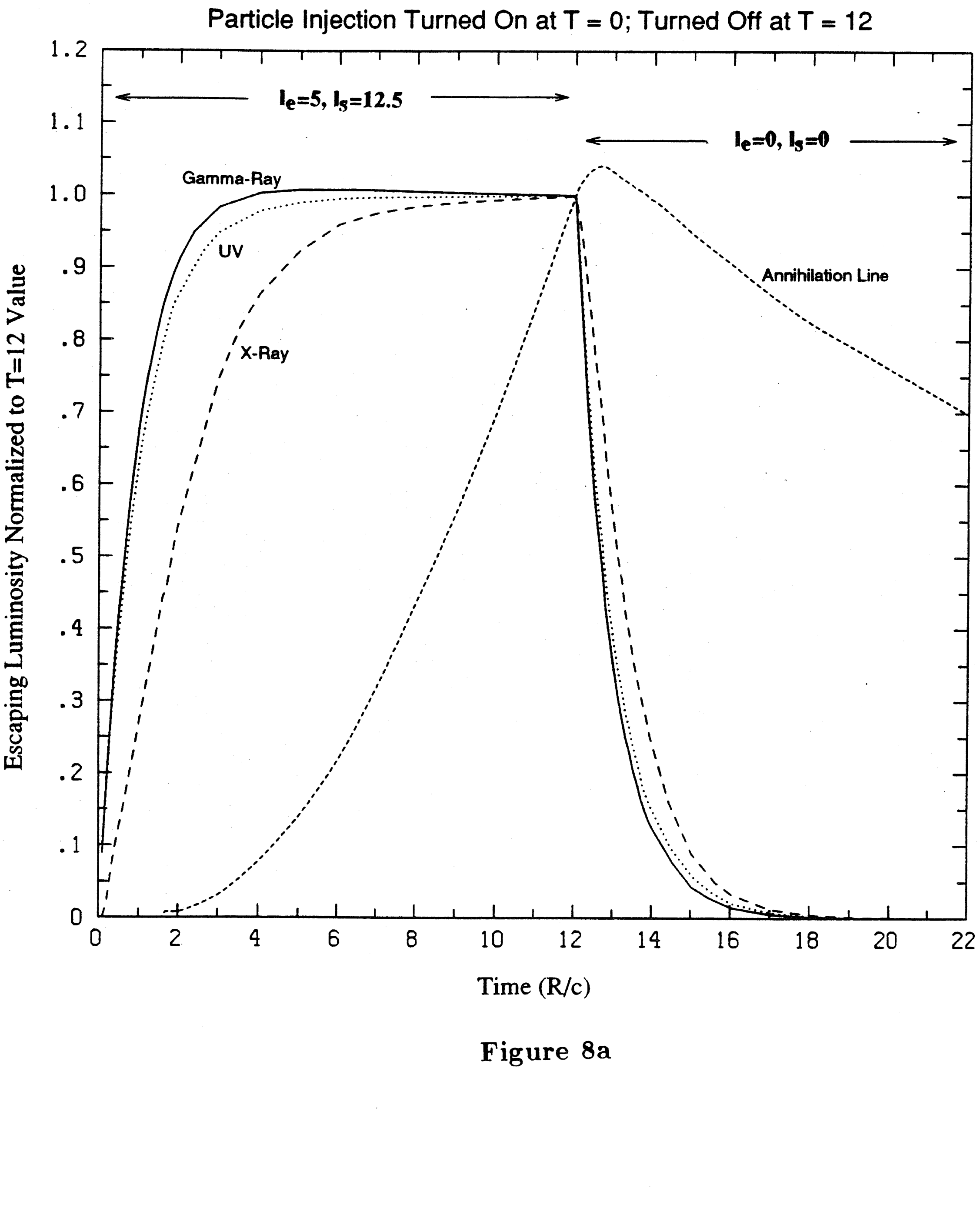
Particle Injection Turned On at T = 0; Turned Off at T = 12
l_e=5, l_s=12.5
l_e=0, l_s=0
Gamma-Ray
UV
X-Ray
Annihilation Line
Escaping Luminosity Normalized to T=12 Value
1.2
1.1
1.0
.9
.8
.7
.6
.5
.4
.3
.2
.1
0
0
2
4
6
8
10
12
14
16
18
20
22
Time (R/c)

Figure 8a

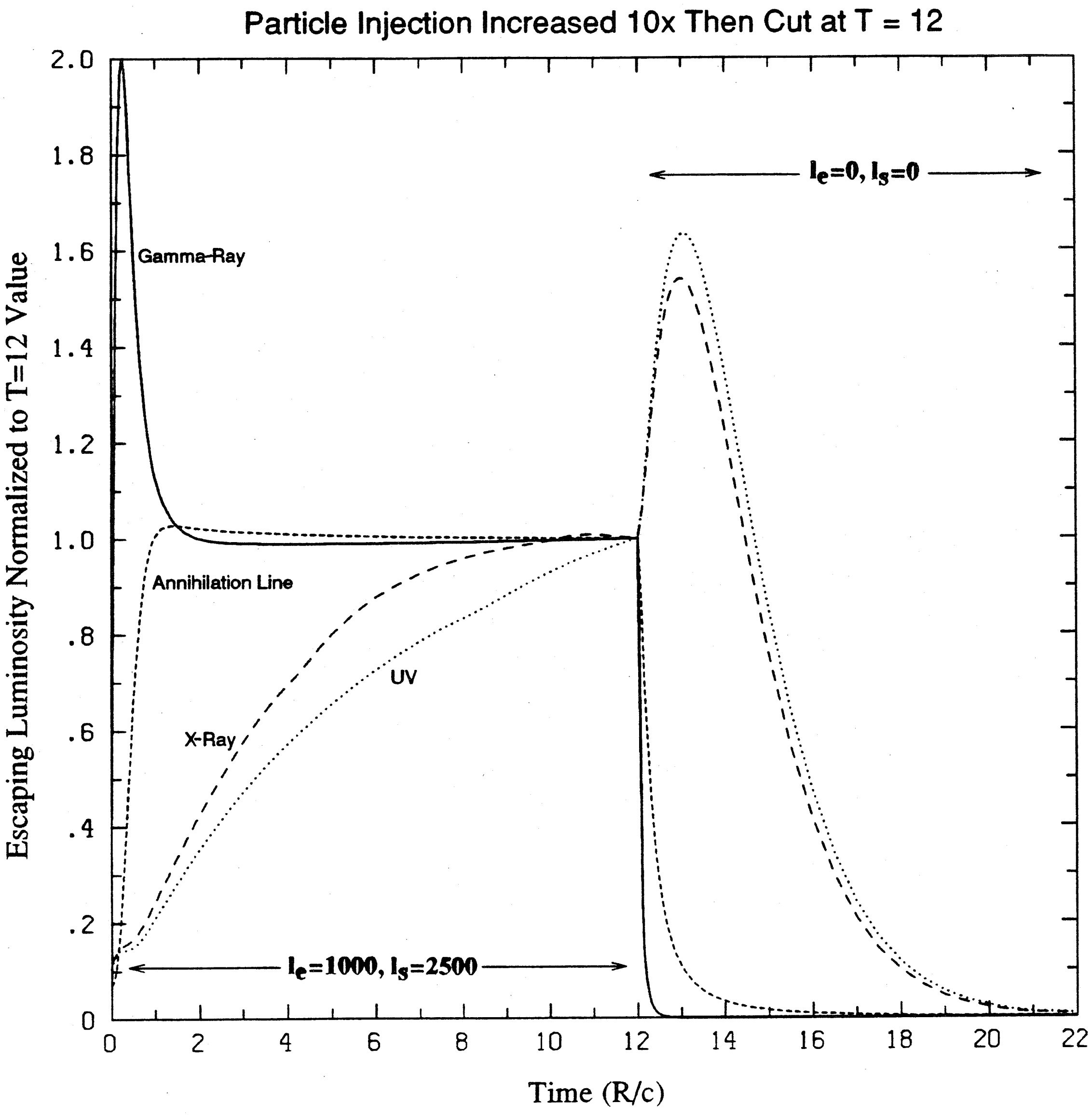
Particle Injection Increased 10x Then Cut at T = 12
Escaping Luminosity Normalized to T=12 Value
Time (R/c)
2.0
1.8
1.6
1.4
1.2
1.0
.8
.6
.4
.2
0
0
2
4
6
8
10
12
14
16
18
20
22
Gamma-Ray
Annihilation Line
X-Ray
UV
l_e=1000, l_s=2500
l_e=0, l_s=0

Figure 8b

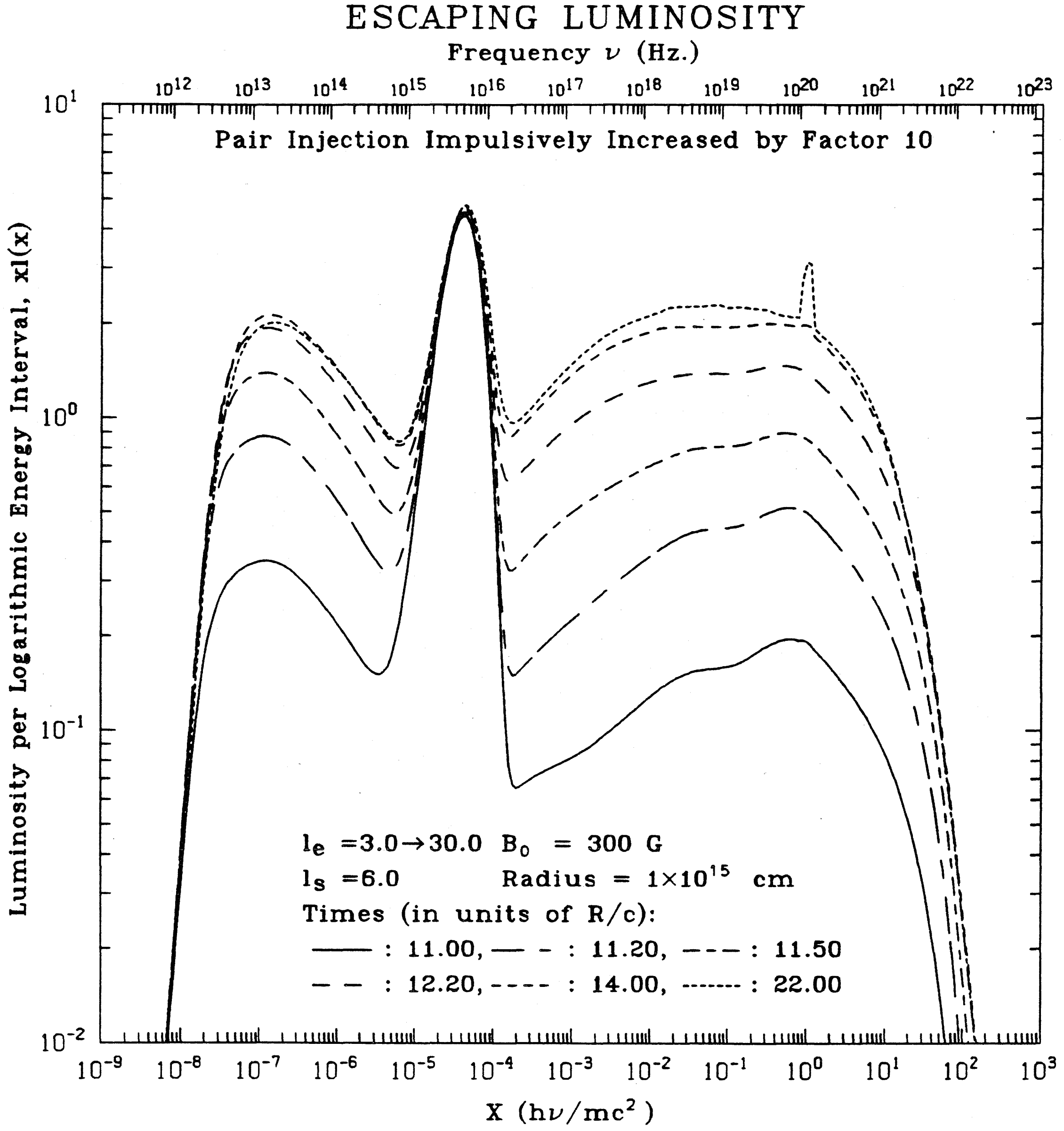
ESCAPING LUMINOSITY
Frequency ν (Hz.)
10^12
10^13
10^14
10^15
10^16
10^17
10^18
10^19
10^20
10^21
10^22
10^23
Pair Injection Impulsively Increased by Factor 10
Luminosity per Logarithmic Energy Interval, xl(x)
10^1
10^0
10^-1
10^-2
le =3.0→30.0 B0 = 300 G
ls =6.0 Radius = 1×10^15 cm
Times (in units of R/c):
—— : 11.00, — - : 11.20, - - - : 11.50
— — : 12.20, - - - - : 14.00, ------- : 22.00
10^-9
10^-8
10^-7
10^-6
10^-5
10^-4
10^-3
10^-2
10^-1
10^0
10^1
10^2
10^3
X (hν/mc²)

Figure 9a

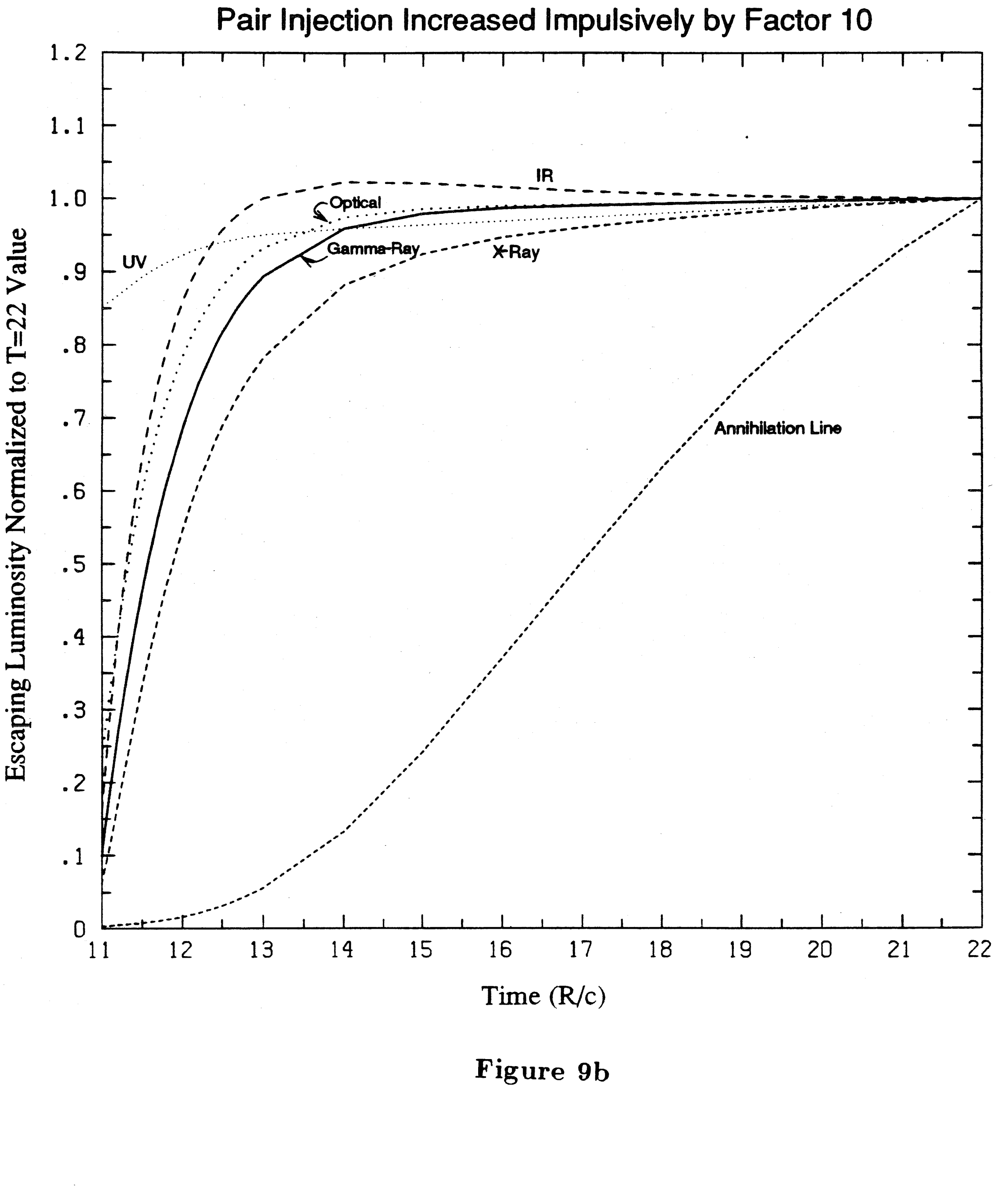

Pair Injection Increased Impulsively by Factor 10
Escaping Luminosity Normalized to T=22 Value
Time (R/c)
IR
Optical
UV
Gamma-Ray
X-Ray
Annihilation Line
0
.1
.2
.3
.4
.5
.6
.7
.8
.9
1.0
1.1
1.2
11
12
13
14
15
16
17
18
19
20
21
22

Figure 9b

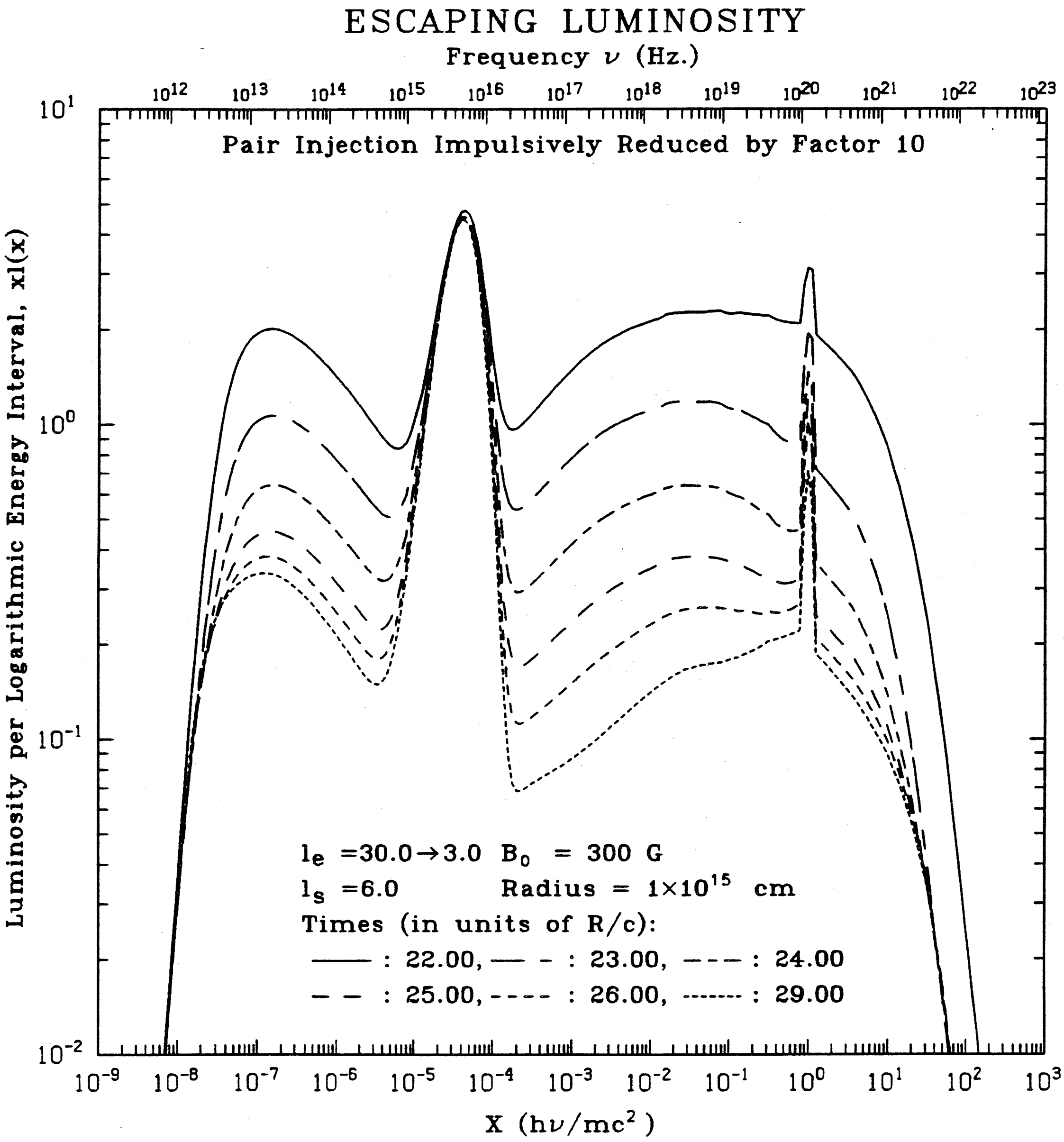
ESCAPING LUMINOSITY
Frequency ν (Hz.)
10^12
10^13
10^14
10^15
10^16
10^17
10^18
10^19
10^20
10^21
10^22
10^23
Pair Injection Impulsively Reduced by Factor 10
Luminosity per Logarithmic Energy Interval, xl(x)
10^1
10^0
10^-1
10^-2
l_e =30.0→3.0 B_0 = 300 G
l_s =6.0 Radius = 1×10^15 cm
Times (in units of R/c):
: 22.00, : 23.00, : 24.00
: 25.00, : 26.00, : 29.00
10^-9
10^-8
10^-7
10^-6
10^-5
10^-4
10^-3
10^-2
10^-1
10^0
10^1
10^2
10^3
X (hν/mc^2)

Figure 10a

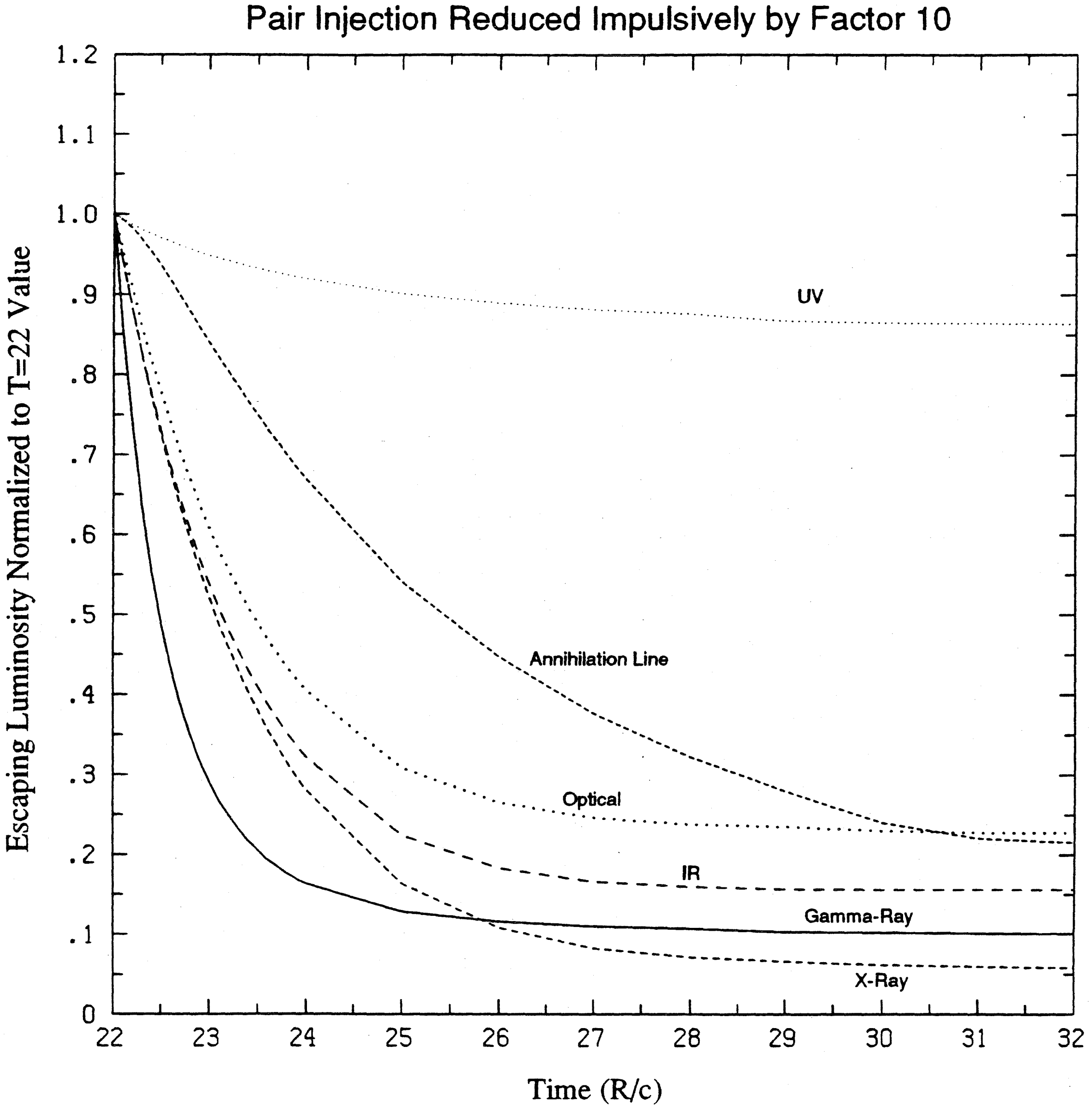
Pair Injection Reduced Impulsively by Factor 10
Escaping Luminosity Normalized to T=22 Value
Time (R/c)
1.2
1.1
1.0
.9
.8
.7
.6
.5
.4
.3
.2
.1
0
22
23
24
25
26
27
28
29
30
31
32
UV
Annihilation Line
Optical
IR
Gamma-Ray
X-Ray

Figure 10b

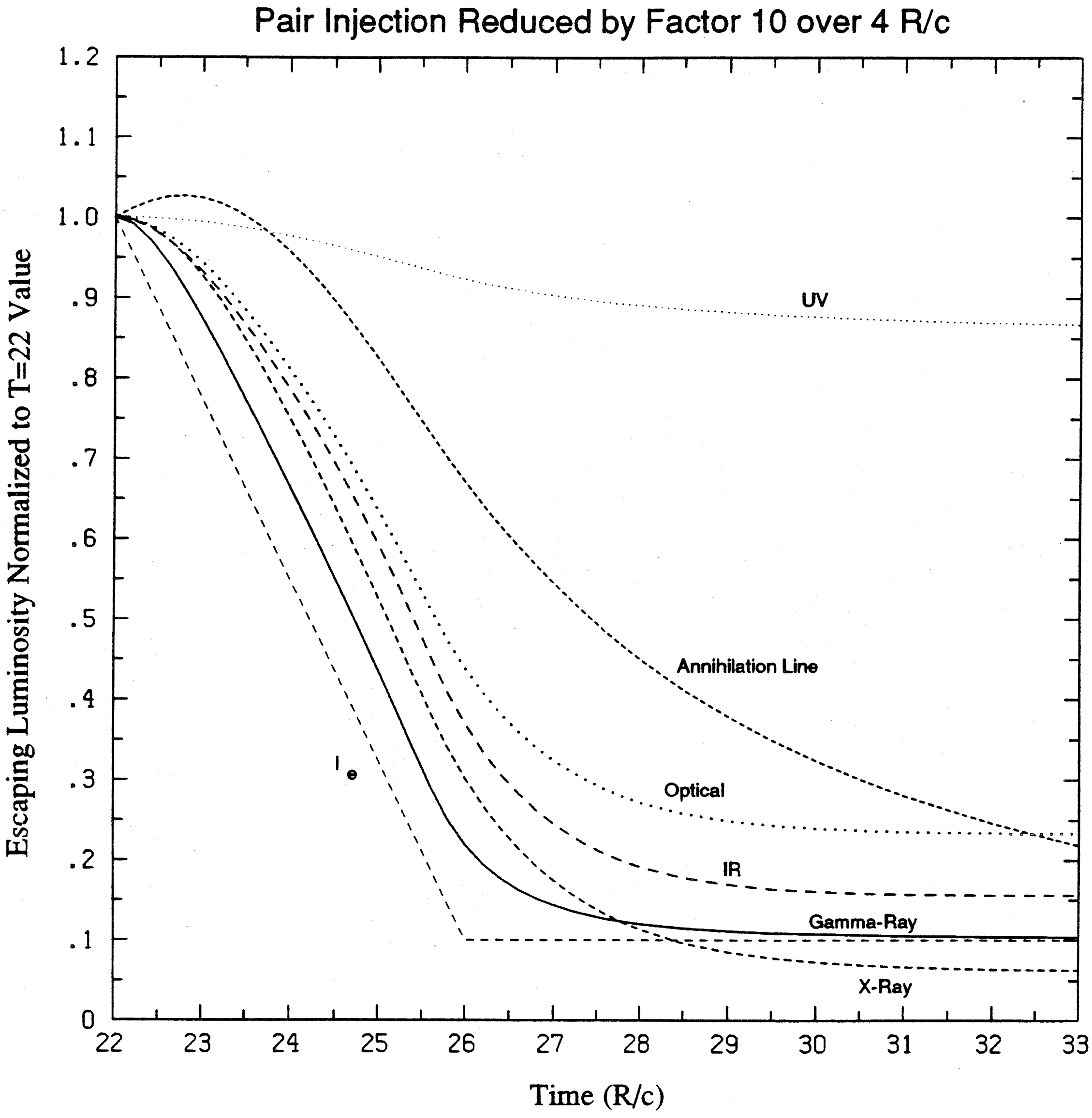
Pair Injection Reduced by Factor 10 over 4 R/c
Escaping Luminosity Normalized to T=22 Value
1.2
1.1
1.0
.9
.8
.7
.6
.5
.4
.3
.2
.1
0
22
23
24
25
26
27
28
29
30
31
32
33
Time (R/c)
UV
Annihilation Line
Optical
IR
Gamma-Ray
X-Ray
l_e

Figure 10c

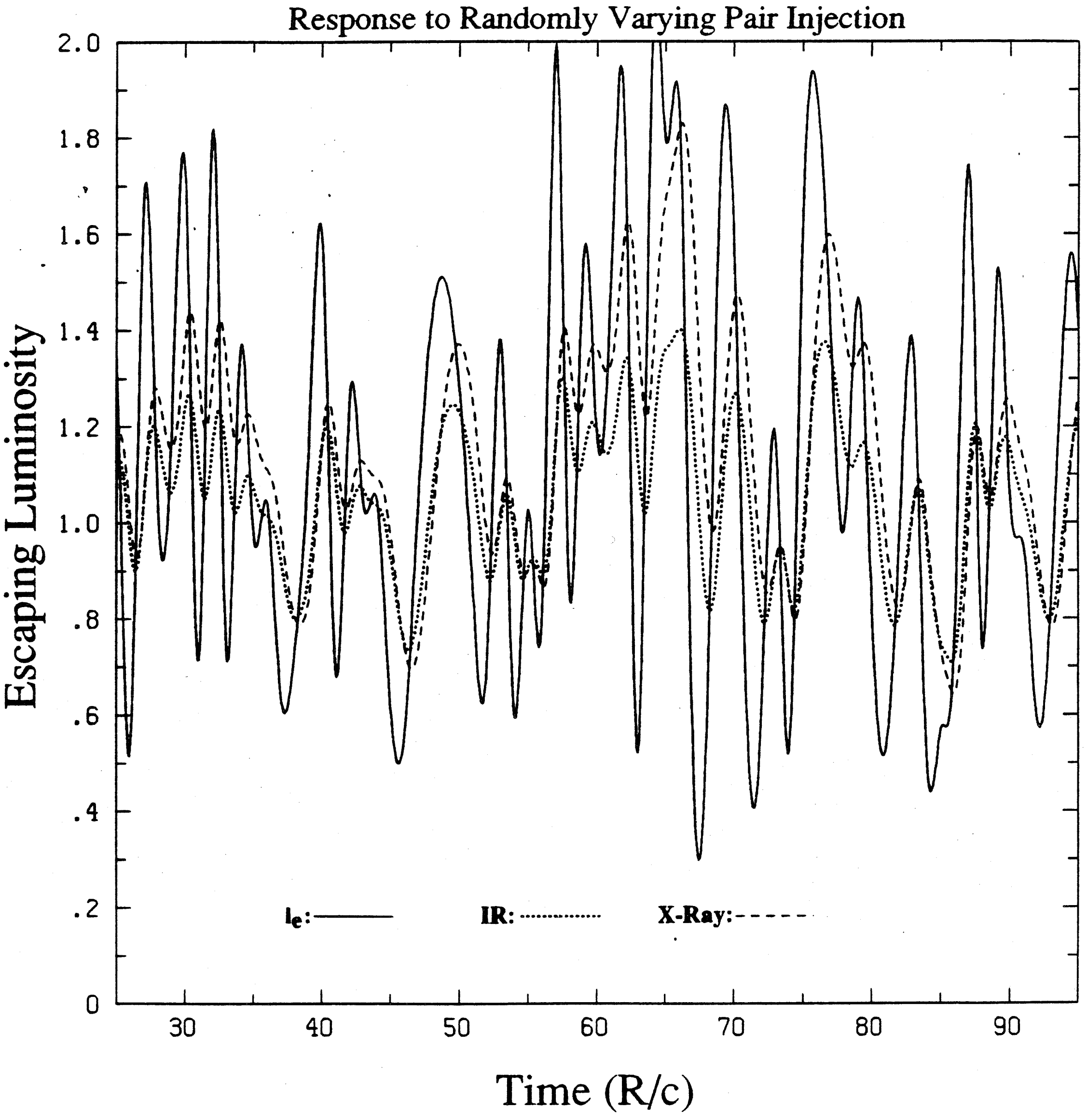
Response to Randomly Varying Pair Injection
Escaping Luminosity
Time (R/c)
2.0
1.8
1.6
1.4
1.2
1.0
.8
.6
.4
.2
0
30
40
50
60
70
80
90
l_e:
IR:
X-Ray:

Figure 11

Chapter 4

PHYSICAL PROCESSES IN PHOTON-STARVED NONTHERMAL PAIR PLASMAS

in collaboration with

Andrzej A. Zdziarski,
Space Telescope Science Institute

Don Q. Lamb,
University of Chicago

Originally appeared in *Astrophysical Journal* (1990), **357**, 149.

Abstract

We study Compton spectra produced by relativistic unmagnetized nonthermal electron-positron pairs injected into "photon-starved" plasmas, i.e., plasmas where the luminosity in soft photons is much less than the power in the nonthermal pair injection. The main physical processes in photon-starved plasmas are as follows: the repeated Compton scattering of individual photons before they escape the source, production of electron-positron pairs in photon-photon collisions, the cooling of pairs to an equilibrium temperature and the formation of the thermal plasma component, and the transfer of energy from the nonthermal pairs to thermal ones via Coulomb collisions. We find the equilibrium temperature is often relativistic and increases with the decreasing compactness parameter L_e/R, where L_e and R are the luminosity in injected electron pairs and radius, respectively. Coulomb interactions are important in such plasmas and may transfer a large fraction of the injected nonthermal power directly to the thermal component, which keeps the Thomson optical depth of the nonthermal component small. For small enough soft photon luminosities, bremsstrahlung emission by the thermal and nonthermal electrons becomes important.

When the compactness in pairs is low, the X-ray photon spectrum is due mostly to moderately Comptonized thermal bremsstrahlung from the semi-relativistic plasma; when the compactness is high, it is due to repeated Compton upscattering of soft photons on a cool, optically thick thermal plasma. The overall spectra are very hard in the X-ray range, peak near 0.1–1 MeV, and are cut off at higher energies with power law tails following the cutoffs. Such spectra are relevant to theoretical models of gamma ray bursts, active galactic nuclei, and the cosmic X-ray and gamma ray backgrounds.

I. Introduction

We study here nonthermal unmagnetized relativistic plasmas in pair equilibrium. The assumptions adopted in this work are similar to those of Zdziarski and Lightman (1985), Zdziarski and Lamb (1986; hereafter ZL86), Fabian *et al.* (1986), Svensson (1987), Lightman and Zdziarski (1987; hereafter LZ87), and Done and Fabian (1989). The basic assumption of those papers as well as of the present work is that a fraction of the available energy is supplied to the isotropic and homogeneous plasma in the form of a flux of relativistic electrons or pairs (nonthermal injection). These injected relativistic pairs lose their energy mostly via Compton scattering of soft photons. The resulting radiation spectrum extends above the threshold for production of e^+e^- pairs, 511 keV. The produced pairs Compton can scatter as well, giving rise to an e^+e^- pair cascade. In steady state, the pair production rate equals the sum of the pair annihilation and pair escape rates (pair equilibrium). For reviews of such pair plasmas and a comparison of their emitted photon spectra to those of cosmic compact objects, see Svensson (1986), Zdziarski and Lightman (1987), and Svensson and Zdziarski (1989).

The work presented here concentrates on the case of photon-starved or photon-deficient plasmas. We will define such plasmas as those where the luminosity in any sources of soft ($h\nu \lesssim m_ec^2$) photons, L_s, is much less than the power injected in the primary relativistic electrons, L_e — so much that the power radiated away by the photons after a single scattering off the cooled nonthermal electron distribution is also much less than the injected power in primary electrons (cf. eq. [2] in § II). Since the escaping photon luminosity must balance the total injected luminosity in a steady state, it follows that repeated scatterings of photons by either thermal or nonthermal electrons have to be important in such cases. Moreover, the spectra of photon-starved plasmas will be hard (i.e., most photons emerge with significantly higher energies than they were injected with) since the luminosity injected in pairs must make its way to the photon distribution (via repeated Compton upscattering). Because of this deficit of soft photons, the Compton cooling times for injected pairs are not necessarily much shorter than other timescales relevant to the problem. Slower processes such as Coulomb cooling and electron-electron bremsstrahlung can then have a significant impact on the equilibrium particle distributions.

There are several effects specific to photon-starved plasmas. First, higher order Compton scatterings are important by the definition above. A typical primary photon will get upscattered several times before leaving the source.

Second, the relativistic electrons cool on the upscattered spectrum rather than on the (deficient) primary soft photons. Typically, the upscattered spectrum extends to high energies. Many Compton scatterings are in the Klein-Nishina regime ($\epsilon\gamma > 1$, where γ is the electron Lorentz factor and ϵ is the photon energy in units of the electron rest mass, $\epsilon \equiv h\nu/m_e c^2$) and Klein-Nishina corrections can no longer be ignored. In particular, the use of a Klein-Nishina cutoff for the scattering rate (e.g., as in LZ87) becomes inappropriate (see Coppi and Blandford 1990, hereafter CB90). Also, the evolution of the pair distribution will no longer be well-described by the continuous cooling approximation, $dN(\gamma)/dt = -(d/d\gamma)[\dot{\gamma}N(\gamma)]$. Here $\dot{\gamma}$ is the cooling rate, and N is the nonthermal pair distribution function. In the Klein-Nishina regime, pairs lose energy in large, discrete steps (Blumenthal and Gould 1970; Zdziarski 1988).

Third, the equilibrium temperature, Θ, to which the relativistic electrons cool will be high ($\Theta \lesssim 1$), and the associated Compton parameter y will be large (> 1). Here $\Theta \equiv kT/m_ec^2$ is the dimensionless electron temperature. The Compton parameter, determining the efficiency of Comptonization by thermal electrons, is given by equation (16) below.

We study here plasmas with negligible magnetic fields. The injected particles are taken to be e^+e^- pairs. We consider only steady (stationary) plasmas where the sum of the injection rate and the rate of pair production by photons equals the sum of the rate of e^+e^- pair annihilation and the rate of escape of pairs from the plasma. For the process of Compton scattering, we assume that some contribution to the cooling rate is from Compton scattering in the classical, Thomson, regime. (Cf. studies of pair cascades in the regime where the injection occurs in the extreme Klein-Nishina regime, e.g., Zdziarski 1988).

Photon-deficient plasmas without magnetic fields were studied before by ZL86, LZ87, and Done and Fabian (1989). In contrast to those papers, we include the process of Coulomb energy loss of the relativistic electrons to the background thermal plasmas. We find the process to be important over a wide range of plasma parameters (see also de Kool and Begelman 1989). Its importance increases with decreasing compactness in the electron injection, ℓ_e, and decreasing ℓ_s/ℓ_e, the ratio of the soft photon and electron injection compactnesses. Here ℓ is the compactness parameter, $\ell \equiv L\sigma_{\rm T}/Rm_ec^3$, determining the importance of e^+e^- pair production and Compton losses in a source. The subscript e corresponds to the primary electron (or pair) injection, while s corresponds to the primary soft photons.

Our results differ somewhat from ZL86 as far as the γ-ray spectra from photon-deficient sources are concerned. ZL86 found that a typical spectrum was a broken power law with a low energy spectral index $\alpha_x < 1$ at $\epsilon \lesssim 1$ and a high energy spectral index $\alpha_\gamma > \alpha_x$ at $\epsilon \gtrsim 1$. Here, the energy spectral index is defined as $F_\nu \propto \nu^{-\alpha}$. We find that Coulomb losses at low compactnesses and Compton losses at large compactnesses cause the optical depth of the nonthermal part of the electron distribution to be always $\ll 1$. This results in a diminished role of scattering by the nonthermal electrons and a spectral turnover at $\epsilon \gtrsim 1$. Beyond the turnover, the amplitude of the high energy, γ-ray part of the spectrum is reduced. Also, the effects of Compton up and down scattering by the thermal plasma and pair annihilation at $\ell \gg 1$ result in additional structure in the spectrum at $\epsilon \lesssim 1$. These effects were not discussed in ZL86.

In the classification scheme of Svensson (1987), nonthermal electron-positron cascades of the type considered by ZL86, LZ87, and the present work fall into his type III. Those cascades are fully nonlinear, by which it is meant that both e^+e^- cooling and pair production occur on photons previously upscattered by the injected relativistic electrons.

One example of a physical situation where the soft photon luminosity, L_s, may be much less than the luminosity injected in relativistic electrons, L_e, may occur is acceleration of electrons in a region which lies several stellar radii above a (weakly magnetized) neutron star. Then only a small fraction of L_e intercepts the stellar surface and is re-emitted as blackbody radiation L_s, providing a source of soft photons in a self-consistent way (see ZL86). Another example is a source (in the vicinity of either a neutron star or a black hole) in which soft photons are produced by synchrotron emission in a magnetic field that is below the equipartition strength, or a source in which bremsstrahlung is the only source of photons.

We compare our theoretical spectra to the spectra of γ-ray bursts and active galactic nuclei (see § V). Some of the theoretical spectra resemble the spectra of some "classical" γ-ray bursts, and some resemble those of "soft γ-ray repeaters."

They may also be relevant to the X-ray and γ-ray spectra of active galactic nuclei. In particular, photon-starved sources may be responsible for the ~ 1 MeV peak observed in several AGN and the cosmic γ-ray background (e.g., Bassani *et al.* 1985). Photon-starved plasmas may also explain the spectral indices less than 0.5 observed in certain AGN (e.g., Mushotzky 1984) and in the cosmic X-ray background (e.g., Marshall *et al.* 1980).

II. Model of the Physical Processes

The treatment of the physical processes we use here is for the most part described in CB90. The method of solving nonlinear pair cascades is analogous to that of Coppi (1990; hereafter C90). For the present work, the main advantages of the method of CB90 and C90 compared to that of LZ87 are as follows: (i) the exact Klein-Nishina Compton scattering rates are used; (ii) the electron kinetic equations are solved directly without relying on the continuity equation (see LZ87); and (iii) the method for treating thermal Comptonization works at relativistic temperatures. The processes we study here are Compton scattering, thermal and nonthermal pair annihilation, two photon pair production, thermal and nonthermal bremsstrahlung, and Coulomb scattering. LZ87 did not include the effects of Coulomb collisions, bremsstrahlung, and nonthermal pair annihilation.

We assume that e^+e^- pairs are continuously injected at a rate $Q(\gamma)$ particles per unit time per unit volume per unit energy, with $\gamma_{\rm min} \leq \gamma \leq \gamma_{\rm max}$. (This contrasts with ZL86 and LZ87, who took the injected particles to be electrons.) We assume that the injection occurs uniformly throughout a spherical volume of radius R. The total power L_e put into the primary pairs is measured by the dimensionless "pair compactness parameter,"

$$\ell_e \equiv \frac{L_e \sigma_{\rm T}}{R m_e c^3} = \frac{4\pi}{3}\frac{\sigma_{\rm T} R^2}{c}\int_{\gamma_{\rm min}}^{\gamma_{\rm max}} \gamma Q(\gamma)\, d\gamma\,, \tag{1a}$$

which is roughly proportional to the optical depth to e^+e^- pair production in photon-photon collisions. Here $\sigma_{\rm T}$ is the Thomson cross section, and m_e is the electron mass. The injected pairs eventually annihilate and contribute their rest mass-energy to the radiated photon spectrum. We therefore include their rest-mass energy in our definition of the power L_e (cf. eq. [2a] of LZ87). The form of the injection function $Q(\gamma)$ is taken to be a power law of index Γ extending from energies $\gamma_{\rm min}$ to $\gamma_{\rm max}$.

One source of soft photons that is always present in a plasma is bremsstrahlung from both thermal and nonthermal electrons. In addition, we assume for some models an injection of blackbody photons with dimensionless temperature $\Theta_{\rm bb}$ ($\equiv kT_{\rm bb}/m_e c^2$) at the rate $\dot{n}_0$ photons per unit time per unit volume per unit energy ϵ. We will take $\Theta_{\rm bb} = 10^{-4}$–$10^{-3}$ in our numerical models. We assume $\Theta_{\rm bb}\gamma_{\rm max} \leq 1$, so that for any pair a nonzero part of the photon spectrum is in the Thomson limit. The "soft photon compactness" is

$$\ell_s \equiv \frac{L_s \sigma_{\rm T}}{R m_e c^3} = \frac{4\pi}{3}\frac{\sigma_{\rm T} R^2}{c}\int_0^{\infty} \epsilon \dot{n}_0(\epsilon)\, d\epsilon\,. \tag{1b}$$

The numerical value of the constant $\sigma_{\rm T}/m_e c^3$ in equations (1a) and (1b) is $1/(3.7 \times 10^{28}\ {\rm erg\,s^{-1}\,cm^{-2}})$. The photon injection is assumed uniform and isotropic throughout the source.

An approximate condition for a plasma to be photon-starved valid at low values of ℓ_e and $\Gamma < 2$ is,

$$\ell_s/\ell_e < {\gamma_{\rm max}}^{3/2}\Theta^{-1/2}\,, \tag{2}$$

(Done and Fabian 1989).

We divide the pair distribution into a thermal and a nonthermal population (Some quantities related to those populations will have superscripts *th* and *nth*, respectively). Let $n(\epsilon)$ and $N(\gamma)$ be the number densities per unit energy of photons and nonthermal pairs, respectively, at a representative interior point of the emission region. The equation governing the nonthermal pair distribution, N, is then,

$$\begin{aligned} P(\gamma) + Q(\gamma) + \int_1^{\gamma_{\max}} N(\gamma')C(\gamma',\gamma)d\gamma' = \\ N(\gamma)\int_1^{\gamma_{\max}} C(\gamma,\gamma')d\gamma' + A^{\rm nth}(\gamma) + \frac{\partial}{\partial\gamma}[(\dot\gamma_B + \dot\gamma_{\rm Coul})N(\gamma)]\,. \end{aligned} \tag{3}$$

Here $P(\gamma)$ is the rate of pair creation per unit volume per unit energy, $Q(\gamma)$ is the rate of injection of primary pairs per unit volume per unit energy, and $C(\gamma',\gamma)$ is the Compton transition rate for scattering from Lorentz factor γ' to γ, which depends on the photon spectrum, n. The $A^{\rm nth}$ is the rate of nonthermal annihilation (see CB90), which includes the contributions from both the thermal pairs and the other nonthermal pairs. The $\dot\gamma_B$ and $\dot\gamma_{\rm Coul}$ are the cooling rates due to $e^\pm e^\pm$ bremsstrahlung and Coulomb cooling, respectively. See CB90 for a more detailed discussion of these terms. As their cooling time is less than R/c at $\ell \gtrsim 1$, pairs cannot leave the sources before cooling completely. Hence we do not include an escape term for the nonthermal pairs. Upon reaching the thermal range of energies, the nonthermal pairs are transferred to the thermal distribution (see discussion after eq. [16] below).

The thermal (Maxwell-Boltzmann) distribution has a dimensionless temperature Θ and a Thomson optical depth $\tau_{\rm T}^{\rm th} = (N_+ + N_-)\sigma_{\rm T}R$. Here N_+, N_- are the densities of thermal positrons and electrons, respectively. We determine Θ

and $\tau_{\rm T}^{\rm th}$ from energy balance and pair balance, respectively (see eqs. [15], [13] below).

The photon kinetic equation is,

$$\dot{n}_0(\epsilon) + \dot{n}_A^{\rm nth}(\epsilon) + \dot{n}_A^{\rm th}(\epsilon) + \dot{n}_B^{\rm nth}(\epsilon) + \dot{n}_B^{\rm th}(\epsilon) + \dot{n}_{\rm C}^{\rm nth}(\epsilon) + \dot{n}_{\rm C}^{\rm th}(\epsilon) = \frac{c}{R} n(\epsilon)[\tau_{\rm C}^{\rm nth}(\epsilon) + \tau_{\gamma\gamma}(\epsilon)] + \frac{c}{R} n(\epsilon) \left[1 + \frac{\tau_{\rm C}^{\rm th}(\epsilon)}{3} f(\epsilon)\right]^{-1} . \tag{4}$$

Here, $\dot{n}_0$, $\dot{n}_A$, $\dot{n}_B$, and $\dot{n}_{\rm C}$ are the rates of production of photons at energy ϵ by soft photon injection, pair annihilation, bremsstrahlung, Compton scattering off nonthermal electrons, and Compton scattering off thermal electrons, respectively. We treat pair annihilation, bremsstrahlung and scattering by thermal and nonthermal electrons separately (see CB90). Photons are removed from energy ϵ by Compton scattering with nonthermal electrons, having Compton optical depth $\tau_{\rm C}^{\rm nth}$ (calculated using the Klein-Nishina cross section and depending on the electron distribution N), and by pair creation, having optical depth $\tau_{\gamma\gamma}$. The removal of photons due to Compton scattering with thermal electrons is included in $\dot{n}_{\rm C}^{\rm th}$. The last term, corresponding to diffusive photon escape, has the same form as in LZ87. The function f accounts for the effect of relativistic forward scattering, which reduces the amount of photon diffusion inside the source, and is given by equation (21b) in LZ87.

We treat Coulomb losses in the same way as in CB90. At relativistic energies $\gamma \gg 1$ and nonrelativistic pair temperatures ($\Theta \ll 1$), the Coulomb loss rate takes the form (e.g., Gould 1975),

$$\dot{\gamma}_{\rm Coul} \approx -\frac{3}{2}\frac{c}{R}\tau_{\rm T}^{\rm th} \ln \frac{\gamma^{1/2}}{\epsilon_p} , \tag{5a}$$

where ϵ_p is the dimensionless plasma frequency,

$$\epsilon_p = \left(\frac{3 a_0 \tau_{\rm T}^{\rm th}}{2R} \right)^{1/2} , \tag{5b}$$

and $a_0 = 5.29 \times 10^{-9}$ cm is the Bohr radius. The factor $\ln \epsilon_p^{-1}$ for $\tau_{\rm T}^{\rm th} = 1$ equals 17.4 for $R = 10^7$ cm and 25.4 for $R = 10^{14}$ cm. At higher temperatures, the Coulomb cooling rate $\dot\gamma_{\rm Coul}$ for energies $\gamma \gg \Theta$ is reduced by a factor $\approx 1/(2\Theta)$ (see CB90 and references therein) relative to equation (5a).

We can compare the magnitude of Compton and Coulomb losses of an electron with the Lorentz factor γ. In a photon-starved plasma, $\ell_s \ll \ell_e$, Coulomb losses dominate below a $\gamma_{\rm cr}$ given by,

$$\gamma_{\rm cr}{}^2 \approx 10 \frac{\tau_{\rm T}^{\rm th}}{\ell_e} \ln \epsilon_p^{-1} . \tag{6a}$$

At $\ell_e \lesssim 10^2$, $\tau_{\rm T}^{\rm th} \propto \ell_e$ (e.g., Svensson 1987), and

$$\gamma_{\rm cr}{}^2 \sim \ln \epsilon_p^{-1} , \tag{6b}$$

and at $\ell_e \gg 10^2$, $\tau_{\rm T}^{\rm th} \propto \ell_e{}^{1/2}$, and

$$\gamma_{\rm cr}{}^2 \sim (100/\ell_e)^{1/2} \ln \epsilon_p^{-1} . \tag{6c}$$

We define the pair yield as the ratio of the power injected in the form of pair rest mass by the creation of e^+e^- pairs to the power injected in the primary pairs (cf. Guilbert, Fabian, and Rees 1983; Svensson 1987; LZ87),

$$Y \equiv \frac{\int_1^{\gamma_{\rm max}} P d\gamma}{\int_{\gamma_{\rm min}}^{\gamma_{\rm max}} \gamma Q \, d\gamma} . \tag{7a}$$

One may define an analogous quantity, Y_Q, for the primary pairs which represents the fraction of their injected energy contained in pair rest mass. For power-law pair injection, $Q(\gamma) = Q_0 \gamma^{-\Gamma}$ for $\gamma_{\rm min} \leq \gamma \leq \gamma_{\rm max}$, Y_Q is

$$Y_Q = \frac{\int_{\gamma_{\rm min}}^{\gamma_{\rm max}} \gamma^{-\Gamma} d\gamma}{\int_{\gamma_{\rm min}}^{\gamma_{\rm max}} \gamma^{-\Gamma+1} d\gamma} = \begin{cases} \frac{(\Gamma-2)({\gamma_{\rm min}}^{1-\Gamma} - {\gamma_{\rm max}}^{1-\Gamma})}{(\Gamma-1)({\gamma_{\rm min}}^{2-\Gamma} - {\gamma_{\rm max}}^{2-\Gamma})}, & \Gamma \neq 2; \\ \frac{{\gamma_{\rm min}}^{-1} - {\gamma_{\rm max}}^{-1}}{\ln(\gamma_{\rm max}/\gamma_{\rm min})}, & \Gamma = 2. \end{cases} \tag{7b}$$

The dimensionless luminosity, $\ell_{\rm ann}^{\rm th}$, in pair annihilation from thermal pairs is then related to both pair yields from the primary and secondary pairs,

$$\ell_{\rm ann}^{\rm th} = \frac{4\pi}{3} \frac{\sigma_{\rm T} R^2}{c} \int_0^\infty \epsilon \dot{n}_A^{\rm th}(\epsilon)\, d\epsilon = \gamma_{\rm th}(Y + Y_Q)\ell_e\,, \tag{8}$$

where $\gamma_{\rm th}$ is the average Lorentz factor in the Maxwell-Boltzmann distribution,

$$\gamma_{\rm th} = 3\Theta + \frac{K_1(1/\Theta)}{K_2(1/\Theta)}\,, \tag{9}$$

and K_n is the modified Bessel function of the second kind of order n.

We will also introduce here the dimensionless power in secondary pairs,

$$\ell_{\rm pair} \equiv \frac{4\pi}{3} \frac{\sigma_{\rm T} R^2}{c} \int_1^{\gamma_{\rm max}} \gamma P(\gamma) d\gamma\,, \tag{10}$$

This power is not directly radiated, and equals the fraction of the power in photons produced inside the source that is absorbed in photon-photon pair production. This quantity will be important for assessing the importance of the Coulomb process (see eqs. [17], [19]).

The escape of thermal pairs is treated as in Zdziarski (1985), by the means of a phenomenological parameter $\beta_{\rm esc}$ defined as the ratio of the travel time across the source to the escape time scale. The escape rate (at $N_+ = N_-$) is then

$$\dot{N}_{\rm esc}^{\rm th} = -2\beta_{\rm esc}(c/R)N_+\,. \tag{11}$$

We neglect here escape of nonthermal pairs (see the paragraph after eq. [3] above), which can be important under some circumstances.

We determine the Thomson optical depth of the thermal pairs by balancing pair annihilation of thermal pairs with both thermal and nonthermal pairs and pair escape with pair production. As the effect of annihilation with the non-thermal pairs is small in most cases, we neglect it in the equations (12)-(13) below,

$$-2N_+N_-\frac{3}{8}\sigma_{\rm T}cg_A - 2N_+\beta_{\rm esc}c/R + \int_1^{\gamma_{\rm max}} [Q(\gamma)+P(\gamma)]\,d\gamma \simeq 0\,. \qquad (12)$$

Here $g_A(\Theta)$ is the relativistic correction to the thermal pair annihilation rate (eq. [68] of Svensson 1982). As $N_+ = N_-$ for pure pair injection, equation (12) yields an estimate of the Thomson optical depth of the thermal pairs as

$$\tau_{\rm T}^{\rm th} \simeq \left[\left(\frac{8\beta_{\rm esc}}{3g_A}\right)^2 + \frac{4}{\pi g_A}(Y+Y_Q)\ell_e\right]^{1/2} - \frac{8\beta_{\rm esc}}{3g_A}\,. \qquad (13)$$

(The effect of nonthermal pair annihilation on pair equilibrium *is* included in our numerical treatment.) The pair escape term in equation (12) becomes equal to the pair annihilation term when $\tau_{\rm T}^{\rm th} = 8\beta_{\rm esc}/3g_A$. Pair escape is then negligible at $\tau_{\rm T}^{\rm th}$ larger than that value. Using the linear dependence between the pair yield and compactness at low ℓ_e (e.g., Svensson 1987), and using equation (13), we find that pair escape is negligible compared to the pair annihilation at

$$\ell_e \gtrsim 10^2\beta_{\rm esc}\,. \qquad (14)$$

The thermal pairs are produced by thermalization of both the primary and secondary pairs, and removed by pair annihilation and escape from the source. They cool and heat through Compton interactions with the photon field $n(\epsilon)$

and through Coulomb interactions with the nonthermal electrons, and cool via thermal bremsstrahlung. The energy balance equation for the thermal pairs is thus

$$\begin{aligned}
&-\int_0^\infty \dot{n}_{\mathrm{C}}^{\mathrm{th}}\epsilon\, d\epsilon - \int_0^\infty \dot{n}_B^{\mathrm{th}}\epsilon\, d\epsilon - \int_0^\infty \dot{n}_A^{\mathrm{th,nth}}\epsilon\, d\epsilon + \gamma_{\mathrm{th}}\dot{N}_{\mathrm{esc}}^{\mathrm{th}} + \\
&\qquad + \gamma_{\mathrm{th}}\int_1^{\gamma_{\max}}(P+Q)d\gamma - \int_1^{\gamma_{\max}}\dot{\gamma}_{\mathrm{Coul}}N\, d\gamma = 0\,.
\end{aligned} \tag{15}$$

A negative term in equation (15) corresponds to removal and a positive one to production of thermal energy, respectively. The factor $\dot{n}_A^{\mathrm{th,nth}}$ includes annihilation of thermal pairs with both thermal and nonthermal pairs. The integral over $\dot{n}_A^{\mathrm{th,nth}}$ gives the rate at which annihilation removes energy from a unit volume of the source, i.e., the integrated annihilation emissivity, and thus the annihilation compactness (see eq. [9]). We use the fit given by Svensson (1982, eq. [70]) for the integrated thermal annihilation emissivity.

The term $\gamma_{\mathrm{th}}\int(P+Q)d\gamma$ gives the rate at which energy is injected into the emission region in the form of nonthermal pairs that cool and become thermal. Since the probability of annihilation increases with decreasing energy, pairs with energies *lower* than γ_{th} predominantly annihilate. Thus the sum of the third, fourth, and fifth, terms in equation (15) is positive and annihilation *heats* the thermal plasma. The heating rate due to annihilation can be comparable to the cooling rate due to bremsstrahlung, the second term in equation (15); for example, both rates are approximately equal at $\Theta = 1$.

The thermal pairs up and down scatter photons present in the source. Low energy photons are predominantly upscattered repeatedly by the thermal pairs. The Compton parameter y is a convenient measure of the efficiency of the thermal upscattering, with $\epsilon_f = e^y\epsilon_i$, where the indices i and f indicate photon before and after scattering, respectively, and $\epsilon_f < \Theta$. The nonrelativistic form of the parameter is given, e.g., by equation (7.41a) in Rybicki and Lightman (1979). An approximate general expression valid at any temperature is

$$y \simeq \ln(1 + 4\Theta + 16\Theta^2)\tau_{\rm T}^{\rm th}\left(1 + \frac{\tau_{\rm T}^{\rm th}}{3}\right) , \tag{16}$$

which reduces to the nonrelativistic form at $\Theta \ll 1$. (Note that eq. [7.41b] in Rybicki and Lightman 1979 for the extreme relativistic Compton parameter appears to have no physical interpretation and is inconsistent with the definition of y by the relation $\epsilon_f = e^y \epsilon_i$.)

In our numerical treatment, we assume that the injected nonthermal pairs cool until they reach energy $\gamma_{\rm th/nth} = 1 + 4\Theta$ at which point they are transferred (along with their energy) to the thermal pair distribution. The results do not depend sensitively on the exact value of the numerical constant in front of the factor Θ.

For low temperatures ($\Theta \lesssim 0.1$), $\dot\gamma_{\rm Coul}$ is roughly constant over a wide of range of pair energies (see eq. [5]). We can obtain an order-of-magnitude estimate of the dimensionless Coulomb cooling rate of the nonthermal pairs (above $\gamma_{\rm th/nth}$), $\ell_{\rm Coul}$, by bringing $\dot\gamma_{\rm Coul}$ outside the integrand and evaluating the integral at $\gamma = 1$,

$$\ell_{\rm Coul} \equiv -\frac{4\pi}{3}\frac{\sigma_{\rm T} R^2}{c}\int_{\gamma_{\rm th/nth}}^{\gamma_{\rm max}} \dot\gamma_{\rm Coul} N(\gamma)\, d\gamma \tag{17a}$$

$$\simeq 2\pi\tau_{\rm T}^{\rm th}\tau_{\rm T}^{\rm nth}\ln\epsilon_p^{-1} , \tag{17b}$$

where equation (17a) defines $\ell_{\rm Coul}$, and $\tau_{\rm T}^{\rm nth}$ is the Thomson optical depth of the nonthermal electrons and positrons,

$$\tau_{\rm T}^{\rm nth} = \sigma_{\rm T} R \int_{\gamma_{\rm th/nth}}^{\gamma_{\rm max}} N(\gamma) d\gamma \, . \tag{18}$$

The energy input from the Coulomb process to the thermal pairs (the last term in eq. [15]) also includes the contribution from nonthermal pairs with $\gamma < \gamma_{\rm th/nth}$. Assuming the nonthermal pairs with $\gamma < \gamma_{\rm th/nth}$ thermalize immediately (via Coulomb scattering), the additional energy input is given by

$$\frac{4\pi}{3}\frac{\sigma_T R^2}{c}\Big[\int_1^{\gamma_{\rm th/nth}} \gamma(Q+P)d\gamma + \gamma_{\rm th/nth}\int_{\gamma_{\rm th/nth}}^{\gamma_{\rm max}}(Q+P)d\gamma - \gamma_{\rm th}\int_1^{\gamma_{\rm max}}(Q+P)d\gamma\Big]\,. \tag{19}$$

Note that the term (19) can in principle be either negative or positive, depending on the form of $P+Q$. In all numerical cases we have considered (see § III), the term (19) is positive and much less than $\ell_{\rm Coul}$ of equation (17a).

To assess the relative importance of Coulomb heating of the thermal distribution, one should use the quantity $\ell_{\rm Coul}/\ell_e$. This quantity gives the fraction of the injected power that is transferred to the thermal distribution through Coulomb interactions. On the other hand, the relative importance of Coulomb cooling of pairs of the nonthermal distribution is determined by the fraction of the nonthermal power in both the primary and secondary pairs that is transferred via Coulomb interactions to the thermal component, which is approximately given by to use $\ell_{\rm Coul}/(\ell_e + \ell_{\rm pair})$. (The $\ell_{\rm pair}$ is defined by eq. [10], and Table 1 in § III lists the values of $\ell_{\rm Coul}/\ell_e$ and $\ell_{\rm pair}/\ell_e$.)

Thermal bremsstrahlung in a pair plasma has contributions from $e^{\pm}e^{\pm}$ and e^+e^- interactions. The nonthermal electrons emit bremsstrahlung while interacting with the thermal plasma and with themselves. As $\tau_{\rm T}^{\rm th} \gg \tau_{\rm T}^{\rm nth}$, the latter contribution is much less than the former. We treat bremsstrahlung in the way described in CB90. The Appendix describes a simple treatment of nonthermal bremsstrahlung at $\gamma \gg 1$.

The thermal bremsstrahlung self-absorption frequency ϵ_{sa}, defined by $\tau_{sa}(\epsilon_{sa}) = 1$, can be written as

$$\epsilon_{sa} = \tau_{\rm T}^{\rm th} \left\{ \frac{3\pi}{8} \frac{a_0}{R} \frac{1}{\Theta} \left[\frac{\epsilon \dot{n}_B^{\rm th} \sigma_{\rm T} R^2}{(\tau_{\rm T}^{\rm th})^2 c \alpha_f} \right] \right\}^{1/2} , \qquad (20)$$

where α_f is the fine-structure constant. The dimensionless factor in brackets is a function of ϵ and Θ only, and is of the order of unity at mildly relativistic temperatures. For $R = 10^7$ cm, $\epsilon_{sa} \sim 10^{-8}$. Since the self-absorbed part of the spectrum contains very little energy compared to the optically thin part, we assume $\dot{n}_B = 0$ below ϵ_{sa}. Self-absorption by nonthermal electrons can be neglected compared to that by the thermal ones (see Appendix).

III. Results

In this section, our numerical results are discussed and interpreted. We will discuss mostly those features in the spectra that are specific to photon-deficient plasmas. We refer the reader to LZ87 for discussion of spectra from nonthermal pair equilibrium plasmas with abundant soft photons.

We consider power-law pair injection, $Q(\gamma) = Q_0 \gamma^{-\Gamma}$ for $\gamma_{\rm min} \leq \gamma \leq \gamma_{\rm max}$. The dimensionless parameters that specify a model are ℓ_e, ℓ_s, $\Theta_{\rm bb}$, Γ, $\gamma_{\rm min}$, $\gamma_{\rm max}$, and $\beta_{\rm esc}$. In most models, we set $\beta_{\rm esc} = 0$. There is also a weak dependence on R through the Coulomb cooling rate (eqs. [5]-[6]), and the bremsstrahlung self-absorption energy (eq. [20]). We assume $R = 10^{14}$ cm and $\epsilon_{sa} = 10^{-9}$.

The main input and output quantities for the models presented in this section are given in Table 1. The quantities y, $\tau_{\rm T}^{\rm nth}$, $\ell_{\rm Coul}$, and $\ell_{\rm pair}$ are defined in equations (16), (18), (17a), and (10), respectively. The quantities ℓ_{2-10} and α_{2-10} are the 2-10 keV compactness and average energy spectral index, respectively. The dimensionless energy ϵ_* corresponds to $\tau_{\gamma\gamma}(\epsilon_*) = 1$. The model numbers in Table 1 correspond to the cases presented in Figures 1-7 below, and *i, ii, iii* correspond to the solid, dotted, and dashed curves, respectively.

Figures 1a, b, c present spectra from sources with power law electrons injected with the index $\Gamma = 2.5$. The compactnesses in the pair injection are (a) $\ell_e = 1$, (b) $\ell_e = 10^3$, and (c) $\ell_e = 30$. Solid curves in Figures 1a, b, c correspond to the only source of photons being bremsstrahlung. Bremsstrahlung radiation is emitted by both the thermal and nonthermal pairs. The dotted and dashed curves correspond to the addition of black body sources of soft photons with $\ell_s = 10^{-2}\ell_e$ and $\ell_s = \ell_e$, respectively (see eq. [2]).

At $\ell_e = 1$ and $\ell_s = 0$ (solid curve in Fig. 1a), the equilibrium temperature is relativistic, $\Theta \simeq 0.9$ as un-Comptonized nonrelativistic bremsstrahlung would radiate only $\ell \ll 1$ (e.g., Svensson 1986). There is little production of secondary pairs. The equilibrium Thomson optical depth of the thermal pairs is relatively small, $\tau_{\mathrm{T}}^{\mathrm{th}} \simeq 0.9$, and is due mostly to cooled primary pairs. The spectrum consists of three components: thermal bremsstrahlung, exponentially cutoff at $\epsilon > \Theta$; a pair annihilation spectrum (mostly thermal) peaked at $\epsilon \sim 1 + (3/2\text{–}3)\Theta$, (the factor in parentheses times Θ represents the average thermal kinetic energy); nonthermal bremsstrahlung, extending up to $\epsilon \sim \gamma_{\mathrm{max}}$. The bremsstrahlung components are shown in Figure 2. Comptonization has a relatively minor effect on the spectrum. The X-ray spectral index of $\alpha_x \sim 0$ is typical for bremsstrahlung. The optical depth of the nonthermal electrons is $\tau_{\mathrm{T}}^{\mathrm{nth}} \simeq 10^{-2} \ll 1$, and the amplitude of the nonthermal bremsstrahlung is much less than that of the thermal one. The thermal electrons are heated by both Compton and Coulomb interactions. Coulomb interactions dominate and transfer about one third of the injected power to the thermal electrons.

The dotted curve in Figure 1a gives the spectrum corresponding to an additional source of blackbody photons at $\Theta_{\rm bb} = 10^{-4}$ with a compactness, ℓ_s, one hundredth the electron compactness, l_e. The $\epsilon \lesssim 1$ spectrum is dominated by the blackbody photons singly scattered by the nonthermal pairs and repeatedly Compton upscattered by the thermal pairs. The 2-10 keV spectral index is $\alpha_{2-10} \simeq 0.5$. The equilibrium temperature is now lower, $\Theta \simeq 0.5$. There is an annihilation feature, which is mostly due to annihilation of pairs from the primary injection, Q, after they have thermalized. At $\epsilon \gg 1$, the spectrum consists of both nonthermal bremsstrahlung emission and upscattered blackbody and X-ray power law photons.

Spectra with parameters similar to those corresponding to the dotted curve were discussed by ZL86. They predicted the spectra to be of the broken power law form with an $\alpha_x < 1$ power law joining onto a steeper $\alpha_\gamma > 1$ power law at $\epsilon \sim 1$. In contrast, our results give a sharp drop of a factor of ~ 10 in the spectrum beyond the annihilation spectrum. The amplitude of the γ-ray power law is reduced by that factor. This is due to the effect of efficient Coulomb cooling ($\ell_{\rm Coul} \simeq 0.3\ell_e$) that affects mostly mildly relativistic nonthermal electrons and reduces their Thomson optical depths to $\tau_{\rm T}^{\rm nth} \ll 1$.

The dashed curve corresponds to a large amplitude of the blackbody photons, $\ell_s = \ell_e$. The resulting spectrum is a "classical" one, with an X-ray and γ-ray power law corresponding to the first order Compton scattering by the nonthermal electrons (see, e.g., LZ87, Svensson 1987). There is also a relatively small component due to Compton upscattering of the blackbody photons by the thermal component, directly following the blackbody spectrum. There is a distinct annihilation feature due to annihilation of the pairs of the primary injection (Q).

Figure 1b shows three cases with the same ratios ℓ_s/ℓ_e, but with a large $\ell_e = 10^3$. The equilibrium optical depths of the thermal pairs are large, which has rather dramatic effects on the spectra. The equilibrium temperatures are now much smaller due to the effect of large $\tau_{\rm T}^{\rm th}$. (A large $\tau_{\rm T}^{\rm th}$ causes a diffusive enhancement of the density of soft photons as well as a softening of their distribution and thus increases the cooling rate of pairs.) The solid curve corresponding to $\ell_s = 0$ gives heavily thermally Comptonized bremsstrahlung spectrum with a Wien peak at $\epsilon \sim 3\Theta \simeq 0.2$. The Wien peak is followed by an annihilation feature and a low-amplitude nonthermal bremsstrahlung spectrum. As some blackbody photons are added to the source (dotted curve), the equilibrium temperature decreases and the Wien peak shifts to lower energies. It is now followed by a dip due to Compton downscattering by the thermal electrons. Note that those spectra also differ from those of ZL86, mostly due to the effect of thermal Comptonization, which was not included in that analysis. When $\ell_s = \ell_e$ (dashed curve) the Wien peak disappears and there is a nonthermal X-ray power law followed by the downscattering dip (cf., e.g., LZ87).

Figure 1c shows cases intermediate between those of Figures 1a and 1b, with an electron compactness of $\ell_e = 30$. The Wien peak in the solid curve ($\ell_s = 0$) coincides with the annihilation feature. The Wien peak at $\ell_s = 0.01\ell_e$ (dotted curve) and the downscattering dip at $\ell_s = \ell_e$ (dashed curve) are much weaker than at $\ell_e = 10^3$.

Note that the dotted spectrum is approximately a broken power law, with a break around 100 keV ($\epsilon \simeq 0.2$). There is a weak annihilation feature superimposed on the γ-ray power law. This spectrum resembles some γ-ray burst spectra (see § IV and, e.g., Figs. 1a, b in Zdziarski 1987).

Figure 3 shows the same cases as Figure 1c, but with $\Gamma = 1.5$. The changed Γ has little effect on the $\epsilon \lesssim 1$ spectra at $\ell_s = 0$ (solid curve) and $\ell_s = 0.01\ell_e$ (dotted curve), with repeated Compton scattering by thermal pairs dominating. In this case, the $\epsilon \gtrsim 1$ spectra are much harder than for $\Gamma = 2.5$, reflecting the hardened distributions of the injected nonthermal electrons. Again, the $\ell_s = 0.01\ell_e$ spectrum resembles the classical γ-ray burst spectra (see § IV). The $\ell_s = \ell_e$ spectrum is dominated by the first order Compton scattering by nonthermal electrons (see, e.g., LZ87).

Figure 4 shows the effect of changing Γ in an $\ell_s \ll \ell_e$ case. The spectrum up to the annihilation peak remains unaffected, as it is mostly thermal. Only the shape of the high energy γ-ray spectrum changes. It becomes steeper and of lower amplitude as Γ increases. Changing Γ in the $\ell_s = \ell_e$ case has a much more pronounced effect, as can be seen in Figures 1c and 3 above, and in, e.g., LZ87. In that case, the overall slope of the spectrum steepens with increasing Γ (see, e.g., LZ87). The downscattering dip becomes more pronounced with increasing Γ, as $\tau_{\mathrm{T}}^{\mathrm{th}}$ increases as well.

Figure 5 shows the effect of changing γ_{max} at $\ell_s = 0.01\ell_e$ and $\ell_e = 100$. The $\epsilon \lesssim 1$ spectrum remains unchanged with changing γ_{max}, which is a consequence of the dominance of the thermal component. Only the cutoff in the γ-ray spectrum moves, with $\epsilon_{\mathrm{max}} \simeq \gamma_{\mathrm{max}}$.

Figure 6 shows the effect of escape of thermal pairs at low compactness, $\ell_e = 1$, and $\ell_s \ll \ell_e$. The equilibrium optical depth of the thermal pairs is reduced by a large factor as escape is a faster process than pair annihilation. As the escaping pairs carry away a large fraction of the injected energy, in both kinetic and rest mass form, the luminosity in photons is reduced by a factor of a few. At larger compactnesses, pair escape has no effect as then pair annihilation is faster (see eq. [14]).

Figure 7 shows the effect of changing the value of the low energy cutoff, $\gamma_{\rm min}$, in the injected distribution in the case of steep injection, $\Gamma = 2.5$. As an increase of $\gamma_{\rm min}$ at constant $\ell_e =$ gives more nonthermal pairs at high energies, the amplitude of the γ-ray spectrum increases as well. Additionally, the total number of injected pairs decreases with increasing $\gamma_{\rm min}$, which causes a reduction in the equilibrium Thomson optical depth of the thermal plasma and a corresponding reduction in the cooling rate of the nonthermal electrons. Note that at $\gamma_{\rm min} = 5$–10 the spectrum is of an approximate broken power law form, similar to the spectra of classical γ-ray bursts (see § V). (In models with the first order Compton scattering dominating, $\ell_s \gtrsim \ell_e$, changing $\gamma_{\rm min}$ results in a changing break in the spectrum at $\sim {\gamma_{\rm min}}^2\Theta$).

Figure 8 shows examples of the steady state nonthermal pair distributions. The distributions correspond to the photon spectra shown in Figure 1c, with $\ell_e = 30$. The distributions are cut off at $\gamma_{\rm th/nth}$, as discussed in § II. The distributions in the two photon-starved cases (solid and dotted line, with $\ell_s/\ell_e = 0$ and 10^{-2}, respectively) have slopes approximately given by $p \simeq \Gamma + \alpha_x$, where $N(\gamma) \propto \gamma^{-p}$ and α_x is the X-ray power law index. This is due to electron cooling dominated by the upscattered X-ray and UV photons, see, e.g., ZL86. Note that most of the scatterings are in the Thomson ($\epsilon\gamma \lesssim 1$) regime. The dashed line corresponds to the case with abundant soft photons, in which $p \simeq \Gamma + 1$ (see, e.g., Blumenthal and Gould 1970).

Finally, Figure 9 plots some of the dependences of the source parameters Θ, $\tau_{\rm T}^{\rm th}$, $\tau_{\rm T}^{\rm nth}$, y, Y, and $\ell_{\rm Coul}/\ell_e$ on the soft photon ratio, ℓ_s/ℓ_e, for the input parameters corresponding to Figures 1c and 8 ($\ell_e = 30$, $\Gamma = 2.5$, $\gamma_{\rm min} = 1.6$).

The plasma temperature (crosses), and the Compton parameter (open cirles) decline quickly with increasing ℓ_s/ℓ_e due to increasing cooling on the soft photons. A corresponding decline in the pair yield (filled circles) is due to the general softening of the spectrum with much fewer photons above the threshold for pair production for large ℓ_s/ℓ_e (see Fig. 1c). The thermal optical depth (open squares) is almost constant, as the bulk of thermal pairs are primary ones from the steep primary injection with low $\gamma_{\rm min}$ (see eqs. [8], [13]). The low value of $\gamma_{\rm min}$ and $\Gamma > 2$ is also responsible for the relatively large $\ell_{\rm Coul}/\ell_e$ (triangles) even at $\ell_s/\ell_e = 1$. Most of the nonthermal power is injected at $\gamma_{\rm min} = 1.6$, where the Coulomb losses are large compared to the Compton ones. Effective Compton and Coulomb cooling is responsible for the low values of $\tau_{\rm T}^{\rm nth}$ (filled squares).

Analysis of the values of $\ell_{\rm Coul}/\ell_e$ and $\ell_{\rm pair}/\ell_e$ in Table 1 shows that Coulomb process is important for heating the thermal pairs and cooling nonthermal ones in a wide range of parameters. (The relative importance of Coulomb heating of the thermal distribution is given by $\ell_{\rm Coul}/\ell_e$, and the importance of Coulomb cooling of the nonthermal distribution, by $\ell_{\rm Coul}/(\ell_e + \ell_{\rm pair})$, see § III.) The Coulomb process is always important when $\ell_s/\ell_e \ll 1$, even at large ℓ_e, although the values of $\ell_{\rm Coul}/\ell_e$ and $\ell_{\rm Coul}/(\ell_e + \ell_{\rm pair})$ diminish with increasing ℓ_e. Coulomb interactions are negligible in most cases for $\ell_s/\ell_e \gtrsim 1$ (cf. eq. [6]). The case when it *is* important for $\ell_s/\ell_e = 1$ is for low ℓ_e and $\Gamma > 2$ (model 1aiii).

IV. Discussion and Conclusions

We have studied relativistic plasmas where energy is supplied in the form of relativistic nonthermal electron-positron pairs and soft photons. The plasma in steady state consists of the thermalized pairs and the nonthermal pairs in the process of cooling. We have considered situations where the power injected in the soft photons is much less than that in the relativistic pairs, i.e., photon-starved plasmas. Our main conclusions can be summarized as follows.

(i) The overall form of the spectra from nonthermal pair-starved plasmas consists of: a rising (νF_ν) spectrum at low energies with $\alpha_x \sim 0$, a single or double peak in the 0.1–1 MeV energy range, a cutoff above the peak, and a γ-ray tail with a varying slope depending on the plasma parameters.

(ii) The low energy power law is mostly due to the primary soft photons being repeatedly upscattered by the hot thermal electrons. The equilibrium temperature of the thermal electrons we have found is in the $\Theta \simeq 0.02$–1 (10 keV to 0.5 MeV) range (see Table 1 except the photon abundant $\ell_s/\ell_e = 1$ cases). The temperature increases with decreasing ℓ_e and ℓ_s/ℓ_e. The relatively narrow range of temperature is due to the efficiency of Comptonization increasing greatly at relativistic energies (see, e.g., Rybicki and Lightman 1979) and the rapid increase of the pair production rate at relativistic temperatures (pair thermostat, see, e.g., Svensson 1984). The Comptonization parameter y is > 1 (see Table 1), which results in hard spectra followed by Wien peaks. This peak is either followed or amplified by the one due to annihilation photons, at 0.5–1 MeV photon energies. The low energy power laws followed by the Wien peaks have largely thermal character and resemble those from thermal plasmas in pair equilibrium (see, e.g., Zdziarski 1984, 1985).

(iii) The γ-ray tail is due to Compton scattering by the nonthermal electrons and nonthermal bremsstrahlung. As the optical depth of the nonthermal electrons is much less than unity due to Coulomb (see [v] below) and Compton cooling, the amplitude of the tail is much below that of the spectrum at lower energies. This results in a characteristic cutoff around 1 MeV. At large ℓ_e, absorption in pair-producing photon-photon collisions further attenuates the γ-ray spectrum.

(iv) Bremsstrahlung is a source of soft photons always present in plasmas. In the absence of external (or synchrotron) soft photons and at small compactnesses, the emitted spectra consist of thermal bremsstrahlung dominating at low energies, a pair annihilation feature at $\epsilon \sim 1 + 3\Theta$, and nonthermal bremsstrahlung dominating at high energies. At large compactnesses, the spectrum is mostly due to Comptonized thermal bremsstrahlung. The nonthermal bremsstrahlung emission is largely downscattered by the optically thick thermal pairs and absorbed in the process of photon-photon pair production.

(v) Coulomb interactions are important in transferring energy from the nonthermal pairs to the thermal component of the plasma. The importance of this process increases with decreasing pair compactness, ℓ_e, decreasing external soft photon input, ℓ_s, and increasing power law injection index, Γ (see Table 1). The relative importance of the Coulomb energy loss for an electron increases with decreasing γ. Coulomb interactions can transfer as much as one half of the power injected in primary nonthermal pairs to the thermal plasma. A consequence of the importance of Coulomb energy transfer is the small nonthermal Thomson depth ($\tau_{\mathrm{T}}^{\mathrm{nth}} \ll 1$) in photon-starved plasmas.

V. Comparison with Observations of Compact Objects

Some of the spectra from photon-starved plasmas resemble the spectra of classical γ-ray bursts. The continuum energy spectrum of those γ-ray bursts is roughly a broken power law $F_E \propto E^{-\alpha}$, with an X-ray spectral index $\alpha_x \sim 0$ and a γ-ray spectral index α_γ varying from $\sim$ 0.5–2 (Epstein 1986; Zdziarski

1987). The transition between the two regimes occurs between 100 keV and 1 MeV, suggesting some link between the shape of γ-ray burst spectra and the rest mass-energy of the electron. The Solar Maximum Mission data, which extend to $\sim$ 5–10 MeV or more, show no clear high energy cut-offs (Matz *et al.* 1985). The spectra shown in dotted curve in Figure 1c, and dotted and dashed curves in Figure 7 do show the broken power law form.

On the other hand, the X-ray and γ-ray spectral indices for those spectra ($\alpha_x \sim 0.4$, $\alpha_\gamma \sim 1$) are perhaps slightly larger than those of typical bursts (Epstein 1986; Zdziarski 1987). Also, spectra from photon-starved plasmas require fine-tuning in order to reproduce the classical γ-ray burst spectra above a few hundred keV. Typical X-ray spectra from photon-starved plasmas do reproduce the $\alpha_x \sim 0$ X-ray power laws of γ-ray bursts, but those are then followed by spectral cutoffs by an order of magnitude at $\sim$ 1 MeV (see § III). This is not seen in the spectra of classical γ-ray bursts.

The so called "soft γ-ray repeaters" (SGRs) have spectra much softer than those of the classical γ-ray bursts. Those bursts include SGR 0526-66, the source of the 1979 March 5 event (Mazets *et al.* 1979, Cline *et al.* 1980), SGR1900+14 (Mazets *et al.* 1982), and SGR 1806-20, the source of the 1979 January 7 event (Laros *et al.* 1986, Atteia *et al.* 1987, Laros *et al.* 1987, Kouveliotou *et al.* 1987). The bursts from these sources typically have color temperatures $\sim$ 50 keV, much less than that of other γ-ray bursts. Some of the spectra from photon-starved plasmas with large compactness may resemble those of soft γ-ray repeaters (see, e.g., the dotted curve in Fig. 1b).

Spectra from photon-starved plasmas are different from the typical X-ray spectra of active galactic nuclei, which have $\alpha_x \sim 0.7$ (e.g., Mushotzky 1984). However, the few AGN observed in soft γ-rays exhibit characteristic peaks at $\sim$ 1

MeV. It is possible that such peaks are typical of most of AGN, as it does not violate the constraints imposed by the cosmic γ-ray background (e.g., Bassani *et al.* 1985). In fact, a similar MeV peak followed by a steep power law is seen in the isotropic cosmic background. Such peaks are characteristic of photon-starved plasmas and could come from AGN source components different than those responsible for the X-ray continua.

On the other hand, photon-starved plasmas can also explain spectra of AGN that are harder than $\alpha_x = 0.5$ (e.g., Mushotzky 1984). Such spectra cannot be explained by either the nonthermal synchrotron model or first order Compton cooling models (see, e.g., Svensson and Zdziarski 1989).

Acknowledgments

This research was supported in part by NASA Grants NAGW-830 (Chicago), NAGW-1301 (Caltech), and NSF Grants AST 86-15325 and AST 84-51725 (Caltech). Two of us (DQL and AAZ) are grateful for the warm hospitality of the Aspen Center for Physics, where part of this work was carried out. The authors acknowledge valuable comments and discussions with Roger Blandford, Alan Lightman, and Roland Svensson.

Appendix

Relativistic Nonthermal Bremsstrahlung

We use the bremsstrahlung cross section in the relativistic limit, $\gamma \gg 1$. It applies in the same form to $e^{\pm}p$, $e^{\pm}e^{\pm}$ and $e^{+}e^{-}$ interactions. Here p denotes protons. In the laboratory frame,

$$\frac{d\sigma_B}{d\epsilon} = \frac{3\alpha_f}{2\pi}\sigma_{\rm T}\frac{d\epsilon}{\epsilon}\frac{\gamma'}{\gamma}\left(\frac{\gamma'}{\gamma}+\frac{\gamma}{\gamma'}-\frac{2}{3}\right)\left(\ln\frac{2\gamma\gamma'}{\epsilon}-\frac{1}{2}\right), \tag{A1}$$

Here, γ' denotes the electron Lorentz factor after the photon emission, $\gamma' = \gamma - \epsilon$. In the case of $e^{\pm}e^{\pm}$ and $e^{+}e^{-}$ interactions, this cross section gives the radiation from the fast electron only.

In treating the interactions of nonthermal pairs with themselves, we follow the approach of Zdziarski (1980). Using the fact that relativistic electrons emit radiation predominantly in the forward direction, we obtain

$$\dot{n}_B^{\rm nth,self}(\epsilon) = \frac{1}{2}2c\int_{\max(\gamma_{\rm th},\epsilon+1)}^{\gamma_{\max}} N(\gamma_1)\frac{d\sigma_B}{d\epsilon_L}\frac{d\epsilon_L}{d\epsilon}d\gamma_1\int_{\gamma_{\rm th}}^{\gamma_{\max}} N(\gamma_2)d\gamma_2\int_0^1 \mu d\mu\,. \tag{A2}$$

Here, ϵ_L, and ϵ are the laboratory frame and the plasma frame photon energies, respectively, $\mu = (1-\cos\vartheta)/2$, ϑ is the collision angle, and $d\sigma_B$ is a function of $\gamma_L = 2\mu\gamma_1\gamma_2$. Photons at energy ϵ are radiated by electrons at γ_1. The factors (1/2) and 2 above account for the double counting of identical particles and the fact that both colliding particles radiate photons, respectively. The colinearity of the radiation emitted by relativistic pairs leads to the relation, $\epsilon_L/\gamma_L = \epsilon/\gamma_1$. Except for the logarithmic term, the cross section (A1) is a function of the factor ϵ/γ, which is invariant. Only the factor γ in the argument of the logarithm is not invariant. Taking into account that $\ln\gamma_L = \ln\gamma_1 + \ln\gamma_2 + \ln 2\mu$, and neglecting the weak dependence on collision angle, we obtain the approximate relationship,

$$d\sigma(\gamma_L) \simeq d\sigma(\gamma_1) + d\sigma(\gamma_2)\,, \tag{A3}$$

The photon production rate (A2) then simplifies to,

$$\dot{n}_B^{\mathrm{nth,self}}(\epsilon) = 2\tau_{\mathrm{T}}^{\mathrm{nth}}\frac{c}{\sigma_{\mathrm{T}}R}\int_{\max(\gamma_{\mathrm{th}},\epsilon+1)}^{\gamma_{\max}} N(\gamma)\frac{d\sigma_B}{d\epsilon}d\gamma\,. \tag{A4}$$

In treating the interactions of nonthermal pairs with the thermal pairs, we take the thermal particles to be at rest, and integrate the cross section (A1) over the distribution $N(\gamma)$. Using equation (A4), we can write the nonthermal bremsstrahlung emissivity from both self-interactions and interactions with thermal pairs in the compact form,

$$\dot{n}_B^{\mathrm{nth}}(\epsilon) = \frac{c}{\sigma_{\mathrm{T}}R}(\tau_{\mathrm{T}}^{\mathrm{th}} + 2\tau_{\mathrm{T}}^{\mathrm{nth}})\int_{\max(\gamma_{\mathrm{th}},\epsilon+1)}^{\gamma_{\max}} N(\gamma)\frac{d\sigma_B}{d\epsilon}d\gamma\,. \tag{A5}$$

The fact that bremsstrahlung from relativistic electrons interacting with themselves is twice as large as that from relativistic electrons interacting with nonrelativistic particles having the same density was noted earlier in the particular case of relativistic thermal plasmas (see, e.g., Haug 1975; Zdziarski 1980). Here we see that it also applies to relativistic nonthermal plasmas. The origin of this general property is the logarithmic dependence on γ of the cross section (A1), which leads to the relationship (A3).

We obtain the bremsstrahlung cooling rate by integrating the cross section (A1) (e.g., Blumenthal and Gould 1970), and taking into account the result (A5),

$$\dot{\gamma}_B = -\frac{3\alpha_f}{2\pi}\frac{c}{R}\left(\tau_{\mathrm{T}}^{\mathrm{th}} + 2\tau_{\mathrm{T}}^{\mathrm{nth}}\right)\left(\ln 2\gamma - \frac{1}{3}\right)\,. \tag{A6}$$

The self-absorption frequency for nonthermal bremsstrahlung is given by a formula analogous to equation (20), but with $\tau_{\rm T}^{\rm th}$ replaced by $(\tau_{\rm T}^{\rm th}\tau_{\rm T}^{\rm nth})^{1/2}$ and Θ replaced by the factor $\sim \gamma$ (~ 1), appropriate to the lowest energy nonthermal electrons which dominate the nonthermal bremsstrahlung emission. Since thermal bremsstrahlung emission typically dominates over the nonthermal bremsstrahlung at $\epsilon \ll 1$, so does thermal bremsstrahlung self-absorption.

References

Atteia, J.-L., *et al.*, 1987. *Astrophys. J. (Letters),* **320**, L105.

Bassani, L., Dean, A.J., Di Cocco, G., & Perotti, F., 1985. In: *Active Galactic Nuclei*, p. 252, ed Dyson, J., Manchester University Press, Manchester.

Blumenthal, G.R. & Gould, R.J., 1970. *Rev. Mod. Phys.,* **42**, 237.

Cline, T.L., *et al.*, 1980. *Astrophys. J. (Letters),* **237**, L1.

Coppi, P.S., 1990. Caltech Theoretical Astrophysics Preprint GRP-209, submitted to *Mon. Not. R. astr. Soc.*

Coppi, P.S. & Blandford, R.D., 1990. *Mon. Not. R. astr. Soc.,* **245**, 453.

de Kool, M. & Begelman, M.C., 1989. *Astrophys. J.,* **345**, 135.

Done, C. & Fabian, A.C., 1989. *Mon. Not. R. astr. Soc.,* **240**, 81.

Epstein, R.I., 1986. In: *Radiation Hydrodynamics in Stars and Compact Objects, IAU Coll. No. 89*, p. 305, eds Mihalas, D. & Winkler, K.-H. A., Springer-Verlag, Berlin.

Fabian, A.C., Blandford, R.D., Guilbert, P.W., Phinney, E.S., & Cuellar, L., 1986. *Mon. Not. R. astr. Soc.,* **221**, 931.

Gould, R.J., 1975. *Astrophys. J.,* **196**, 689.

Guilbert, P.W., Fabian, A.C., & Rees, M., 1983. *Mon. Not. R. astr. Soc.,* **205**, 593.

Haug, E., 1975. *Naturforsch,* **30a**, 1546.

Kouveliotou, C., *et al.*, 1987. *Astrophys. J. (Letters),* **322**, L21.

Laros, J.G., *et al.*, 1986. *Nature,* **322**, 152.

Laros, J.G., *et al*, 1987. *Astrophys. J. (Letters),* **320**, L111.

Lightman, A.P. & Zdziarski, A.A., 1987. *Astrophys. J.,* **319**, 643.

Marshall, H., *et al.*, 1980. *Astrophys. J.,* **235**, 4.

Matz, S.M., Forrest, D.J., Vestrand, W.T., Chupp, E.L., Share, G.H., & Rieger, E., 1985. *Astrophys. J. (Letters),* **288**, L37.

Mazets, E.P., Golenetskii, S.V., Gur'yan, Yu.A., & Il'inskii, V.N., 1982. *Astrophys. Space Sci.,* **84**, 173..

Mazets, E.P., Golenetskii, S.V., Il'inskii, V.N., Aptekar', R.L., & Guryan, Yu.A., 1979. *Nature,* **282**, 587.

Mushotzky, R.F., 1984. *Adv. Space Res.*, **3**, Nos. 10–12, p. 157.

Rybicki, G. & Lightman, A.P., 1979. *Radiative Processes in Astrophysics*, John Wiley & Sons, New York.

Svensson, R., 1982. *Astrophys. J.,* **258**, 321.

Svensson, R., 1984. *Mon. Not. R. astr. Soc.,* **209**, 175.

Svensson, R., 1986. In: *Radiation Hydrodynamics in Stars and Compact Objects, IAU Coll. No. 89*, p. 325, eds Mihalas, D. & Winkler, K.-H. A., Springer-Verlag, Berlin.

Svensson, R., 1987. *Mon. Not. R. astr. Soc.,* **227**, 403.

Svensson, R. & Zdziarski, A.A., 1989. In: *STScI-GSFC Workshop on Ultra-Hot Plasmas and Electron-Positron Pairs in Astrophysics*, p. 1, eds Zdziarski, A.A. & Kazanas, D., STScI Publ., Baltimore.

Zdziarski, A.A., 1980, N. Copernicus Astronomical Center No. 115, preprint.

Zdziarski, A.A., 1984. *Astrophys. J.,* **283**, 842.

Zdziarski, A.A., 1985. *Astrophys. J.,* **289**, 514.

Zdziarski, A.A., 1987. In: *Proceedings of the 13th Texas Symposium on Relativistic Astrophysics*, p. 553, ed Ulmer, M., World Scientific Press, Singapore.

Zdziarski, A.A., 1988. *Astrophys. J.,* **335**, 786.

Zdziarski, A.A. & Lamb, D.Q., 1986. *Astrophys. J. (Letters),* **309**, L79.

Zdziarski, A.A. & Lamb, D.Q., 1986b. *Adv. Space Res.*, **6**, No. 4, 85.

Zdziarski, A.A. & Lightman, A.P., 1985. *Astrophys. J. (Letters),* **294**, L79.

Zdziarski, A.A. & Lightman, A.P., 1987. In: *Proceedings of Workshop on Variability in Galactic and Extragalactic X-ray Sources*, p. 121, ed Treves, A., Associazione per l'Avanzamento dell'Astronomia, Milan.

Figure Captions

Figure 1. Effect of varying external soft photon injection for steep pair injection, $\Gamma = 2.5$. The solid curves has no external soft photon injection, i.e., all photons come from bremsstrahlung. The dotted curves have $\ell_s = 10^{-2}\ell_e$, while the dashed curves have $\ell_s = \ell_e$. Models in a) have $\ell_e = 1$; models in b) have $\ell_e = 10^3$; and models in c) have $\ell_e = 30$. The other input and output model parameters are given in Table 1 (models 1a, b, c; i, ii, iii).

Figure 2. The thermal (dotted curve) and nonthermal (dashed curve) bremsstrahlung contribution to the spectrum of the solid curve in Fig. 1a.

Figure 3. The effect of varying external soft photon injection for flat pair injection, $\Gamma = 1.5$. The solid, dotted, and dashed curves correspond to $\ell_s/le = 0$, 10^{-2}, and 1, respectively. The input and output parameters are given in Table 1, models 3i, ii, iii.

Figure 4. The effect of varying Γ in an $\ell_s = 10^{-3}\ell_e$ case. The solid, dotted, and dashed curves correspond to $\Gamma = 1, 2, 3$, respectively. See Table 1, models 4i, ii, iii for the parameters.

Figure 5. The effect of varying $\gamma_{\rm max}$ in an $\ell_s = 10^{-2}\ell_e$ case. The solid, dotted, and dashed curves correspond to $\gamma_{\rm max} = 10$, 10^2, 10^3, respectively. See Table 1, models 5i, ii, iii for the parameters.

Figure 6. The effect of pair escape in a low compactness, $\ell_e = 1$, case. The solid curve corresponds to escape of thermal pairs with $\beta_{\rm esc} = 0.3$ whereas the dotted curve is for the same parameters but $\beta_{\rm esc} = 0$. See Table 1, models 6i, 1aii for the parameters.

Figure 7. The effect of varying $\gamma_{\rm min}$ in an $\ell_s = 10^{-2}\ell_e$ case. The solid, dotted, and dashed curves correspond to $\gamma_{\rm min} = 1.6$, 5, 10, respectively. See Table 1, models 1cii, 7ii, iii, for the parameters.

Figure 8. The steady state pair distributions corresponding to the photon spectra shown in Fig. 1c.

Figure 9. Dependence of Θ (crosses), $\tau_{\rm T}^{\rm th}$ (open squares), $\tau_{\rm T}^{\rm nth}$ (filled squares), the Compton parameter y (open cirles), the pair yield Y (filled circles), and $\ell_{\rm Coul}/\ell_e$ (triangles) on ℓ_s/ℓ_e for $\ell_e = 30$. Other plasma parameters correspond to the cases given in Figures 1c and 8.

Table 1
Results for the Models Presented

ℓ_e	ℓ_s/ℓ_e	$\gamma_{\rm max}$	Γ	Θ_{bb}	Θ	$\tau_{\rm T}^{\rm th}$	$\tau_{\rm T}^{\rm nth}$	y	Y	$\ell_{\rm Coul}/\ell_e$	α_{2-10}	ℓ_{2-10}/ℓ_e	ϵ_*	model
1	0	10^3	2.5	-	0.91	0.94	0.0078	3.6	0.0069	0.34	0.06	0.0031	$> 10^3$	1ai,2i
1	10^{-2}	10^3	2.5	10^{-4}	0.51	0.73	0.0069	1.8	0.0056	0.34	0.51	0.030	$> 10^3$	1aii,6ii
1	1	10^3	2.5	10^{-4}	0.098	0.56	0.0051	0.29	0.0015	0.37	1.36	0.13	400	1aiii
10^3	0	10^3	2.5	-	0.081	25	0.10	83	0.25	0.31	-0.21	0.0017	1	1bi
10^3	10^{-2}	10^3	2.5	10^{-4}	0.016	20	0.033	10	0.090	0.12	-0.44	0.11	1	1bii
10^3	1	10^3	2.5	10^{-4}	0.0011	18	0.011	.56	0.025	0.044	2.11	0.26	1	1biii
30	0	10^3	2.5	-	0.30	4.7	0.037	16	0.19	0.48	0.00	0.0027	3	1ci
30	10^{-2}	10^3	2.5	10^{-4}	0.11	3.4	0.032	3.6	0.048	0.45	0.36	0.047	5	1cii,7i
30	1	10^3	2.5	10^{-4}	0.012	3.0	0.013	0.29	0.011	0.24	1.06	0.18	11	1ciii
30	0	10^3	1.5	-	0.52	3.6	0.055	17	0.16	0.55	-0.02	0.046	6	3i
30	10^{-2}	10^3	1.5	10^{-4}	0.15	3.3	0.037	4.7	0.10	0.35	0.42	0.039	5	3ii
30	1	10^3	1.5	10^{-4}	0.016	1.7	0.0087	0.18	0.054	0.090	0.70	0.10	9	3iii
10^2	10^{-3}	10^3	1	10^{-4}	0.16	6.0	0.082	13	0.24	0.56	0.06	0.0061	2	4i
10^2	10^{-3}	10^3	2	10^{-4}	0.15	6.4	0.074	14	0.19	0.54	0.05	0.0066	2	4ii
10^2	10^{-3}	10^3	3	10^{-4}	0.11	7.6	0.053	13	0.087	0.54	0.04	0.0077	2	4iii
10^2	10^{-2}	10	2.5	10^{-3}	0.11	7.4	0.053	13	0.067	0.45	0.06	0.010	2	5i
10^2	10^{-2}	10^2	2.5	10^{-3}	0.12	7.0	0.060	13	0.11	0.49	0.07	0.0095	2	5ii
10^2	10^{-2}	10^3	2.5	10^{-3}	0.12	6.9	0.062	12	0.12	0.50	0.08	0.0094	2	5iii
1	10^{-2}	10^3	2.5	10^{-4}	0.88	0.18	0.027	0.54	0.00034	0.20	0.58	0.015	$> 10^3$	6i
30	10^{-2}	10^3	2.5	10^{-4}	0.14	2.5	0.044	3.0	0.072	0.44	0.38	0.043	5	7ii
30	10^{-2}	10^3	2.5	10^{-4}	0.15	2.3	0.042	2.8	0.090	0.39	0.40	0.040	5	7iii

Notes: $\gamma_{\rm min} = 1.6$, $R = 10^{14}$ cm, $\epsilon_{sa} = 10^{-9}$, $\beta_{\rm esc} = 0$ in all models except: model 6i where $\beta_{\rm esc} = 0.3$ and the luminosity emitted in escaping photons $\ell_{\rm em} = 0.31$; model 7ii where $\gamma_{\rm min} = 5$; and model 7iii where $\gamma_{\rm min} = 10$.

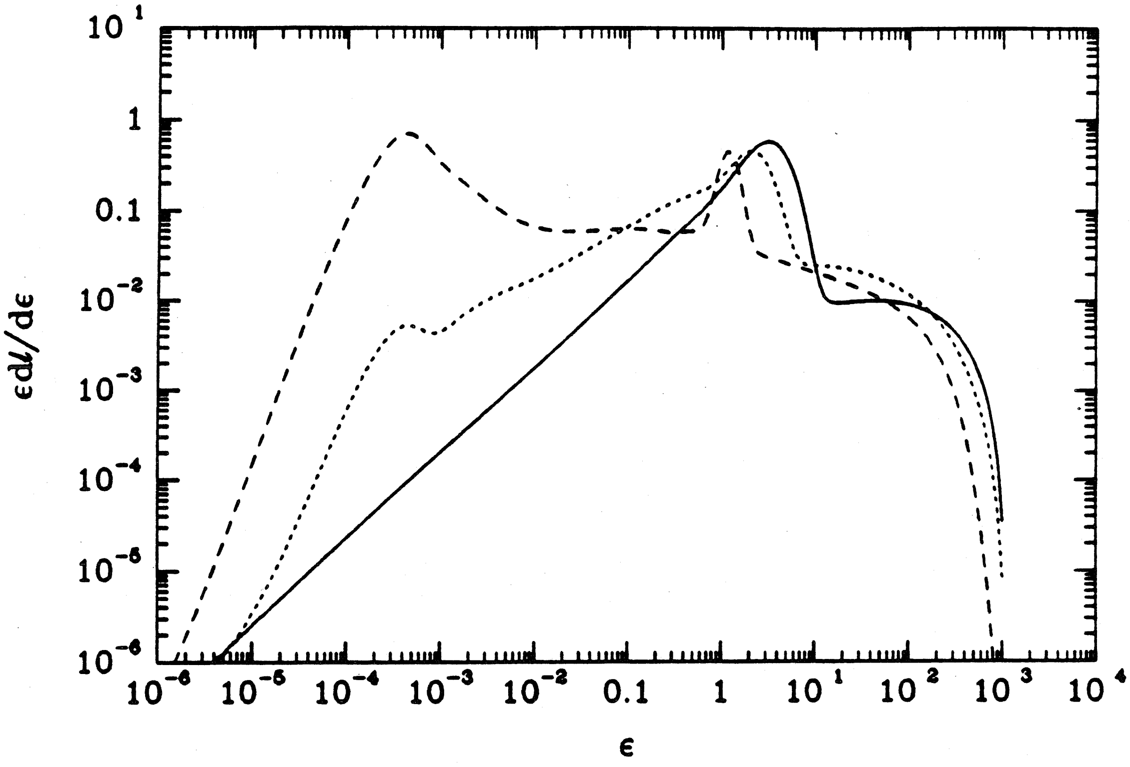

10^{1}
1
0.1
10^{-2}
10^{-3}
10^{-4}
10^{-5}
10^{-6}
$\epsilon d\ell/d\epsilon$
10^{-6}
10^{-5}
10^{-4}
10^{-3}
10^{-2}
0.1
1
10^{1}
10^{2}
10^{3}
10^{4}
ϵ

Figure 1a

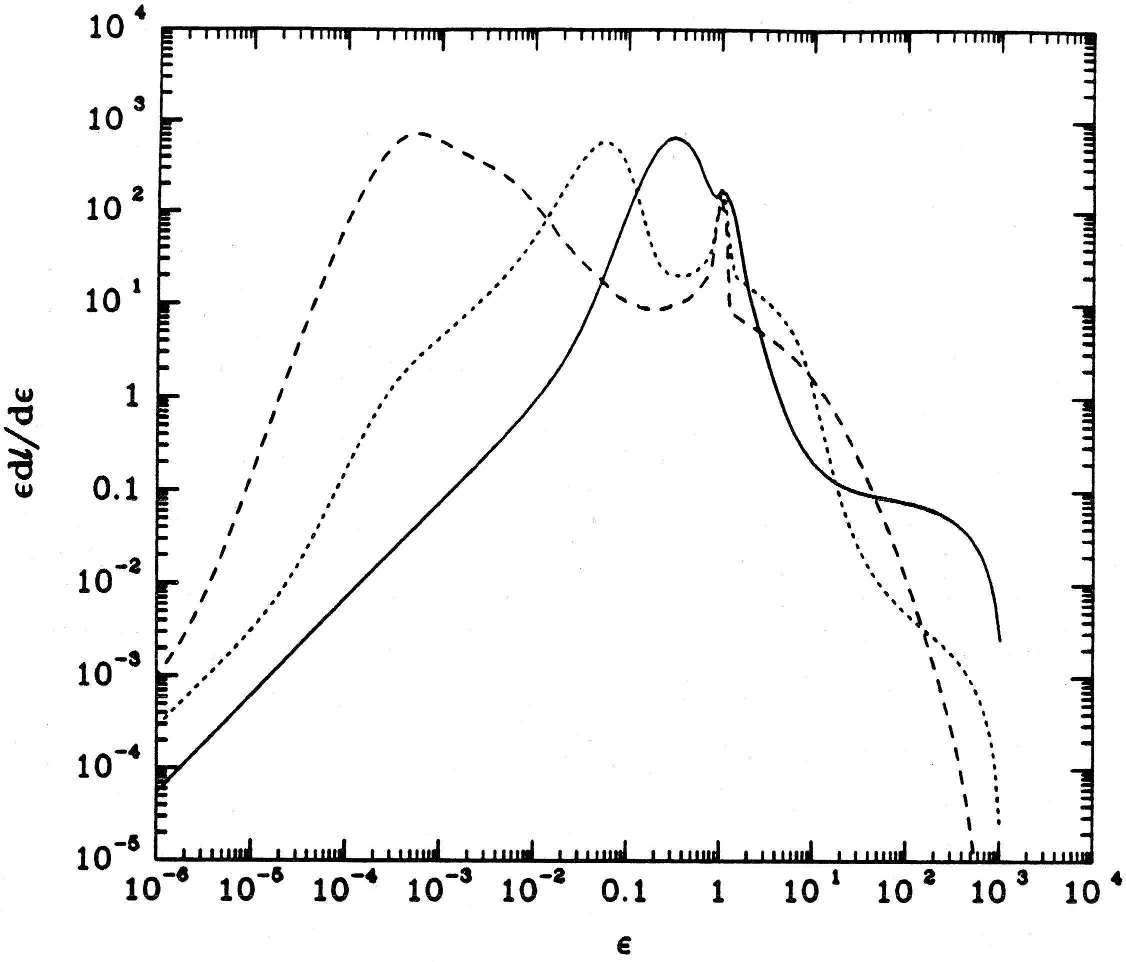
10^4
10^3
10^2
10^1
1
0.1
10^-2
10^-3
10^-4
10^-5
εdℓ/dε
10^-6
10^-5
10^-4
10^-3
10^-2
0.1
1
10^1
10^2
10^3
10^4
ε

Figure 1b

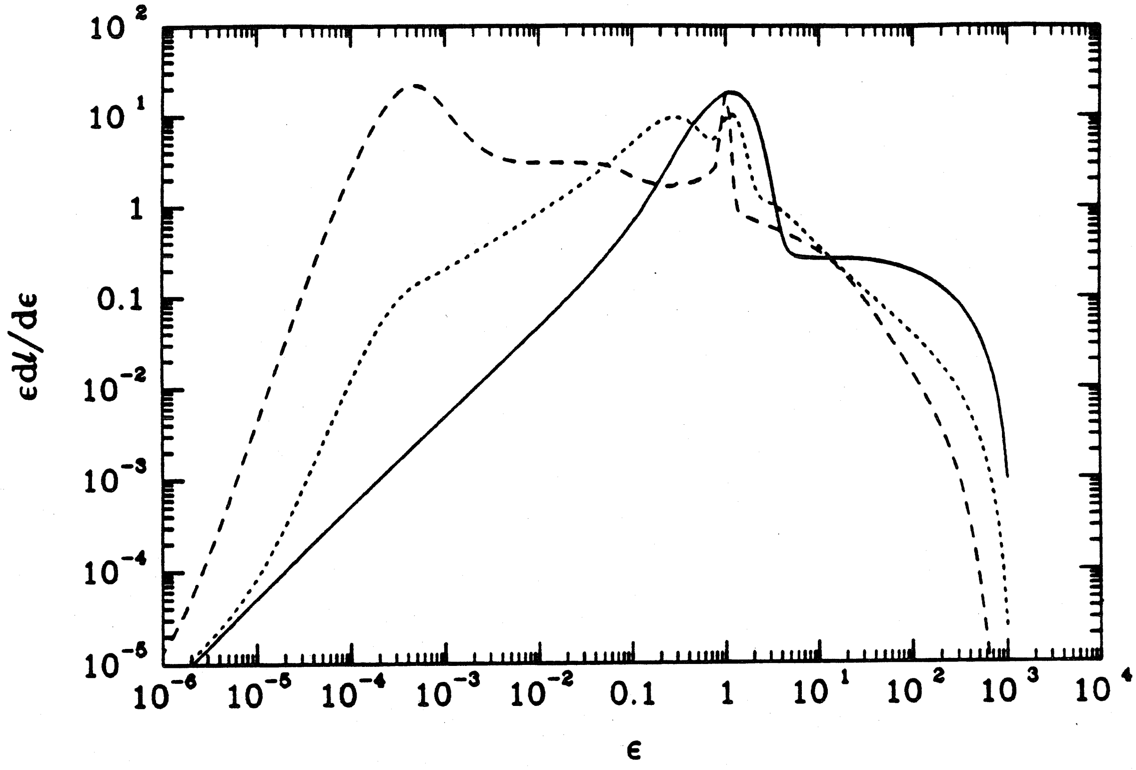
10^{2}
10^{1}
1
0.1
10^{-2}
10^{-3}
10^{-4}
10^{-5}
10^{-6}
10^{-5}
10^{-4}
10^{-3}
10^{-2}
0.1
1
10^{1}
10^{2}
10^{3}
10^{4}
$\epsilon d\ell/d\epsilon$
ϵ

Figure 1c

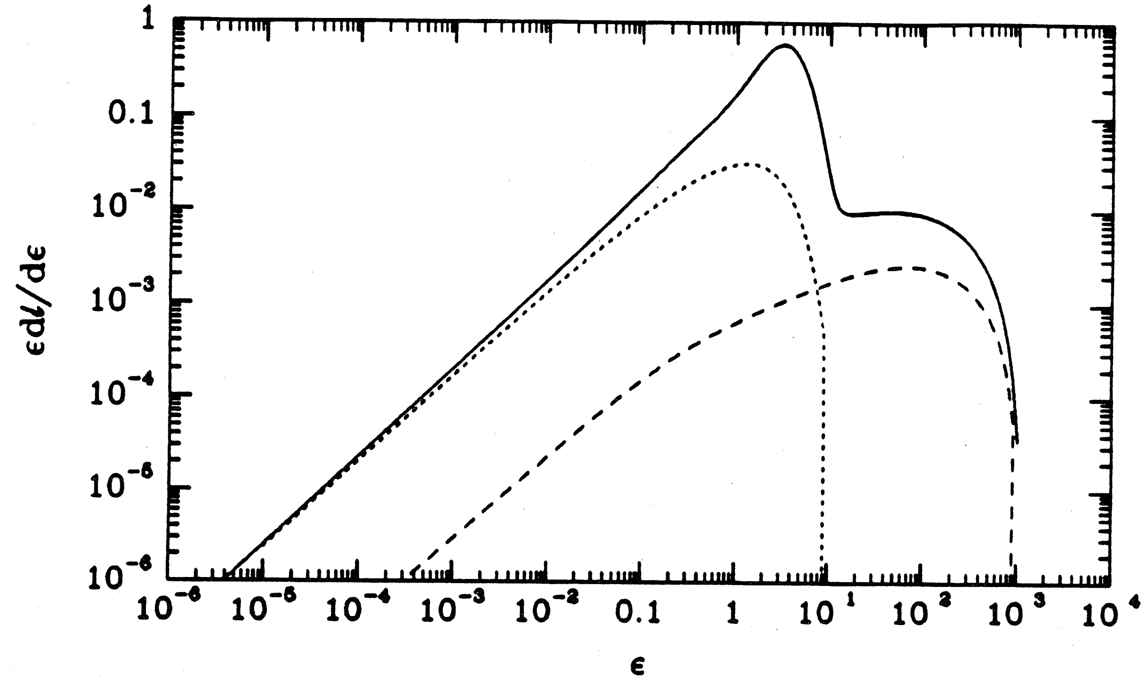
1
0.1
10^{-2}
10^{-3}
10^{-4}
10^{-5}
10^{-6}
$\epsilon d\ell/d\epsilon$
10^{-6}
10^{-5}
10^{-4}
10^{-3}
10^{-2}
0.1
1
10^{1}
10^{2}
10^{3}
10^{4}
ϵ

Figure 2

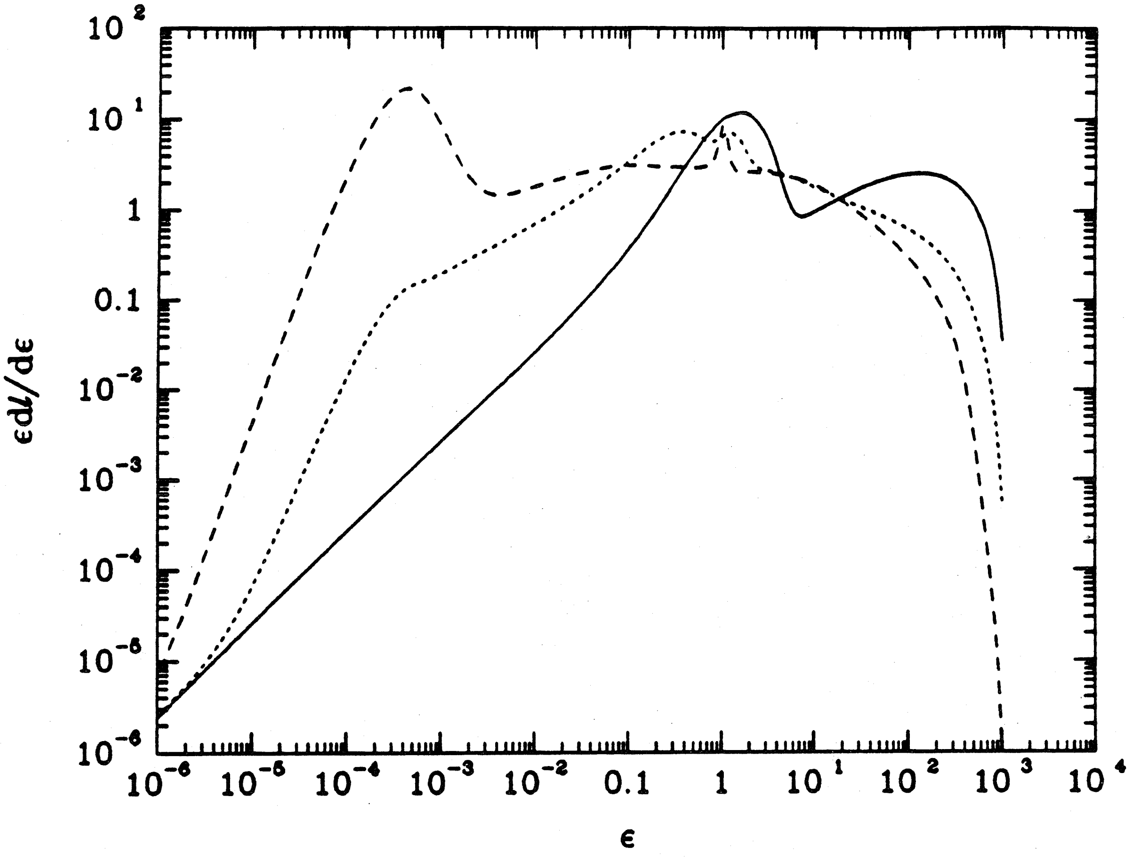

10^2
10^1
1
0.1
10^{-2}
10^{-3}
10^{-4}
10^{-5}
10^{-6}
$\epsilon d\mathcal{L}/d\epsilon$
10^{-6}
10^{-5}
10^{-4}
10^{-3}
10^{-2}
0.1
1
10^1
10^2
10^3
10^4
ϵ

Figure 3

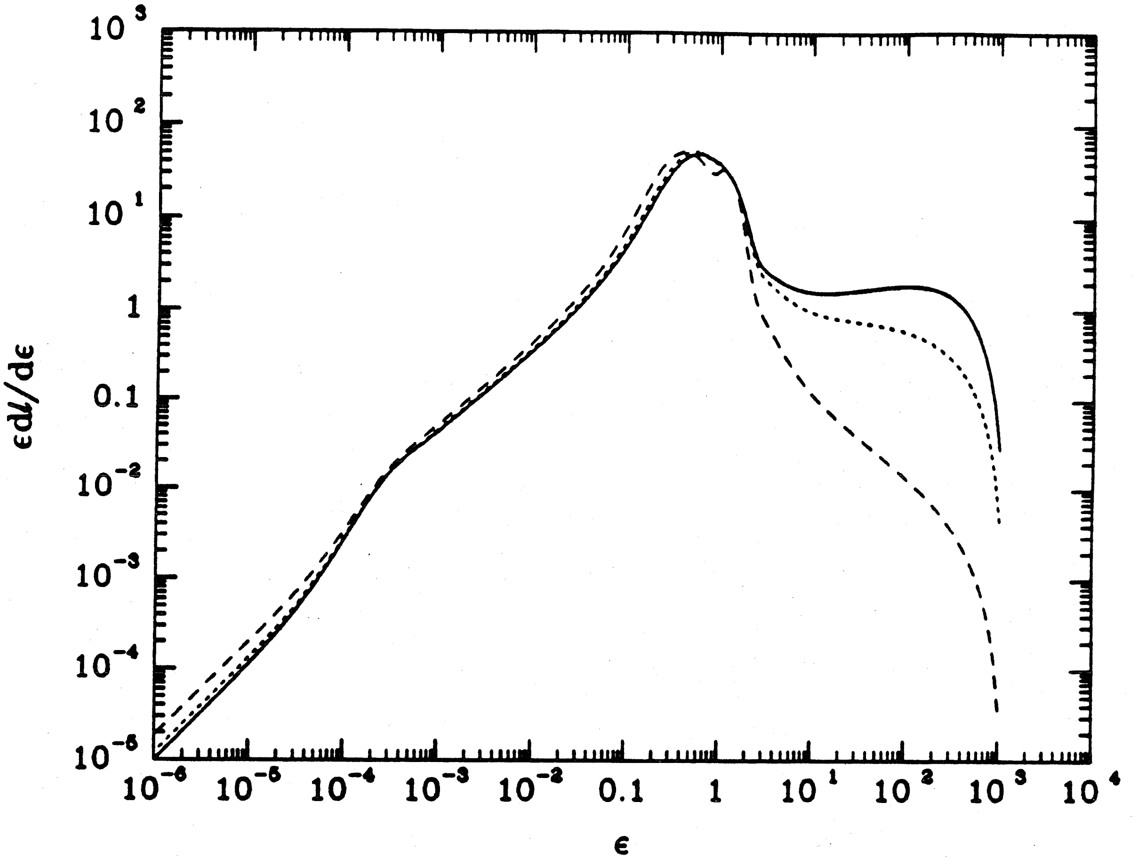
10^3
10^2
10^1
1
0.1
10^{-2}
10^{-3}
10^{-4}
10^{-5}
$\epsilon d\mathcal{L}/d\epsilon$
10^{-6}
10^{-5}
10^{-4}
10^{-3}
10^{-2}
0.1
1
10^1
10^2
10^3
10^4
ϵ

Figure 4

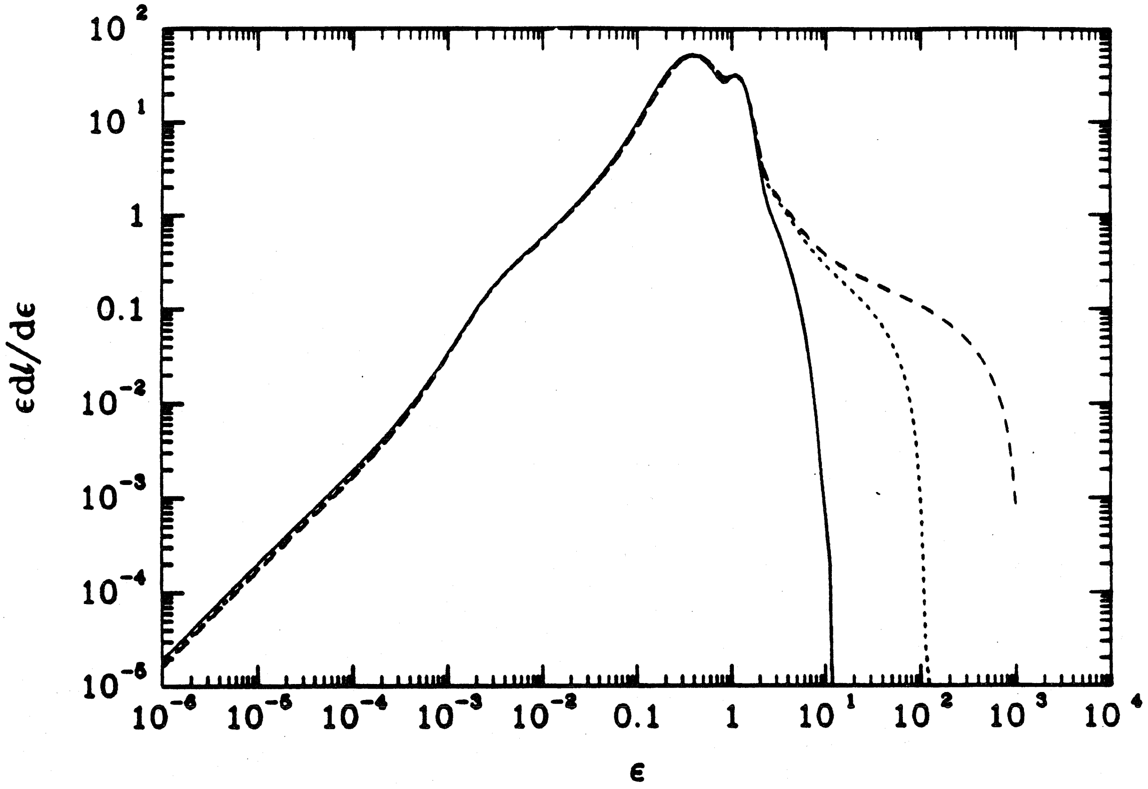
10 2
10 1
1
0.1
10-2
10-3
10-4
10-5
εdℓ/dε
10-6
10-5
10-4
10-3
10-2
0.1
1
10 1
10 2
10 3
10 4
ε

Figure 5

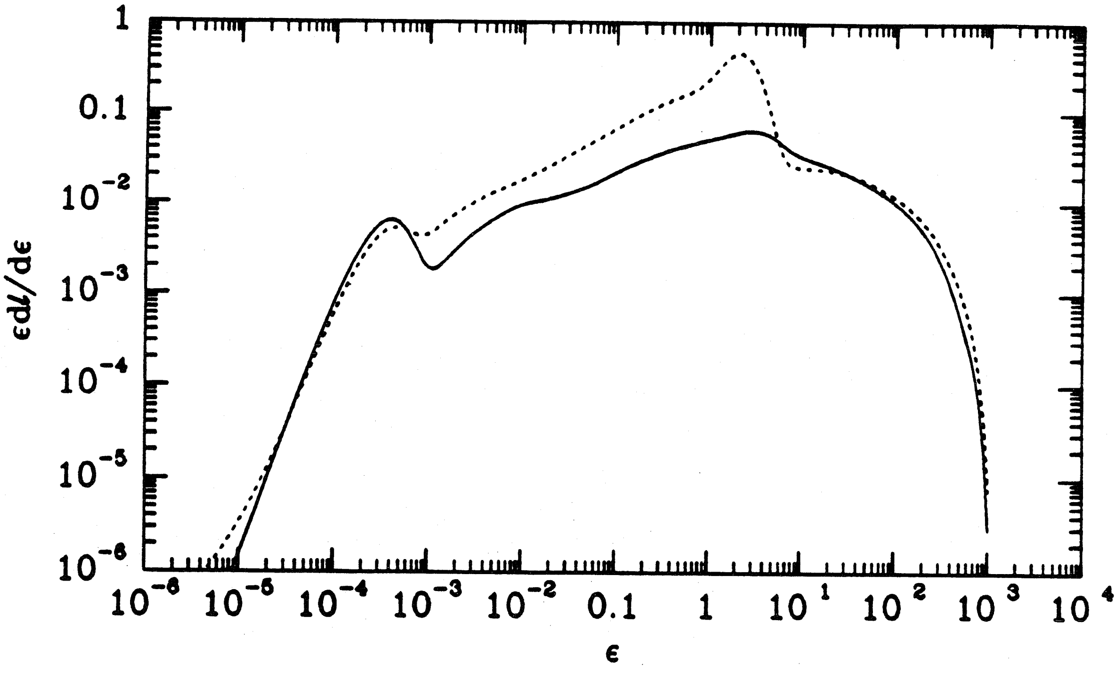
1
0.1
10^{-2}
10^{-3}
10^{-4}
10^{-5}
10^{-6}
$\epsilon dL/d\epsilon$
10^{-6}
10^{-5}
10^{-4}
10^{-3}
10^{-2}
0.1
1
10^{1}
10^{2}
10^{3}
10^{4}
ϵ

Figure 6

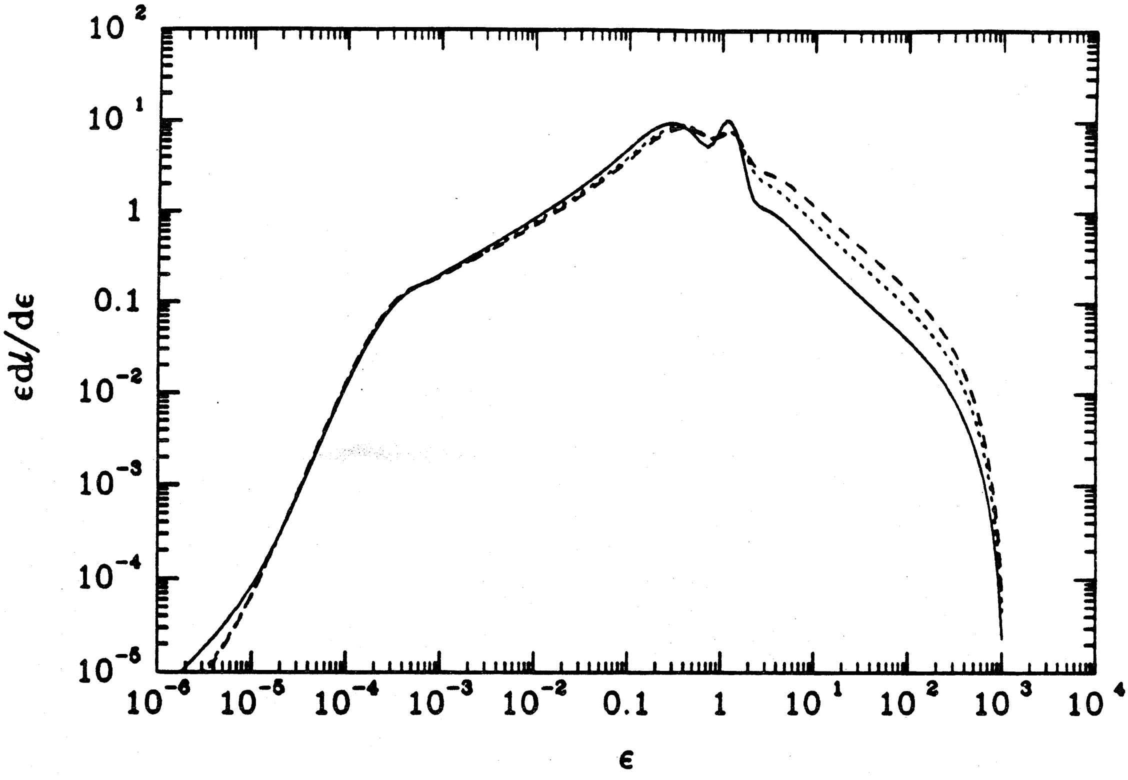
10^2
10^1
1
0.1
10^{-2}
10^{-3}
10^{-4}
10^{-5}
$\epsilon d\mathcal{L}/d\epsilon$
10^{-6}
10^{-5}
10^{-4}
10^{-3}
10^{-2}
0.1
1
10^1
10^2
10^3
10^4
ϵ

Figure 7

Chapter 5

VARIABLE SOFT X-RAY EXCESSES IN AGN FROM NONTHERMAL ELECTRON-POSITRON PAIR CASCADES

in collaboration with

Andrzej A. Zdziarski,
Space Telescope Science Institute

Submitted to *Astrophysical Journal*

Abstract

We study the formation of soft X-ray excesses, similar to those observed below ~ 1 keV from AGN, in nonthermal electron-positron pair cascade models. The soft X-ray excesses appear in those models due to Comptonization of soft photons of the UV bump by the pairs decelerated by the cascade process and thermalized to a nonrelativistic equilibrium temperature. We derive the conditions on parameters of the nonthermal pair source needed for the appearance of the excesses as well as simple formulae for the parameter y governing the thermal Comptonization and for the spectral form of the excesses. The major spectral effect is the formation of a steep power law superimposed on both the tail of the UV bump and on the flat nonthermal power law.

We study time variability of the soft excesses. We find that the time variability patterns of the soft and hard X-rays may be distinctly different (as often seen in AGN), in spite of their common origin in the nonthermal source. This is because the form and the amplitude of the soft excesses strongly depend on the luminosity in the soft UV photons. On the other hand, the hard X-ray emission is roughly independent on the UV luminosity. We classify the soft vs. hard X-ray variability patterns as a function of the relative variability of the UV luminosity and the power supplied to the relativistic electrons.

Finally, we find that the parameters of the nonthermal pair cascade sources required for the appearance of the soft X-ray excesses nearly coincide with those determined in a recently developed unified model for the UV and X-ray radiation from the central engines of AGN. In that model, a nonthermal pair cascade takes place in the vicinity of cold optically thick matter, which implies that the spectrum from the EUV through γ-rays is the sum of the direct cascade radiation

and direct and reprocessed radiation emitted by the cold matter. Thus, the presence of soft excesses in AGN can be understood as an (indirect) consequence of the presence of both cold matter and nonthermal sources in the central engines of AGN.

I. Introduction

The picture of X-ray spectra of AGN that has emerged in recent years is that of a hard X-ray spectrum in the $\sim$ 1–20 keV range with the canonical average energy spectral index of $\alpha \sim 0.7$ (Rothschild *et al.* 1983; Turner and Pounds 1989) and a variety of spectral forms below $\sim$ 1 keV (Elvis, Wilkes, and Tananbaum 1985; Wilkes and Elvis 1987; Elvis *et al.* 1987; Turner and Pounds 1989; Urry *et al.* 1989). In particular, $\gtrsim$ 50–70% of AGN exhibit strong soft excesses below the energy of $\sim$ 1 keV above the extrapolation of the hard X-ray power law (Wilkes and Elvis 1987; Turner and Pounds 1989; Urry *et al.* 1989). Due to poor spectral resolution of both the *Einstein* and *Exosat* soft X-ray detectors, the form of the soft excesses has not been well established yet; they have been fitted by either steep power law, bremsstrahlung or blackbody spectra (e.g., Urry *et al.* 1989). The excesses sometimes extend to 1 keV or more; characteristic energies of the fits to the soft excess spectra in Urry *et al.* (1989) are from a few tens to a few hundred eV. Hopefully, the spectral form of the excesses will be determined with future data from *Rosat.*

The time variability of the soft excesses exhibits a large variety of patterns. In some cases, the soft excesses and the hard X-rays appear correlated to a certain degree (e.g., Arnaud *et al.* 1985; Pounds, Turner, and Warwick 1986). In other cases, the soft excesses vary much more than the hard X-rays (e.g., Piro *et al.* 1988). For example, declines by factors of 10 and 2 in the soft and hard X-rays, respectively, have been observed in QSO 1821+643 (Warwick, Barstow, and Yaqoob 1989). In QSO MR 2251-178, the normalizations of both the hard and soft components and the power law index of soft component were required to vary in order to fit the variability data (Pan, Steward, and Pounds 1990).

In a few cases the soft fluxes remained constant with varying hard X-rays (e.g., Turner and Pounds 1988). Finally, a pivot point at ~ 2 keV has been observed in the variable X-ray spectrum of 3C120 (Maraschi *et al.* 1990), implying an anticorrelation of the soft and hard X-ray bands.

The origin of these soft excesses has thus far been a major puzzle in the study of AGN. As recently reviewed by Begelman (1990), the explanations proposed so far are in doubt as either unlikely to account for the relatively high energies of the excesses (intrinsic radiation of an accretion disk, e.g., Arnaud *et al.* 1985), or as requiring fine tuning of their parameters (the warm absorber model, e.g., Halpern 1984; Yaqoob, Warwick and Pounds 1989; Pan, Steward and Pounds 1990).

These explanations, however, have largely ignored another source of "warm" matter that is likely to exist in the interior of AGN and that could account for at least part of (if not all of) the observed soft excesses. As noted, for example, in Fabian *et al.* 1986, constraints on the size of the X-ray emitting region obtained from the rapid X-ray variability observed in many AGN lead to the conclusion that this source region is "compact," i.e., that it would be optically thick to any gamma-rays trying to escape through it. Because AGN are among the most energetic sources known and gamma-rays have been observed to come from them, it is therefore probable that the X-ray emitting regions contain a sufficient number of electron-positron pairs (produced in the annihilation of gamma-rays with lower energy x-rays) to have a Thomson optical depth across the source of order unity. Such a "pair plasma" could not be ignored as it would reprocess and significantly modify the spectrum of any radiation passing through it. In particular, it could add or subtract a significant amount of luminosity in the range of the soft x-ray excess energies – a complication that *any* model of the soft excess should be prepared to confront.

We will concentrate here on the possibility that the pair plasma is directly responsible for most of the soft x-ray excess. Steep soft X-ray power laws joining onto flatter hard X-ray power laws (qualitatively similar to those seen in observed spectra) have been obtained in nonthermal e^+e^- pair cascade models for some combinations of parameters (Fabian *et al.* 1986; Svensson 1987, hereafter S87; Lightman and Zdziarski 1987, hereafter LZ87). Those models have been proposed to account for the canonical hard X-ray spectra of AGN, with $\alpha \simeq 0.7$. In those models, relativistic pairs with large Lorentz factor are injected within a compact region. The relativistic pairs Compton-upscatter soft photons of the AGN UV bump to the X-ray and γ-ray energies. Photon-photon collisions convert some of the γ-rays into secondary e^+e^- pairs, which in turn produce new X-rays and γ-rays. The pairs lose energy and finally thermalize at an equilibrium Compton temperature T_C (typically $kT_C > 1$ keV), at which Compton losses of the thermal pairs are balanced by Compton energy gains. The thermal pairs Comptonize the UV photons, which gives rise to a steep power law spectral component superimposed on the flatter (nonthermal) hard X-ray power law. The steep component may well account for the observed soft X-ray excesses.

This possibility that AGN soft X-ray excesses come from nonthermal pair cascade sources has already been pointed out in Ghisellini *et al.* (1989). However, it has in general not received much attention in either the theoretical or observational literature. In this work, we examine the mechanism in more detail and investigate the constraints on the parameters of the pair cascade sources required for the formation of the excesses, the spectral form of the excesses, and their variability patterns.

What follows will be divided into two main sections. The first focuses on understanding the response of the soft excess to changes in pair plasma's energy inputs. Some analytic approximations are given as guides to help visualize the behavior. From these, general constraints on the plasma input parameters are derived such that an observable soft excess be produced by the pair cascade. The second section presents numerical calculations of a more realistic model which further illustrate the behavior discussed in the first section. The model is essentially that of Zdziarski *et al.* (1990) (hereafter Z90) and includes the effect of Compton reflection and reprocessing of x-rays by cold matter located near the pair plasma. We chose this model as it currently appears the most promising in simultaneously accounting for: the canonical average hard (2-10 keV) X-ray spectral index of .7, the presence of a K_α iron line and the short lag in its response to continuum changes, the hardening of the X-ray spectrum above $\sim$ 10 keV, and constraints from the γ-ray background (see Z90). We note that the allowed parameter space for this model roughly coincides with that for formation of a soft excess. The model may thus also explain why most AGN appear to show soft X-ray excesses.

II. Constraints on Soft Excesses from Cascade Sources

We study here the conditions on the parameters of nonthermal pair cascade sources required for the appearance of observable soft X-ray excesses in their spectra. We will constrain our analysis to pair cascades from monoenergetic (or flat) pair injection, assumed in most pair cascade models of AGN (e.g., LZ87, S87, Z90). This is the simplest case to understand and has the fewest adjustable parameters. The analysis for more complicated models such as those involving steep injection ($\propto \gamma^{-\Gamma}$, $\Gamma > 2$; e.g., LZ87; Zdziarski, Coppi, and Lamb 1990, hereafter ZCL90) or pair loading (e.g., Done, Ghisellini, and Fabian 1990) is similar and the conclusions drawn here are not significantly affected. In the case of pair loading, for example, the Thomson optical depth for a given set of input parameters is lower and soft excesses consequently appear only at higher rates of energetic pair injection. The shape and origin of the excesses is the same, however, and the overall parameter space in which they are visible is the same to within a factor ~ 2.

a) The Spectral Form of Soft Excesses

The main parameter governing formation of the soft excesses is the thermal Comptonization parameter y (e.g., Rybicki and Lightman 1979). For the model presented here (where the thermal pairs are almost always non-relativistic), the relevant form of y is given

$$y = 4\Theta_C \left(\tau_{\mathrm{T}} + \frac{\tau_{\mathrm{T}}^2}{3} \right) . \tag{2.1}$$

Here, $\Theta_C \equiv kT_C/m_e c^2$ is the dimensionless Compton temperature, m_e is the electron mass, τ_{T} is the Thomson optical depth of the thermal pairs, and the factor in parentheses is the average number of scatterings in the source. The y-parameter is determined mainly by the dimensionless compactness parameters of the nonthermal source:

$$\ell_h \equiv \frac{L_h \sigma_{\mathrm{T}}}{R m_e c^3}, \qquad \ell_s \equiv \frac{L_s \sigma_{\mathrm{T}}}{R m_e c^3}, \tag{2.2}$$

where L_h, L_s, R, and σ_{T}, are the X-γ-ray luminosity, the part of the UV luminosity that is intercepted by the nonthermal source, the characteristic source size, and the Thomson cross section, respectively. The photon energy up to which the soft excess thermal power law dominates the hard X-ray nonthermal power law depends in turn on the typical energy of the soft photons in the part of the UV bump that is produced close to the nonthermal source. We will approximate those UV photons as a blackbody with a temperature T_s and the corresponding dimensionless temperature $\Theta_s \equiv kT_s/m_ec^2$. The most important of these parameters in a pair cascade source is probably the compactness ℓ_h.

The optical depth of the thermal pairs, $\tau_{\rm T}$, is related to ℓ_h and the pair yield Y,

$$\tau_{\rm T} = [(4/\pi)Y\ell_h]^{1/2}\,, \tag{2.2}$$

(Guilbert, Fabian and Rees 1983; S87). At low compactnesses, $\ell_h \ll 25$, $Y \ll 0.1$, and consequently $\tau_{\rm T} \ll 1$. Thermal Comptonization is effective at such low optical depths only if the pair temperature is relativistic, which occurs only for $\ell_s \ll \ell_h$. However, soft excesses do not appear in this case, as the amplitude of the blackbody peak does not exceed the amplitude of the power law spectrum from the nonthermal Compton scattering (see below; ZCL90). Thus, we will consider here only the range of $\ell_h \gtrsim 25$.

In the absence of thermal Comptonization, a pair cascade spectrum has an approximate power law form. The power law joins at low energies onto the soft photon input spectrum. At high energies, the spectrum steepens gradually, which reflects high energy breaks in the pair distribution at the maximum energies of pairs from the subsequent pair generations (S87). Above 511 keV, the spectrum also breaks due to pair absorption.

The optically thick thermal pairs modify this spectrum in three ways. First, the thermal pairs downscatter the hard radiation. This causes a steepening in the spectrum above the "break"energy

$$\epsilon_b \simeq 3/\tau_{\rm T}^2\,, \tag{2.4}$$

where $\epsilon \equiv E/m_ec^2$ denotes a dimensionless photon energy. At energy $\epsilon \sim \epsilon_b$ the spectral index α increases by 0.5–1 (see Sunyaev and Titarchuk, hereafter ST80; S87). The form of the steepening is independent of the pair Compton temperature, Θ_C, provided $\Theta_C < \epsilon_b$. Second, the input soft photons are upscattered by the thermal pairs and form a power law tail superimposed on the blackbody and the nonthermal power law spectra. Third, the nonthermal power law is upscattered as well, which results in an increase of its amplitude. The latter two effects strongly depend on the pair temperature, as well as on the optical depth $\tau_{\rm T}$. We will present a formalism describing their effect on pair cascade spectra below.

The pair yield saturates at very high ℓ_h, reaching the values of $\lesssim 0.2$ (S87; LZ87). In the range of $25 \lesssim \ell_h \lesssim 1000$, which we will consider here, the pair yield slowly increases with ℓ_h. A fit to our numerical results (see § III) using the method of LZ87 (with inclusion of Coulomb cooling, see ZCL90) accurate to $\sim 20\%$ is

$$Y \simeq 0.1(\ell_h/100)^{1/4}, \qquad 25 \lesssim \ell_h \lesssim 1000\,. \tag{2.5}$$

Then, the optical depth, equation (2.3), becomes,

$$\tau_{\rm T} \simeq 3.6(\ell_h/100)^{5/8}, \qquad 25 \lesssim \ell_h \lesssim 1000\,. \tag{2.6}$$

In order to calculate the interior equilibrium Compton temperature (e.g., Krolik, McKee & Tarter 1981), we will approximate the interior spectrum as a blackbody followed by the nonthermal power law cut off at ϵ_b. The luminosity in the cut off power law is taken to be $\ell_h/2$, which roughly agrees with our numerical results. As we consider here saturated cascades, the index of the nonthermal power law will be $\alpha \simeq 1$ (S87). Then, the Compton temperature,

Θ_C, becomes,

$$\Theta_C \simeq \frac{\Theta_s \ell_s + \ell_c [8 \ln(\ell_c / 5\Theta_s \ell_h)]^{-1}}{\ell_s + \ell_h/2}, \qquad 25 \lesssim \ell_h \lesssim 1000 \tag{2.7}$$

$$\sim \frac{\text{constant}}{\ell_s + \ell_h/2}, \qquad \text{for } \Theta_s \ell_s \ll 1, \tag{2.8}$$

Here, $5\Theta_s$ approximately equals the minimum power law energy, ℓ_c is the luminosity at which the cutoff energy $\epsilon_b = 1$, and the pair yield, Y, was assumed here to be a constant related to ℓ_c. (Inclusion of the slow increase of Y with ℓ_h, eq. [2.5], turned out not to improve the accuracy of eq. [2.7].) We have found that $\ell_c = 50$ provides a good fit to the numerical results in the parameter range of interest here. The maximum deviation of the Compton temperature (2.7) from that found numerically is ~ 25% for the cases presented in § III. Note that Θ_C of equation (2.7) decreases slowly with ℓ_h at $\ell_h \sim \ell_s = \text{constant}$. The term $\Theta_s \ell_s$ in the numerator is always negligible for AGN. When it is negligible, the thermal pairs only lose (but do not gain) energy in Compton scatterings with the thermal bump. Then, the Compton temperature is independent of the blackbody temperature.

The Compton parameter, equation (2.1), with τ_T and Θ_C of equations (2.6)-(2.7) differs at most by ~ 20% from that obtained using the values of τ_T and Θ_C calculated numerically, for the cases presented in § III. We note that for $\ell_h \gtrsim 25$, when $\tau_T \gtrsim 2$, the term $\tau_T^2/3$ in equation (2.1) dominates. Then, the Compton parameter can be expressed as,

$$y \sim \frac{Y \times \text{constant}}{\ell_s/\ell_h + 1/2}, \tag{2.9}$$

Substituting the fit of equation (2.5) for Y, we obtain,

$$y \simeq \frac{0.25(\ell_h/100)^{1/4}}{\ell_s/\ell_h + 1/2}, \qquad 25 \lesssim \ell_h \lesssim 1000\,, \tag{2.10}$$

where the constant gives a good fit to our numerical results. This approximation, in fact, appears to work better than the original one obtained using equations (2.6), (2.7).

The parameter y is the main parameter governing thermal Comptonization. A narrow initial spectrum acquires a high-energy power law tail with the index δ,

$$\delta \simeq \left(\frac{9}{4}+\frac{4}{y}\right)^{1/2} - \frac{3}{2}, \tag{2.11}$$

(Shapiro, Lightman, and Eardley 1976). The thermal spectral index δ has the values 5, 2.8, 1.7, 1, for y equal 0.1, 0.25, 0.5, and 1, respectively. Using equation (16) of ST80, we may obtain an approximate for the spectrum from Comptonization of a blackbody spectrum at $\epsilon \gg \Theta_s$:

$$\left.\frac{d\ell}{d\epsilon}\right|_{\rm th,bb} \approx \frac{\ell_s}{\Theta_s}\frac{15\delta\Gamma(\delta+4)\zeta(\delta+3)}{\pi^4(2\delta+3)}\left(\frac{\epsilon}{\Theta_s}\right)^{-\delta}, \tag{2.12}$$

(compare ST80). Here Γ is the Gamma function, and $\zeta(x)$ is the Riemann zeta function, which approaches rapidly unity for x larger than a few (e.g., $\zeta[4] \simeq 1.08$). An example of how well this approximation works is shown in Fig. 1. To compute the value of δ, we made use of approximation (2.10) which appears to work better overall than the combination of equations (2.6) and (2.7). We note, though, that care should always be used in the determination of δ. A relatively small error in a power law index can lead to much larger errors in the actual spectrum.

The nonthermal power law gets thermally Comptonized as well. A power law spectrum with the index α extending from ϵ_a to ϵ_b, $(d\ell/d\epsilon)(\epsilon) = A\epsilon^{-\alpha}$, becomes (using equation 16 of ST80 again)

$$\left.\frac{d\ell}{d\epsilon}\right|_{\rm th,pl} \approx \frac{A\delta(\delta+3)\epsilon^{-\alpha}}{\delta(\delta+3)-\alpha(\alpha+3)} - \frac{A\delta(\delta+3)\epsilon_a^{(\delta-\alpha)}\epsilon^{-\delta}}{(2\delta+3)(\delta-\alpha)}, \qquad \epsilon < \Theta_C, \tag{2.13}$$

(the first term above is given in ST80).

We see that for $\delta > \alpha$, the original spectral index α is approximately preserved but its normalization increases as shown by the first factor in equation (2.13). This effect may be clearly seen in Fig. 1. The normalization constant of the nonthermal power law for saturated pair cascades with $\alpha = 1$ and the compactness $\ell_h/2$ is,

$$A \simeq \frac{\ell_h}{2\ln(10/\Theta_s \ell_h)}, \tag{2.14}$$

consistent with the approximations used for deriving equation (2.7).

b) The Condition for Observable Soft X-Ray Excesses

We can now specify conditions on the parameters of the plasma necessary for the appearance of soft excesses. We note first that y of equation (2.10) reaches the maximum for a given ℓ_h, $y \simeq 0.5(\ell_h/100)^{1/4}$, when ℓ_s/ℓ_h becomes small. This corresponds to the Compton heating and cooling on the nonthermal power law only. In this case y reaches the maximum of unity for $\ell_h \sim 10^3$. For larger ℓ_h, y no longer increases significantly as the pair yield, Y, saturates. In order for an excess to be visible, the thermal power law must be steeper than the nonthermal one (with $\alpha \sim 1$), i.e., y must be < 1. For the case $\ell_s \ll \ell_h$, then, a condition for the appearance of a soft excess is thus

$$\ell_h \lesssim 1000. \tag{2.15}$$

For $\ell_s \gtrsim \ell_h$, the y parameter will be reduced relative to the case $\ell_s \ll \ell_h$ (see equation [2.10]) and one might expect a visible excess at higher values of ℓ_h. This is indeed the case. However, another limiting effect sets in when $\ell_s \sim \ell_h \gg 1$. Although the pair yield Y saturates, the Thomson optical depth continues to grow as $\ell_h^{1/2}$, and eventually the break energy ϵ_b (due to thermal Compton downscattering) moves into the keV energy range giving spectra that are almost certainly ruled out by observations. This happens for $\ell_h \gtrsim 1500$ (see [2.4,2.6]). The constraint $\ell_h \lesssim 1500$ therefore seems to be a general one for all pair cascade models.

At a low ℓ_s/ℓ_h, the peak of the blackbody spectrum is just at the level of the nonthermal power law. We find that the peak of the blackbody spectrum is above the nonthermal power law for,

$$\frac{\ell_s}{\ell_h} > \frac{3}{2\ln(10/\Theta_s\ell_h)} \sim \frac{1}{5}. \tag{2.16}$$

This is a necessary condition for the thermal Comptonization power law tail, equation (2.12), to be visible when superimposed on the nonthermal power law. (Note that when ℓ_s/ℓ_h becomes much smaller than the ratio given by eq. [2.14], the source becomes photon-starved, other physical effects become important, and its spectrum is no longer of the form assumed for deriving eq. [2.8], see ZCL90.)

On the other hand, when ℓ_s/ℓ_h becomes large, y of equation (2.10) becomes small, and the thermal power law tail becomes steep and invisible when superimposed on the sum of the blackbody and nonthermal power law spectra again. For y to be larger than some y_*, the compactness ratio must satisfy,

$$\frac{\ell_s}{\ell_h} < \frac{0.25}{y_*}\left(\frac{\ell_h}{100}\right)^{1/4} - \frac{1}{2}. \tag{2.17}$$

For $y_* = 0.25$, corresponding to $\delta \sim 3$, the conditions (2.16) and (2.17) become mutually exclusive for $\ell_h \lesssim 25$.

We can also derive the condition for the thermal power law to dominate over the (thermally Comptonized) nonthermal power law below a given energy, ϵ_*. This will put constraints on the temperature of the soft photons. This can be done by equating the spectral luminosities (2.13) and (2.12) at ϵ_*, with A and δ

specified by equations (2.14) and (2.10)-(2.11), respectively. This equality defines a 2-D surface in the 3-D space of ℓ_s, ℓ_h, and T_s. As the allowed range for ℓ_s/ℓ_h is relatively narrow (eqs. [2.16]-[2.17]), we can set, e.g., $\ell_s/\ell_h = 1/3$ and get a constraint in the T_s–ℓ_h plane. Carrying out this procedure for energies $\epsilon_* \sim .1$ keV leads to the rough condition $T_s \gtrsim$ 5–10 eV.

Summarizing the results of this section, we find the constraints for a soft excess to be produced are $25 \lesssim \ell_h \lesssim 1500$, $\ell_s \sim \ell_h$, and $T_s \gtrsim$ 5–10 eV.

c) Time Variability of Soft Excesses

With the above results, we can now make predictions regarding time variability of the soft excesses. First, we consider $\ell_h =$ constant and decreasing ℓ_s. At $\ell_s \gg \ell_h$, the parameter $y \ll 1$, and there is no observable thermal Comptonization. With decreasing ℓ_s, an increasingly flatter thermal Comptonization tail develops. The tail originates near the blackbody peak, which decreases. Also, the normalization of the nonthermal power law increases (eq. [2.13]). Thus, at low enough ℓ_s, the power law tail from thermal Comptonization of blackbody photons disappears again, being negligible compared to the Comptonized nonthermal power law. This range of behavior is shown in Fig. 2. Note that as y increases with decreasing ℓ_s, there is an anticorrelation between the soft and hard X-ray fluxes.

When ℓ_s is constant and ℓ_h increases, the source exhibits a similar behavior. As before, the soft excess power law is negligible at $\ell_s/\ell_h \gg 1$ and $\ll 1$, and it is observable in an intermediate interval of ℓ_h. The quantitative differences are that now y increases faster with decreasing ℓ_s/ℓ_h than before, as implied by equation (2.10). Also, the amplitude of the nonthermal power law increases somewhat faster than proportional to ℓ_h (eq. [2.14]).

When both ℓ_s and ℓ_h increase proportionally, there is only a slow increase of y with ℓ_h (eq. [2.10]), and the increase of the amplitude of the nonthermal power law according to equation (2.13). The appearance of a soft excess power law will depend on the specific values of ℓ_s and ℓ_h. Some illustrative examples of this and the other types of behavior discussed are presented below in § 3.

III. Model Calculations

In this section, we will present numerical examples illustrating the results of § II in the context of what currently appears to be the pair model with the best chance of meeting observational constraints. The model is essentially that of Z90, which is distinguished from previous models by the inclusion of a component made up of the intrinsic pair plasma radiation Compton-reflected off some nearby distribution of cold matter. The motivation for this type of model stems from the growing body of evidence that the AGN hard X-ray spectra contain a large contribution from reflection of a nonthermal power law from cold matter and are not consistent with single power laws (Pounds *et al.* 1989, 1990; Nandra, Pounds and Steward 1990; Matsuoka *et al.* 1990; Piro, Yamauchi, and Matsuoka 1990; Turner *et al.* 1990; Pounds 1990).

Z90 have found that in order for the composite spectrum to have the average 2–20 keV index of $\alpha \sim 0.7$ and the γ-ray spectrum not to exceed the constraint imposed by the cosmic γ-ray background (e.g., Bignami *et al.* 1979) the hard compactness (ℓ_h) of the nonthermal pair source must be in the range $30 \lesssim \ell_h \lesssim 300$. This finding has resolved previous difficulties with the pair cascade model, in which the requirement of $\alpha \sim 0.7$ lead to a γ-ray excess above the constraint from the γ-ray background (Bignami *et al.* 1979). In the sample calculations presented here, we will therefore also restrict ourselves to this region of parameter space.

We note that this is a subset of the parameter space described above in which we would expect to find an observable soft excess. (The reflected component does not directly affect the soft excesses, as a Compton-reflected spectrum appears only above a few keV, see Lightman and White 1988. Hence the discussion presented above goes through unchanged.) Compton reflection models of the type described in Z90 therefore seem to predict that a soft x-ray excess should appear in the spectra of "average" AGN to which the model applies – as indeed seems to be the case observationally.

We will consider here an idealized geometry with a compact nonthermal source of the radius, R, located close above the surface of a slab (possibly an accretion disk), as shown in Figure 3. The power L_h is supplied to e^+e^- pairs in the nonthermal source and radiated as X-rays and γ-rays. A half of L_h is intercepted by the slab, i.e., the covering factor of the nonthermal source by the slab is 0.5. This and the assumption made below that the covering factor of the slab by the source is also 0.5 are motivated by the observations of a short lag time between variations of the fluorescence iron K_α line in the X–ray-reflected spectrum and the incident continuum (Kunieda *et al.* 1990). This suggests that the nonthermal source is in close proximity to the cold matter, and that the area of the cold matter that reprocesses the nonthermal radiation is comparable to the area of the nonthermal source.

Of the $L_h/2$ of luminosity that is the hitting the slab, a fraction $a \simeq 0.1$–0.15 (typical values for the integrated albedo) is Compton-reflected by the slab (White, Lightman, and Zdziarski 1988; Lightman and White 1988; Z90). The remainder is absorbed and reemitted in the form of blackbody radiation. This contributes to the total thermal luminosity of the slab, some of which will be re-intercepted by the pair plasma. The cold matter thus provides a means of self-consistently generating soft photons. As noted, we assume here that the covering factor of the irradiated part of the slab by the nonthermal source is also 0.5. Then, the blackbody luminosity of the irradiated area equals $2L_s$, as L_s is the soft photon luminosity incident on the nonthermal source. The luminosity L_s is isotropically reemitted by the nonthermal source, and a half of it returns to the slab. Thus, from energy balance, $L_s \gtrsim L_h/3$, where the equality corresponds to no energy generation intrinsic to the disk. Thermal energy may, of course, be internally generated in the slab and radiated (as is the case, e.g., in an accretion disk). Z90 assumed rough equipartition between this internal energy generation and the input of energy to the pair plasma in the form of energetic pairs, i.e., considered the case $L_s \sim L_h$. Here we will allow the internal energy generation (and hence L_s) to be varied as free parameter.

We will take the observer to be at an angle so that he/she sees both the nonthermal source and the reflecting portion of the slab. The total flux seen by the observer corresponds then to the sum of the luminosities emitted into the 2π solid angle, $(L_s + L_h)/2 + aL_h/2 + 2L_s$. The three factors here correspond to the direct emission of the nonthermal source, to Compton reflection, and to the thermal emission of the slab, respectively.

The luminosity $2L_s$ is emitted by an area somewhat larger than the projection of the nonthermal source onto the slab. We will here take this area to be $2\pi R^2$. Then, the blackbody temperature of this region is,

$$kT_s \simeq 10 \left(\frac{\ell_s}{10^2}\right)^{1/4} \left(\frac{R}{10^{14}\,\mathrm{cm}}\right)^{-1/4} \mathrm{eV}\,. \tag{3.1}$$

We have performed steady state pair cascade calculations as described in LZ87 and ZCL90, with the compactnesses ℓ_s and ℓ_h, the blackbody temperature T_s given by equation (3.1), and monoenergetic pairs injected at $\gamma_{\max} = 2 \times 10^3$

(the X-ray spectra are weakly dependent on the choice of $\gamma_{\max}$). We have compared the results with those of the time-dependent code of Coppi (1990) and Coppi and Blandford (1990). We found that if ℓ_s and ℓ_h are changed on time scales $\gtrsim 2R/c$, then the time evolution of the pair source follows approximately a sequence of steady states, for the range of $\ell_h \leq 300$ considered here. To describe the response of the spectra it therefore suffices to present only the steady state spectra for the initial and asymptotic final states. For example, if a comparison of the initial and final states showed that the hard X-rays softened, an examination of the corresponding time sequence would show a steadily (monotonically) softening hard X-ray spectrum.

Using these steady state spectra, the spectra reflected from the slab were then calculated using the method of Lightman and White (1988), White, Lightman, and Zdziarski (1988), and cosmic abundances of Morrison and McCammon (1983) (see analogous calculations in Z90). We remark that this step is not entirely self-consistent as the slab was assumed to be cold, i.e., its ionization state was not self-consistently calculated taking into account the (non-negligible) incoming flux of hard radiation. The final composite spectra presented below were then constructed by the direct pair radiation, the reflected component, and the thermal emission of the slab, as discussed above.

As pointed out in Z90, addition of the reflected spectra hardens the composite spectra. For $30 \lesssim \ell_h \lesssim 300$, the 2–20 keV spectral indices of the composite spectra are then $0.6 \lesssim \alpha \lesssim 0.85$ (a very desirable feature of this model). A further consequence of this hardening of the spectrum from the underlying $\alpha \sim 1$ to $\alpha \sim .7$ is to enhance the amount of the perceived soft excess (determined by subtracting off from the observed flux a power law extrapolated from the 2-10 kev range). Decomposition of total spectra into the direct and the reflected components is given in Z90. The various features that appear in the direct pair spectra have been extensively discussed elsewhere, e.g., in LZ87, and will not be reanalyzed here as we are interested only in the behavior of the soft excesses relative to the hard X-rays.

We present in Fig. 4 some representative examples of the composite spectra we computed. Depending on the variability pattern of the input ℓ_h and ℓ_s, we can observe distinct variability patterns of the soft and hard X-rays. The spectra presented illustrate three possible types of variability which correspond to the three characteristic AGN variability patterns discussed in § I:

1. Variable l_s, constant l_h. Figure 4a shows two spectra for $\ell_h = 100$ and varying $\ell_s = 100, 300$. It can be seen that the spectrum above 1 keV only slightly softens while dramatic variations occur in the spectrum and flux below ~ 0.5 keV (see Table 1). This is because the hard X-rays are mostly due to emission of the nonthermal pairs, which for $l_h \lesssim l_s$ is roughly independent of the blackbody temperature and luminosity (Zdziarski and Lightman 1985). Note that for $\ell_h < \ell_s$ and for large enough ℓ_h, the hard flux becomes even anticorrelated with the soft flux, as illustrated in Figure 4b. This is due to the effect of upscattering by the thermalized pairs of the nonthermal power law, which is an effect increasing with increasing ℓ_h and decreasing ℓ_s (see, e.g., ZCL90).

2. Proportional variations of the powers released in both the nonthermal source and the disk. Figure 4c shows the case with $\ell_h = 30, 100$ and a proportional increase in the power generated inside the disk. In that case, both the soft and hard X-ray fluxes are approximately correlated, with the hard X-ray spectra softening with increasing compactness, which is a general feature of pair models (e.g., S87; LZ87). The energies to which the soft X-ray excesses extend increase with the compactness.

3. Constant power released in the disk and variable ℓ_h. In this case, one can obtain the soft X-ray spectra approximately constant while the hard X-ray fluxes vary provided $L_s \gg L_h$, for which the increase of L_s due to reemission of L_h can be neglected. This is illustrated in Figure 4d. Again, the hard X-ray spectra harden with the increasing compactness ℓ_h.

IV. Discussion and Conclusions

Current explanations of the hard X-ray spectrum in AGN rely on the existence of a pair plasma in their interiors. In this mechanism, energetic pairs upscatter soft photons to x-ray energies, quickly losing most of their energy in the process. From both simple order of magnitude estimates based on observed X-ray luminosities and variability timescales (e.g., Guilbert, Fabian & Rees 1983) and the best guesses from more sophisticated (albeit still rather crude) pair plasma models, one suspects that enough of these cooled pairs accumulate to form a Thomson thick thermal plasma. This plasma can have rather significant effects on the observed source spectrum, adding, for example, a annihilation feature at .5 MeV. Of interest to us, if these pairs have a temperature of order a few keV, we have seen that they will produce an excess of emission at $\sim .05 - 1$ keV on top of the pre-existing hard X-ray power law. This will complement any other source of soft x-ray emission one might envision such as the inner edge of an accretion disk. In this regard, we note that a cloud of warm pairs plays a role identical to (and probably is precisely) the "hot corona" referred to in some accretion disk models (e.g., Czerny & Elvis 1987) as a way of extending disk emission and producing a soft excess.

One possible argument against having the soft excess come from the same source as the hard X-rays is that the two components do not always show correlated time variability. When a pair plasma is involved, however, different energy bands may respond in quite different manners to changes in the pair plasma inputs (e.g., see Coppi 1990). As shown above, the soft excess vs. hard X-ray behavior is such a case. It appears possible to construct scenarios that reproduce all the types of currently observed variability behavior (variable soft X-rays and constant hard X-rays, constant soft X-rays and variable hard X-rays, and an overall correlation between the soft and hard X-rays). Unfortunately, this means that pair models of the soft excess currently have little predictive power with respect to variability. While the soft excess produced by a pair plasma varies in a very definite manner in response to changes in the incident soft photon spectrum or energetic pair injection (see § II), current observations are not sufficient for determining what exactly these changes were. (Simultaneous observations in a wide range of energy bands would be needed.)

Another test for or constraint on pair plasma-based models of the soft excess come from the detailed shape and amplitude of the excess. Again, however, current observations are not of high enough quality to address this issue (although ROSAT may soon change the situation). An important question that needs to be (somehow) answered is that of the shape of the underlying soft photon continuum. It would be important to know what the source looked like in a low or quiescent state. Alternatively, one could search for an envelope to the variations. (The contribution to the soft photon luminosity ℓ_s due to internal energy generation in a disk might vary on a significantly longer timescale than the pair injection luminosity ℓ_h.)

Finally we note that if the reflection model discussed in § III proves to be qualitatively correct and the compactness ℓ_h falls in the range discussed, it is a prediction of the pair plasma picture that soft excesses should be a fairly common occurrence. (The reflection model requires $ls \sim \ell_h$, $30 \lesssim \ell_h \lesssim 300$, which is a parameter range consistent with that derived for the production of an observable excess, $\ell_s \lesssim \ell_h$, $30 \lesssim 1500$.) This is to be contrasted with the accretion disk picture where current models (without hot coronas) typically need to be viewed almost face-on to give excess luminosities extending to sufficiently high energies, i.e., where soft excesses would be relatively rare.

Acknowledgments

The authors acknowledge valuable comments on this work by Roland Svensson and Roger Blandford. One of us (PSC) has been supported in part by NASA Grant NAGW-1301 and NSF Grants AST 86-15325 and AST 89-15326.

References

Arnaud, K.A., Branduardi-Raymont, G., Culhane, J.L., Fabian, A.C., Hazard, C., McGlynn, T.A., Shafer, R.A., Tennant, A.F., & Ward, M.J., 1985. *Mon. Not. R. astr. Soc.,* **217**, 105.

Begelman, M., 1990. Talk delivered at the Workshop on *Variability of Active Galactic Nuclei*, Atlanta, GA, May 1990.

Coppi, P.S., 1990. Caltech Theoretical Astrophysics Preprint GRP-209, submitted to *Mon. Not. R. astr. Soc.*

Coppi, P.S. & Blandford, R.D., 1990. *Mon. Not. R. astr. Soc.,* **245**, 453.

Done, C. & Fabian, A.C., 1989. *Mon. Not. R. astr. Soc.,* **240**, 81.

Done, C., Ghisellini, G., & Fabian, A.C., 1990. *Mon. Not. R. astr. Soc.,* **245**, 1.

Elvis, M., Green, R.F., Bechtold, J., Schmidt, M., Neugebauer, G., Soifer, B.T., Matthews, K., & Fabbiano, G., 1986. *Astrophys. J.,* **310**, 291.

Elvis, M., Wilkes, B.J., & Tananbaum, H., 1985. *Astrophys. J.,* **292**, 357.

Fabian, A.C., Blandford, R.D., Guilbert, P.W., Phinney, E.S., & Cuellar, L., 1986. *Mon. Not. R. astr. Soc.,* **221**, 931.

Ghisellini, G., Done, C., & Fabian, A.C., 1989. In: *23rd Eslab Symposium*, p. 789, eds Hunt, J. & Battrick, B., ESA SP-296.

Guilbert, P., Fabian, A.C., & Rees, M.J., 1983. *Mon. Not. R. astr. Soc.,* **205**, 593.

Guilbert, P. & Rees, M.J., 1988. *Mon. Not. R. astr. Soc.,* **233**, 475.

Halpern, J.P., 1984. *Astrophys. J.,* **281**, 90.

Krolik, J.H., McKee, C.F., & Tarter, C.B., 1981. *Astrophys. J.,* **249**, 422.

Kunieda, H., Turner, T. J., Awaki, H., Koyama, K., Mushotzky, R.F., & Tsusaka, Y., 1990. *Nature,* **345**, 786.

Lightman, A.P. & White, T.R., 1988. *Astrophys. J.,* **335**, 57.

Lightman, A.P. & Zdziarski, A.A., 1987. *Astrophys. J.,* **319**, 643.

Maraschi, L., Chiapetti, L., Falomo, R., Garilli, B., Malkan, M., Tagliaferri, G., Tanzi, E.G., & Treves, A., 1990. *Astrophys. J.*, submitted.

Matsuoka, M., Piro, L., Yamauchi, M. & Murakami, T., 1990. *Astrophys. J.*, in press.

Morrison, R. & McCammon, D., 1983. *Astrophys. J.,* **270**, 119.

Nandra, K., Pounds, K.A., & Steward, G.C., 1990. *Mon. Not. R. astr. Soc.,* **242**, 660.

Pan, H.C., Stewart, G.C., & Pounds, K.A., 1990. *Mon. Not. R. astr. Soc.,* **242**, 177.

Piro, L., Massaro, E., Perola, G.C., & Molteni, D., 1988. *Astrophys. J. (Letters),* **325**, L25.

Piro, L., Yamauchi, M., & Matsuoka, M., 1990. *Astrophys. J. (Letters)*, in press.

Pounds, K.A., 1990. *Mon. Not. R. astr. Soc.,* **242**, 20P.

Pounds, K.A., Nandra, K., Stewart, G.C., George, I.M., & Fabian, A.C., 1989. *Nature,* **344**, 132.

Pounds, K.A., Turner, T.J., & Warwick, R.S., 1986. *Mon. Not. R. astr. Soc.,* **221**, 7P.

Rothschild, R.E., Mushotzky, R.F., Baity, W.A., Gruber, D.E., Matteson, J.L., & Peterson, L.E., 1983. *Astrophys. J.,* **269**, 423.

Rybicki, G. & Lightman, A.P., 1979. *Radiative Processes in Astrophysics*, John Wiley & Sons, New York.

Sunyaev, R.A. & Titarchuk, L.G., 1980. *Astr. Astrophys.,* **86**, 121.

Svensson, R., 1987. *Mon. Not. R. astr. Soc.,* **227**, 403.

Turner, T.J., *et al.*, 1990. *Mon. Not. R. astr. Soc.,* **244**, 310.

Turner, T.J. & Pounds, K.A., 1988. *Mon. Not. R. astr. Soc.,* **232**, 463.

Turner, T.J. & Pounds, K.A., 1989. *Mon. Not. R. astr. Soc.,* **240**, 833.

Urry, C.M., Arnaud, K., Edelson, R.A., Kruper, J.S., & Mushotzky, R.F., 1989. In: *23rd Eslab Symposium*, p. 789, eds Hunt, J. & Battrick, B., ESA SP-296.

Warwick, R.S., Barstow, M.A., & Yaqoob, T., 1989. *Mon. Not. R. astr. Soc.,* **238**, 917.

White, T.R., Lightman, A.P., & Zdziarski, A.A., 1988. *Astrophys. J.,* **331**, 939.

Wilkes, B.J. & Elvis, M., 1987. *Astrophys. J.,* **323**, 243.

Zdziarski, A.A., Coppi, P.S., & Lamb, D.Q., 1990. *Astrophys. J.,* **357**, 149.

Zdziarski, A. A., Ghisellini, G., George, I. M., Svensson, R., Fabian, A. C., & Done, C., 1990. *Astrophys. J. (Letters)*, in press.

Zdziarski, A.A. & Lightman, A.P., 1985. *Astrophys. J. (Letters),* **294**, L79.

Figure Captions

Figure 1. Decomposition of spectrum illustrating the effects of thermal Comptonization discussed in § II. The spectrum was computed using the code of Coppi (1990) and does not include Compton reflection effects. The model used assumed monoenergetic pair injection at $\gamma_{max} = 10^3$ and had input parameters $\ell_s = 70$, $\ell_h = 200$,$\theta_s = 1 \times 10^{-5}$. The thermal pairs had a numerically computed Thomson optical depth of $\tau_T = 5.52$ and temperature $\theta_C = 6 \times 10^{-3}$, giving a Compton y parameter of 0.376. The solid curve is the total computed spectrum. The long dashed curved is the contribution of the Comptonized blackbody to that spectrum. The short dashed curve shows the equilibrium spectrum computed omitting thermal Comptonization (but including the effects of an increased photon escape time due to $\tau_T > 1$), i.e., the underlying non-Comptonized non-thermal power law and blackbody. Note the dramatic "amplification" of the non-thermal power law by thermal Comptonization. The dot-dashed and dotted curves are respectively the spectra of eqn. 2.10 and 2.11 computed using the approximations of § II.

Figure 2. Spectra computed in the same manner as for Fig. 1 but with input parameters $\ell_s = 200$ and $\ell_h = 40$ (dotted curve; $y \ll 1$, negligible thermal Comptonization), $\ell_h = 200$ (solid curve; prominent soft excess), $lh = 1000$ (short dashed curve; significant thermal Comptonization, "amplified" non-thermal power law dominates). The long dashed curve shows the un-Comptonized input blackbody spectrum (with temperature $\theta_s = 1 \times 10^{-5}$).

Figure 3. A schematic representation of the source region used in the model of § III.

Figure 4. Composite spectra from pair cascade sources located above a slab of cold material. The parameters of different models are given in Table 1. The solid and dotted curves in Figs. 4a, b, c, d correspond to models a, b, c, d numbered 1 and 2 in Table 1, respectively. See § III for discussion. The K_α iron line at 6.4 keV is not included. The normalization of the spectra correspond to emission of the nonthermal source on one side of the slab of cold matter.

TABLE 1

Parameters and Results for the Models Presented in Section III

ℓ_h	ℓ_s	kT_s[eV]	kT_C[keV]	τ_T	a	$\ell_{0.1-1\mathrm{keV}}$	$\ell_{2-20\mathrm{keV}}$	$\alpha_{2-20\mathrm{keV}}$	model
100	100	10	2.8	3.6	0.15	28	24	0.68	a1
100	300	13	1.2	3.5	0.15	120	23	0.70	a2
300	100	10	2.4	7.6	0.12	98	92	0.82	b1
300	300	13	1.3	7.1	0.11	210	74	0.85	b2
30	37.5	7.8	5.0	1.5	0.17	3.5	6.9	0.66	c1
100	125	11	2.4	3.6	0.15	33	24	0.68	c2
60	315	13	0.90	2.5	0.16	110	13	0.69	d1
180	345	14	1.2	5.1	0.13	190	42	0.75	d2

Notes: $\gamma_{\max} = 2000$, $R = 10^{14}$ cm in all models. The quantity a is the integrated slab albedo (see § 3).

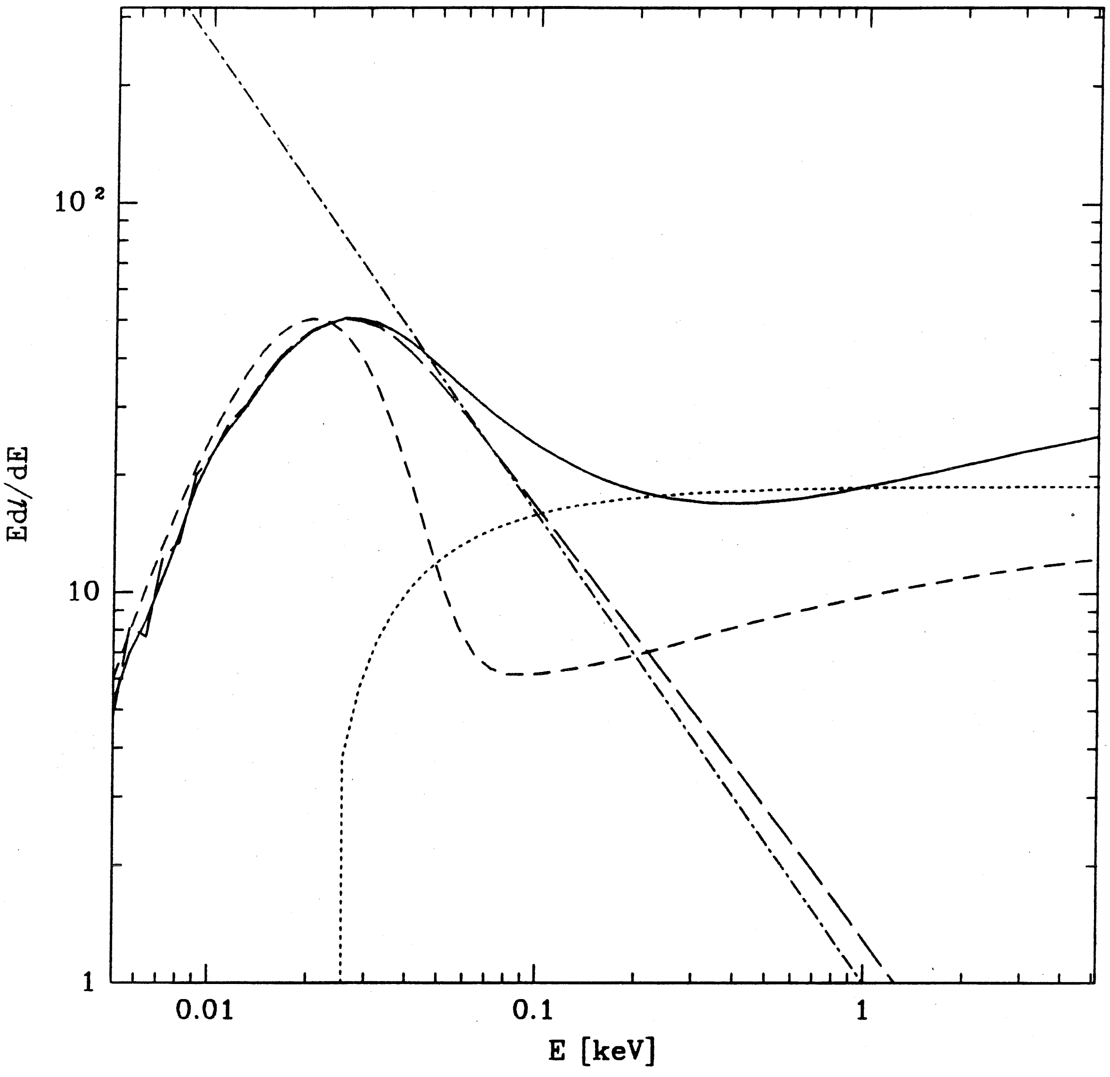

Figure 1

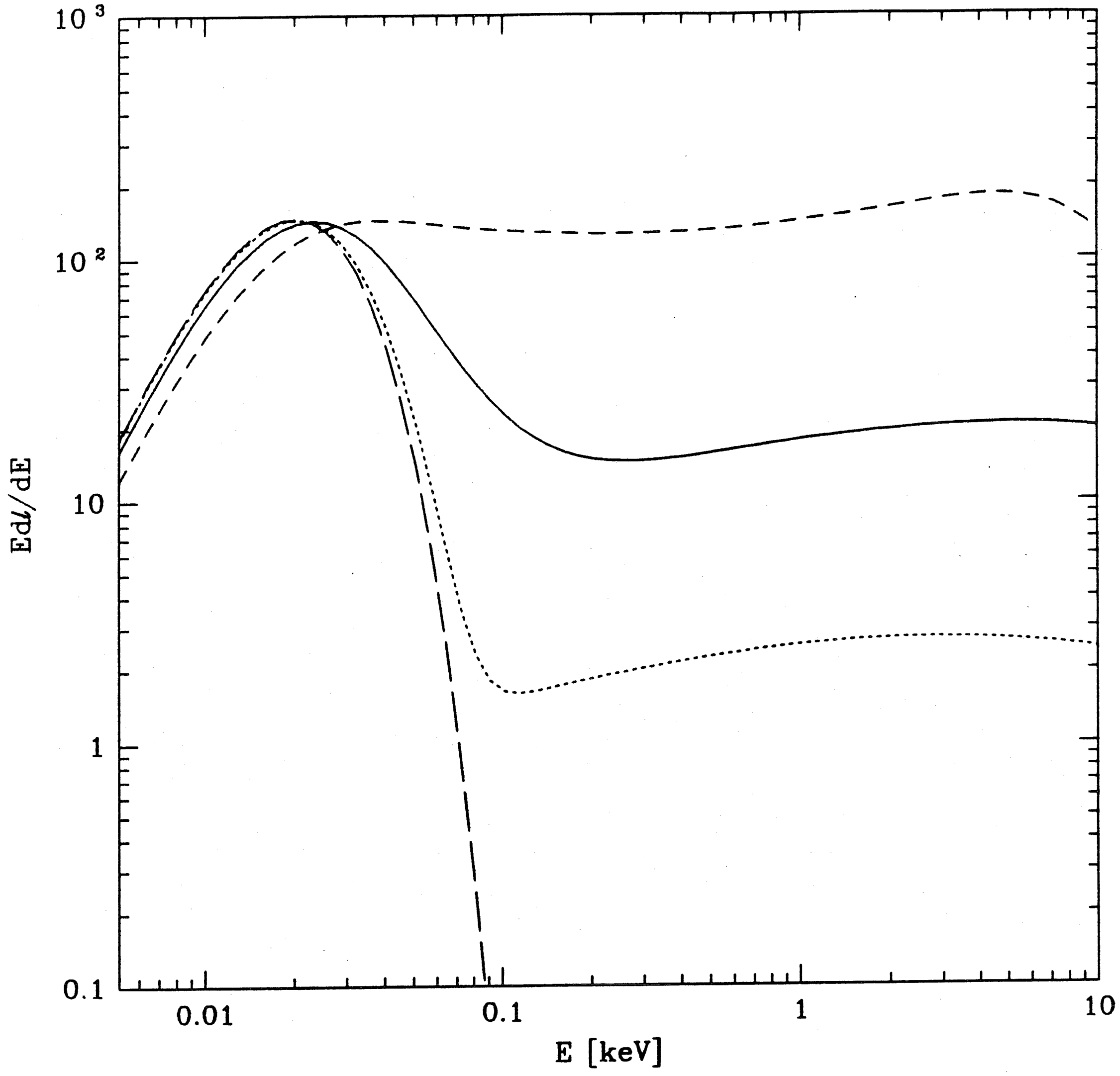

Figure 2

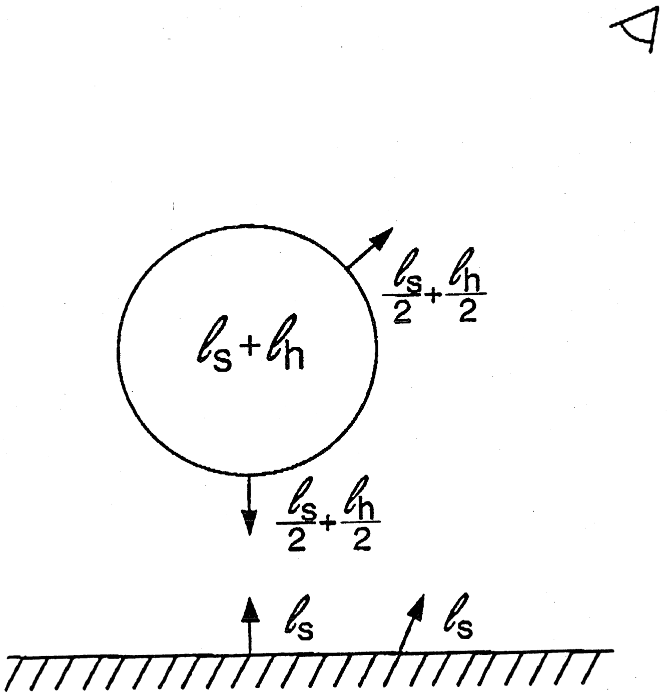

$\ell_s + \ell_h$
$\frac{\ell_s}{2} + \frac{\ell_h}{2}$
$\frac{\ell_s}{2} + \frac{\ell_h}{2}$
ℓ_s
ℓ_s

Figure 3

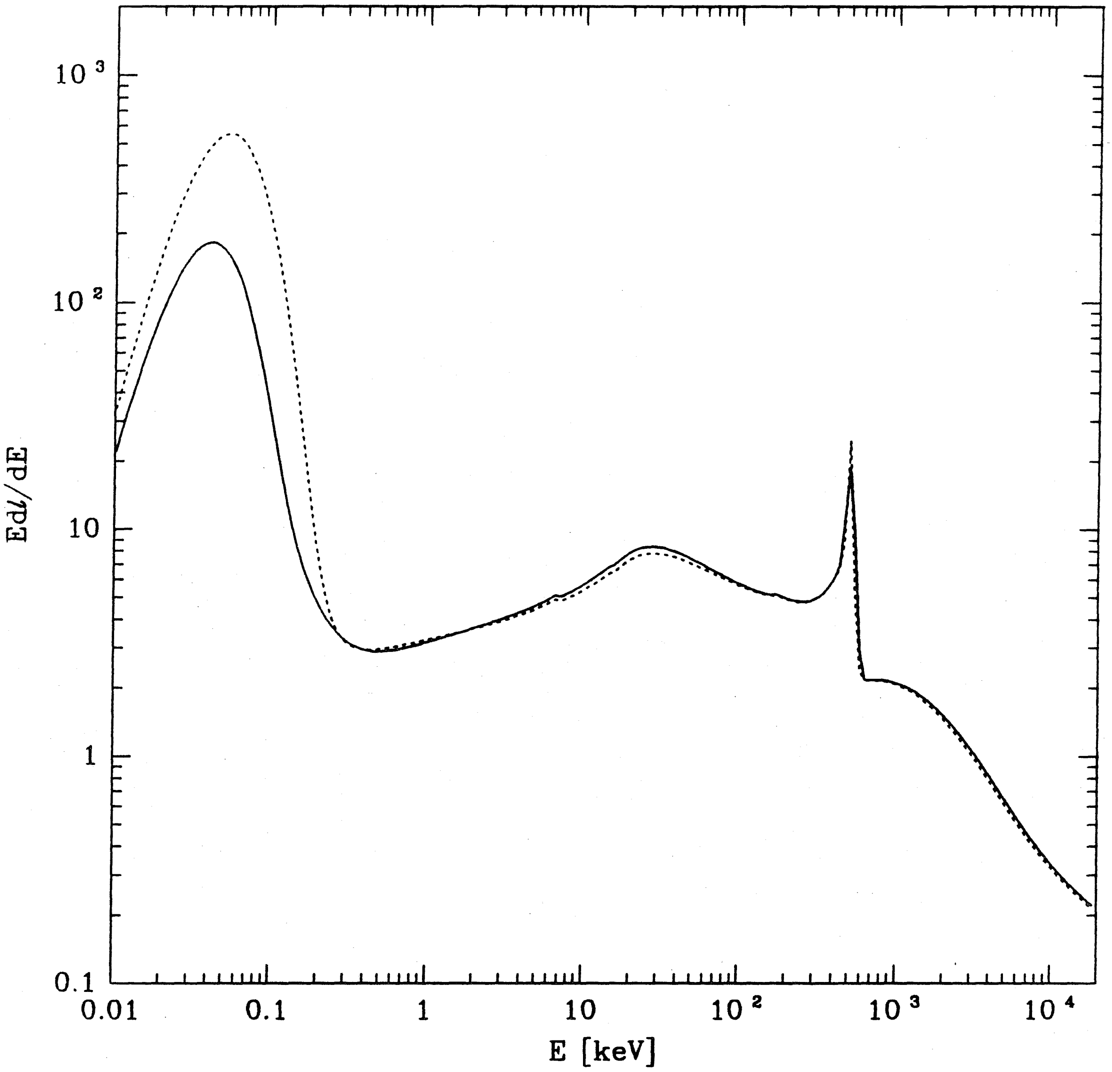

Figure 4a

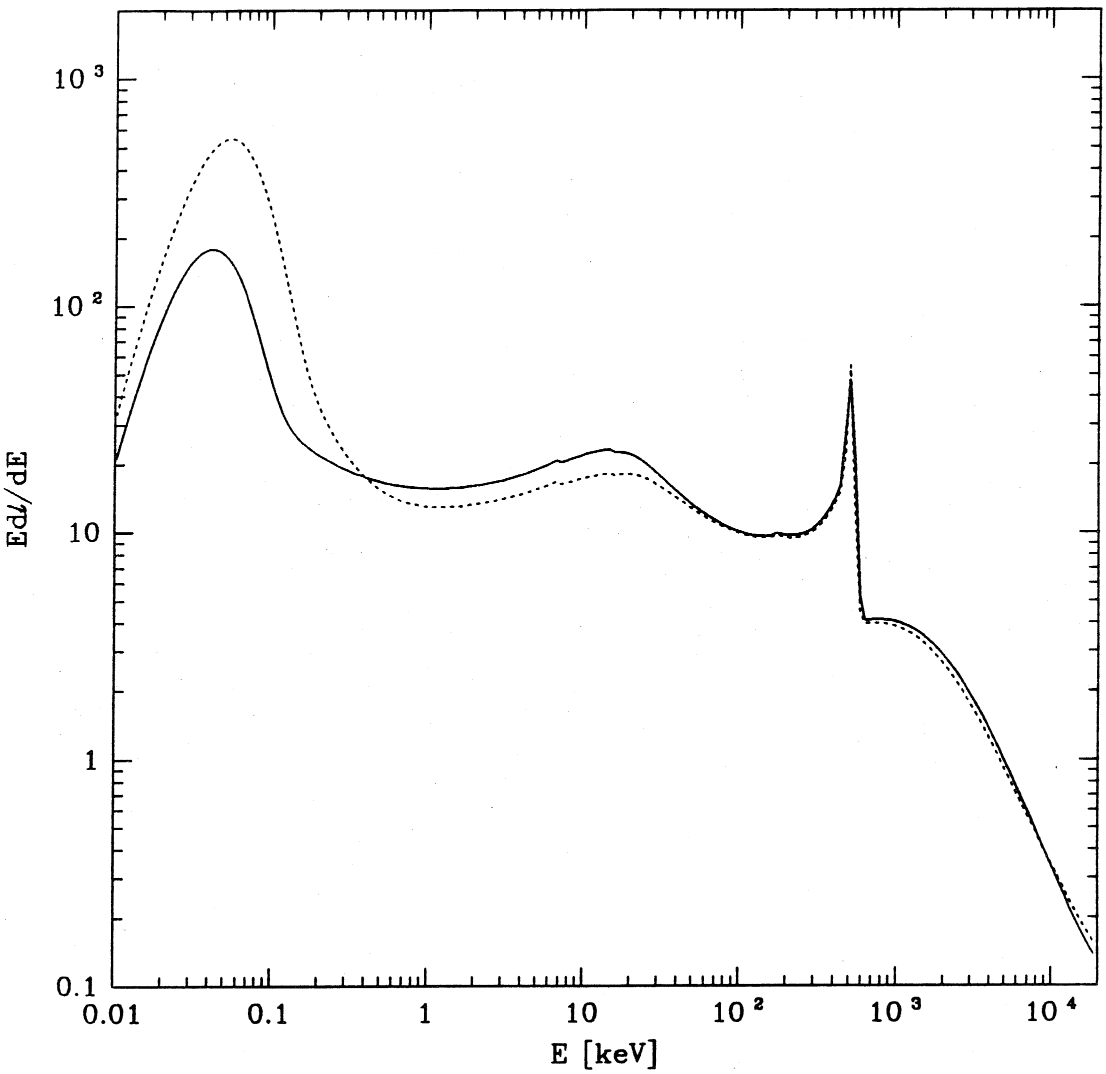

Figure 4b

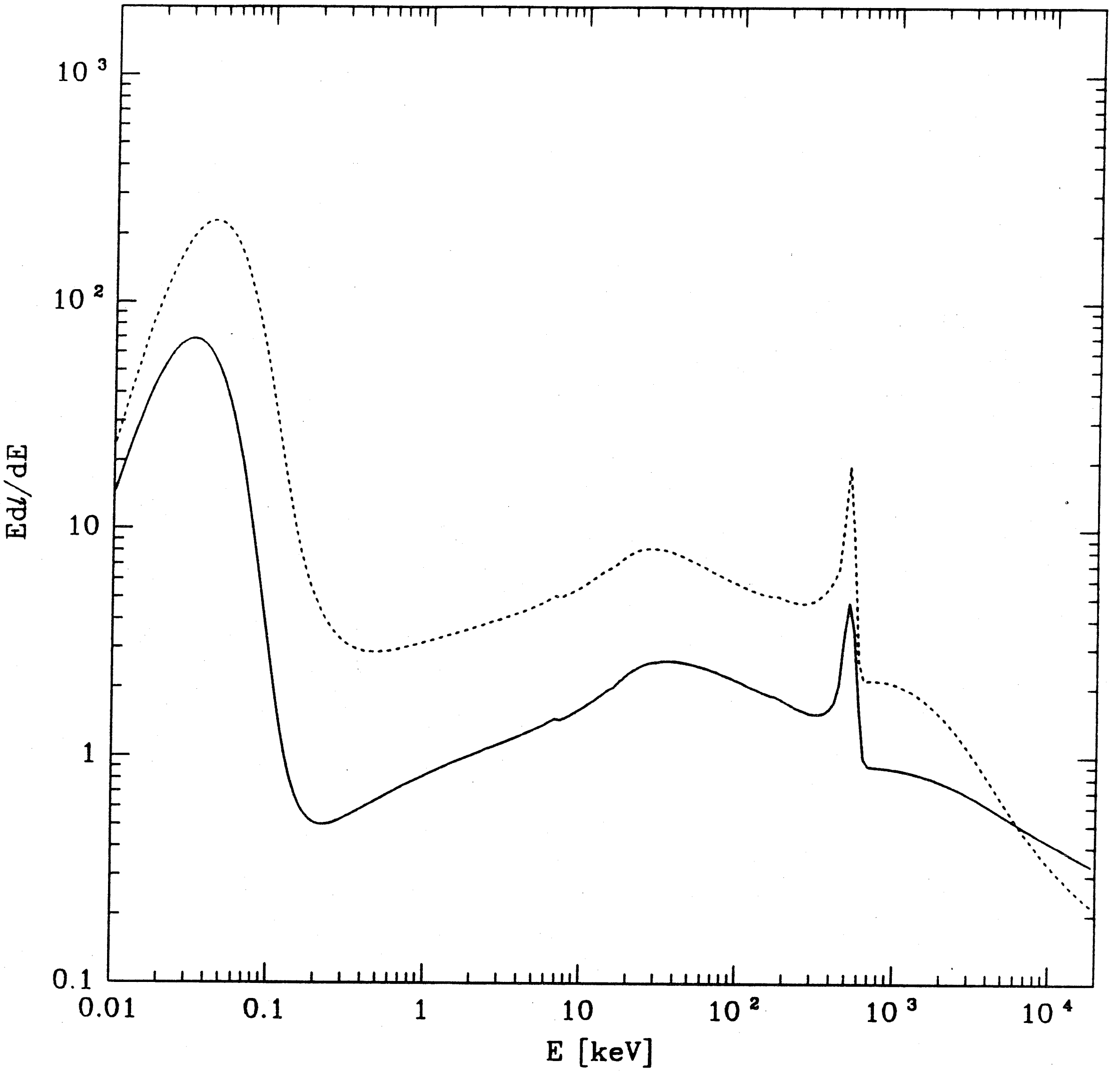

Figure 4c

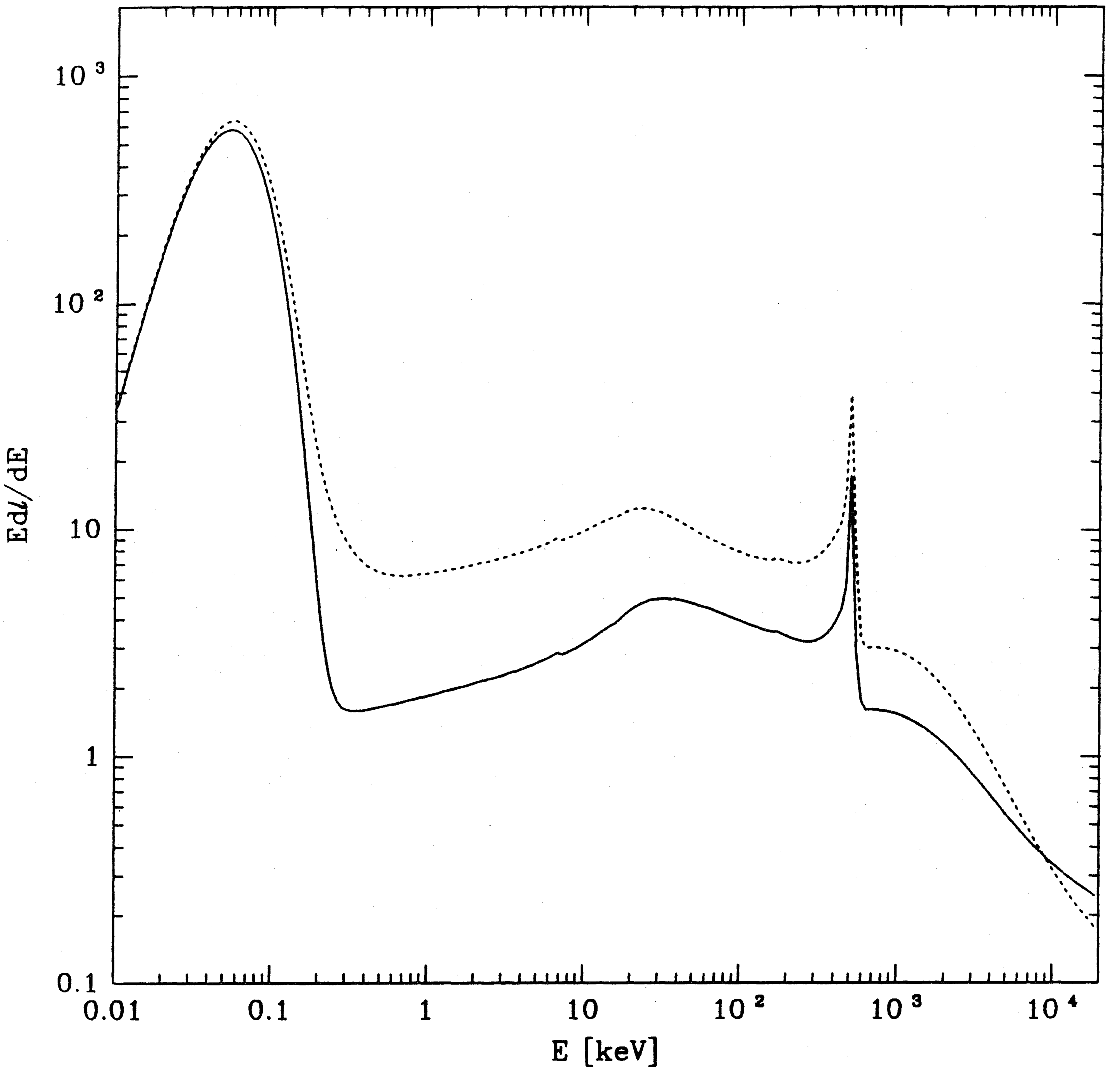

Figure 4d